Numerical Investigation of Echogenicity for 3D-Printed Tissue-Mimicking Material Toward the Development of Synthetic Organs' Digital Twins

Hossein Kamalinia

THESE DE DOCTORAT

NNT : 2023UPAST102

Numerical Investigation of Echogenicity for 3D-Printed Tissue-Mimicking Material Toward the Development of Synthetic Organs' Digital Twins

Étude numérique de l'échogénicité des matériaux imprimés en 3D imitant les tissus pour le développement de jumeaux numériques d'organes synthétiques

Thèse de doctorat de l'université Paris-Saclay

Thèse préparée à CentraleSupélec, Laboratoire de Mécanique Paris-Saclay(LMPS).
École doctorale n° 579 : sciences mécaniques et énergétiques, matériaux et géosciences (SMEMAG)
Spécialité de doctorat: mécanique des solides
Graduate School : Sciences de l'ingénierie et des systèmes, Référent : CentralSupélec

Thèse préparée dans l'unité de recherche LMPS - Laboratoire de Mécanique Paris-Saclay (Université Paris-Saclay, CentraleSupélec, ENS Paris-Saclay, CNRS) sous la direction de Bing TIE, Chargée de recherche, HDR, le co-encadrement de Andrea BARBARULO, Maître de conférences, et Elsa VANNAT, Professeure des Universités.

Thèse soutenue à Paris-Saclay, le 13 juillet 2023, par

Hossein KAMALINIA

Composition du jury

Alain LHÉMERY Directeur de recherche, Université Paris-Saclay	Président
Michael BRUN Professeur, Université de Lorraine	Rapporteur
Bruno LOMBARD Directeur de recherche, Aix-Marseille Université	Rapporteur
Anne-Sophie BONNET-BEN DHIA Directrice de recherche, Ensta Paris	Examinatrice
Thomas HEUZÉ Maître de conférences, Ecole Centrale de Nantes	Examinateur

Acknowledgement

First and foremost, I would like to express my sincere gratitude to my supervisors, Bing Tie, Andrea Barbarulo, and Elsa Vennat. They dedicated countless hours to our weekly meetings, helped me prepare every single conference presentation, and provided invaluable guidance throughout this exciting and challenging journey. Despite their busy schedules, they always made time for me and patiently explained everything I asked about. I started working with Elsa from my Master's degree internship; I'm so glad that she believed that I was the right person for this job. Andrea was the person everybody needs as a supervisor, someone you can approach with any question or problem and come back with an answer. His guidance significantly contributed to my growth as an engineer, a problem solver, and a presenter. And my special gratitude to Bing, who dedicated an extensive amount of time to review papers and equations meticulously, and helped me with debugging C++ code, regardless of whether it was a Monday morning or a Saturday evening. I was fortunate to collaborate with these three exceptional supervisors, who felt like a second family to me.

I want to convey my sincere appreciation to Biomodex and Région Île-de-France for financing this thesis. I'm incredibly grateful to all the engineers at Biomodex, with a special mention to Frédéric Champ for their professionalism, kindness, and exceptional responsiveness throughout this endeavor. I also wish to express my appreciation to the members of the jury of my thesis: Alain Lhémery, Bruno Lombard, Michael Brun, Anne-Sophie Bonnet-Ben Dhia, and Thomas Heuzé, for their valuable discussions and feedback during my defense.

My sincere gratitude also goes to all researchers and staff members in the LMPS laboratory (which was called MSSMat when I started my thesis there), as well as all my colleagues and friends, which will be a long list of the Ph.D. students of the LMPS and also SPMS Laboratory. We had a great time during the lunch breaks in our beloved coffee room, discussing a wide range of topics with our peculiar sense of humor that was not funny to everyone. I'm not writing a list of names here because it would be a very long one. My list would be all the people who read these words with a smile on their faces and some memories in their minds!

I would like to thank my close friend and neighbor, Saeed Rasouli, who has been by my side throughout the last two years of my thesis, sharing both the highs and lows of our lives. I also with to thank my close friends from nearly two decades ago, dating back to my primary school days in Iran: Ali Abasimoghadam, Mobin Akbarpour, and Peyman Samanian. My special friends from my undergraduate studies at Tehran Polytechnic, the amazing people I lived with for more than five years during one of the most critical stages of my life: Habib Molaei, Hadi Namdar, Arman Torkfar, Esmaeil Aryanpour, Mostafa Babaei, Pouya Farokhzad, and Vahid Ahmadi. I eagerly wait for the day when we can finally end the era of video calls and reunite again in person, except for Mostafa, whose memory we will forever cherish.

My lovely beautiful girlfriend Hosna whom I had the pleasure to meet at the beginning of my thesis journey, and has stood by my side ever since. Your unwavering support has meant the

world to me, and I'm incredibly fortunate to have you in my life. Thank you for your love and encouragement.

And last but not least, I want to express my heartfelt gratitude to my family—my mother, father, young sister, and 7-year-old brother. It has been a challenging four years since I last saw them in person, and their absence has weighed heavily on my heart. Their kindness, selflessness, and sacrifices have been a constant source of support in my life and have shaped me into who I am today. Witnessing my brother Parsa, growing up right before my eyes, and my sister Pegah, becoming a more wonderful person every single day, although through video calls, has been both a joy and a bittersweet reminder of the moments I've missed. Their love and presence is a cherished part of my life, and I'm deeply thankful for their enduring support.

université PARIS-SACLAY

ÉCOLE DOCTORALE
Sciences mécaniques et énergétiques, matériaux et géosciences (SMEMAG)

Titre: Étude numérique de l'échogénicité des matériaux imprimés en 3D imitant les tissus pour le développement de jumeaux numériques d'organes synthétique

Mots clés: Impression 3D, Modélisation par éléments finis, Méthode de Galerkin discontinue, Homogénéisation auto-cohérente, Propagation des ondes, Echocardiographie

Résumé: Cette thèse explore l'utilisation de matériaux imprimés en 3D imitant les tissus pour créer des jumeaux fantômes anatomiques. Ces jumeaux sont destinés à fournir aux praticiens médicaux des stations d'entraînement sophistiquées pour répéter des interventions complexes spécifiques au patient. L'objet principal de cette étude est un matériau synthétique imprimé en 3D qui imite le tissu cardiaque pour fournir des images échographiques similaires à celles du tissu biologique réel. Or, les images ultrasonores actuelles des matériaux imprimés en 3D ne correspondent pas à celles des tissus biologiques. Pour résoudre ce problème, un matériau composite à base de polymère avec une microstructure de type matrice-inclusion est en cours de développement pour reproduire les propriétés acoustiques du tissu réel. La microstructure des matériaux imprimés en 3D joue un rôle essentiel dans leur réponse aux ultrasons en raison de l'interaction ultrasons-microstructure aux longueurs d'onde d'intérêt impliquées. Cependant, la relation entre la microstructure imprimée en 3D et la réponse ultrasonique du tissu synthétique n'est pas entièrement comprise. Cette thèse vise à établir cette corrélation à l'aide de simulations numériques et d'observations expérimentales. Pour cela, des techniques numériques avancées sont nécessaires pour dépasser les limites des outils standard pour simuler avec précision la propagation des ondes dans des microstructures hétérogènes dont les longueurs caractéristiques sont du même ordre de grandeur que les longueurs d'onde propagées.

La méthode des éléments finis de Galerkin discontinu (dG) est choisie pour effectuer la simulation numérique de la propagation des ultrasons dans les composites de type matrice-inclusion en raison de sa faible dispersion numérique et de la possibilité de développer des solveurs massivement parallèles. Un cadre mathématique unifié pour la propagation des ondes acoustiques et élastiques est présenté et des flux numériques upwind pour les interfaces acoustiques-acoustiques, élastiques-élastiques et acoustiques-élastiques sont développés en résolvant le problème de Riemann. Le solveur dG couplé acoustique-élastique basé sur ces flux numériques est implémenté et ensuite validé par comparaison avec la solution analytique d'un domaine acoustique contenant une inclusion élastique circulaire. En utilisant le solveur dG développé, une approche numérique par éléments finis est introduite pour étudier le comportement de diffusion de la microstructure et estimer la vitesse de phase et le coefficient d'atténuation induit par la diffusion. Cette approche numérique est validée par comparaison avec la solution analytique obtenue à partir du cadre d'homogénéisation auto-cohérent proposé par Willis. Les propriétés élastiques du milieu effectif peuvent être obtenues analytiquement, ainsi que la vitesse de phase et le coefficient d'atténuation. L'approche numérique validée est ensuite utilisée pour estimer la vitesse de phase et le coefficient d'atténuation pour les tissus synthétiques imprimés en 3D, en tenant compte des différentes caractéristiques de la microstructure. Un modèle numérique simplifié du transducteur à ultrasons est également proposé et développé pour simuler la propagation des ondes dans la microstructure des matériaux imprimés en 3D pour la reconstruction de l'image B-mode ultrasonore. Un algorithme de reconstruction d'image est utilisé et l'échogénicité des tissus synthétiques avec différentes caractéristiques microstructurales est comparée quantitativement. La forme réelle des inclusions imprimées en 3D est également observée expérimentalement et incorporée dans la simulation numérique.

Title: Numerical Investigation of Echogenicity for 3D-Printed Tissue-Mimicking Material Toward the Development of Synthetic Organs' Digital Twins

Keywords: 3D printing, Finite element modeling, discontinuous Galerkin method, Self-consistent homogenization, Ultrasonic wave propagation, Echocardiography

Abstract: This thesis explores the use of tissue-mimicking 3D-printed materials to create anatomical phantom twins. These twins are intended to provide sophisticated training stations for medical practitioners to rehearse patient-specific interventions. The main target of this study is a 3D-printed synthetic material that mimics cardiac tissue to provide ultrasound images similar to those of real biological tissue. However, the current ultrasound images of the 3D printed material do not match those of biological tissue. To overcome this problem, a polymer-based composite material with a matrix inclusion microstructure is being developed to replicate the acoustic properties of real tissue. The microstructure of 3D printed materials plays a critical role in their response to ultrasound due to the ultrasound-microstructure interaction over the involved wavelengths. However, the relationship between the 3D printed microstructure and the ultrasonic response of the synthetic tissue is not fully understood. This thesis aims to step toward establishing this correlation using numerical simulations and experimental observations. For this, advanced numerical techniques are required to overcome the standard tools' limitations to accurately simulate wave propagation in heterogeneous microstructures with characteristic lengths of the same order of magnitude as the propagated wavelengths.

The discontinuous Galerkin (dG) finite element method is chosen to perform the numerical simulation of ultrasound propagation in matrix-inclusion composites due to its low numerical dispersion and the possibility of using the solver on supercomputers with massively parallel solvers. A unified mathematical framework of the acoustic and elastic wave propagation is presented, and upwind numerical fluxes for acoustic-acoustic, elastic-elastic, and acoustic-elastic interfaces are developed by solving the Riemann problem. The coupled acoustic-elastic dG solver based on these numerical fluxes is implemented and then validated by comparison with the analytical solution of an acoustic domain containing a circular elastic inclusion. Using the developed dG solver, a finite element-based approach is introduced to study the scattering behavior of the microstructure and estimate the phase velocity and scattering-induced attenuation coefficient. This numerical approach is validated by comparing it to the analytical solution obtained from Willis' self-consitent homogenization framework. The elastic properties of the effective medium can be analytically obtained, as well as the phase velocity and attenuation coefficient. The validated numerical approach is subsequently used to estimate the phase velocity and attenuation coefficient for 3D-printed synthetic tissue, considering different microstructure characteristics. A simplified numerical model of the ultrasound transducer is also proposed and developed to simulate wave propagation in the microstructure of 3D-printed materials for B-mode ultrasound image reconstruction. An image reconstruction algorithm is used, and the echogenicity of synthetic tissues with different microstructural characteristics is quantitatively compared. The actual shape of 3D printed inclusions is also observed experimentally and incorporated into the numerical simulation.

Table of Contents

Introduction

Phantom anatomical twins have become increasingly popular in various surgical procedures for planning and simulating operations, developing new surgical instruments, and training purposes. However, these phantoms are limited in their anatomical precision and fabrication from hard plastics with inconsistent material properties from the target organ. The use of 3D printing technology has provided the ability to manufacture synthetic organs that are geometrically identical, but the lack of knowledge and control over the characteristics of printed materials and their physical properties is not fully understood. In order to address these issues and improve the technology, Biomodex®, a startup company based in Paris, aims to create sophisticated training and personalized rehearsal solutions for physicians through the utilization of 3D printing technology. By providing medical practitioners with practical training tools, Biomodex aims to improve patient outcomes and reduce the risks associated with medical procedures.

This thesis focuses on the study of synthetic tissue-mimicking 3D-printed materials and their ultrasonic behavior, with the goal of mimicking the acoustic characteristics of biological tissues with different material properties and microstructures. The microstructure of the 3D-printed material plays an important role in the ultrasonic response due to the ultrasound-microstructure interaction within the high-frequency range of ultrasonic imaging. To achieve this goal, a combination of numerical modeling and experimental observations will be used to guide the printing of materials with a desired microstructure.

The first chapter is dedicated to a review of the tissue-mimicking anatomical phantoms and focuses on Biomodex's solution for a 3D-printed anatomical phantom with a matrix-inclusion composite microstructure. This particular phantom is used for training surgeons in a cardiovascular intervention called left atrial appendage closure (LAAC) and is designed to replicate the acoustic properties of cardiac tissue and provide similar ultrasonic images to those of the actual heart. Furthermore, the chapter discusses ultrasonic imaging in detail, including the working principle of transducers, various image modes, and the stages involved in reconstructing medical images. A literature review on wave scattering in matrix-inclusion composites is also presented. Finally, the chapter explores the previous works on the discontinuous Galerkin finite element method, which is the numerical technique used to simulate wave propagation in this thesis.

In the second chapter of this thesis, we present the discontinuous Galerkin finite element method used for ultrasonic wave propagation simulation. The chapter begins by explaining the mathematical framework for acoustic and elastic wave propagation, using an intrinsic tensorial notation to develop a unified strong form and variational formulation. The eigenstructure of the governing hyperbolic systems is then analysed. The chapter then proceeds to develop the numerical fluxes for acoustic-acoustic, elastic-elastic and acoustic-elastic interfaces by solving the corresponding Riemann problem and presenting their explicit closed-form expressions. The coupled acoustic-elastic dG solver is then validated through numerical/analytical comparison, which considers an example of an acoustic domain containing a circular elastic inclusion.

The third chapter begins by introducing the analytical framework proposed by Willis *et al.* for determining the phase velocity and attenuation coefficient in matrix-inclusion composites with randomly distributed inclusions. This involves employing a self-consistent scheme to replace the heterogeneous composite medium with a homogenous material, which enables the study of harmonic wave propagation. The chapter then proceeds to present a finite element-based numerical approach that allows for calculating the numerical attenuation coefficient. A comparison is made between the analytical and numerical results for a specific composite, and the differences are quantified. The validated numerical results are subsequently utilized to estimate the phase velocity and attenuation coefficient for the 3D-printed synthetic tissue, considering the area fraction of inclusions, size, and material properties.

The fourth chapter is dedicated to numerically modeling the ultrasonic transducer and simulating the ultrasonic wave propagation within the microstructure of the 3D-printed material. In this chapter, we tackle a coupled acoustic-elastic wave propagation problem since a layer of water surrounds the layer of 3D-printed material. This layer of water represents the presence of blood in the actual cardiovascular intervention. The simulation results are used to reconstruct ultrasonic images associated with different microstructure characteristics, including area fraction and size of the inclusion. On the other hand, the printed material's real microstructure is acquired through experiments to attain a more precise comprehension of the printed tissue. Eventually, this experimental data serves as the input for numerical simulation, resulting in more realistic outcomes.

The fifth and final section of this thesis encompasses the conclusions drawn from the research findings and provides insights into potential future work based on this work.

Chapter 1
State of the art

Contents

1.1 Patient-specific tissue-mimicking phantoms

Phantom anatomical twins, used for planning and simulating operations, developing new surgical instruments, and training purposes, have become increasingly popular due to their advantages over animal models. Despite their vital role in research, animal models have several disadvantages, including ethical considerations, different morphology and tissue properties from human organs, expensive preparation, and rapid degradation [1]. Anatomical phantoms are currently being used in various surgical procedures, such as operative urology and craniofacial surgery [1, 2], despite their limited anatomical precision and fabrication from hard plastics with inconsistent material properties from the target organ [1,3]. Moreover, phantoms can be tailored to simulate specific tissues when imaged with different modalities, including ultrasound [4], computed tomography (CT), and magnetic resonance imaging (MRI), and novel imaging techniques such as photoacoustics [5].

Nowadays, advancements in 3D-printing technology provide unique opportunities to create patient-specific anatomical twins. This technology has demonstrated diverse applications in medical education, such as teaching the structure of different body organs, including the heart, kidney, and liver [6–8]. Studies have explored the feasibility of generating such models through 3D-printing techniques, including creating vascular models, cranial models, optic nerves, and the renal system. Although several studies have described the process of converting medical imaging data into 3D printed models, such as for the brain and the human sinus [9–16].

The whole process of creating the anatomical phantom, after the acquisition of the medical image, could be generally divided into three steps: (1) image segmentation, (2) surface reconstruction and refinement, and (3) printing process (see Figure 1.1). Image segmentation involves dividing the image into labeled regions to locate objects and boundaries. Basic segmentation approaches rely on the range of pixel intensities to distinguish between different tissue types and identify their boundaries. After image segmentation, the 3D model can be refined using various computer-aided design tools. The post-processing of segmentation is necessary for repairing errors and discontinuities, smoothing out the surfaces, and appending the segmentation to other structures. These steps are crucial for producing a printable and accurate 3D model [17].

Among all the suitable 3D-printing techniques for creating anatomical phantoms, three groups are more common: extrusion printing, photopolymerization, and powder-based printing. Extrusion printing involves melting and depositing material through a nozzle, while photopolymerization involves selectively curing liquid polymers. In powder-based techniques, a powdered material is bound together either by using a liquid binding agent or by fusing the particles using heat. Table 1.1 reports the mentioned 3D-printing techniques with their advantages and disadvantages and some examples of their medical application. 3D printing could also be combined with other manufacturing techniques to create an anatomical phantom. Adams *et al.* use 3D wax printing in combination with molding to create a kidney phantom using three different materials: agarose gel, silicone elastomer, and polydimethylsiloxane (PDMS) [1]. As an example, Figure 1.2 shows the ultrasound images of these three phantoms compared to a real human kidney.

The main focus of this thesis is studying the phantom twins that mimic the acoustic properties of the biological tissue under ultrasonic imaging in interventional cardiology procedures such as Left Atrial Appendage Closure (LAAC). Nowadays, in cardiology, open surgery is being replaced by so-called

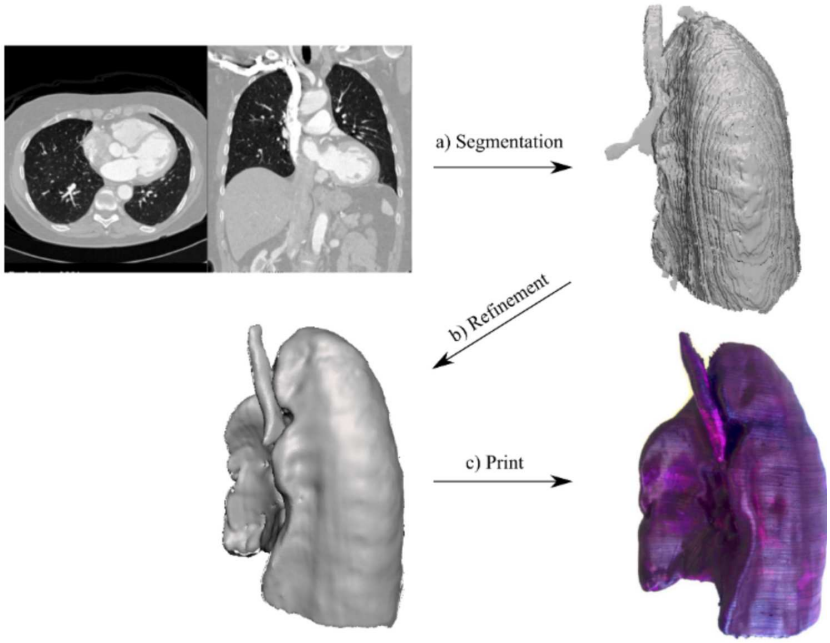

Figure 1.1. The workflow from medical image to 3D-printed anatomical phantom: (a) image segmentation, (b) surface reconstruction and refinement, and (c) 3D-printing process [17]

Table 1.1. Several important 3D printing technologies with medical applications [17]

Printing techniques	Advantages	Disadvantages	Examples of medical application
Extrusion printing: Filament Deposition Modelling (FDM)	• Low material costs • Low cost printers available • Simple to use	• Rippled and porous surface • Fragile along z-axis	• Kidney • Liver • Sinus
Photopolymerisation: Stereolithography (SLA) & Digital Light Processing (DLP)	• Moderate cost • Good surface finish / high resolution	• Prints are prone to slight distortions • Curing resins need to be handled with care	• Prosthetics
Photopolymerisation: Material Jetting (MJ)	• Very good surface finish / high resolution • Ability to gradually combine different polymers	• High material cost • Curing resins need to be handled with care	• Vessels • Spine
Powder Binding: Binder Jetting (BJ)	• Can include colour • Quick • Low material costs • Many materials available	• Printers are expensive • Rough surface finish	
Powder Binding: Selective Laser Sintering (SLS)	• Prints are strong • Many materials available	• Printers are expensive • Rough surface finish	• Brain • Heart

minimally invasive endovascular procedures. This emerging field, known as interventional cardiology, involves using real-time medical imaging techniques to guide the procedures. Among these techniques, ultrasonic imaging tends to become a standard since it is inexpensive and non-invasive. An example of an interventional cardiology procedure is the LAAC, performed due to atrial fibrillation to reduce the risk of strokes. Atrial fibrillation (AF) is a cardiac arrhythmia characterized by an irregular heartbeat rate when the two atria receive erratic electrical impulses. The heart rate in AF can increase from 100 to 175 beats per minute. Patients with atrial fibrillation are 4 to 5 times more exposed to strokes, which is responsible for 15% to 20% of all strokes, particularly among the elderly. Left atrial appendage (LAA), a small pouch connected to the left atrium, is known to be the primary source of 90% of strokes caused by blood clots in AF patients [18]. When conventional anticoagulation strategies

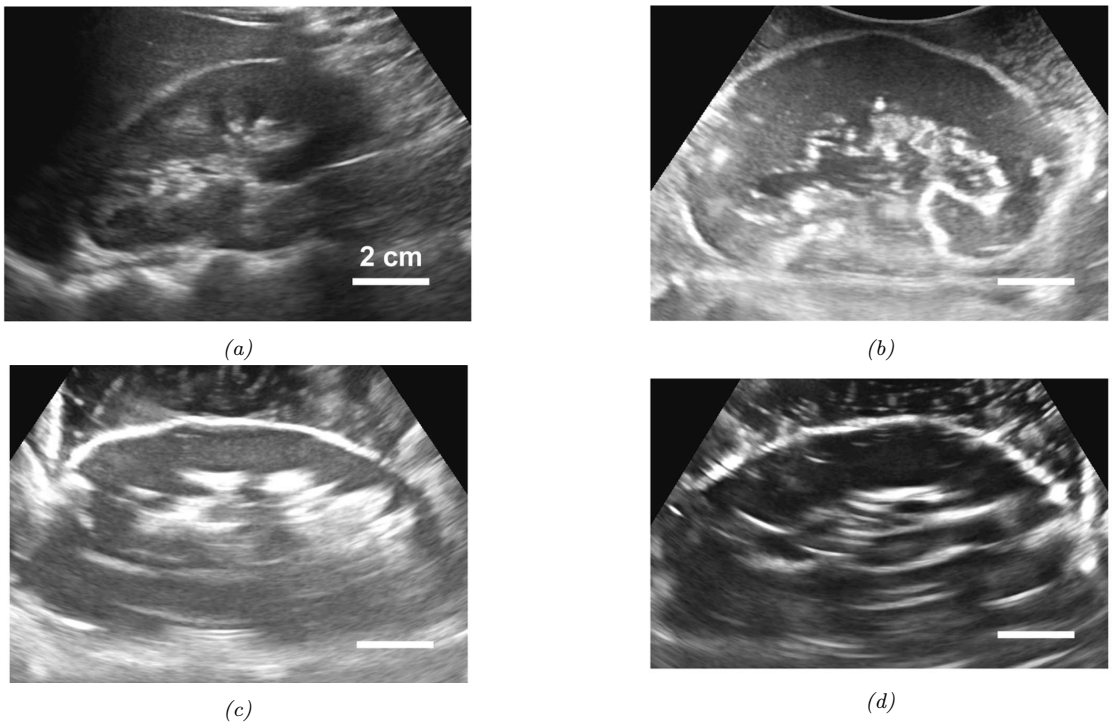

Figure 1.2. Ultrasound images of the real human kidney (a), in comparison with three phantoms made of different materials: (b) agarose gel, (c) silicone elastomer, and (d) PDMS [1]

are ineffective in reducing the risk of blood clots in the LAA, doctors may recommend LAAC as an alternative. This procedure is typically performed under general anesthesia, during which a delivery catheter is inserted through the femoral vein (in the groin area) and guided up to the heart. This delivery catheter carries a device to occlude the LAA that prevents the blood clots formed in the LAA from entering the bloodstream. After reaching the right atrium, the catheter is maneuvered through the tissue separating the two atria to reach the left atrium. The catheter is then guided toward the LAA, where the occluding device is permanently implanted. Ultrasonic imaging is used continuously to verify the path of the catheter and ensure precise navigation by physicians. Figure 1.3 illustrates a section of the heart during the LAAC intervention. A challenge associated with this intervention is that the shape of LAA is patient-specific, meaning that it differs from one patient to another. Biomodex **LAACS**™ (Left Atrial Appendage Closure System) product, illustrated in Figure 1.5a, is a 3D-printed anatomical twin that is used in LAAC interventions designed to provide a training experience that closely resembles the actual procedure. This LAACS cartridge is along with a designed station. The station provides a path for the transducer and the catheter, similar to the actual intervention. The cartridge is submerged in water, which simulates the blood present in the atria. However, the motion of the blood is not considered in the simulator. Figure 1.4 shows the LAACS simulator station with the cartridge in it. The ultrasonic transducer is navigated through a designated path to the back of the cartridge and provides the image. On the other hand, the catheter is also navigated to the LAACS cartridge from the other considered path in the station on the opposite side. One of the challenges that physicians face during cardiovascular interventions, such as LAAC, is the need for accuracy when navigating catheters through the heart to avoid damage to heart tissue. Therefore, the synthetic organ must closely mimic the acoustic properties of the heart to provide a similar echocardiography image

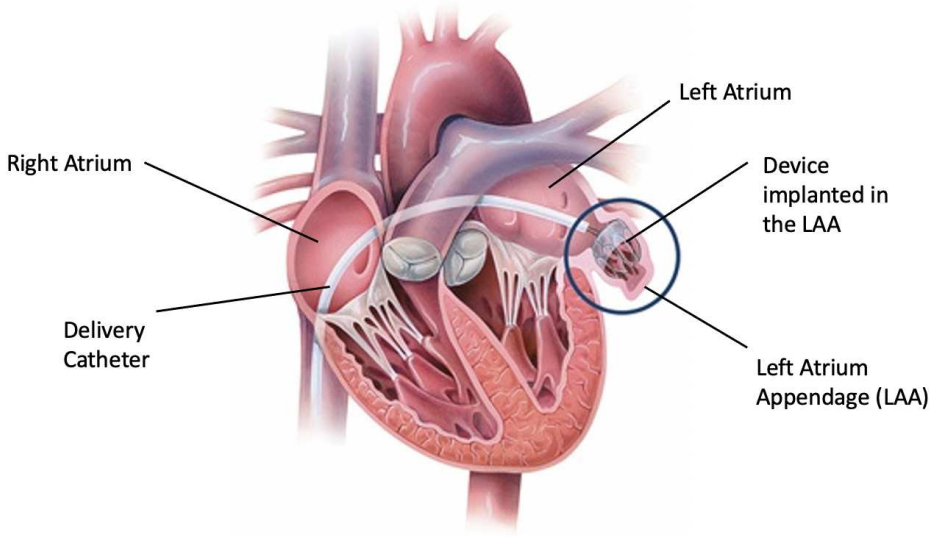

Figure 1.3. Schematic depiction of a section of heart in LAAC intervention [Web Source: John Hopkins Medicine]

and create an accurate training experience, which is a complicated task considering that the materials available in this 3D printer is very different from the biological tissues. Figure 1.5 shows an LAA Closure System (LAACS) 3D-printed by Biomodex and acomparison between the 2D echocardiography image of the LAACS during the intervention and an actual heart in the clinic.

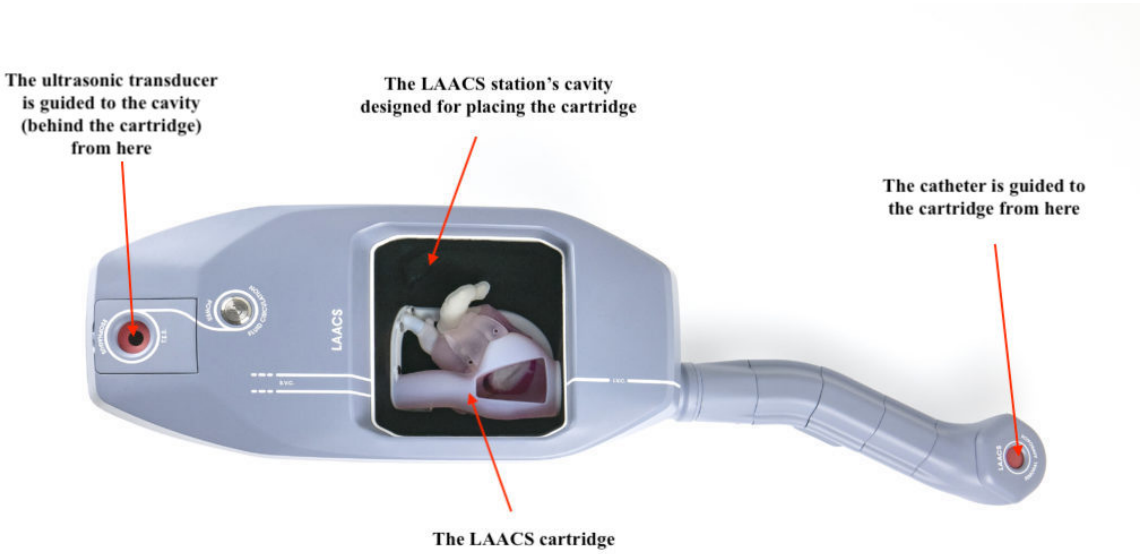

Figure 1.4. LAACS simulator station and the cartridge. The ultrasonic transducer is navigated to the back of the cartridge. The catheter is also navigated to the LAACS cartridge from the another considered path. [Biomodex's internal report]

Looking at Figure 1.5b, one can observe that the 2D echocardiography image obtained from the LAACS product is not always sufficiently compatible with the actual heart. This lack of compatibility includes the unclear depiction of the interface between the left and right atrium and the loss of some details at the bottom right side of the image.

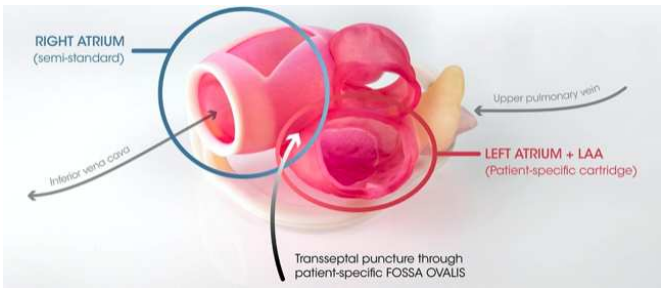

(a)

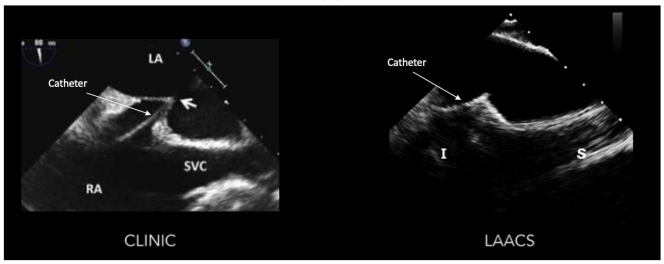

(b)

Figure 1.5. (a) LAA Closure System (LAACS), 3D-printed by Biomodex (b) 2D echo of LAACS during the intervention, compared to the real heart in the clinic [Biomodex's internal report]

1.1.1 MultiJet 3D-printing technology

Biomodex uses a particular MultiJet 3D-printing technology for creating tissue-mimicking phantoms. The multiJet 3D printer works by depositing layers of liquid photopolymers onto a build platform, which are then cured by UV light. This 3D printer can print multiple different materials simultaneously, with a resolution of less than 30µm in the "high quality" mode of printing, creating objects with a wide range of colors, textures, and material properties. Here are the most important base materials available in the 3D printer:

- **RTOP materials**: a family of Rigid Transparent or Opaque Polymer materials known for their strength, durability, and dimensional stability. A wide range of these types of materials with different properties and colors are offered.

- **ERLE material**: an Enhanced Rubber-Like Elastomer material ideal for applications requiring high elasticity and durability components. It is a soft, flexible, and tear-resistant material available again in different opaque, transparent, and translucent colors.

- **GLM**: a Gel-Like Material used as a support material for 3D-printed structures, meant to be removable with alkaline cleaning solutions or mechanically removable by hand or waterjet.

Notably, several more base materials are available in the 3D printer, including. These base materials could be mixed in different proportions to obtain new digital materials (DM) with various properties and colors. Notably, the material properties of these materials are generally different from those of the biological tissues, including the propagation speed of the ultrasonic wave. Among all the materials available in the 3D printer, the GLM has the most similar acoustic properties compared to the cardiac tissue (see Table 1.2).

Table 1.2. Material properties of the cardiac tissue and the 3D-printed materials found in the literature

Material	Frequency of measurement	ρ (kg/m^3)	C_p (m/s)
Cardiac tissue [19]	-	1060	1580
GLM [20]	20MHz	1157	1620
ERLE [21]	2MHz	1128	2090
RTOP [20]	20MHz	1179	2630

1.1.2 Microstructure of the tissue-mimicking 3D-printed material

At the microstructural level, cardiac tissues consist of multiple layers, each possessing different acoustic properties [22] that can impact the signal captured by the ultrasonic probe and, ultimately, the resulting medical image. This complicated, multilayered microstructure of the cardiac tissue yields sufficient contrast to visualize the tissue's thickness during ultrasonic imaging. Biomodex proposes a sandwich composite microstructure to achieve echogenicity similar to biological tissue using synthetic 3D-printed material. The proposed microstructure uses GLM as the matrix material, acting as the primary wave propagation medium due to its comparable acoustic properties to biological tissue. To create sufficient contrast in the ultrasonic image and visualize the entire thickness of the layer, spherical inclusions with varying wave propagation properties are dispersed throughout the gel matrix. The difference in acoustic impedances between GLM and other PolyJet materials scatters the wave, and the reflected wave from the matrix-inclusion interface increases the echogenicity of the synthetic tissue. The gel-based composite is enveloped by an outer layer of PolyJet material due to the mechanical properties of the gel, which is incapable of maintaining the geometry of a patient-specific heart. During the 3D-printing process, removing the support could easily damage the composite, making the PolyJet surrounding layer necessary to prevent its destruction. Figure 1.6 depicts a schematic representation of the proposed microstructure in an arbitrary section of the 3D-printed anatomical phantom. The PolyJet inner and outer layer is illustrated in black, the spherical inclusions are in red, and the space between the PolyJet layers is filled with GLM material. The proposed microstructure does not identify which base or digital materials yield better echogenicity in the 3D-printed tissue. Furthermore, the inclusions' optimal area fraction, size, and shape for achieving the best performance remain undetermined.

1.2 Medical ultrasonic imaging

Medical ultrasonic imaging, also known as ultrasound or ultrasonography, is a medical diagnostic imaging technique that uses high-frequency sound waves to generate images of the body's internal structures, such as soft tissues, organs, and blood vessels. This technique is widely used in various medical fields, including cardiology, to evaluate heart function and diagnose heart conditions such as arrhythmia or heart valve problems [23]. According to [24], in 2000, an estimated 5 million ultrasound exams were carried out worldwide in a week.

Ultrasound imaging operates on the principles of acoustic physics, using high-frequency sound waves, which are transmitted via a transducer into the biological tissue. These sound waves propagate through the medium, interacting with various anatomical structures, and the reflections return to the transducer. Subsequently, a computer system processes the returning echoes to generate a two-

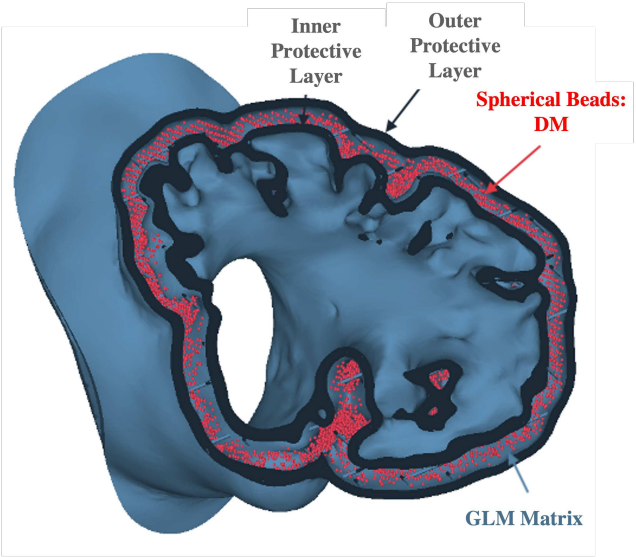

Figure 1.6. Schematic representation of the proposed microstructure in an arbitrary section of the 3D-printed anatomical phantom: the PolyJet inner and outer layers in black, and the spherical inclusions in red. The space between the PolyJet layers is filled with GLM material. [Biomodex's internal report]

dimensional visual depiction or a three-dimensional reconstruction of a particular region. This imaging technique has several advantages over alternative methods such as X-rays and CT scans. One notable benefit is its non-use of ionizing radiation, which is known to pose a threat to the human body. As a result, it is considered a safer option for imaging individuals in vulnerable groups such as pregnant women and young children. Additionally, this technique can produce dynamic images, giving medical practitioners a real-time view of how organs and tissues function.

As mentioned before, medical ultrasound is a widely used medical diagnostic imaging technique due to its convenience and safety. However, specific organs are not easily accessible from the outside; it is essential to insert probes into the body to capture high-quality images, which may cause some discomfort for the patient but is imperative for obtaining precise diagnostic information. There are generally two intrusive ultrasonic imaging techniques [25]:

- **Semi invasive** imaging, in which the probes can be inserted into the body without causing any wound, such as transesophageal echo (TEE), intra-vaginal imaging, and transrectal imaging.
- **Invasive** imaging, in which a special cut is made on the body to guide the probe inside the body, such as intravascular imaging, intraventricular imaging, and laparoscopic ultrasonic imaging. Invasive methods are commonly employed in cardiovascular applications.

This thesis mainly investigates the Left Atrium Appendage Closure (LAACS) procedure guided by TEE. This technique is used to overcome the acoustic obstacles in the path from the transducer to the heart. The air in the lungs has a significantly smaller acoustic impedance than the soft tissue, which causes strong reflection at the interface. On the other hand, the acoustic impedance of the ribs (mainly made of bones) is substantially higher than those of soft tissues, which again leads to a strong reflection of the sound wave. Furthermore, the echo would be considerably attenuated while propagating through the ribs. Consequently, the probe is guided to the esophagus through the patient's mouth, schematically depicted in Figure 1.7. TEE provides a sector ultrasonic image called a B-mode

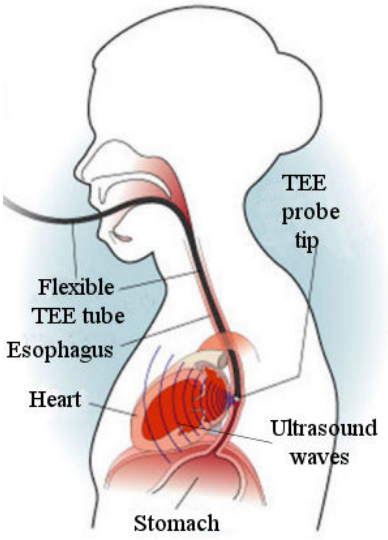

Figure 1.7. Schematic illustration of Transesophageal Echo (TEE) procedure. [Web Source]

image of different heart sections through mechanical and electronic steering. Because the esophagus is located close to the heart and no obstructions impede the transmission of sound waves, TEE can provide clear, high-quality images of the heart with both high resolution and signal-to-noise ratio [25, 26].

1.2.1 Image modes in ultrasonic imaging

In the current imaging systems that provide a discrete representation of the image, each image is represented as a matrix of numerical values, denoted as $I(i, j)$, where i and j are the horizontal and vertical coordinates, respectively. The numerical value assigned to these coordinates represents the corresponding gray level, and each gray level is associated with the smallest unit of an image called a "pixel". In three dimensions the matrix is three-dimensional, and each unit of the image represents a cube referred to as a "voxel". Moreover, here are some fundamental definitions:

- **Image Contrast**

  In imaging, contrast refers to the degree of distinguishability or difference in gray levels between an object and its surroundings and between adjacent regions in the image. This difference in intensity or gray level provides visual information that can aid in accurate and precise image analysis. A higher contrast image shows clear and well-defined boundaries between different tissue types or structures, while a low contrast image may make it more challenging to differentiate between different areas.

- **Signal-to-Noise Ratio**

  Any factor affecting the image quality that is not originated from the imaged object is considered noise. This may include random electronic signals generated by detectors, cables, or circuits and physical factors that violate the reconstruction assumptions, such as reverberations or refractions. The Signal-to-Noise Ratio (SNR) is a commonly used metric for evaluating the quality of an image.

- **Resolution**

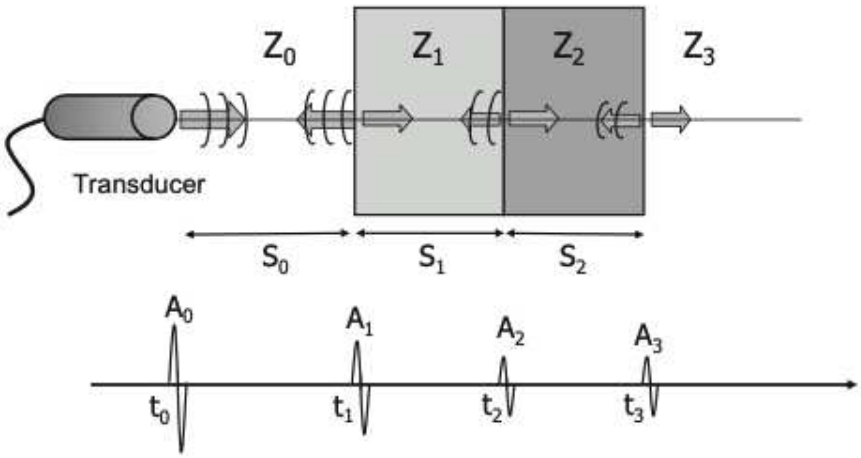

Figure 1.8. ***(top)****: Schematic illustration of ultrasonic wave propagation in a multilayer structure, excluding the reverberations.* ***(bottom)****: the corresponding A-mode signal. Z is the acoustic impedances of media, "S" is the distance and "A" is the amplitude of the signal [25].*

In evaluating the ultrasonic image quality, resolution is a crucial parameter defined in two distinct ways. The first definition, known as spatial resolution, refers to the ability of an imaging system to distinguish and capture details in the object. In other words, the smallest discernible detail that can be resolved in an image. Spatial resolution is typically expressed in the number of pixels or voxels per unit area or volume. The second definition, temporal resolution, refers to the minimum time required to complete the data acquisition process and produce an image of the tissue.

Here we introduce the main medical imaging modes: A-mode, B-mode, and M-mode.

A-mode (Amplification Modulation)

A-mode (or A-line) is the building block of pulse-echo-based ultrasonic imaging, in which the signal's amplitude is displayed on the vertical axis as a function of time or depth on the horizontal axis. This mode is commonly used in ophthalmology to measure the length of the eye [27]. To create an A-mode display, several assumptions must be made. First, it is assumed that the transmitted wave propagates through a straight line from the transducer and comes back to it in a straight line. This wave is a very short pulse in time and could be approximated by a delta function. Second, it is assumed that the targets could be considered as a set of parallel plates. Finally, it is assumed all the objects are placed perpendicular to the direction of propagation. Therefore only axial reflections and transmissions would happen. Figure 1.8 shows a schematic illustration of ultrasonic wave propagation through a multilayer structure and the corresponding A-mode signal.

B-mode (Brightness Modulation)

B-mode is the most popular imaging method that is based on the pulse-echo technique. B-mode images are created by combining many A-mode signals obtained from different lines of ultrasonic scanning and converting them into a gray-scale image. The same transducer is used to transmit and receive the ultrasound waves. Hence, only the backscattered waves are detected by the transducer. There are two common scanning strategies used in B-mode imaging: cartesian scanning and Sector

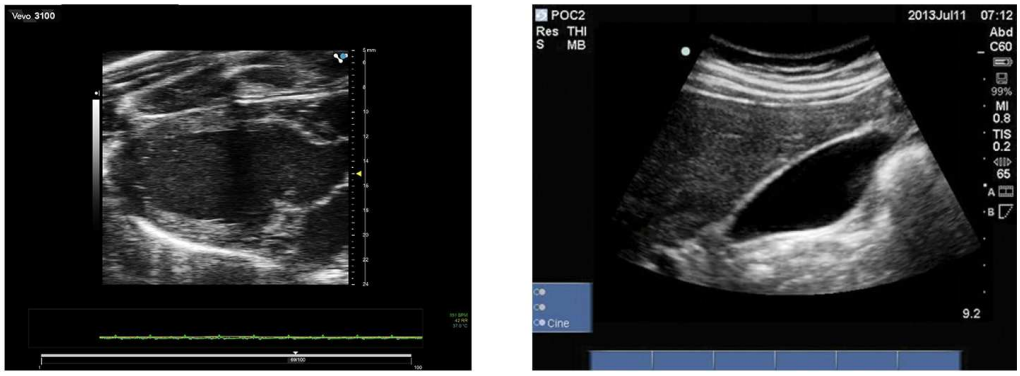

Figure 1.9. Schematic illustration of Cartesian B-mode ***(left)****, and Sector B-mode****(right)****.*

scanning. In cartesian scanning, the image is obtained by scanning the transducer in a rectangular pattern. In sector scanning, the image is obtained by scanning the transducer in a circular sector. The choice of scanning strategy depends on the area of the body being imaged and the diagnostic requirements.(see Figure 1.9).

To generate an ultrasound image from the acquired data, two additional steps are necessary. Firstly, the A-mode signal is transformed into a vector of gray levels. This process is known as contrast generation. Secondly, the gray levels are assigned to their corresponding locations in the image space, a step referred to as spatial mapping.

M-Mode (Motion Modulation)

M-mode is a widely used method for imaging, especially in echocardiography. In this technique, the transducer is positioned perpendicular to the direction of motion of a moving object, and it continuously transmits and receives echoes along the same line. The resulting image displays the distance of the object's interfaces over time. For example, when imaging a contracting heart, the M-mode image shows the variation of the heart wall thickness during the cardiac cycle. In Figure 1.10, a real-time M-mode image of a contracting heart is presented. The top part of the figure shows a 2D sector B-mode image of a section of the heart. The M-mode image of a specific line is displayed at the bottom of the figure. As the ultrasound beam penetrates deeper into the heart, the image reveals different regions, including the chest wall, right ventricle (RV) cavity, septum, left ventricle (LV) cavity, and posterior wall of the heart. The M-mode image shows the change in the LV cavity over time, which indicates the heart's contraction.

1.2.2 Medical ultrasonic Transducers

There are various sources by which the waves are created in a medium. Basically, any change in the pressure field in fluids or the stress field in solids can lead to the creation of waves. Among the most suitable options for this application are piezoelectric materials that can transmit and detect echoes within a system simultaneously. Until the early 1970s, almost all ultrasonic imaging techniques needed several seconds to generate an image. Consequently, it was not possible to observe moving targets in medical images. However, with advancements in piezoelectric element manufacturing, acoustic pulse generation, reception, and post-processing are now nearly instantaneous. Because the speed of sound in soft tissues is approximately 1540m/s and the distances of interest in medical examinations are

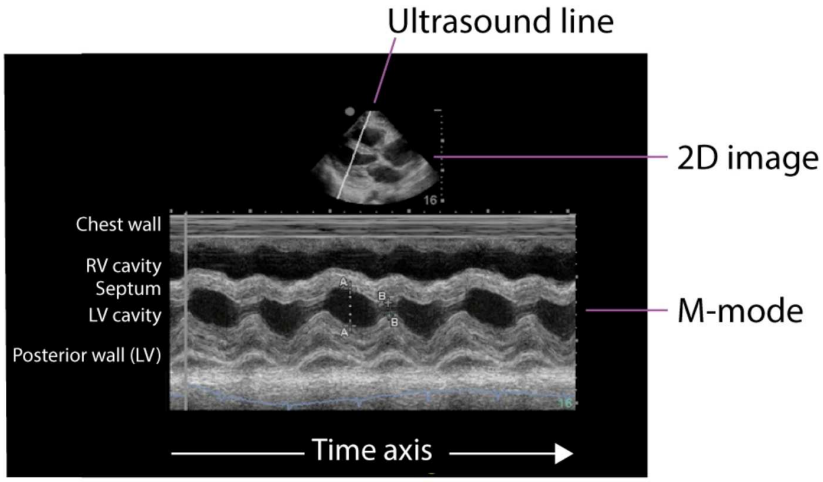

Figure 1.10. M-mode image of a contracting heart [web source].

generally a few centimeters, the duration for a wave to propagate over such distances is relatively brief (on the order of tens of microseconds). As a result, numerous waves can be transmitted quickly and provide adequate data to observe real-time dynamic changes inside the body. Nowadays, piezoelectric ultrasonic transducers have found widespread implementation in various applications, with their efficiency continually improving over time. Furthermore, these transducers can be manufactured in diverse geometries, varying in size from large 10cm diameter disks to devices smaller than a catheter's needle [25, 28].

According to the properties of piezoelectric materials, applying a voltage to them causes mechanical deformation on the opposite sides. Hence, using two electrodes soldered to two sides of the piezoelectric element, a voltage with specific characteristics is delivered to the element, and an oscillatory motion is obtained on opposite faces of the transducer. This leads to generating a wave with desired specifications, which can be transmitted to the adjacent medium. Conversely, when a wave impacts the surface of the piezoelectric material, the corresponding deformation produces a voltage in the electrodes, leading to wave detection (as illustrated schematically in Figure 1.11a). Piezoelectric crystals can be made from either natural crystals or manufactured compounds. Natural crystals such as quartz and "Rochelle salt" (sodium potassium tartrate tetrahydrate) were more commonly used in the past. However, nowadays, ceramic crystals such as PZT (lead zirconate titanate) are mostly preferred, and piezoelectric polymers like PVDF are desirable as well [25, 29].

Piezoelectric materials are usually used in a sandwich structure to attain better performance, as in Figure 1.11b. They are typically bonded to two other materials: an **impedance matching** layer at the front and a **backing layer** at the back. The impedance matching Layer is essential to achieve good efficiency since there is a substantial discrepancy between the impedance of the piezoelectric material, which is primarily a solid material (such as a ceramic crystal), and the soft tissues that are in contact with it. This mismatch results in an inefficient energy transfer between the piezoelectric element and the surrounding medium, leading to energy loss in the form of heat within the element, which can adversely impact both transmit and receive modes. This layer also serves as sacrificial protection for the transducer [30]. On the other hand, the backing layer is employed to absorb the energy transmitted to the back of the element (which is not the desired side). This layer is made of a particular material

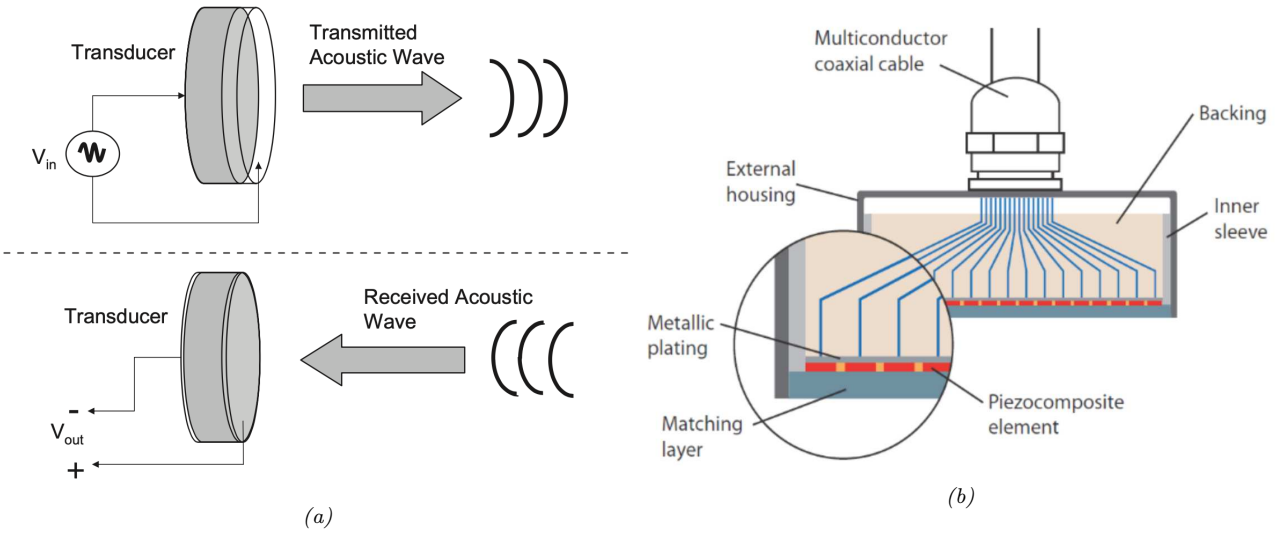

Figure 1.11. (a) Piezoelectric material working as a transmitterand a receiver [25]. (b) Multi-layer structure of the Transducer [30]

with a specific impedance and attenuation coefficient that help dampen the mechanical oscillation [25].

This thesis examines two main types of scanners that employ different beam steering techniques: (1) sequential linear array and (2) linear phased-array transducers. Sequential Linear Array Scanners are ultrasound scanners that use a specific number of transducers placed in a linear arrangement. The imaging process in this method involves the transmission of ultrasound waves by one element or a small group of elements and the reception of the echo by the same element. Each line of the B-mode image is formed through one complete transmit/receive cycle, after which the adjacent element repeats the same procedure to generate the following line in the image. The sequential image formation process produces a rectangular image with a limited field of view equal to the length of the array's line. An example of the rectangular image obtained by sequential linear array scanning is depicted in Figure 1.12a.

On the other hand, the B-mode images produced by phased array transducers rely on electronic beam steering rather than mechanical methods, allowing for precise control over the acoustic field and the ability to focus on specific regions of interest [25, 28, 31]. This technique also enables all transducer elements to be involved in producing an individual B-mode line and provides advanced signal processing capabilities beyond those available with traditional scanning methods. Furthermore, phased array systems offer the potential for parallel processing to improve data acquisition rates [28]. A phased-array transducer allows for the electronic steering and focusing of the acoustic beam at a specific focal point. The principles of how a phased-array transducer can steer or focus the acoustic beam are explained in the following.

- **Steering and Focusing in Transmit Mode**

The acoustic beam can be steered and focused in a phased-array transducer by exciting the piezoelectric elements with specific time delays. The process is illustrated in Figure 1.13a, where the first piezoelectric element generates a circular wave-front, followed by adjacent elements with specific time delays Δt_s until the last element generates the echo pulse. The resulting waves interact with each other, and a single wave with maximum intensity propagates along a line at a particular angle. The

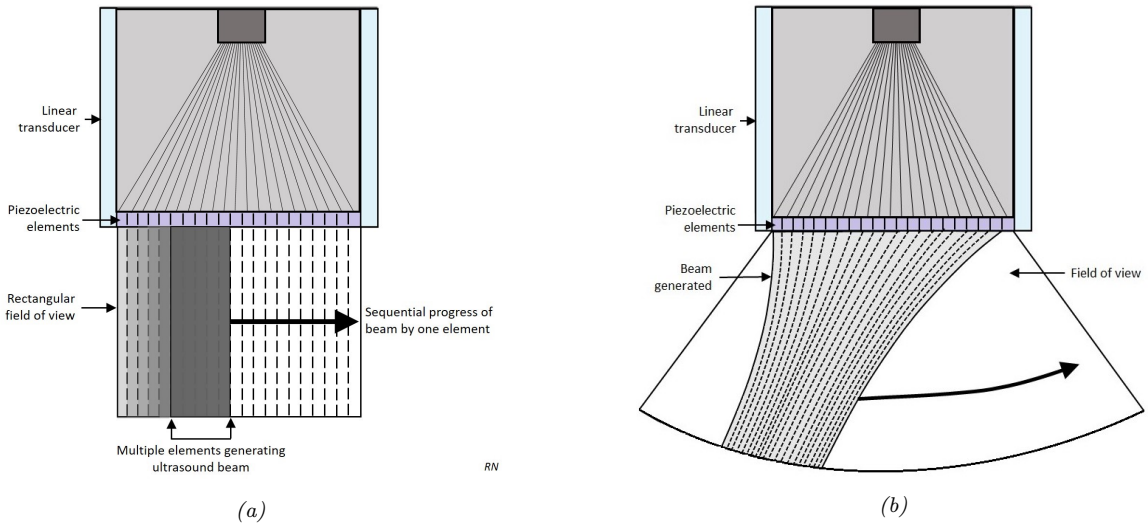

Figure 1.12. Working principle of two different real-time scanning methods: (a) Sequential linear array [32] and (b) Phased-Array [33] scanners

time delay can be formulated as a function of the array's geometrical parameters and the angle θ_s. To achieve a steering angle of θ_s, it is necessary to apply the following time delay to each of the individual elements [28]:

$$\Delta t_{s_n} = n\frac{d}{c}\sin(\theta_s) + t_0 \tag{1.1}$$

where $n = 0, \pm1, \pm2, ...$ enumerates the individual, equally-spaced elements from the center element, d is the length of a single element, c is the average propagation speed, and t_0 is the constant time placed in the equation to avoid negative time delays. If the successive activation of piezoelectric elements is considered a moving loading with velocity v_m, then we have $d = v_m * dt_{s_n}$. Hence, by obtaining $c/v_m = sin(\theta_s)$ and $v_m > c$, we enter into the supersonic regime, and the obtained wavefront corresponds to the well-known Mach cone. The time delays can also be set to maximize the intensity of the resulting signal at a desired point with a specific distance from the transducer, resulting in the beam focusing on a particular focal length. Combining a linear time delay pattern and a spherical time delay pattern makes it possible to achieve both steering of the acoustic wave to a specific azimuth angle θ_s and focusing of the wave on a designated focal point located at a distance of F. (see Figure 1.13b) The corresponding time delay Δt_f is obtained as following:

$$\Delta t_{f_n} = \frac{F}{c}\left(1 - \sqrt{1 + \left(\frac{nd}{F}\right)^2 - 2\frac{nd}{F}\sin(\theta_s)}\right) + t_0 \tag{1.2}$$

- **Steering and Focusing in Receive Mode**

As the echoes return to the transducers, the signal received by each transducer is delayed accordingly, based on the previously calculated and stored data regarding the delay time [34]. The information from all the channels is then accumulated and processed to obtain brightness information

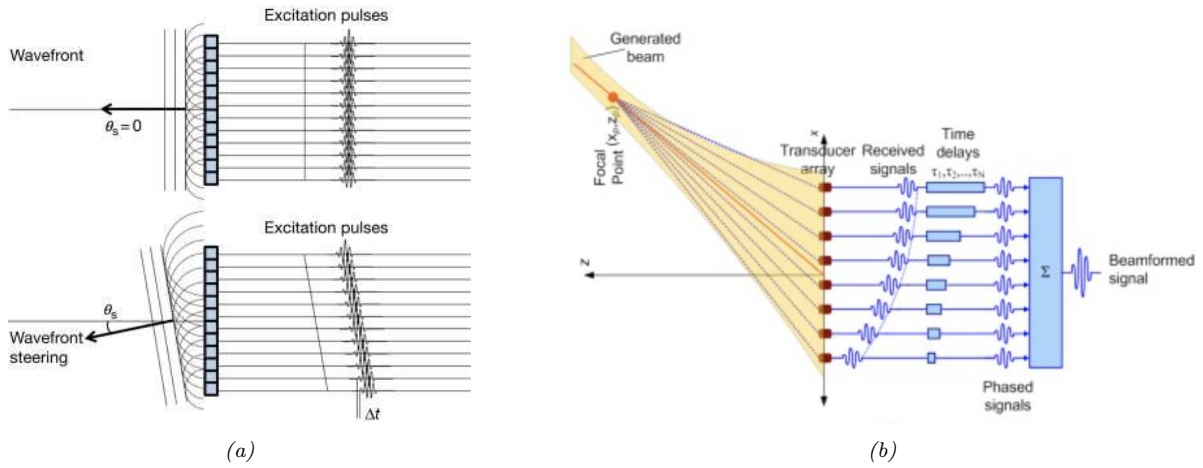

Figure 1.13. The principle of phased array excitation for (a) steering an acoustic beam within a specific angle, (b) Principle of receiving a beam by a phased array transducer, both steering and focusing, by applying the appropriate time delays to the piezoelectric elements (Δt_{s_n} and Δt_{f_n} respectively).

for the corresponding line with a specific angle. This technique incorporates a mechanism that effectively minimizes the impact of echoes originating from points on the lines with different angles on the outcome. Once all the echoes from the farthest point on a given line are captured, the transmit circuit is restarted, and the transducer generates a new pulse in a different direction. This process continues until a B-mode image is constructed [28].

All the conventional B-mode images consist of individual lines whose total number depends upon three parameters: desired number of image frames per second, sound propagation speed inside the material, and reset time required for electronics. Notably, the speed of propagation in tissues puts a maximum limit on the number of lines per frame in a B-mode image.

1.2.3 Reconstruction algorithm of the B-mode images

As previously discussed, the signal detected by the transducer is prone to significant noise levels from different sources like electronics and other physical phenomena that may defy assumptions. Therefore, it becomes crucial to preprocess the raw signal. A block diagram of a suggested signal processing procedure is presented in Figure 1.14. Notably, all the steps might not be necessary for some applications. The first step in this process involves high-pass filtering since lower frequencies in the transmitted signal can introduce errors that are especially problematic in medical applications where frequencies are in the order of several megahertz. However, this filter can be omitted if one is interested in monitoring cavitations or bubbles. Next, low-pass filtering is employed to reduce the noise caused by high frequencies and prepare the signal for digitization. The maximum frequency threshold for the low-pass filter is determined according to the principles described in detail in [35]. Finally, the Time Compensation Gain (TGC) filter amplifies echoes from deeper layers, partially compensating for non-uniform propagation speed and cumulative signal attenuation. The TGC filter is set empirically during the imaging process by the operator [25]. Subsequently, the analog signal can be digitized using an analog/digital converter. It is recommended to employ a median filter (followed by a 2D median filter to remove both speckles and smearing effects) to remove isolated peaks of the signal. The next step involves envelope detection of the signal, which can be achieved through the utilization of the Hilbert transform [25, 36].

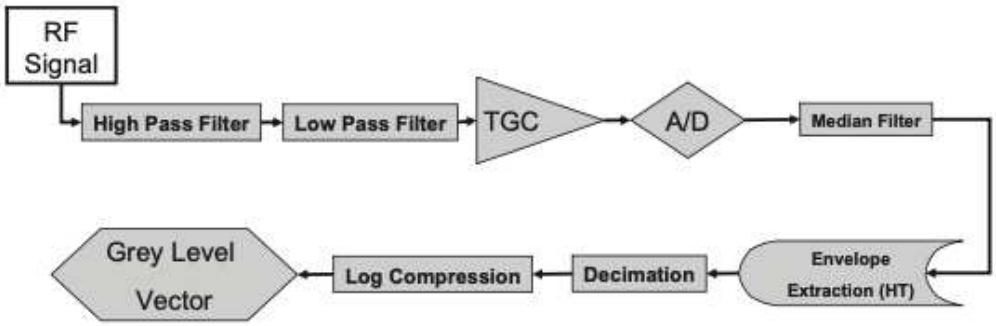

Figure 1.14. Block diagram of signal processing stages [25].

To convert the time scale to the distance scale, a decimation process is applied after extracting the envelope. This process utilizes the average wave propagation speed in the medium. Log compression is employed when there is a significant difference in signal amplitudes to improve the system's visualization of both weak and strong amplitudes in the same image. The two first stages could also be merged and presented as a single Band-Pass Filter (BPF). Figure 1.15a illustrates an exemplary signal at two stages of the signal processing procedure.

Eventually, the last stage is transforming a signal to a vector of gray levels. For this purpose, first, a display range $[W_{min}, W_{max}]$ and a number of gray levels N_g should be specified. Afterward, the transformation is done by:

$$G(t) = \begin{cases} A(t) < W_{min} \longrightarrow \text{Black} \\ A(t) > W_{max} \longrightarrow \text{White} \\ \text{else} \quad G(t) = round\left(\frac{A(t)-W_{min}}{W_{max}-W_{min}}\right) \end{cases} \tag{1.3}$$

where $G(t)$ is the gray level and $A(t)$ is the signal's envelope. A demonstrative example is provided in Figure 1.15b. In this example, corresponding parameters were set as $[W_{min} = 0, W_{max} = 54, N_g = 54]$.

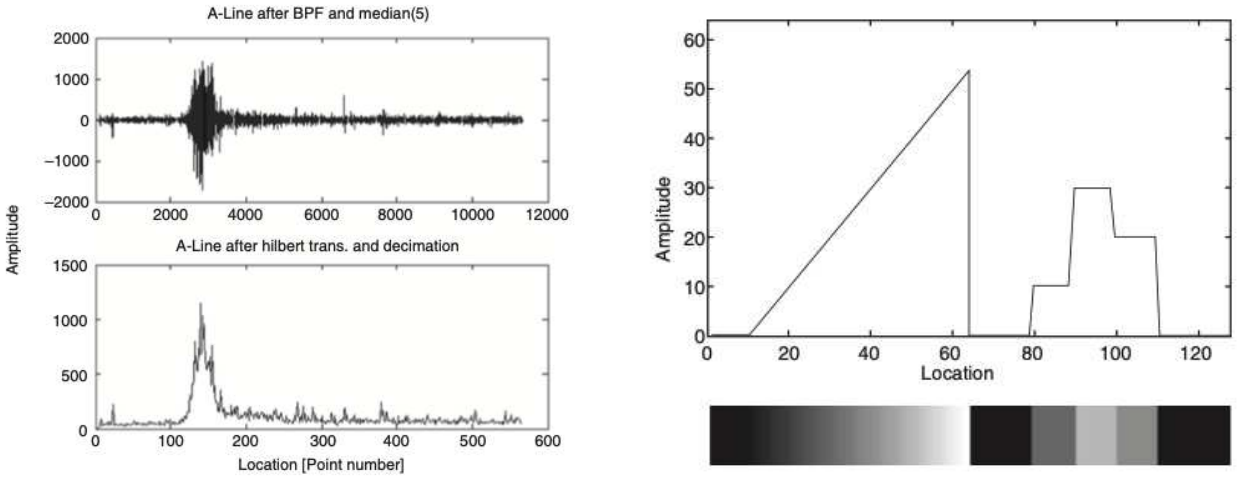

(a) *(b)*

*Figure 1.15. (a) An exemplary signal at two different stages of processing: (**Top**) after BPF and median Filter (**Bottom**) after envelope extraction and decimation. (b) An example of transforming a signal to a vector of gray levels. High amplitudes illustrated with bright colors and smaller amplitudes with dark colors [25].*

1.3 Numerical simulation of wave propagation

Using numerical simulations to study the behavior of acoustic and elastic waves is a highly effective technique that finds applications in various fields, such as ultrasound imaging and seismology. Numerical modeling of acoustic and elastic wave propagation can now be carried out with high reliability and efficiency in many applications.

Let us introduce the elastic wave propagation in a homogeneous medium in an open domain $\Omega \subseteq \mathbb{R}^3$, where $\mathbb{R}^3$ represents the general three-dimensional Euclidean space. The density of the medium is denoted by ρ. The displacement field is represented by $u(t,x) : (0,T) \times \Omega \to \mathbb{R}^3$, where $x \in \Omega$ is the spatial position vector. The second-order Cauchy stress tensor is represented by $\sigma(t,x)$, and f denotes the density of body force.

However, it can be a difficult task in heterogeneous media if the characteristic size of the medium is comparable to the wavelength such that the wave interacts with the complicated physical interfaces of heterogeneities. In this case, the obtained waveforms contain vast information about the material's interior structures. Hence, there is a need to develop more efficient numerical methods for accurate wave propagation simulation.

This problem could be even more complicated when dealing with multi-physics modeling, such as fluid-solid coupling. Some of the numerical techniques are extended to solve coupled wave propagation problems, including acoustic-elastic coupling, which exists in a broad range of problems, including seismic waves that interact with the outer core of the earth or the ocean, the ultrasonic waves generated by transducers for medical imaging of patients, which propagate through human tissues and bones, and the blood inside the organs. In these cases, high-order methods are required to reduce the numerical dispersion and dissipation errors, and more effort is needed to maintain the high accuracy on the coupled interface [37]. Several numerical methods are introduced in the literature for solving the second-order or first-order wave equations in elastic and acoustic domains, including the acoustic-elastic interface.

When dealing with problems in dynamics, the typical numerical approach involves a combination of space discretization and a time-stepping scheme. The finite difference (FD) scheme and finite element (FE) are widely used for space discretization. Other methods, such as the boundary element method (BEM) and finite volume method (FVM), are also popular techniques.

FD method for the simulation of elastic waves is developed for both regular grids and unstructured meshes. This method is based on direct discretization of the strong formulation of the partial differential equations and could also be applied to anisotropic materials. However, this method is mainly adapted to simple geometries [38–44]. Early studies, such as the work of Alford *et al.* [45], used FD to solve acoustic wave propagation in geophysics and demonstrated that this could produce accurate results provided that an appropriate number of grid points per wavelength and time step are used. Afterward, FD was used for isotropic elastic materials, with a very dispersive shear wave propagation [46]. Staggered-grid frameworks were then introduced and became popular since they resolved the dispersive shear wave issue [47–49]. Di Bartolo *et al.* propose a finite difference framework with an optimized memory use based on staggered-grid schemes. This scheme is also extended to take into account the fluid-solid interfaces [50–53]. Lombard and Piraux also used the FD method to solve coupled acoustic-elastic wave propagation problems, considering 2D arbitrary-shaped interfaces. The solution in this work is validated by comparing the results to the corresponding analytical solution [54].

The FE method relies on the PDE's variational or weak form, allowing for greater flexibility in handling complex geometries. This approach involves dividing the domain into smaller elements that satisfy the weak form of the PDE. Although FEM can better handle complicated geometries than finite difference methods (FDM), it sometimes requires more memory space for numerical simulations [55–58].

SEM is a particular form of FE that uses hexahedral elements to subdivide the computational domain. A crucial advantage of the SEM is that its mass matrix is constructed to be diagonal, which results in considerable savings in terms of computational time and memory requirements. This method could be used in the form of a massively parallel solver. This property makes the SEM particularly suited for simulations of wave propagation problems in three-dimensional space where a large number of degrees of freedom are involved [59–65]. The SEM is also used in [64, 66] to model seismic waves with different strategies for considering the acoustic-elastic coupling on the fluid-solid interfaces.

The BEM is a numerical technique that transforms a boundary value problem, described by a partial differential equation (PDE), into an equivalent representation using integral equations. However, the resulting BEM matrix is unsymmetric and full, with non-zero coefficients, in contrast to the much larger yet sparsely populated FE matrix. This means that the FE matrix can be stored and solved more efficiently. The transformation of the PDE to boundary integral equations requires the use of the Green function, which can be challenging and restricts the applicability of the BEM, particularly for problems in heterogeneous media [67, 68].

The FVM relies on the strong formulation of PDEs, and involves dividing the computational domain into elements or control volumes. The divergence formula is then employed to obtain an integral formulation of the fluxes over the boundary of each control volume. The FVM is commonly used for solving fluid flow problems, particularly those involving complex geometries and non-uniform grids. However, it could be used for numerical solving of the hyperbolic equations such as wave propagation equation [69–72]. This method is also extended to solve wave propagation problems with a fluid-solid interface [73, 74].

On the other hand, various techniques could be implemented for time-stepping, including low-ordered schemes such as second-order Newmark type schemes and Runge-Kutta method, and higher order techniques such as arbitrary high-order derivatives (ADER) approach [57, 75, 76].

1.3.1 Space discontinuous Galerkin FE for coupled acoustic-elastic wave propagation

The space discontinuous Galerkin (DG) is a well-established method that combines the advantages of finite element and finite volume frameworks. Moreover, the space dG method can be incorporated with high-order time integration schemes and allows the development of massively parallel solvers. In the past two decades, the dG method was extensively used for numerical modeling of wave propagation in elastic media [70, 77–82], as well as in more complex media involving multi-physical media.

Unlike the continuous FE method, the space dG FE method is based on the use of discontinuous basis functions between finite elements. However, the continuity across the elements is weakly imposed by these numerical fluxes. Hence, developing and implementing the appropriate numerical fluxes is essential to the success of the dG method. The DG schemes and implementing Runge-Kutta time integration methods within a coherent framework is firstly done by Cockburn *et al.* between 1989 and 2000 [77, 83–86]. Dumbser and Kaser used a rigorous and accurate numerical flux obtained from the exact solution of the Riemann problem on element interfaces for elastic wave propagation in

a heterogeneous isotropic solid material in two and three-dimensional problems. The ADER time integration is used in these works to achieve high accuracy in both space and time [78,79]. This method is later extended to the anisotropic and viscoelastic materials [80]. Tie *et al.* also developed a unified multidimensional variational framework for elastic wave propagation in anisotropic media [81, 82]. Otherwise, the Lax-Friedrich or penalty flux is another rigorous alternative for calculating the numerical fluxes [87–93]. More particularly for the elastic-acoustic coupling, Wilcox *et al.* introduced a unified dG framework for isotropic elastic/acoustic media [37], while Zhan *et al.* considered a dG framework for arbitrary anisotropic elastic/acoustic media [94]. They all used the velocity-strain formulation and developed the upwind numerical fluxes by exactly solving the Riemann interface problem. Zhan *et al.* then extended their approach to a more general case involving poroelastic media [95]. Besides, using the first-order elastic velocity-strain and acoustic velocity-pressure formulations, Ye *et al.* obtained a stable algorithm with a penalty flux defined on element interfaces [88], while Guo *et al.*, using the first-order elastic velocity-stress and acoustic velocity-pressure formulations, presented a weight-adjusted dG method also with a dissipative penalty flux defined on element interfaces [91].

The second chapter of this thesis presents a development of the upwind numerical fluxes in the most general case of multidimensional anisotropic elastic/acoustic media with discontinuous material properties using the wave-oriented variational framework previously proposed in [81, 82]. Within the framework of the first-order elastic velocity-stress and acoustic velocity-pressure formulations, the numerical fluxes on the interfaces, including the elastic/acoustic interfaces, are obtained in terms of the exact solution of the associated Riemann problem, unlike the penalty flux method implemented in [88]. Moreover, unlike the approach used in [94,95], we use a coordinate-free vector and tensor notation and a wave-oriented eigenanalysis of the first-order hyperbolic system. Thanks to the proposed approach, the Riemann problem is analytically solved for the general anisotropic elasticity tensor, and explicit closed-form expressions of the numerical fluxes in terms of wave propagation modes are obtained. These explicit expressions of fluxes are implemented in our code, and they are computed only once and stored at the beginning of each dynamic calculation.

In this thesis, the space discontinuous Galerkin (DG) framework is used to perform wave propagation simulation, and all the numerical results are obtained using this numerical technique.

1.3.2 OOFE (Object-Oriented Finite Element) code

Object-oriented finite element (OOFE) code is an in-house code developed in the LMPS laboratory, containing different static and dynamic solvers. This code is written in C++ language and has three main dynamic solvers for performing wave propagation simulation:(1) classical Newmark scheme, (2) the time discontinuous space-time Galerkin (tDG) solver, with the capability of adaptive re-meshing, and (3) space discontinuous Galerkin (DG) framework.

The tDG solver, which is an implicit unconditionally stable solver, employs an adaptive re-meshing method, which subdivides the space-time domain into space-time slabs [96, 97], and treats discontinuities of the unknown fields in the weak formulation, resulting in a higher computational accuracy compared to the classical Newmark scheme [98–102]. In addition, the OOFE code demonstrated its ability to capture shock wave fronts by simulating the elastic wave propagation in plates and shells under moving loads. This method was then used to analyze and predict the behavior of elastic shock waves in hexagonal honeycomb sandwich panels, which have potential applications in space launchers [103].

The space DG solver is explicit and conditionally stable. This type of solver offers a better numerical dispersion performance. Due to the global mass matrix of the space DG solver, which consists of uncoupled elementary mass matrices, a parallel version of the solver that uses the Message Passing Interface (MPI) is employed to decompose the numerical domain into different subdomains and carries out parallel computations on a cluster. This allows for efficient parallelization of the solver, enabling the simulation of large-scale problems that are computationally intensive.

1.4 Wave scattering in heterogeneous media

The propagation of waves in heterogeneous media gives rise to several complex phenomena. Reflection occurs when waves encounter boundaries of different material properties, while refraction occurs when waves change direction at the interface between two materials of different properties. Diffraction occurs when waves bend around corners or slits and propagate when encountering obstacles. The loss of wave amplitude due to absorption, scattering, and mode conversion is referred to as attenuation. Scattering, on the other hand, refers to wave radiation from heterogeneities that act as secondary radiation sources due to excitation by the incident wave.

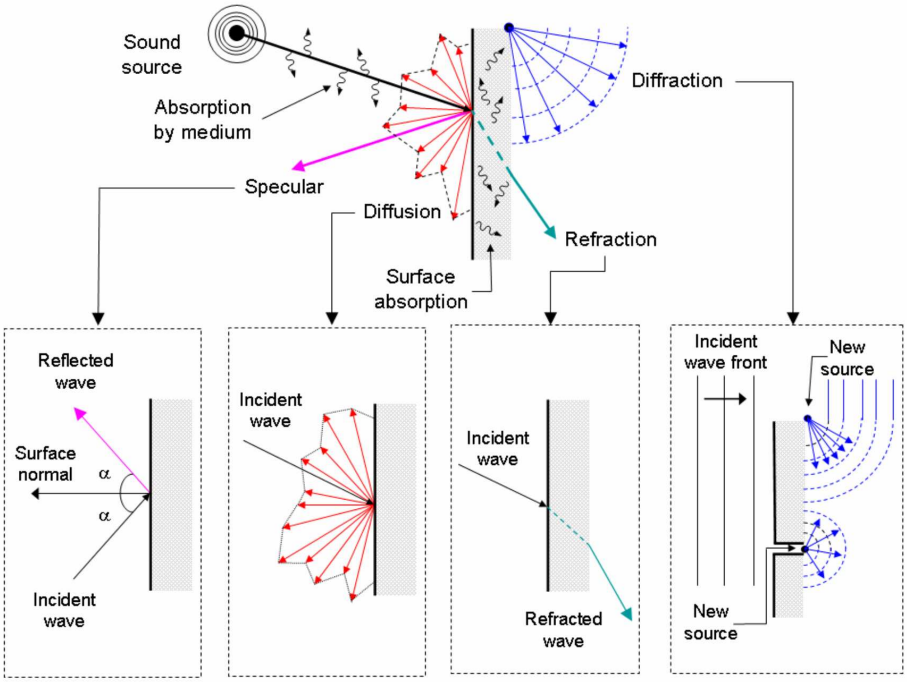

Figure 1.16. Different phenomena during acoustic wave propagation, including specular reflection, diffuse reflection, refraction, and diffraction [104]

The microstructure of the heterogeneous media scatters the energy of the incident ultrasonic wave, whether the microstructure consists of reinforced fibers in metal matrix composites, spherical beads in 3D-printed materials, or grains in polycrystalline materials. Scattering can be categorized into different regimes based on the characteristic length scales. Wave propagation in heterogeneous media is a multi-scale problem mathematically and numerically, and different phenomena occur for different scales [105]. There are three fundamental length scales for wave propagation problems: the propagation distance L, the characteristic length of heterogeneity l_c (the scale at which the heterogeneous medium varies),

and the dominant wavelength λ. Different values of dimensionless parameters $x_0 := kl_c = 2\pi l_c/\lambda$ and $\epsilon := \lambda/L$, where k is the wavenumber, can describe the following scattering regimes [106]:

- **Rayleigh** scattering regime: In the Rayleigh scattering regime, $0.01 \leq x_0 < 0.1$. The amount of scattered energy in 3D is apparent, resulting in an observable attenuation of high frequencies [107, 108].
- **Stochastic** scattering regime: $0.1 \leq x_0 \leq 10$, and $\epsilon \ll 1$. In this regime, where the scale length of the heterogeneity is comparable to the wavelength and small compared to the propagation distance, and the fluctuations of the inhomogeneities are weak, full interactions between wave fields and media are observed [109].
- **Geometric** scattering regime: In this regime, where $x_0 \gg 1$, the wavelength is small compared to the length of heterogeneity [110].

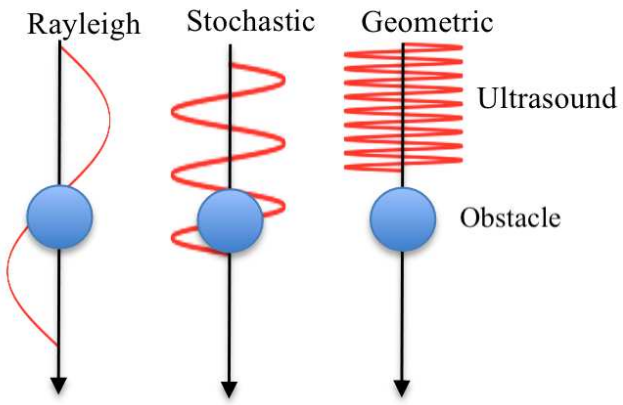

Figure 1.17. Schematic of three scattering regimes [111]

Due to the scattering, there are typically two parts to analyze in the wave signals: coherent wavefronts through the variation of phase velocity and attenuation coefficient and the incoherent part (noises) through the scattering coefficient. Many studies have focused on the scattering of the elastic waves by obstacles, including the smooth obstacles [112–116]. Later, these studies are extended to highly irregular scatterers, which increase the complexity of the problem in geophysics, noise control, and medical applications [117–119] significantly.

In the context of nondestructive testing of polycrystalline materials, the scattering of the elastic waves occurs at the grain boundary because of the discontinuities in the mechanical properties. Several important theoretical and numerical studies have been performed on the microstructural noise and scattering-induced attenuation in polycrystalline materials [120–128].

Estimating the attenuation coefficient resulting from the ultrasonic waves' scattering in matrix-inclusion composite materials has been studied for many years. There are several studies on analytical estimation of the scattering-induced attenuation coefficient in the literature, mainly for the Rayleigh ($\lambda \gg d$) and stochastic ($\lambda \approx d$) scattering domains, where λ is the wavelength, and d is the characteristic size of the microstructure. Willis introduced in [129] an integral analytical formulation for the scattering problem of the elastic wave in the presence of a single inclusion. This approach was used

by Sabina *et al.* in [130] to calculate the attenuation coefficient employing a self-consistent scheme for multiphase matrix-inclusion composites in common practice cases where no statistical data other than volume concentrations are available. The obtained attenuation coefficient is based on the so-called "single-scattering" assumption, meaning that the inclusions are placed far enough from each other in the matrix so that the scattered wave from one inclusion does not interact with the other inclusions. Under this assumption, the spatial correlation of the inclusions is indeed not necessary. The theoretical formulation was also developed in [131], trying to account for multiple scattering by incorporating additional spatial statistical information, a factor containing an integral of the pair distribution function. However, the solution provided by this method is more challenging to obtain the attenuation coefficient in matrix-inclusion composites and is not considered in the present work.

Using the single-scattering assumption, the calculation of the attenuation coefficient was extended to matrix-inclusion composite with aligned spheroidal inclusions in [132], randomly oriented spheroidal inclusions in the two-dimensional case in [133] and three-dimensional case in [134]. Willis' approach estimates the attenuation coefficient by defining an effective medium whose mechanical properties are obtained using a self-consistent homogenization scheme. However, it needs to be specified that the single-scattering assumption is valid up to what volume fraction of inclusions. In other words, when the attenuation coefficient is reported for a specific volume fraction, it is difficult to simply determine whether the single-scattering assumption is met for that volume fraction by using the introduced analytical framework. Moreover, quantitative information on the distance between inclusions is missing for the single-scattering assumption to be valid. Kim compared eight different theoretical models for estimating the effective properties, including the effective wave speed and attenuation coefficient in [135]. These eight models include the model of Sabina and Willis [130] for the single-scattering assumption, as well as models of Waterman and Truell [136], Lloyd and Berry [137], and Kanaun and Levin [138] for the multiple-scattering assumption.

Among the numerical methods, the boundary element method was frequently used to solve the integral formulation of the scattering problem for cylindrical, spherical, and elliptical-shaped inclusions, including partially debonded inclusions [139–142]. Dravinski *et al.* in [143] also used the direct boundary integral equation method to study the scattering of inclusions of arbitrary shapes distributed in multiple layers. Extended finite element method (XFEM) is also used by Liu *et al.* [144] for estimation of the attenuation of ultrasonic wave in polymer matrix particulate composites.

In this thesis, we aim to understand better and validate the analytical formulas of the scattering-induced attenuation coefficient of matrix-inclusion composites proposed by Willis *et al.* using a finite element-based numerical approach. The phase velocity and the attenuation coefficient of the compression wave in a two-dimensional two-phase composite with randomly distributed embedded circular inclusions are considered. The numerical approach is very similar to the method already used and validated for calculating the scattering attenuation coefficient of the polycrystalline materials in the nondestructive evaluation context [126–128]. The advantage of the finite element method is that the microstructure can be accurately represented, and all scattering phenomena can be fully simulated without any simplifying assumptions. The objective is twofold by considering the analytical and numerical approaches in parallel. First, the numerical approach can be validated by an analytical/numerical comparison of the phase velocity and the attenuation coefficient in the case of a relatively low inclusion

area fraction (2%). Second, the validated numerical approach is used to perform a parametric study for different inclusion area fractions and for different inclusion sizes to study the limits of the analytical formula.

The validated numerical approach can be applied to calculate the phase velocity and the attenuation coefficient when the analytical formula is no longer available. According to [133], the analytical solution is valid for the wavelengths down to the diameter of the inclusion. In quasi-incompressible materials, the propagation speed of the shear wave travels substantially slower than the compression wave, so the shear wave's wavelength is much shorter than the compression wave's. Therefore, for the frequency range of ultrasonic imaging, the wavelength of the shear wave is considerably smaller than the size of the 3D-printed inclusions, and the analytical framework considered here cannot be used. In the case of the phantoms with 3D-printed synthetic tissues, the matrix of the matrix-inclusion microstructure is made of the GLM material, which is a quasi-incompressible material. Hence, the analytical approach is not applicable. Therefore the phase velocity and the attenuation coefficient are acquired using the finite element-based numerical approach.

Chapter 2
Space dG method for the coupled acoustic-elastic wave propagation

Contents

This chapter aims to present a discontinuous Galerkin finite element framework for coupled acoustic-elastic wave propagation simulation. The unified strong form and variational frameworks are developed for acoustic and elastic media based on an intrinsic tensorial notation presented in [82]. After investigating the eigenstructure of the hyperbolic systems, the upwind numerical fluxes are developed in the most general case of multidimensional anisotropic elastic/acoustic media with discontinuous material properties using a wave-oriented variational framework. The numerical fluxes on the interfaces (acoustic-acoustic, elastic-elastic, and acoustic-elastic) are obtained in terms of the exact solution of the associated Riemann problem. Thanks to the proposed approach, the Riemann problem is analytically solved for the general anisotropic elasticity tensor, and explicit closed-form expressions of the numerical fluxes in wave propagation modes are obtained. These explicit expressions are computed only at the beginning of each dynamic calculation once, stored, and used for all the timesteps in the calculations. To complete the description of the method, the numerical fluxes associated with the

boundary conditions and external forces are also presented. The numerical flux on the elastic-elastic interface has been already developed [82]. The original contribution here are:

- developing the numerical fluxes for the acoustic-acoustic interface using the intrinsic tensorial notation presented in [82], as well as the fluxes on the boundary elements
- developing the numerical fluxes on the coupled acoustic-elastic interface for the most general case of multidimensional anisotropic elastic solid and acoustic fluid.

In the last section, the coupled acoustic-elastic dG solver is validated using the developed upwind numerical fluxes. This validation is performed through a numerical/analytical comparison, considering the example of an acoustic domain with a circular elastic inclusion.

2.1 Governing equations and the variational framework

This section presents the governing equations for both the elastic and acoustic media in detail, using a unified strong and variational formulation for the system. In the space discontinuous Galerkin framework, the classical second-order hyperbolic wave propagation equation is not applicable, and one needs to employ the first-order hyperbolic equation instead. The first-order hyperbolic wave propagation equation could be written in a general form as follows:

$$\boldsymbol{M}(\partial_t \boldsymbol{U}) + \boldsymbol{A}^{\partial_x}(\boldsymbol{U}) = \boldsymbol{0} \tag{2.1}$$

This tensorial compact form in (2.1) is defined in [81] within the frameworks of elastic waves. No source term is considered in the equilibrium equation without loss of generality. The $\boldsymbol{U}(\boldsymbol{x},t)$ in (2.1) is the generalized unknown, which vary depending on the type of the wave (acoustic or elastic wave) and the employed formulation (velocity-stress, velocity-strain, and velocity-pressure). Similarly, the operator $\boldsymbol{M}$ and space derivative operator $\boldsymbol{A}^{\partial_x}$ in (2.1) are defined accordingly.

2.1.1 First-order velocity-pressure acoustic wave equations

Let us consider an acoustic fluid $\Omega \subset \mathbb{R}^d$ of space dimension d ($d = 1, 2, 3$) and over a time interval $[0, T]$. The governing equations of acoustic wave propagation in the form of a first-order velocity-pressure system can be expressed in a general form as follows: $\forall (\boldsymbol{x}, t) \in \Omega \times]0, T[$

$$\begin{aligned} \rho_f \partial_t \boldsymbol{v} - \boldsymbol{\nabla}_{\boldsymbol{x}} p &= \boldsymbol{0} \\ \lambda_f^{-1} \partial_t p - \mathrm{div}_{\boldsymbol{x}} \boldsymbol{v} &= 0 \end{aligned} \tag{2.2}$$

where the velocity and pressure fields are the primary unknowns, and ρ_f and λ_f respectively denote the fluid's density and bulk modulus. The generalized unknown $\boldsymbol{U}(\boldsymbol{x},t) = (\boldsymbol{v}(\boldsymbol{x},t)\ p(\boldsymbol{x},t))^T$ consists of $\boldsymbol{v}$ the velocity and p the pressure, with $(\,\cdot\,)^T$ the adjoint operator. Hence, $\boldsymbol{U}(\boldsymbol{x},t)$ is a field in $\mathbb{R}^d \times \mathbb{R}$ and defined over the open set $\Omega \times]0, T[$. The operator $\boldsymbol{M}$, the space derivative operator $\boldsymbol{A}^{\partial_x}$ and the adjoint of the derivative operator $\boldsymbol{A}^{\partial_x}$are defined as follows: $\forall\ \boldsymbol{W} = (\boldsymbol{w}\ q)^T$

$$\boldsymbol{M}\begin{pmatrix} \boldsymbol{w} \\ q \end{pmatrix} = \begin{pmatrix} \rho_f \boldsymbol{w} \\ \lambda_f^{-1} q \end{pmatrix},\ \boldsymbol{A}^{\partial_x}\begin{pmatrix} \boldsymbol{w} \\ q \end{pmatrix} = \begin{pmatrix} -\boldsymbol{\nabla}_{\boldsymbol{x}} q \\ -\mathrm{div}_{\boldsymbol{x}} \boldsymbol{w} \end{pmatrix},\ \boldsymbol{A}^{\partial_x, T}\begin{pmatrix} \boldsymbol{w} \\ q \end{pmatrix} = \begin{pmatrix} -\boldsymbol{\nabla}_{\boldsymbol{x}}(\lambda_f q) \\ -\mathrm{div}_x(\rho^{-1}\boldsymbol{w}) \end{pmatrix} \tag{2.3}$$

This adjoint operator is used later in the section 2.1.3 in for developing the weak formulation. We recall the following space gradient and divergence operators defined on an orthonormal basis $(\boldsymbol{e}_i)_{i=1,\dots,d}$:

$$\boldsymbol{\nabla}_{\boldsymbol{x}} q \equiv \mathbf{D}_{\boldsymbol{x}}\, q = \frac{\partial q}{\partial x_i}\boldsymbol{e}_i\ ,\ \mathrm{div}_{\boldsymbol{x}} \boldsymbol{w} = \frac{\partial \boldsymbol{w}}{\partial x_i} \cdot \boldsymbol{e}_i \tag{2.4}$$

Herein, the Einstein summation convention is applied throughout, and all vectors and tensors are represented using bold letters. It is also helpful to define the dot product in the vectorial space $\mathbb{R}^d \times \mathbb{R}$: $\forall\ \boldsymbol{W}_i = (\boldsymbol{w}_i\ q_i)^T, (i = 1, 2)$,

$$\boldsymbol{W}_1 \cdot \boldsymbol{W}_2 = \boldsymbol{w}_1 \cdot \boldsymbol{w}_2 + q_1 q_2 \tag{2.5}$$

According to (2.4), on the boundary ∂D of any subdomain $D \subseteq \Omega$, the flux operator $\boldsymbol{F}_{\boldsymbol{n}}$ for $\boldsymbol{n} = n_i \boldsymbol{e}_i$, the outward unit normal vector defined on ∂D, and associated to the first-order system

(2.2), is: $\forall\ \boldsymbol{W} = (\boldsymbol{w}\ q)^T$,

$$\boldsymbol{F_n}(\boldsymbol{W}) = \boldsymbol{A_n}(\boldsymbol{W}) = \boldsymbol{A_n}\begin{pmatrix} \boldsymbol{w} \\ q \end{pmatrix} = \begin{pmatrix} -q\boldsymbol{n} \\ -\boldsymbol{n}\cdot\boldsymbol{w} \end{pmatrix} \tag{2.6}$$

In (2.6), the subscript index "$\boldsymbol{n}$" indicates the dependency of $\boldsymbol{F_n}$ and of $\boldsymbol{A_n}$ on $\boldsymbol{n}$. From now on, the local orthonormal basis defined on ∂D will be denoted by $(\boldsymbol{n}, \{\boldsymbol{t}_\alpha\}_{\alpha=1,\ldots,d-1})$.

Finally, to complete the definition of the acoustic wave propagation framework, the following boundary conditions are considered:

$$p = p_D, \qquad \text{on } \partial\Omega_D\times]0,T[\tag{2.7a}$$

$$\boldsymbol{v}\cdot\boldsymbol{n} = v_{nN}, \qquad \text{on } \partial\Omega_N\times]0,T[\tag{2.7b}$$

Here, both equations of (2.7) denote respectively the boundary conditions with the prescribed pressure p_D and normal velocity v_{nN}. $\partial\Omega_N \cup \partial\Omega_D = \partial\Omega$ and $\partial\Omega_N \cap \partial\Omega_D = \emptyset$ should be respected. On the other hand, for the initial conditions, we have:

$$p(\boldsymbol{x},0) = p_0(\boldsymbol{x}) \qquad \forall \boldsymbol{x}\in\Omega \tag{2.8a}$$

$$\partial_t p(\boldsymbol{x},0) = \lambda_f \mathrm{div}_{\boldsymbol{x}}\boldsymbol{v}_0(\boldsymbol{x}), \qquad \forall \boldsymbol{x}\in\Omega \tag{2.8b}$$

Remark 2.1 It is worth noticing that the method proposed in this work can be easily applied to this velocity-strain acoustic formulation.The acoustic first-order velocity-strain wave governing equations is written as follows:

$$\begin{aligned} \rho_f\partial_t\boldsymbol{v} - \boldsymbol{\nabla_x}(\lambda_f \mathrm{tr}(\boldsymbol{\varepsilon})) &= \boldsymbol{0} \\ \partial_t\boldsymbol{\varepsilon} - \boldsymbol{\varepsilon}(\boldsymbol{v}) &= \boldsymbol{0} \end{aligned} \tag{2.9}$$

Applying the tensorial compact form to this equation, with the generalized unknown $\boldsymbol{U}(\boldsymbol{x},t) = (\boldsymbol{v}(\boldsymbol{x},t)\ \boldsymbol{\varepsilon}(\boldsymbol{x},t))^T$ where $\boldsymbol{\varepsilon}$ is the strain field $\forall(\boldsymbol{x},t)\in\Omega\times]0,T[$, the operator $\boldsymbol{M}$ and the space derivative operator $\boldsymbol{A}^{\partial_x}$ defined as follows: $\forall\ \boldsymbol{W} = (\boldsymbol{w}\ \boldsymbol{\tau})^T$

$$\boldsymbol{M}\begin{pmatrix} \boldsymbol{w} \\ \boldsymbol{\tau} \end{pmatrix} = \begin{pmatrix} \rho_f\boldsymbol{w} \\ \boldsymbol{\tau} \end{pmatrix},\ \boldsymbol{A}^{\partial_x}\begin{pmatrix} \boldsymbol{w} \\ \boldsymbol{\tau} \end{pmatrix} = \begin{pmatrix} -\boldsymbol{\nabla_x}(\lambda_f \mathrm{tr}(\boldsymbol{\tau})) \\ -\boldsymbol{\varepsilon}(\boldsymbol{w}) \end{pmatrix} \tag{2.10}$$

Then, the flux operator $\boldsymbol{F_n}$ associated to the first-order system (2.9) and the Jacobian operator $\boldsymbol{A_n}$ in the $\boldsymbol{n}$ direction verify the following equations: $\forall\ \boldsymbol{W} = (\boldsymbol{w}\ \boldsymbol{\tau})^T$,

$$\boldsymbol{F_n}(\boldsymbol{W}) = \boldsymbol{A_n}(\boldsymbol{W}) = \begin{pmatrix} -\lambda_f \mathrm{tr}(\boldsymbol{\tau})\boldsymbol{n} \\ -\boldsymbol{n}\otimes_s\boldsymbol{w} \end{pmatrix} \tag{2.11}$$

However, in the following sections, the velocity-strain formulation is not considered anymore. Because the genralized unknown in this formulation for the acoustic case contains the strain tensor, but on the velocity-pressure formulation, the pressure is a primary unknown. Therefore, the velocity-pressure formulation appears to be more memory efficient, particularly in 2D and 3D cases, since there is less number of degrees of freedom per each node in the finite element calculation.

2.1.2 First-order velocity-stress elastic wave equations

Let us consider the wave propagation in an elastic medium $\Omega \subset \mathbb{R}^d$ of space dimension d ($d = 1, 2, 3$) and in a time interval $[0, T]$. The first-order velocity-stress governing equations is written in the following form: $\forall (\boldsymbol{x}, t) \in \Omega \times]0, T[$

$$\begin{aligned} \rho \partial_t \boldsymbol{v} - \mathbf{Div}_{\boldsymbol{x}} \boldsymbol{\sigma} &= \mathbf{0} \\ \boldsymbol{C}^{-1} : \partial_t \boldsymbol{\sigma} - \boldsymbol{\varepsilon}(\boldsymbol{v}) &= \mathbf{0} \end{aligned} \tag{2.12}$$

One can write these equations within the general unified formulation, with the following definitions of operators:

$$\boldsymbol{M}\begin{pmatrix} \boldsymbol{w} \\ \boldsymbol{\tau} \end{pmatrix} = \begin{pmatrix} \rho \boldsymbol{w} \\ \boldsymbol{C}^{-1} : \boldsymbol{\tau} \end{pmatrix}, \ \boldsymbol{A}^{\partial_x}\begin{pmatrix} \boldsymbol{w} \\ \boldsymbol{\tau} \end{pmatrix} = \begin{pmatrix} -\mathbf{Div}_{\boldsymbol{x}} \boldsymbol{\tau} \\ -\boldsymbol{\varepsilon}(\boldsymbol{w}) \end{pmatrix}, \ \boldsymbol{A}^{\partial_x, T}\begin{pmatrix} \boldsymbol{w} \\ \boldsymbol{\tau} \end{pmatrix} = \begin{pmatrix} -\mathbf{Div}_{\boldsymbol{x}}(\boldsymbol{C} : \boldsymbol{\tau}) \\ -\rho^{-1}\boldsymbol{\varepsilon}(\boldsymbol{w}) \end{pmatrix} \tag{2.13}$$

In the elastic case, the generalized unknown is $\boldsymbol{U}(\boldsymbol{x}, t) = (\boldsymbol{v}(\boldsymbol{x}, t)\ \boldsymbol{\sigma}(\boldsymbol{x}, t))^T$ with $\boldsymbol{\sigma}$ the stress unknown. In (2.12) and (2.13), ρ is the density of the solid, $\boldsymbol{C}$ the fourth-order elasticity tensor, and ":" the usual double dot product between two tensors defined as $(\boldsymbol{C} : \boldsymbol{\tau})_{ij} = C_{ijkl}\tau_{kl}$. We recall the definition of the second-order infinitesimal strain tensor $\boldsymbol{\varepsilon}$:

$$\boldsymbol{\varepsilon}(\boldsymbol{w}) = \frac{1}{2}\Big(\mathbf{D}_{\boldsymbol{x}} \boldsymbol{w} + \mathbf{D}_{\boldsymbol{x}}^T \boldsymbol{w} \Big) = \frac{\partial \boldsymbol{w}}{\partial x_i} \otimes_s \boldsymbol{e}_i \tag{2.14}$$

where "$\otimes_s$" is the symmetrized tensor product defined as: $(\boldsymbol{a} \otimes_s \boldsymbol{b})_{ij} = \frac{1}{2}(a_i b_j + a_j b_i)$. The following space gradient and divergence operators are also defined using an orthonormal basis $(\boldsymbol{e}_i)_{i=1,\dots,d}$:

$$\mathbf{D}_{\boldsymbol{x}} \boldsymbol{w} = \frac{\partial \boldsymbol{w}}{\partial x_i} \otimes \boldsymbol{e}_i \ , \ \mathbf{Div}_{\boldsymbol{x}} \boldsymbol{\tau} = \frac{\partial \boldsymbol{\tau}}{\partial x_i} \cdot \boldsymbol{e}_i \tag{2.15}$$

where "$\otimes$" is the tensor product defined as: $(\boldsymbol{a} \otimes \boldsymbol{b})_{ij} = a_i b_j$.

Similar to the acoustic wave framework, it is helpful to define the dot product this time in the vectorial space of $\mathbb{R}^d \times \mathbb{R}^{d \times d_{sym}}$: $\forall\ \boldsymbol{W}_i = (\boldsymbol{w}_i\ \boldsymbol{\tau}_i)^T, (i = 1, 2)$,

$$\boldsymbol{W}_1 \cdot \boldsymbol{W}_2 = \boldsymbol{w}_1 \cdot \boldsymbol{w}_2 + \boldsymbol{\tau}_1 : \boldsymbol{\tau}_2 \tag{2.16}$$

The flux operator $\boldsymbol{F}_{\boldsymbol{n}}$ on the boundary ∂D of any subdomain $D \subseteq \Omega$ is defined as: $\forall\ \boldsymbol{W} = (\boldsymbol{w}\ \boldsymbol{\tau})^T$,

$$\boldsymbol{F}_{\boldsymbol{n}}(\boldsymbol{W}) = \boldsymbol{A}_{\boldsymbol{n}}\begin{pmatrix} \boldsymbol{w} \\ \boldsymbol{\tau} \end{pmatrix} = \begin{pmatrix} -\boldsymbol{\tau} \cdot \boldsymbol{n} \\ -\boldsymbol{n} \otimes_s \boldsymbol{w} \end{pmatrix} \tag{2.17}$$

The following boundary conditions are considered for completing the definition of the elastic wave propagation framework:

$$\boldsymbol{\sigma} \cdot \boldsymbol{n} = \boldsymbol{g}, \qquad \text{on } \partial\Omega_D \times]0, T[\tag{2.18a}$$

$$\boldsymbol{v} = \partial_t \boldsymbol{u}_D, \qquad \text{on } \partial\Omega_N \times]0, T[\tag{2.18b}$$

The equation (2.18a) denotes the Neumann boundary condition, where $\boldsymbol{g}$ is the surface loading. The

second equation (2.18b) shows the Dirichlet boundary conditions with prescribed displacement $\boldsymbol{u}_D$. Again, the condition $\partial\Omega_N \cup \partial\Omega_D = \partial\Omega$ and $\partial\Omega_N \cap \partial\Omega_D = \emptyset$ should be respected. Moreover, the initial conditions are written as follows:

$$\boldsymbol{\sigma}(\boldsymbol{x}, 0) = \boldsymbol{C} : \varepsilon(\boldsymbol{u}_0(\boldsymbol{x})), \qquad \forall \boldsymbol{x} \in \Omega \tag{2.19a}$$

$$\boldsymbol{v}(\boldsymbol{x}, 0) = \boldsymbol{v}_0(\boldsymbol{x}), \qquad \forall \boldsymbol{x} \in \Omega \tag{2.19b}$$

Remark 2.2 The first-order elastic wave propagation governing equations could be also written using velocity-strain formulation as follows: $\forall(\boldsymbol{x}, t) \in \Omega\times]0, T[$

$$\begin{aligned} \rho\partial_t \boldsymbol{v} - \mathbf{Div}_{\boldsymbol{x}}(\boldsymbol{C} : \boldsymbol{\varepsilon}) &= \mathbf{0} \\ \partial_t \boldsymbol{\varepsilon} - \boldsymbol{C} : \boldsymbol{\varepsilon}(\boldsymbol{v}) &= \mathbf{0} \end{aligned} \tag{2.20}$$

The operator $\boldsymbol{M}$ and the space derivative operator $\boldsymbol{A}^{\partial_x}$ are defined as follows: $\forall \boldsymbol{W} = (\boldsymbol{w}\ \boldsymbol{\tau})^T$

$$\boldsymbol{M}\begin{pmatrix} \boldsymbol{w} \\ \boldsymbol{\tau} \end{pmatrix} = \begin{pmatrix} \rho\boldsymbol{w} \\ \boldsymbol{\tau} \end{pmatrix}, \ \boldsymbol{A}^{\partial_x}\begin{pmatrix} \boldsymbol{w} \\ \boldsymbol{\tau} \end{pmatrix} = \begin{pmatrix} -\mathbf{Div}_{\boldsymbol{x}}(\boldsymbol{C} : \boldsymbol{\tau}) \\ -\boldsymbol{\varepsilon}(\boldsymbol{w}) \end{pmatrix} \tag{2.21}$$

Then, the flux operator $\boldsymbol{F}_{\boldsymbol{n}}$ associated to the first-order system (2.20) and the Jacobian operator $\boldsymbol{A}_{\boldsymbol{n}}$ in the $\boldsymbol{n}$ direction verify the following equations: $\forall \boldsymbol{W} = (\boldsymbol{w}\ \boldsymbol{\tau})^T$,

$$\boldsymbol{F}_{\boldsymbol{n}}(\boldsymbol{W}) = \boldsymbol{A}_{\boldsymbol{n}}(\boldsymbol{W}) = \begin{pmatrix} -(\boldsymbol{C} : \boldsymbol{\tau}) \cdot \boldsymbol{n} \\ -\boldsymbol{n} \otimes_s \boldsymbol{w} \end{pmatrix} \tag{2.22}$$

2.1.3 Variational framework of discontinuous Galerkin method

Now that all the required operators and parameters are defined, the unified variational framework can be introduced. Within the discontinuous Galerkin FE method framework, we look for an approximated solution $\boldsymbol{U}_h$, discontinuous across the element interfaces, of the generalized unknown $\boldsymbol{U}$. This discontinuous character of $\boldsymbol{U}_h$ makes it possible to integrate the concept of well-established numerical fluxes within the framework of the finite volume method [78].

Let us consider $\mathcal{M}_h = \{\Omega_k\}_k$ a FE mesh of the domain Ω. For the sake of simplicity, from now on, any element Ω_k of the mesh $\mathcal{M}_h$ will be denoted by E and any of the neighboring elements of E by E'. To obtain the dG variational formulation of the coupled acoustic-elastic system for any element E, the integration by parts formula is used. The discontinuous flux $\boldsymbol{F}_n(\boldsymbol{U}_h)$ on the element boundary ∂E is replaced by a numerical flux $\hat{\boldsymbol{F}}_{\boldsymbol{n}}(\boldsymbol{U}_h, \boldsymbol{U}'_h)$, which depends on the solution in both E and the adjacent element E'. Then we get: $\forall\ \boldsymbol{W}_h(\boldsymbol{x})$,

$$(\boldsymbol{W}_h, \boldsymbol{M}(\partial_t \boldsymbol{U}_h))_E - (\boldsymbol{A}^{\partial_x, T}(\boldsymbol{W}_h), \boldsymbol{U}_h)_E + < \boldsymbol{W}_h, \hat{\boldsymbol{F}}_{\boldsymbol{n}}(\boldsymbol{U}_h, \boldsymbol{U}'_h) >_{\partial E} = 0 \tag{2.23}$$

where $\boldsymbol{U}_h$ and $\boldsymbol{U}'_h$ are the discontinuous solutions in E and E', respectively. $\boldsymbol{W}_h(\boldsymbol{x})$ are the test functions, and we have $\boldsymbol{W}_h(\boldsymbol{x}) = (\boldsymbol{w}_h(\boldsymbol{x})\ q_h(\boldsymbol{x}))^T$ in the acoustic case and $\boldsymbol{W}_h(\boldsymbol{x}) = (\boldsymbol{w}_h(\boldsymbol{x})\ \boldsymbol{\tau}_h(\boldsymbol{x}))^T$ in the elastic case. In (2.23), considering the definition of dot product given in (2.5) and (2.16), the inner products are defined as following:

$$
\begin{aligned}
&(\boldsymbol{w}_1, \boldsymbol{w}_2)_E = \int_E \boldsymbol{w}_1 \cdot \boldsymbol{w}_2 \, \mathrm{d}V, (q_1, q_2)_E = \int_E q_1 q_2 \, \mathrm{d}V \\
&(\boldsymbol{W}_1, \boldsymbol{W}_2)_E = \int_E \boldsymbol{W}_1 \cdot \boldsymbol{W}_2 \, \mathrm{d}V = (\boldsymbol{w}_1, \boldsymbol{w}_2)_E + (q_1, q_2)_E
\end{aligned}
\tag{2.24}
$$

By redoing the integration by parts in (2.23), the following equivalent form of variational formulation is obtained: $\forall\ \boldsymbol{W}_h(\boldsymbol{x})$,

$$
(\boldsymbol{W}_h, \boldsymbol{M}(\partial_t \boldsymbol{U}_h))_E - (\boldsymbol{W}_h, \boldsymbol{A}^{\partial_x}(\boldsymbol{U}_h))_E + < \boldsymbol{W}_h, \hat{\boldsymbol{F}}_{\boldsymbol{n}}(\boldsymbol{U}_h, \boldsymbol{U}'_h) - \boldsymbol{F}(\boldsymbol{U}_h) >_{\partial E} = 0 \tag{2.25}
$$

In the present work, we use the variational formulation (2.25) to implement the dG solver as it involves the slightly more common operator $\boldsymbol{A}^{\partial_x}$, instead of $\boldsymbol{A}^{\partial_x, T}$.

The following sections are dedicated to developing the upwind numerical fluxes for multidimensional coupled anisotropic elastic-acoustic wave equations with discontinuous material properties (i.e., media including physical interfaces). This development is done first on the internal element boundary $\partial E_{int} = \partial E \backslash (\partial E \cap \partial\Omega)$, and second, on the external element boundary $\partial E_{ext} = \partial E \cap \partial\Omega$, where a ghost neighbor element E' with the same properties as E is considered [70], as well as the numerical flux associated to the elements with external loadings.

2.2 Calculation of the upwind numerical fluxes

This section is dedicated to the development of the numerical fluxes across the internal elements' interface $\partial E_{int} = \partial E \backslash (\partial E \cap \partial\Omega)$. For this purpose, it is necessary to develop the upwind numerical fluxes for acoustic-acoustic, elastic-elastic, and acoustic-elastic interfaces. Upwind numerical fluxes for the elastic-elastic interface for heterogeneous anisotropic solid are previously studied in detail in [81,82]. The main contribution of this thesis is the development of numeric fluxes on the acoustic-acoustic and acoustic-elastic interfaces. The acoustic-acoustic case is quite simple and has already been treated in the literature. Still it is interesting to present the numerical fluxes expressed using the proposed notations.

The upwind numerical fluxes on the interfaces are obtained in terms of exact solutions of relevant Riemann problems. Thanks to the proposed approach, explicit closed-form expressions of the upwind numerical fluxes are obtained on the acoustic-elastic interface for the general case of multidimensional anisotropic heterogeneous solid media coupled with acoustic fluids. However, before defining the Riemann problem on the interfaces, it is necessary to analyze the characteristic structure of the wave equations (2.1) for both acoustic and elastic cases by performing analysis of the corresponding eigenvalue problem defined with the operator $\boldsymbol{M}$ and the Jacobian operator $\boldsymbol{A}_{\boldsymbol{n}}$ as follows:

$$
\boldsymbol{A}_{\boldsymbol{n}}(\boldsymbol{R}_{\boldsymbol{n}}) = \lambda_{\boldsymbol{n}} \boldsymbol{M}(\boldsymbol{R}_{\boldsymbol{n}}) \tag{2.26}
$$

Eigenanalysis of the acoustic wave equation

In the acoustic case, we get $m = d + 1$ eigenvalues $\{\lambda_{\boldsymbol{n},k}\}_{k=1,\dots m}$ and the m associated right eigenvectors $\{\boldsymbol{R}_{\boldsymbol{n},k}\}_{k=1,\dots m}$ from (2.26). Rewriting the eigenproblem (2.26) in the following form:

$$
\overline{\boldsymbol{A}}_{\boldsymbol{n}}(\boldsymbol{R}_{\boldsymbol{n}}) = \lambda_{\boldsymbol{n}} \boldsymbol{R}_{\boldsymbol{n}} \tag{2.27}
$$

with $\overline{\boldsymbol{A}}_{\boldsymbol{n}} = \boldsymbol{M}^{-1}.\boldsymbol{A}$, the solving of the eigenvalue problem (2.27) arises the two non-zero eigenvalues and the associated right eigenvectors:

$$\lambda_{\boldsymbol{n}}^{\pm} = \pm\sqrt{\frac{\lambda_f}{\rho_f}}\ ,\ \boldsymbol{R}_{\boldsymbol{n}}^{\pm} = \begin{pmatrix} \frac{1}{\sqrt{2}}\boldsymbol{n} \\ -\frac{1}{\sqrt{2}}\lambda_f(\lambda_{\boldsymbol{n}}^{\pm})^{-1} \end{pmatrix} = \begin{pmatrix} \frac{1}{\sqrt{2}}\boldsymbol{n} \\ -\frac{1}{\sqrt{2}}z_{\boldsymbol{n}}^{\pm} \end{pmatrix} \tag{2.28}$$

where $z_{\boldsymbol{n}}$ is the acoustic impedance defined as $z_{\boldsymbol{n}}^{\pm} = \lambda_f(\lambda_{\boldsymbol{n}}^{\pm})^{-1} = \rho_f\lambda_{\boldsymbol{n}}^{\pm}$.

For the calculation of the left eigenvectors of (2.27), which are also the right eigenvectors of the tensor $\overline{\boldsymbol{A}}_{\boldsymbol{n}}^T$ defined as:

$$\overline{\boldsymbol{A}}_{\boldsymbol{n}}^T(\boldsymbol{W}) = \begin{pmatrix} -\lambda_f q\boldsymbol{n} \\ -\rho_f^{-1}\boldsymbol{n}\cdot\boldsymbol{w} \end{pmatrix} \tag{2.29}$$

It can be shown that:

$$\boldsymbol{L}_{\boldsymbol{n}}^{\pm} = \begin{pmatrix} \frac{1}{\sqrt{2}}\boldsymbol{n} \\ -\frac{1}{\sqrt{2}}(z_{\boldsymbol{n}}^{\pm})^{-1} \end{pmatrix}\ ,\ \boldsymbol{M}(\boldsymbol{R}_{\boldsymbol{n}}^{\pm}) = \rho_f\boldsymbol{L}_{\boldsymbol{n}}^{\pm} \tag{2.30}$$

Hence, we get the following decompositions of the flux (or jacobian) tensors:

$$\overline{\boldsymbol{A}}_{\boldsymbol{n}} = \lambda_{\boldsymbol{n}}^{\pm}\boldsymbol{R}_{\boldsymbol{n}}^{\pm}\otimes\boldsymbol{L}_{\boldsymbol{n}}^{\pm}\ ,\ \boldsymbol{A}_{\boldsymbol{n}} = z_{\boldsymbol{n}}^{\pm}\boldsymbol{L}_{\boldsymbol{n}}^{\pm}\otimes\boldsymbol{L}_{\boldsymbol{n}}^{\pm} \tag{2.31}$$

The system (2.26) is therefore symmetric and has $\boldsymbol{R}_{\boldsymbol{n}}^{\pm}$ as eigenvectors.

Eigenanalysis of the elastic wave equation

The characteristic structure of the first-order hyperbolic velocity-stress equation is studied in [81]. In this section, we recall some of the essential relations. Among the $m = d + d(d+1)/2$ eigenvalues of $\boldsymbol{A}_{\boldsymbol{n}}$, there are d strictly negative eigenvalues and d strictly positive eigenvalues, representing the propagation speed of quasi-longitudinal "qL" and quasi transverse "qT" wave modes propagating in the $\boldsymbol{n}$ direction.

The right and left eigenmodes corresponding to the nonzero eigenvalues of $\overline{\boldsymbol{A}}_{\boldsymbol{n}} = \boldsymbol{M}^{-1}\cdot\boldsymbol{A}_{\boldsymbol{n}}$ are the following: $\forall k = qL, \{qT_\alpha\}_{\alpha=1,\cdots,d-1}$

$$\boldsymbol{R}_{\boldsymbol{n},k}^{\pm} = \begin{pmatrix} \boldsymbol{w}_{\boldsymbol{n},k} \\ -\rho(z_{\boldsymbol{n},k}^{\pm})^{-1}\boldsymbol{C} : (\boldsymbol{n}\otimes_s\boldsymbol{w}_{\boldsymbol{n},k}) \end{pmatrix}\ ,\ \boldsymbol{L}_{\boldsymbol{n},k}^{\pm} = \begin{pmatrix} \boldsymbol{w}_{\boldsymbol{n},k} \\ -(z_{\boldsymbol{n},k}^{\pm})^{-1}\boldsymbol{n}\otimes_s\boldsymbol{w}_{\boldsymbol{n},k} \end{pmatrix} \tag{2.32}$$

where $z_{\boldsymbol{n},k}^{\pm} = \rho\lambda_{\boldsymbol{n},k}^{\pm}$ denotes the acoustic impedance of kth eigenmode and $\boldsymbol{w}_{\boldsymbol{n},k} = \frac{1}{\sqrt{2}}\boldsymbol{\gamma}_{\boldsymbol{n},k}$ with $\boldsymbol{\gamma}_{\boldsymbol{n},k}$ unit eigenvectors of $\boldsymbol{\Gamma}_{\boldsymbol{n}}$ the Christoffel tensor:

$$\boldsymbol{\Gamma}_{\boldsymbol{n}}\cdot\boldsymbol{\gamma}_{\boldsymbol{n},k} = \lambda_{\boldsymbol{n},k}^2\boldsymbol{\gamma}_{\boldsymbol{n},k},\quad k = qL, \{qT_\alpha\}_{\alpha=1,\cdots,d-1} \tag{2.33}$$

We recall that:

$$\boldsymbol{\Gamma}_{\boldsymbol{n}}\cdot\boldsymbol{w} = \left(\rho^{-1}\boldsymbol{C} : (\boldsymbol{n}\otimes_s\boldsymbol{w}_{\boldsymbol{n},k})\right)\cdot\boldsymbol{n}, \forall\boldsymbol{w} \tag{2.34}$$

Finally, as in the acoustic case, the following equations hold:

$$\boldsymbol{M}(\boldsymbol{R}_{\boldsymbol{n},k}^{\pm}) = \rho\boldsymbol{L}_{\boldsymbol{n},k}^{\pm}\ ,\ \boldsymbol{A}_{\boldsymbol{n}} = z_{\boldsymbol{n},k}^{\pm}\boldsymbol{L}_{\boldsymbol{n},k}^{\pm}\otimes\boldsymbol{L}_{\boldsymbol{n},k}^{\pm} \tag{2.35}$$

It is noteworthy that the associated eigenvalue and eigenvectors of the two equivalent forms of the governing equations, (2.1) and (2.49), are identical.

2.2.1 Numerical fluxes across the acoustic-acoustic interfaces

We consider the interface of two adjacent elements E and E', governed by the previously presented velocity-pressure acoustic wave equations and having respectively $(\rho_f, \lambda_f, \boldsymbol{U}_h)$ and $(\rho'_f, \lambda'_f, \boldsymbol{U}'_h)$ as densities, bulk modulus and initial states (Figure 2.1). All the following equations are written in the 3D case without loss of generality. The Riemann problem defines the states that are the results of the propagation of the discontinuity $\boldsymbol{U}_h - \boldsymbol{U}'_h$:

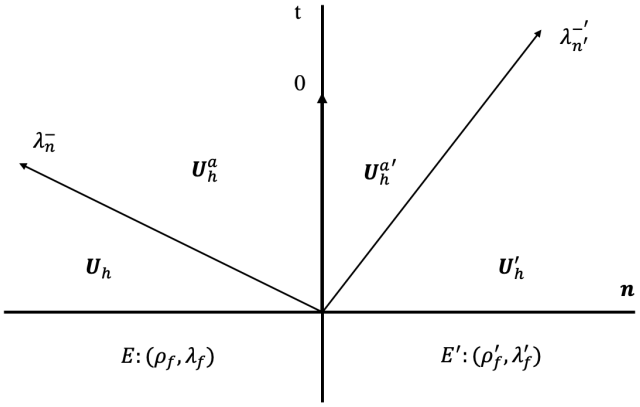

Figure 2.1. Sketch illustration of the Rankine-Hugoniot jump condition in the Riemann problem at an acoustic-acoustic element interface

$$\boldsymbol{A_n}(\boldsymbol{U}_h - \boldsymbol{U}_h^a) = \lambda_{\boldsymbol{n}}^- \boldsymbol{M}(\boldsymbol{U}_h - \boldsymbol{U}_h^a) \tag{2.36a}$$

$$\boldsymbol{A_n}(\boldsymbol{U}_h^a) + \boldsymbol{A'_{n'}}(\boldsymbol{U}_h^{a'}) = \boldsymbol{0} \tag{2.36b}$$

$$\boldsymbol{A'_{n'}}(\boldsymbol{U}'_h - \boldsymbol{U}_h^{a'}) = \lambda_{\boldsymbol{n'}}^{-'} \boldsymbol{M'}(\boldsymbol{U}'_h - \boldsymbol{U}_h^{a'}) \tag{2.36c}$$

We note that the two outward unit normal vectors $\boldsymbol{n}$ and $\boldsymbol{n'}$ of E and E' on their interface verify $\boldsymbol{n} + \boldsymbol{n'} = \boldsymbol{0}$. According to the definition of the eigenvalues and eigenvectors of (2.26), the discontinuity terms in (2.36) can be decomposed as follows within the right eigenvectors basis:

$$\boldsymbol{U}_h - \boldsymbol{U}_h^a = \alpha \boldsymbol{R}_{\boldsymbol{n}}^- \ , \ \boldsymbol{U}'_h - \boldsymbol{U}_h^{a'} = \alpha' \boldsymbol{R}_{\boldsymbol{n'}}^{-'} \tag{2.37}$$

By applying (2.37) and the second equation of (2.30), the Rankine–Hugoniot jump conditions (2.36) finally become:

$$\boldsymbol{A_n}(\boldsymbol{U}_h) - \boldsymbol{A_n}(\boldsymbol{U}_h^a) = \alpha z_{\boldsymbol{n}}^- \boldsymbol{L}_{\boldsymbol{n}}^- \tag{2.38a}$$

$$\boldsymbol{A_n}(\boldsymbol{U}_h^a) + \boldsymbol{A'_{n'}}(\boldsymbol{U}_h^{a'}) = \boldsymbol{0} \tag{2.38b}$$

$$\boldsymbol{A'_{n'}}(\boldsymbol{U}'_h) - \boldsymbol{A'_{n'}}(\boldsymbol{U}_h^{a'}) = \alpha' z_{\boldsymbol{n'}}^{-'} \boldsymbol{L}_{\boldsymbol{n'}}^{-'} \tag{2.38c}$$

It is worth noting that, according to the definition of the Jacobian operator (2.17), the equation (2.38b) corresponds to the following classical interface conditions for perfect fluids:

$$p_h^a - p_h^{a'} = 0 \ , \ \boldsymbol{v}_h^a \cdot \boldsymbol{n} + \boldsymbol{v}_h^{a'} \cdot \boldsymbol{n'} = 0 \tag{2.39}$$

Solving the Riemann problem (2.38) leads to the determination of the two unknown states $\{\boldsymbol{U}^a, \boldsymbol{U}^{a'}\}$, *i.e.*, the two characteristic coefficients $\{\alpha, \alpha'\}$. By adding the three equations of (2.38), the unknown states $\{\boldsymbol{U}^a, \boldsymbol{U}^{a'}\}$ are eliminated and one obtains:

$$\boldsymbol{A_n}(\boldsymbol{U}_h) - \alpha\lambda_{\boldsymbol{n}}^- \boldsymbol{M}(\boldsymbol{R}_{\boldsymbol{n}}^-) + \boldsymbol{A'_{n'}}(\boldsymbol{U}'_h) - \alpha'\lambda_{\boldsymbol{n'}}^{-'} \boldsymbol{M'}(\boldsymbol{R}_{\boldsymbol{n'}}^{-'}) = \boldsymbol{0} \tag{2.40}$$

Regarding the definition of $\boldsymbol{M}$ (2.3), the Jacobian operator (2.17) and the eigenmodes (2.28) and (2.30), one can obtain the following equations by applying the $\wp_{vect}$ and $\wp_{scalar}$ on (2.40):

$$-p_h \boldsymbol{n} - p'_h \boldsymbol{n'} = \alpha z_{\boldsymbol{n}}^- \frac{1}{\sqrt{2}} \boldsymbol{n} + \alpha' z_{\boldsymbol{n'}}^{-'} \frac{1}{\sqrt{2}} \boldsymbol{n'} \tag{2.41a}$$

$$-\boldsymbol{n} \cdot \boldsymbol{v}_h - \boldsymbol{n'} \cdot \boldsymbol{v}'_h = -\frac{1}{\sqrt{2}}\alpha - \frac{1}{\sqrt{2}}\alpha' \tag{2.41b}$$

Hence, one obtains a linear system of two equations for two unknowns $\{\alpha, \alpha'\}$. Two operators $\wp_{vect}(\,\cdot\,)$ and $\wp_{scalar}(\,\cdot\,)$ are introduced to treat the vectorial and scalar part of a generalized field $\boldsymbol{W} = (\boldsymbol{w}\ q)^T$ separately, and they are defined as follows:

$$\wp_{vect}(\boldsymbol{W}) = \boldsymbol{w} \ , \ \wp_{scalar}(\boldsymbol{W}) = q \tag{2.42}$$

In order to calculate α and α', following manipulations should be performed:

- To obtain α
  $-\frac{\overline{z_{\boldsymbol{n}}^-}^R}{z_{\boldsymbol{n}}^-}\frac{1}{\sqrt{2}}(\frac{\boldsymbol{n'}}{z_{\boldsymbol{n'}}^{-'}} \cdot \text{Eq.(2.41a)} + \text{Eq.(2.41b)})$ leads to:

$$\tilde{\boldsymbol{L}}_{\boldsymbol{n}}^- \cdot (\boldsymbol{U}_h - \boldsymbol{U}'_h) = \alpha \tag{2.43}$$

- To obtain α'
  $-\frac{\overline{z_{\boldsymbol{n}}^-}^R}{z_{\boldsymbol{n'}}^{-'}}\frac{1}{\sqrt{2}}(\frac{\boldsymbol{n'}}{z_{\boldsymbol{n}}^-} \cdot \text{Eq.(2.41a)} + \text{Eq.(2.41b)})$ leads to:

$$\tilde{\boldsymbol{L}}_{\boldsymbol{n'}}^{-'} \cdot (\boldsymbol{U}'_h - \boldsymbol{U}_h) = \alpha' \tag{2.44}$$

In (2.43) and (2.44), $\{\tilde{\boldsymbol{L}}_{\boldsymbol{n},k}^-, \tilde{\boldsymbol{L}}_{\boldsymbol{n'},k}^{-'}\}$ are two "perturbed" eigenmodes calculated as follows by coupling the material properties of the adjacent elements E and E':

$$\tilde{\boldsymbol{L}}_{\boldsymbol{n}}^- = \begin{pmatrix} C_z^- \wp_{vect}(\boldsymbol{L}_{\boldsymbol{n}}^-) \\ C_z^{-'} \wp_{scalar}(\boldsymbol{L}_{\boldsymbol{n}}^-) \end{pmatrix} \ , \ \tilde{\boldsymbol{L}}_{\boldsymbol{n'}}^{-'} = \begin{pmatrix} C_z^{-'} \wp_{vect}(\boldsymbol{L}_{\boldsymbol{n'}}^{-'}) \\ C_z^- \wp_{scalar}(\boldsymbol{L}_{\boldsymbol{n'}}^{-'}) \end{pmatrix} \tag{2.45}$$

With:

$$C_z^- = \frac{\overline{\overline{z_{\boldsymbol{n}}^-}}^R}{z_{\boldsymbol{n}}^-} = \frac{z_{\boldsymbol{n}}^{-'}}{\overline{\overline{z_{\boldsymbol{n}}^-}}^V} > 0 \ , \ C_z^{-'} = \frac{\overline{\overline{z_{\boldsymbol{n}}^-}}^R}{z_{\boldsymbol{n}'}^{-'}} = \frac{z_{\boldsymbol{n}}^-}{\overline{\overline{z_{\boldsymbol{n}}^-}}^V} > 0 \tag{2.46}$$

$\overline{\overline{z_{\boldsymbol{n}}^-}}^R$ and $\overline{\overline{z_{\boldsymbol{n}}^-}}^V$ respectively denote the harmonic and arithmetic means, between E and E', of the acoustic impedance of the eigenvector. Finally, the upwind numerical fluxes defined as $\hat{\boldsymbol{F}}_{\boldsymbol{n}}(\boldsymbol{U}_h, \boldsymbol{U}'_h) = \boldsymbol{A}_{\boldsymbol{n}}(\boldsymbol{U}_h^a) = \frac{1}{2}(\boldsymbol{A}_{\boldsymbol{n}}(\boldsymbol{U}_h^a) - \boldsymbol{A}'_{\boldsymbol{n}'}(\boldsymbol{U}_h^{a'}))$ can be calculated by replacing the estimated characteristic coefficients in following equivalent equations:

$$\hat{\boldsymbol{F}}_{\boldsymbol{n}}(\boldsymbol{U}_h, \boldsymbol{U}'_h) = \frac{1}{2}\big(\boldsymbol{A}_{\boldsymbol{n}}(\boldsymbol{U}_h) - \boldsymbol{A}'_{\boldsymbol{n}'}(\boldsymbol{U}'_h) - \alpha z_{\boldsymbol{n}}^- \boldsymbol{L}_{\boldsymbol{n}}^- + \alpha' z_{\boldsymbol{n}'}^{-'} \boldsymbol{L}_{\boldsymbol{n}'}^{-'}\big) \tag{2.47a}$$

$$= \boldsymbol{A}_{\boldsymbol{n}}(\boldsymbol{U}_h) - \alpha z_{\boldsymbol{n}}^- \boldsymbol{L}_{\boldsymbol{n}}^- \tag{2.47b}$$

Remark 2.3. The first-order hyperbolic governing acoustic wave equation could also be written in another equivalent form:

$$\begin{aligned} \partial_t \boldsymbol{v} - \rho_f^{-1} \boldsymbol{\nabla}_{\boldsymbol{x}} p &= \boldsymbol{0} \\ \partial_t p - \lambda_f \mathrm{div}_{\boldsymbol{x}} \boldsymbol{v} &= 0 \end{aligned} \tag{2.48}$$

which can be written in the following general form:

$$\partial_t \boldsymbol{U} + \overline{\boldsymbol{A}}^{\partial_x}(\boldsymbol{U}) = \boldsymbol{0} \tag{2.49}$$

with the following definitions of operators for the velocity-pressure acoustic wave equation:

$$\overline{\boldsymbol{A}}^{\partial_x}\begin{pmatrix} \boldsymbol{w} \\ q \end{pmatrix} = \begin{pmatrix} -\rho_f^{-1} \boldsymbol{\nabla}_{\boldsymbol{x}} q \\ -\lambda_f \mathrm{div}_{\boldsymbol{x}} \boldsymbol{w} \end{pmatrix} , \ \overline{\boldsymbol{A}}_{\boldsymbol{n}}\begin{pmatrix} \boldsymbol{w} \\ q \end{pmatrix} = \begin{pmatrix} -\rho_f^{-1} q \boldsymbol{n} \\ -\lambda_f \boldsymbol{n} \cdot \boldsymbol{w} \end{pmatrix} \tag{2.50}$$

Using this form of strong formulation and following the same steps as followed in section 2.2.1, the following physical interface condition is obtained:

$$\frac{p_h^a}{\rho_f^E} - \frac{p_h^{a'}}{\rho_f^{E'}} = 0 \ , \quad \lambda_f^E \boldsymbol{v}_h^a \cdot \boldsymbol{n} + \lambda_f^{E'} \boldsymbol{v}_h^{a'} \cdot \boldsymbol{n}' = 0 \tag{2.51}$$

This interface condition is generally not valid when the element interface is also a physical interface. This issue has already been discussed in the elastic case in [82]. Hence, the strong formulation in the equation (2.1) and the associated Jacobian operator are considered for calculating the numerical fluxes.

2.2.2 Numerical fluxes across elastic-elastic interfaces

We consider the interface of two adjacent elements E and E' having respectively $(\rho, \boldsymbol{C}, \boldsymbol{U}_h)$ and $(\rho', \boldsymbol{C}', \boldsymbol{U}'_h)$ as densities, elastic moduli and initial states (Figure 2.2). The Riemann problem defines the states that are results of the propagation of the discontinuity $\boldsymbol{U}_h - \boldsymbol{U'}_h$. Assuming that $\lambda_{\boldsymbol{n},qL}^- < \lambda_{\boldsymbol{n},qT_1}^- < \lambda_{\boldsymbol{n},qT_2}^-$, the Rankine–Hugoniot jump conditions (Figure 2.2) are written as follows:

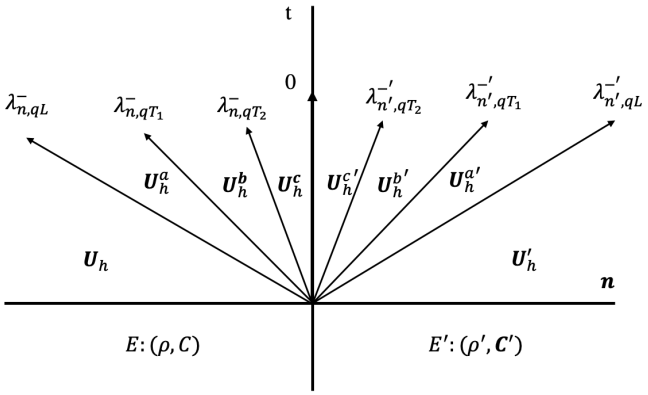

Figure 2.2. Sketch illustration of the Rankine-Hugoniot jump condition in the Riemann problem at an elastic-elastic element interface

$$\boldsymbol{A_n}(\boldsymbol{U}_h - \boldsymbol{U}^a_h) = \lambda^-_{\boldsymbol{n},qL}\boldsymbol{M}(\boldsymbol{U}_h - \boldsymbol{U}^a_h) \tag{2.52a}$$
$$\boldsymbol{A_n}(\boldsymbol{U}^a_h - \boldsymbol{U}^b_h) = \lambda^-_{\boldsymbol{n},qT_1}\boldsymbol{M}(\boldsymbol{U}^a_h - \boldsymbol{U}^b_h), \boldsymbol{A_n}(\boldsymbol{U}^b_h - \boldsymbol{U}^c_h) = \lambda^-_{\boldsymbol{n},qT_2}\boldsymbol{M}(\boldsymbol{U}^b_h - \boldsymbol{U}^c_h) \tag{2.52b}$$
$$\boldsymbol{A_n}(\boldsymbol{U}^c_h) + \boldsymbol{A'_{n'}}(\boldsymbol{U}^{c'}_h) = \boldsymbol{0} \tag{2.52c}$$
$$\boldsymbol{A'_{n'}}(\boldsymbol{U}^{b'}_h - \boldsymbol{U}^{c'}_h) = \lambda^{-'}_{\boldsymbol{n'},qT_2}\boldsymbol{M}(\boldsymbol{U}^{b'}_h - \boldsymbol{U}^{c'}_h), \boldsymbol{A'_{n'}}(\boldsymbol{U}^{a'}_h - \boldsymbol{U}^{b'}_h) = \lambda^{-'}_{\boldsymbol{n'},qT_1}\boldsymbol{M}(\boldsymbol{U}^{a'}_h - \boldsymbol{U}^{b'}_h) \tag{2.52d}$$
$$\boldsymbol{A'_{n'}}(\boldsymbol{U}'_h - \boldsymbol{U}^{a'}_h) = \lambda^{-'}_{\boldsymbol{n},qL}\boldsymbol{M}(\boldsymbol{U}'_h - \boldsymbol{U}^{a'}_h) \tag{2.52e}$$

According to the definition of the eigenvalues and eigenvectors of $\boldsymbol{A_n}$, the following equations hold:

$$\boldsymbol{U}_h - \boldsymbol{U}^a_h = \alpha_{qL}\boldsymbol{R}^-_{\boldsymbol{n},qL}, \boldsymbol{U}^a_h - \boldsymbol{U}^b_h = \alpha_{qT_1}\boldsymbol{R}^-_{\boldsymbol{n},qT_1}, \boldsymbol{U}^b_h - \boldsymbol{U}^c_h = \alpha_{qT_2}\boldsymbol{R}^-_{\boldsymbol{n},qT_2} \tag{2.53a}$$
$$\boldsymbol{U}'_h - \boldsymbol{U}^{a'}_h = \alpha'_{qL}\boldsymbol{R}^{-'}_{\boldsymbol{n'},qL}, \boldsymbol{U}^{a'}_h - \boldsymbol{U}^{b'}_h = \alpha'_{qT_1}\boldsymbol{R}^{-'}_{\boldsymbol{n'},qT_1}, \boldsymbol{U}^{b'}_h - \boldsymbol{U}^{c'}_h = \alpha'_{qT_2}\boldsymbol{R}^{-'}_{\boldsymbol{n'},qT_2} \tag{2.53b}$$

By respectively adding the three first equations given by (2.52a)–(2.52b) and the three last equations given by (2.52d)–(2.52e), and applying (2.53), the Rankine–Hugoniot jump conditions finally become:

$$\boldsymbol{A_n}(\boldsymbol{U}_h) - \boldsymbol{A_n}(\boldsymbol{U}^c_h) = \alpha_k z^-_{\boldsymbol{n},k}\boldsymbol{L}^-_{\boldsymbol{n},k} \tag{2.54a}$$
$$\boldsymbol{A_n}(\boldsymbol{U}^c_h) + \boldsymbol{A'_{n'}}(\boldsymbol{U}^{c'}_h) = \boldsymbol{0} \tag{2.54b}$$
$$\boldsymbol{A'_{n'}}(\boldsymbol{U}'_h) - \boldsymbol{A'_{n'}}(\boldsymbol{U}^{c'}_h) = \alpha'_k z^{-'}_{\boldsymbol{n'},k}\boldsymbol{L}^{-'}_{\boldsymbol{n'},k} \tag{2.54c}$$

After determination of the six characteristic coefficients $\{\alpha_k, \alpha'_k\}_{k=qL,qT_1,qT_2}$, the upwind numerical fluxes defined as $\hat{\boldsymbol{F}}_{\boldsymbol{n}}(\boldsymbol{U}_h, \boldsymbol{U}'_h) = \boldsymbol{A_n}(\boldsymbol{U}^c_h) = \frac{1}{2}(\boldsymbol{A_n}(\boldsymbol{U}^c_h) - \boldsymbol{A'_{n'}}(\boldsymbol{U}^{c'}_h))$ can be calculated by using the following two equivalent forms:

$$\hat{\boldsymbol{F}}_{\boldsymbol{n}}(\boldsymbol{U}_h, \boldsymbol{U}'_h) = \frac{1}{2}(\boldsymbol{A_n}(\boldsymbol{U}_h) - \boldsymbol{A'_{n'}}(\boldsymbol{U}'_h) - \alpha_k z^-_{\boldsymbol{n},k}\boldsymbol{L}^-_{\boldsymbol{n},k} + \alpha'_k z^{-'}_{\boldsymbol{n},k}\boldsymbol{L}^{-'}_{\boldsymbol{n},k}) \tag{2.55a}$$
$$= \boldsymbol{A_n}(\boldsymbol{U}_h) - \alpha_k z^-_{\boldsymbol{n},k}\boldsymbol{L}^-_{\boldsymbol{n},k} \tag{2.55b}$$

Beside the operator $\wp_{vect}(\,\cdot\,)$ in (2.42), the new operator $\wp_{tens}(\,\cdot\,)$ is defined: when applied to a generalized vector $\boldsymbol{W} = (\boldsymbol{w}\ \boldsymbol{\tau})^T$, it gives the tensorial component $\wp_{tens}(\boldsymbol{W}) = \boldsymbol{\tau}$. Using $\wp_{vect}$ and $\wp_{tens}$, the vectorial part and the tensorial parts of the equations (2.54) can be separately manipulated.

According to the definition of the Jacobian operator (2.22) and the definition of the Christoffel tensor $\mathbf{\Gamma}_{\boldsymbol{n}}$, (2.54b) is rewritten as follows:

$$\boldsymbol{\sigma}_h^c \cdot \boldsymbol{n} + \boldsymbol{\sigma}_h^{c'} \cdot \boldsymbol{n}' = \mathbf{0} \ , \ \boldsymbol{v}_h^c - \boldsymbol{v}_h^{c'} = \mathbf{0} \tag{2.56}$$

This equation verifies the continuity on the element interface for the velocity and stress components.

To solve the Riemann problem (2.54), the same technique presented in the preceding section is used to determine the characteristic coefficients $\{\alpha_k, \alpha'_k\}_{k=qL,qT_1,qT_2}$ of the Riemann problem (2.54). By adding the three equations of (2.54), *i.e.* Eq.(2.54a) + Eq.(2.54b) + Eq.(2.54c), we get:

$$\boldsymbol{A_n}(\boldsymbol{U}_h) - \alpha_k \lambda^-_{\boldsymbol{n},k} \boldsymbol{M}(\boldsymbol{R}^-_{\boldsymbol{n},k}) + \boldsymbol{A'_{n'}}(\boldsymbol{U}'_h) - \alpha'_k \lambda^{-'}_{\boldsymbol{n}',k} \boldsymbol{M'}(\boldsymbol{R}^{-'}_{\boldsymbol{n}',k}) = \mathbf{0} \tag{2.57}$$

According to the definition of $\boldsymbol{A_n}$ (2.17), the eigenmodes (2.32) and the equation (2.30), we obtain the following equations by considering separately $\wp_{vect}$(eq.(2.58a)) and $\wp_{tens}$(eq.(2.58b)):

$$\boldsymbol{\sigma}_h \cdot \boldsymbol{n} + \boldsymbol{\sigma}'_h \cdot \boldsymbol{n}' = -\sum_l \alpha_l z^-_{\boldsymbol{n},l} \frac{\boldsymbol{\gamma}_{\boldsymbol{n},l}}{\sqrt{2}} - \sum_l \alpha'_l z^{-'}_{\boldsymbol{n}',l} \frac{\boldsymbol{\gamma}'_{\boldsymbol{n}',l}}{\sqrt{2}} \tag{2.58a}$$

$$\boldsymbol{v}_h - \boldsymbol{v}'_h = \sum_l \alpha_l \frac{\boldsymbol{\gamma}_{\boldsymbol{n},l}}{\sqrt{2}} - \sum_l \alpha'_l \frac{\boldsymbol{\gamma}'_{\boldsymbol{n}',l}}{\sqrt{2}} \tag{2.58b}$$

To obtain (2.58b), we have used the fact that $\boldsymbol{w} \otimes_s \boldsymbol{n} = \mathbf{0}$ implies $\boldsymbol{w} = \mathbf{0}$. Then, the next step is to apply the following manipulations on (2.58):

- For the first three equations corresponding to $\{\alpha_k\}$
  $\frac{\overline{z^-_{\boldsymbol{n},k}}^R}{z^-_{\boldsymbol{n},k}} \frac{\boldsymbol{\gamma}_{\boldsymbol{n},k}}{\sqrt{2}} \cdot (-\frac{1}{z^{-'}_{\boldsymbol{n}',k}}$(2.58a) + (2.58b)) leads to:

$$\tilde{\boldsymbol{L}}^-_{\boldsymbol{n},k} \cdot (\boldsymbol{U}_h - \boldsymbol{U}'_h) = \tilde{\alpha}_k - \frac{1}{2} \sum_{l \neq k} (\frac{\overline{z^-_{\boldsymbol{n},k}}^R}{z^-_{\boldsymbol{n},k}} \frac{\delta z^{-'}_{\boldsymbol{n}',kl}}{z^{-'}_{\boldsymbol{n}',k}} \boldsymbol{\gamma}_{\boldsymbol{n},k} \cdot \boldsymbol{\gamma}'_{\boldsymbol{n}',l}) \alpha'_l \tag{2.59}$$

- For the last three equations corresponding to $\{\tilde{\alpha}'_k\}$
  $\frac{\overline{z^-_{\boldsymbol{n},k}}^R}{z^{-'}_{\boldsymbol{n}',k}} \frac{\boldsymbol{\gamma}'_{\boldsymbol{n}',k}}{\sqrt{2}} \cdot (-\frac{1}{z^-_{\boldsymbol{n},k}}$(2.58a) + Eq.(2.58b)) leads to:

$$\tilde{\boldsymbol{L}}^{-'}_{\boldsymbol{n}',k} \cdot (\boldsymbol{U}'_h - \boldsymbol{U}_h) = \tilde{\alpha}'_k - \frac{1}{2} \sum_{l \neq k} (\frac{\overline{z^-_{\boldsymbol{n},k}}^R}{z^{-'}_{\boldsymbol{n}',k}} \frac{\delta z^-_{\boldsymbol{n},kl}}{z^-_{\boldsymbol{n},k}} \boldsymbol{\gamma}'_{\boldsymbol{n}',k} \cdot \boldsymbol{\gamma}_{\boldsymbol{n},l}) \alpha_l \tag{2.60}$$

The equations (2.59) and (2.60) could be written in the following matrix form:

$$\begin{bmatrix} [I_d] & [B] \\ [B'] & [I_d] \end{bmatrix} \cdot \begin{pmatrix} \{\alpha_k\} \\ \{\alpha'_k\} \end{pmatrix} = \begin{pmatrix} \{\tilde{\boldsymbol{L}}^-_{\boldsymbol{n},k} \cdot (\boldsymbol{U}_h - \boldsymbol{U}'_h)\} \\ \{\tilde{\boldsymbol{L}}^{-'}_{\boldsymbol{n}',k} \cdot (\boldsymbol{U}'_h - \boldsymbol{U}_h)\} \end{pmatrix} \tag{2.61}$$

In (2.61), $[I_d]$ is the $d \times d$ identity matrix and $[B]$ and $[B']$ are $d \times d$ matrices with zero diagonal terms

and the following extra-diagonal terms:

$$B_{kl,k\neq l} = -\frac{C^-_{z,k}}{2}\frac{\delta z^{-'}_{\boldsymbol{n}',kl}}{z^{-'}_{\boldsymbol{n}',k}}\boldsymbol{\gamma}_{\boldsymbol{n},k}\cdot\boldsymbol{\gamma}'_{\boldsymbol{n}',l}\ ,\ B'_{kl,k\neq l} = -\frac{C^{-'}_{z,k}}{2}\frac{\delta z^{-}_{\boldsymbol{n},kl}}{z^{-}_{\boldsymbol{n},k}}\boldsymbol{\gamma}'_{\boldsymbol{n}',k}\cdot\boldsymbol{\gamma}_{\boldsymbol{n},l} \tag{2.62}$$

with $\delta z^-_{\boldsymbol{n},kl} = z^-_{\boldsymbol{n},k} - z^-_{\boldsymbol{n},l}$, $\delta z^{-'}_{\boldsymbol{n}',kl} = z^{-'}_{\boldsymbol{n}',k} - z^{-'}_{\boldsymbol{n}',l}$, and :

$$C^-_{z,k} = \frac{\overline{\overline{z^-_{\boldsymbol{n},k}}}^R}{z^-_{\boldsymbol{n},k}} = \frac{z^{-'}_{\boldsymbol{n},k}}{\overline{\overline{z^-_{\boldsymbol{n},k}}}^V} > 0\ ,\ C^{-'}_{z,k} = \frac{\overline{\overline{z^-_{\boldsymbol{n},k}}}^R}{z^{-'}_{\boldsymbol{n}',k}} = \frac{z^-_{\boldsymbol{n},k}}{\overline{\overline{z^-_{\boldsymbol{n},k}}}^V} > 0 \tag{2.63}$$

$\{\tilde{\boldsymbol{L}}^-_{\boldsymbol{n},k}, \tilde{\boldsymbol{L}}^{-'}_{\boldsymbol{n}',k}\}$ are the perturbed left eigenmodes of $\{\boldsymbol{A}_{\boldsymbol{n}}, \boldsymbol{A}'_{\boldsymbol{n}'}\}$ calculated by using the material properties of the adjacent element in the following way:

$$\tilde{\boldsymbol{L}}^-_{\boldsymbol{n},k} = \begin{pmatrix} C^-_{z,k}\wp_{vect}(\boldsymbol{L}^-_{\boldsymbol{n},k}) \\ C^{-'}_{z,k}\wp_{tens}(\boldsymbol{L}^-_{\boldsymbol{n},k}) \end{pmatrix}\ ,\ \tilde{\boldsymbol{L}}^{-'}_{\boldsymbol{n}',k} = \begin{pmatrix} C^{-'}_{z,k}\wp_{vect}(\boldsymbol{L}^{-'}_{\boldsymbol{n}',k}) \\ C^-_{z,k}\wp_{tens}(\boldsymbol{L}^{-'}_{\boldsymbol{n}',k}) \end{pmatrix} \tag{2.64}$$

To calculate the numerical flux on the elastic-elastic interface for the acoustic element E, we recall that the equation (2.55b) is used. So, one needs to find α_k by solving the system of equations (2.78), which gives rise to:

$$\begin{pmatrix} \{\alpha_k\} \\ \{\alpha'_k\} \end{pmatrix} = [R^{ee}]^{-1}\cdot \begin{bmatrix} \{\tilde{\boldsymbol{L}}^-_{\boldsymbol{n},k}\cdot(\boldsymbol{U}_h - \boldsymbol{U}'_h)\} \\ \{\tilde{\boldsymbol{L}}^{-'}_{\boldsymbol{n}',k}\cdot(\boldsymbol{U}'_h - \boldsymbol{U}_h)\} \end{bmatrix} \tag{2.65}$$

with $[R^{ee}]^{-1}$ defined as:

$$[R^{ee}]^{-1} = \begin{bmatrix} [I_d] & [B] \\ [B'] & [I_d] \end{bmatrix}^{-1} = \begin{bmatrix} [D] & -[H] \\ -[H'] & [D'] \end{bmatrix} \tag{2.66}$$

with $[D]$, $[D']$, $[H]$ and $[H']$ four $d\times d$ matrices defined by the decomposition of the inverse matrix of $[R^{ee}]$.Finally after solving the system of equations (2.61) for characteristic equations, one gets:

$$\alpha_k = D_{kl}(\tilde{\boldsymbol{L}}^-_{\boldsymbol{n},l}\cdot(\boldsymbol{U}_h - \boldsymbol{U}'_h)) - H_{kl}(\tilde{\boldsymbol{L}}^{-'}_{\boldsymbol{n}',l}\cdot(\boldsymbol{U}'_h - \boldsymbol{U}_h)) \tag{2.67}$$

2.2.3 Numerical fluxes across the acoustic-elastic interfaces

Let us consider the interface of two adjacent elements, E, and E'. But now the element E is governed by the acoustic wave equations with $(\rho_f, \lambda_f, \boldsymbol{U}_h)$ as density, bulk modulus, and initial state. In contrast, E' is governed by the elastic wave equations with $(\rho', C', \boldsymbol{U}'_h)$ as density, elasticity tensor and initial state (Figure 2.3). In this case, the Rankine-Hugoniot jump conditions are written as follows:

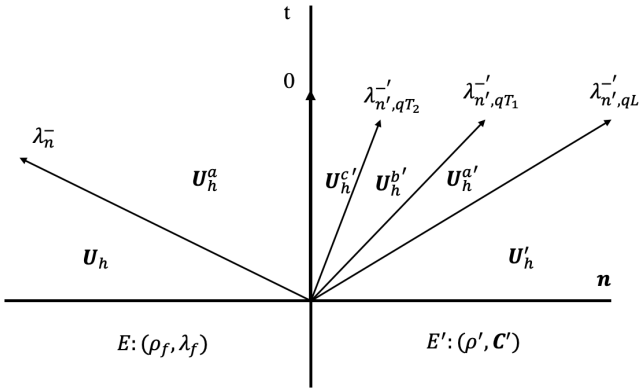

Figure 2.3. Sketch illustration of the Rankine-Hugoniot jump condition in the Riemann problem at an acoustic-elastic element interface

$$\boldsymbol{A_n}(\boldsymbol{U}_h - \boldsymbol{U}^a_h) = \lambda^{-}_{\boldsymbol{n}}\boldsymbol{M}(\boldsymbol{U}_h - \boldsymbol{U}^a_h) \tag{2.68a}$$

$$\boldsymbol{A_n}(\boldsymbol{U}^a_h) + \boldsymbol{\Pi}_{\boldsymbol{n}'}(\boldsymbol{A}'_{\boldsymbol{n}'}(\boldsymbol{U}^{c'}_h)) = \boldsymbol{0} \tag{2.68b}$$

$$\boldsymbol{A}'_{\boldsymbol{n}'}(\boldsymbol{U}^{b'}_h - \boldsymbol{U}^{c'}_h) = \lambda^{-'}_{\boldsymbol{n}',qT_2}\boldsymbol{M}'(\boldsymbol{U}^{b'}_h - \boldsymbol{U}^{c'}_h) \tag{2.68c}$$

$$\boldsymbol{A}'_{\boldsymbol{n}'}(\boldsymbol{U}^{a'}_h - \boldsymbol{U}^{b'}_h) = \lambda^{-'}_{\boldsymbol{n}',qT_1}\boldsymbol{M}'(\boldsymbol{U}^{a'}_h - \boldsymbol{U}^{b'}_h) \tag{2.68d}$$

$$\boldsymbol{A}'_{\boldsymbol{n}'}(\boldsymbol{U}'_h - \boldsymbol{U}^{a'}_h) = \lambda^{-'}_{\boldsymbol{n},qL}\boldsymbol{M}'(\boldsymbol{U}'_h - \boldsymbol{U}^{a'}_h) \tag{2.68e}$$

In (2.68), the operator $\boldsymbol{\Pi}_{\boldsymbol{n}'}$ from $\mathbb{R}^d \times \mathbb{R}^{d\times d_{sym}}$ to $\mathbb{R}^d \times \mathbb{R}$ is defined as follows: $\forall \boldsymbol{W} = (\boldsymbol{w}\ \boldsymbol{\tau})^T \in \mathbb{R}^d \times \mathbb{R}^{d\times d_{sym}}$,

$$\boldsymbol{\Pi}_{\boldsymbol{n}'}(\boldsymbol{W}) = \begin{pmatrix} \boldsymbol{w} \\ (\boldsymbol{n}' \otimes \boldsymbol{n}') : \boldsymbol{\tau} \end{pmatrix} \tag{2.69}$$

Then, it can be shown that according to the definition of $\boldsymbol{A_n}$ in both acoustic and elastic media, and to the definition of $\boldsymbol{\Pi}_{\boldsymbol{n}'}$, the equation (2.68b) corresponds to the following classical perfect fluid-solid interface conditions:

$$p^a_h\boldsymbol{n} + \boldsymbol{\sigma}^{c'}_h \cdot \boldsymbol{n}' = \boldsymbol{0}\ ,\ \boldsymbol{n}\cdot\boldsymbol{v}^a_h + \boldsymbol{n}'\cdot\boldsymbol{v}^{c'}_h = 0 \tag{2.70}$$

Now, as in the acoustic-acoustic case, the discontinuity terms in (2.68) are decomposed as follows within the right eigenvectors basis:

$$\boldsymbol{U}_h - \boldsymbol{U}^a_h = \alpha\boldsymbol{R}^{-}_{\boldsymbol{n}} \tag{2.71a}$$

$$\boldsymbol{U}'_h - \boldsymbol{U}^{a'}_h = \alpha'_{qL}\boldsymbol{R}^{-'}_{\boldsymbol{n}',qL},\ \ \boldsymbol{U}^{a'}_h - \boldsymbol{U}^{b'}_h = \alpha'_{qT_1}\boldsymbol{R}^{-'}_{\boldsymbol{n}',qT_1},\ \ \boldsymbol{U}^{b'}_h - \boldsymbol{U}^{c'}_h = \alpha'_{qT_2}\boldsymbol{R}^{-'}_{\boldsymbol{n}',qT_2} \tag{2.71b}$$

By adding the three last equations given by (2.68c)–(2.68e), and by applying (2.71), the second equation of (2.30), and the first equation of (2.35), the Rankine–Hugoniot jump conditions (2.68) finally become:

$$\boldsymbol{A_n}(\boldsymbol{U}_h) - \boldsymbol{A_n}(\boldsymbol{U}^a_h) = \alpha z^{-}_{\boldsymbol{n}}\boldsymbol{L}^{-}_{\boldsymbol{n}} \tag{2.72a}$$

$$\boldsymbol{A_n}(\boldsymbol{U}^a_h) + \boldsymbol{\Pi}_{\boldsymbol{n}'}(\boldsymbol{A}'_{\boldsymbol{n}'}(\boldsymbol{U}^{c'}_h)) = \boldsymbol{0} \tag{2.72b}$$

$$\boldsymbol{A}'_{\boldsymbol{n}'}(\boldsymbol{U}'_h) - \boldsymbol{A}'_{\boldsymbol{n}'}(\boldsymbol{U}^{c'}_h) = \alpha'_k z^{-'}_{\boldsymbol{n}',k}\boldsymbol{L}^{-'}_{\boldsymbol{n}',k} \tag{2.72c}$$

First we consider the numerical flux in an acoustic element E having an interface with an adjacent

elastic element E'. By applying the operator $\mathbf{\Pi}_{\boldsymbol{n}'}$ to (2.72c) and then adding it to the other two equations of (2.72), the unknown states $\{\boldsymbol{U}^a, \boldsymbol{U}^{c'}\}$ are eliminated and one obtains:

$$\boldsymbol{A}_{\boldsymbol{n}}(\boldsymbol{U}_h) - \alpha z_{\boldsymbol{n}}^{-} \boldsymbol{L}_{\boldsymbol{n}}^{-} + \mathbf{\Pi}_{\boldsymbol{n}'}(\boldsymbol{A}'_{\boldsymbol{n}'}(\boldsymbol{U}'_h)) - \alpha'_k z_{\boldsymbol{n}',k}^{-'} \mathbf{\Pi}_{\boldsymbol{n}'}(\boldsymbol{L}_{\boldsymbol{n}',k}^{-'}) = \mathbf{0} \tag{2.73}$$

Regarding the definition of the Jacobian operator by (2.17) and (2.17), the left eigenvectors by (2.30) and (2.28), one can obtain the following equations by applying the $\wp_{vect}$ and $\wp_{scalar}$ on (2.73):

$$-p_h \boldsymbol{n} - \boldsymbol{\sigma}'_h \cdot \boldsymbol{n}' = \alpha z_{\boldsymbol{n}}^{-} \frac{1}{\sqrt{2}} \boldsymbol{n} + \sum_l \alpha'_l z_{\boldsymbol{n}',l}^{-'} \frac{\boldsymbol{\gamma}'_{\boldsymbol{n}',l}}{\sqrt{2}} \tag{2.74a}$$

$$-\boldsymbol{n} \cdot \boldsymbol{v}_h - \boldsymbol{n}' \cdot \boldsymbol{v}'_h = -\alpha \frac{1}{\sqrt{2}} - \sum_l \alpha'_l (\boldsymbol{n}' \cdot \frac{\boldsymbol{\gamma}'_{\boldsymbol{n}',l}}{\sqrt{2}}) \tag{2.74b}$$

Hence, one obtains a linear system of four equations for four unknowns $\{\alpha, \{\alpha'_k\}\}$. For that purpose, the following manipulations are performed on the system of equations in (2.74):

- First equation (for α):
  $\frac{1}{\sqrt{2}}(-\frac{\boldsymbol{n}}{z_{\boldsymbol{n}}^{-}} \cdot$ Eq.(2.74a) + Eq.(2.74b)) leads to:

$$\boldsymbol{L}_{\boldsymbol{n}}^{-} \cdot (\boldsymbol{U}_h - \mathbf{\Pi}_{\boldsymbol{n}'}(\boldsymbol{U}'_h)) = \alpha - \sum_l \frac{z_{\boldsymbol{n}}^{-} - z_{\boldsymbol{n}',l}^{-'}}{2 z_{\boldsymbol{n}}^{-}} (\boldsymbol{n} \cdot \boldsymbol{\gamma}'_{\boldsymbol{n}',l}) \alpha'_l \tag{2.75}$$

- Equations for $\{\alpha'_k\}$:
  For each k, $\sqrt{2}\frac{\boldsymbol{\gamma}'_{\boldsymbol{n}',k}}{z_{\boldsymbol{n}',k}^{-'}} \cdot$ (Eq.(2.74a)) leads to:

$$2\wp_{tens}(\boldsymbol{L}_{\boldsymbol{n}',k}^{-'}) : \wp_{tens}(\boldsymbol{U}'_h - \mathbf{\Psi}_{\boldsymbol{n}}(\boldsymbol{U}_h)) = \frac{z_{\boldsymbol{n}}^{-}}{z_{\boldsymbol{n}',k}^{-'}} \boldsymbol{n} \cdot \boldsymbol{\gamma}'_{\boldsymbol{n}',k} \alpha + \alpha'_k \tag{2.76}$$

where the operator $\mathbf{\Psi}_{\boldsymbol{n}}$ from $\mathbb{R}^d \times \mathbb{R}$ to $\mathbb{R}^d \times \mathbb{R}^{d \times d_{sym}}$ is defined as follows: $\forall \boldsymbol{W} = (\boldsymbol{w}\ q)^T \in \mathbb{R}^d \times \mathbb{R}$,

$$\mathbf{\Psi}_{\boldsymbol{n}}(\boldsymbol{W}) = \begin{pmatrix} \boldsymbol{w} \\ q\boldsymbol{n} \otimes \boldsymbol{n} \end{pmatrix} \tag{2.77}$$

The equations (2.75) and (2.76) could be written in the form of the following linear system of equations:

$$\begin{bmatrix} 1 & [B^{ae}]_{1\times 3} \\ [B^{ae'}]_{3\times 1} & [Id]_{3\times 3} \end{bmatrix} \cdot \begin{pmatrix} \alpha \\ \{\alpha'_k\} \end{pmatrix} = \begin{bmatrix} \boldsymbol{L}_{\boldsymbol{n}}^{-} \cdot (\boldsymbol{U}_h - \mathbf{\Pi}_{\boldsymbol{n}'}(\boldsymbol{U}'_h)) \\ \{2\wp_{tens}(\boldsymbol{L}_{\boldsymbol{n}',k}^{-'}) : \wp_{tens}(\boldsymbol{U}'_h - \mathbf{\Psi}_{\boldsymbol{n}}(\boldsymbol{U}_h))\} \end{bmatrix} \tag{2.78}$$

where the components of the matrices $[B^{ae}]$ and $[B^{ae'}]$ are:

$$B_{1k}^{ae} = -\frac{z_{\boldsymbol{n}}^{-} - z_{\boldsymbol{n}',k}^{-'}}{2 z_{\boldsymbol{n}}^{-}} \boldsymbol{n} \cdot \boldsymbol{\gamma}'_{\boldsymbol{n}',k}\ ,\ B_{k1}^{ae'} = \frac{z_{\boldsymbol{n}}^{-}}{z_{\boldsymbol{n}',k}^{-'}} \boldsymbol{n} \cdot \boldsymbol{\gamma}'_{\boldsymbol{n}',k} \tag{2.79}$$

To calculate the numerical flux on the acoustic-elastic interface for the acoustic element E, we recall

that the equation (2.47b) is used. So, one needs to find α by solving the system of equations (2.78), which gives rise to:

$$\begin{pmatrix} \alpha \\ \{\alpha'_k\} \end{pmatrix} = [R^{ae}]^{-1} \cdot \begin{bmatrix} \boldsymbol{L}^{-}_{\boldsymbol{n}} \cdot (\boldsymbol{U}_h - \boldsymbol{\Pi}_{\boldsymbol{n}'}(\boldsymbol{U}'_h)) \\ \{2\wp_{tens}(\boldsymbol{L}^{-'}_{\boldsymbol{n}',k}) : \wp_{tens}(\boldsymbol{U}'_h - \boldsymbol{\Psi}_{\boldsymbol{n}}(\boldsymbol{U}_h))\} \end{bmatrix} \tag{2.80}$$

with $[R^{ae}]^{-1}$ defined as:

$$[R^{ae}]^{-1} = \begin{bmatrix} 1 & [B^{ae}]_{1\times 3} \\ [B^{ae'}]_{3\times 1} & [Id]_{3\times 3} \end{bmatrix}^{-1} = \begin{bmatrix} D^{ae}_{11} & -[H^{ae}]_{1\times 3} \\ -[H^{ae'}]_{3\times 1} & [D^{ae'}]_{3\times 3} \end{bmatrix} \tag{2.81}$$

After solving the system of equations (2.78) for characteristic equations, one finally gets:

$$\alpha = D^{ae}_{11}\boldsymbol{L}^{-}_{\boldsymbol{n}} \cdot (\boldsymbol{U}_h - \boldsymbol{\Pi}_{\boldsymbol{n}'}(\boldsymbol{U}'_h)) - 2H^{ae}_{1k}\wp_{tens}(\boldsymbol{L}^{-'}_{\boldsymbol{n}',k}) : \wp_{tens}(\boldsymbol{U}'_h - \boldsymbol{\Psi}_{\boldsymbol{n}}(\boldsymbol{U}_h)) \tag{2.82}$$

Then, the numerical flux is calculated within the acoustic element E using the equation (2.47b).

When the elastic element E' is isotropic, we get on pure longitudinal "L" mode and two pure transverse "T" modes, and we have:

$$\boldsymbol{n} \cdot \boldsymbol{\gamma}'_{\boldsymbol{n}',L} = 0 \ , \ \boldsymbol{n} \cdot \boldsymbol{\gamma}'_{\boldsymbol{n}',T_1} = 0 \ , \ \boldsymbol{n} \cdot \boldsymbol{\gamma}'_{\boldsymbol{n}',T_2} = 0 \tag{2.83}$$

According to (2.78)-(2.79), α, the acoustic wave in E, is only coupled to α'_L, the elastic longitudinal wave in E', which is a well-known classic result. Otherwise, the quasi-transverse elastic waves are always coupled to the acoustic wave through an acoustic-elastic interface.

2.2.4 Numerical fluxes across the elastic-acoustic interfaces

In the object-oriented structure of the OOFE code, each element has information about the fluxes on its interfaces,with the neighboring elements. Therefore, it is interesting to have an explicit expression for the flux term, considering that the element E is governed by elastic wave equations and the neighbor element E' is governed by acoustic wave equations. By reversing the role of E and E' in the preceding equations (2.68), (2.71) and (2.72), the characteristic coefficients $\{\alpha, \alpha'_k\}$ of the Riemann problem (2.72) are solutions of the following linear system of equations:

$$\begin{bmatrix} [Id]_{3\times 3} & [B^{ea}]_{3\times 1} \\ [B^{ea'}]_{1\times 3} & 1 \end{bmatrix} \cdot \begin{pmatrix} \{\alpha_k\} \\ \alpha' \end{pmatrix} = \begin{bmatrix} \{2\wp_{tens}(\boldsymbol{L}^{-}_{\boldsymbol{n},k}) : \wp_{tens}(\boldsymbol{U}_h - \boldsymbol{\Psi}_{\boldsymbol{n}'}(\boldsymbol{U}'_h))\} \\ \boldsymbol{L}^{-'}_{\boldsymbol{n}'} \cdot (\boldsymbol{\Pi}_{\boldsymbol{n}}(\boldsymbol{U}_h) - \boldsymbol{U}'_h) \end{bmatrix} \tag{2.84}$$

where the components of the matrices $[B^{ea}]$ and $[B^{ea'}]$ are:

$$B^{ea}_{k1} = \frac{z^{-'}_{\boldsymbol{n}'}}{z^{-}_{\boldsymbol{n},k}}\boldsymbol{n}' \cdot \boldsymbol{\gamma}_{\boldsymbol{n},k} \ , \ B^{ea'}_{1k} = -\frac{z^{-}_{\boldsymbol{n},k} - z^{-'}_{\boldsymbol{n}'}}{2z^{-'}_{\boldsymbol{n}'}}\boldsymbol{n}' \cdot \boldsymbol{\gamma}_{\boldsymbol{n},k} \tag{2.85}$$

To calculate the numerical flux on the elastic-acoustic interface for the elastic element E, we recall

that the following equation is used:

$$\hat{\boldsymbol{F}}_{\boldsymbol{n}}(\boldsymbol{U}_h, \boldsymbol{U}'_h) = \boldsymbol{A}_{\boldsymbol{n}}(\boldsymbol{U}_h) - \alpha_k z^-_{\boldsymbol{n},k} \boldsymbol{L}^-_{\boldsymbol{n},k} \tag{2.86}$$

So, one needs to find α_k by solving the system of equations (2.84), which gives rise to:

$$\begin{pmatrix} \{\alpha_k\} \\ \alpha' \end{pmatrix} = [R^{ea}]^{-1} \cdot \begin{bmatrix} \{2\wp_{tens}(\boldsymbol{L}^-_{\boldsymbol{n},k}) : \wp_{tens}(\boldsymbol{U}_h - \boldsymbol{\Psi}_{\boldsymbol{n}'}(\boldsymbol{U}'_h))\} \\ \boldsymbol{L}^{-'}_{\boldsymbol{n}'} \cdot (\boldsymbol{U}'_h - \boldsymbol{\Pi}_{\boldsymbol{n}}(\boldsymbol{U}_h)) \end{bmatrix} \tag{2.87}$$

with $[R^{ae}]^{-1}$ is defined here:

$$[R^{ea}]^{-1} = \begin{bmatrix} [Id]_{3\times 3} & [B^{ea}]_{3\times 1} \\ [B^{ea'}]_{1\times 3} & 1 \end{bmatrix}^{-1} = \begin{bmatrix} [D^{ea}]_{3\times 3} & -[H^{ea}]_{3\times 1} \\ -[H^{ea'}]_{1\times 3} & D^{ea'}_{11} \end{bmatrix} \tag{2.88}$$

After solving the system of equations (2.84) for characteristic equations, one finally gets:

$$\alpha_k = 2D^{ea}_{kl}\wp_{tens}(\boldsymbol{L}^-_{\boldsymbol{n},l})) : \wp_{tens}(\boldsymbol{U}_h - \boldsymbol{\Psi}_{\boldsymbol{n}'}(\boldsymbol{U}'_h)) - H^{ea}_{k1}\boldsymbol{L}^{-'}_{\boldsymbol{n}'} \cdot (\boldsymbol{\Pi}_{\boldsymbol{n}}(\boldsymbol{U}_h) - \boldsymbol{U}'_h) \tag{2.89}$$

Implementation of the numerical fluxes

In the OOFE code, each element stores information about the fluxes on its interfaces with neighboring elements. The code explicitly defines the numerical fluxes for both acoustic and elastic elements. When computing the flux term for an element, the code determines the type of the neighboring element and selects the appropriate flux based on both the type of the main element and the type of the neighboring element. This ensures that the correct flux is used, whether the neighboring element is an acoustic or elastic element.

Let us consider first the acoustic element, denoted as E; on the interface ∂E^{aa} with a neighbor acoustic element E', taking into account (2.47b) and (2.43), The flux term in (2.25) becomes:

$$\begin{aligned} & < \boldsymbol{W}_h, \hat{\boldsymbol{F}}_{\boldsymbol{n}}(\boldsymbol{U}_h, \boldsymbol{U}'_h) - \boldsymbol{F}(\boldsymbol{U}_h) >_{\partial E^{aa}} \\ =& - < \boldsymbol{W}_h, \alpha z^-_{\boldsymbol{n}} \boldsymbol{L}^-_{\boldsymbol{n}} >_{\partial E^{aa}} \\ =& - \int_{\partial E^{aa}} \left(\boldsymbol{W}_h \cdot \boldsymbol{L}^-_{\boldsymbol{n}}\right) z^-_{\boldsymbol{n}} \left(\tilde{\boldsymbol{L}}^-_{\boldsymbol{n}} \cdot \boldsymbol{U}_h\right) \\ & + \int_{\partial E^{aa}} \left(\boldsymbol{W}_h \cdot \boldsymbol{L}^-_{\boldsymbol{n}}\right) z^-_{\boldsymbol{n}} \left(\tilde{\boldsymbol{L}}^-_{\boldsymbol{n}} \cdot \boldsymbol{U}'_h\right) \end{aligned} \tag{2.90}$$

If the neighbor element $E'$is an elastic element, taking into account (2.47b) and (2.82), The flux term becomes:

$$\begin{aligned} & < \boldsymbol{W}_h, \hat{\boldsymbol{F}}_{\boldsymbol{n}}(\boldsymbol{U}_h, \boldsymbol{U}'_h) - \boldsymbol{F}(\boldsymbol{U}_h) >_{\partial E^{ae}} \\ =& - < \boldsymbol{W}_h, \alpha z^-_{\boldsymbol{n}} \boldsymbol{L}^-_{\boldsymbol{n}} >_{\partial E^{ae}} \\ =& - \int_{\partial E^{ae}} \left(\boldsymbol{W}_h \cdot \boldsymbol{L}^-_{\boldsymbol{n}}\right) z^-_{\boldsymbol{n}} \left(D^{ae}_{11}\boldsymbol{L}^-_{\boldsymbol{n}} \cdot \boldsymbol{U}_h + 2H^{ae}_{1k}\wp_{tens}(\boldsymbol{L}^{-'}_{\boldsymbol{n}',k}) : \wp_{tens}(\boldsymbol{\Psi}_{\boldsymbol{n}}(\boldsymbol{U}_h)\right) \\ & + \int_{\partial E^{ae}} \left(\boldsymbol{W}_h \cdot \boldsymbol{L}^-_{\boldsymbol{n}}\right) z^-_{\boldsymbol{n}} \left(D^{ae}_{11}\boldsymbol{L}^-_{\boldsymbol{n}} \cdot \boldsymbol{\Pi}_{\boldsymbol{n}'}(\boldsymbol{U}'_h) + 2H^{ae}_{1k}\wp_{tens}(\boldsymbol{L}^{-'}_{\boldsymbol{n}',k}) : \wp_{tens}(\boldsymbol{U}'_h)\right) \end{aligned} \tag{2.91}$$

Then, we exchange the role of acoustic and elastic elements. Let us consider the elastic element, now denoted E; on the interface ∂E^{ee} with a neighbor elastic element E', taking into account (2.86) and (2.67), The flux term in (2.25) becomes:

$$\begin{aligned}
&< \boldsymbol{W}_h, \hat{\boldsymbol{F}}_{\boldsymbol{n}}(\boldsymbol{U}_h, \boldsymbol{U}'_h) - \boldsymbol{F}(\boldsymbol{U}_h) >_{\partial E^{ee}} \\
=&- < \boldsymbol{W}_h, \alpha_k z^-_{\boldsymbol{n},k} \boldsymbol{L}^-_{\boldsymbol{n},k} >_{\partial E^{ee}} \\
=&- \int_{\partial E^{ee}} \left(\boldsymbol{W}_h \cdot \boldsymbol{L}^-_{\boldsymbol{n},k}\right) z^-_{\boldsymbol{n},k} \left(D_{kl} \tilde{\boldsymbol{L}}^-_{\boldsymbol{n},l} \cdot \boldsymbol{U}_h - H_{kl} \boldsymbol{L}^{-'}_{\boldsymbol{n}',l} \cdot \boldsymbol{U}_h\right) \\
&+ \int_{\partial E^{ee}} \left(\boldsymbol{W}_h \cdot \boldsymbol{L}^-_{\boldsymbol{n},k}\right) z^-_{\boldsymbol{n},k} \left(D_{kl} \tilde{\boldsymbol{L}}^{-'}_{\boldsymbol{n}',l} \cdot \boldsymbol{U}'_h - H_{kl} \boldsymbol{L}^{-'}_{\boldsymbol{n}',l} \cdot \boldsymbol{U}'_h\right)
\end{aligned} \tag{2.92}$$

And finally on the interface ∂E^{ee} with a neighbor acoustic element E', taking into account (2.86) and (2.89), The flux term in (2.25) becomes:

$$\begin{aligned}
&< \boldsymbol{W}_h, \hat{\boldsymbol{F}}_{\boldsymbol{n}}(\boldsymbol{U}_h, \boldsymbol{U}'_h) - \boldsymbol{F}(\boldsymbol{U}_h) >_{\partial E^{ea}} \\
=&- < \boldsymbol{W}_h, \alpha_k z^-_{\boldsymbol{n},k} \boldsymbol{L}^-_{\boldsymbol{n},k} >_{\partial E^{ea}} \\
=&- \int_{\partial E^{ea}} \left(\boldsymbol{W}_h \cdot \boldsymbol{L}^-_{\boldsymbol{n},k}\right) z^-_{\boldsymbol{n},k} \left(2D^{ea}_{kl} \wp_{tens}(\boldsymbol{L}^-_{\boldsymbol{n},l}) : \wp_{tens}(\boldsymbol{U}_h) - H^{ea}_{k1} \boldsymbol{L}^{-'}_{\boldsymbol{n}'} \cdot \boldsymbol{\Pi}_{\boldsymbol{n}}(\boldsymbol{U}_h)\right) \\
&+ \int_{\partial E^{ea}} \left(\boldsymbol{W}_h \cdot \boldsymbol{L}^-_{\boldsymbol{n},k}\right) z^-_{\boldsymbol{n},k} \left(2D^{ea}_{kl} \wp_{tens}(\boldsymbol{L}^-_{\boldsymbol{n},l}) : \wp_{tens}(\boldsymbol{\Psi}_{\boldsymbol{n}'}(\boldsymbol{U}'_h)) - H^{ea}_{k1} \boldsymbol{L}^{-'}_{\boldsymbol{n}'} \cdot \boldsymbol{\Pi}_{\boldsymbol{n}}(\boldsymbol{U}'_h)\right)
\end{aligned} \tag{2.93}$$

In all four cases, when a FE discretization is applied, we obtained two flux matrices, one for E itself and the other coupling E with E'. We note that the three matrices $[R^{ee}]$, $[R^{ae}]$ and $[R^{ea}]$ being analytically inverted, all terms are explicitly implemented, and the flux matrices are calculated once at the beginning of each dynamic calculation and stored. In other words, they are not calculated in each time step, so their computational cost is limited.

2.3 Boundary conditions and numerical fluxes on the boundary elements

This section is dedicated to calculating the upwind numerical fluxes on the boundary elements for the acoustic medium. This approach is considered for the elastic external element boundary elaborated in [82]. Our contribution is implementing a similar method for the acoustic external element boundary.

2.3.1 Pressure and velocity boundary conditions in acoustic elements

To calculate the numerical fluxes of the boundary conditions, a ghost neighbor element E' having the same acoustic behavior as E is introduced. Here we recall the flux equation:

$$\hat{\boldsymbol{F}}_{\boldsymbol{n}}(\boldsymbol{U}_h, \boldsymbol{U}'_h) = \frac{1}{2}\left(\boldsymbol{A}_{\boldsymbol{n}}(\boldsymbol{U}_h) - \boldsymbol{A}'_{\boldsymbol{n}'}(\boldsymbol{U}'_h) - \alpha z^-_n \boldsymbol{L}^-_n + \alpha' z^{-'}_n \boldsymbol{L}^{-'}_n\right) \tag{2.94}$$

Using the definition of the flux operator (2.6) and the left eigenvector (2.30), we get:

$$\hat{\boldsymbol{F}}_{\boldsymbol{n}}(\boldsymbol{U}_h, \boldsymbol{U}'_h) = \frac{1}{2}\begin{pmatrix} -(p_h + p'_h)\boldsymbol{n} \\ -(\boldsymbol{v}_h + \boldsymbol{v}'_h).\boldsymbol{n} \end{pmatrix} - \frac{1}{4}\begin{pmatrix} z^-_n \boldsymbol{n}.(\boldsymbol{v}_h - \boldsymbol{v}'_h)\boldsymbol{n} \\ \frac{1}{z^-_n}(p_h - p'_h) \end{pmatrix} \tag{2.95}$$

In the case of an acoustic medium, one should prescribe $p'_h = 2p_D - p_h$ and $\boldsymbol{v}'_h \cdot \boldsymbol{n} = \boldsymbol{v}_h \cdot \boldsymbol{n}$ on the

Dirichlet bounday $\partial E \cap \partial\Omega_D$, and $p'_h = p_h$ and $\boldsymbol{v}'_h \cdot \boldsymbol{n} = 2v_{nN} - \boldsymbol{v}_h \cdot \boldsymbol{n}$ on Neumann boundary$\partial E \cap \partial\Omega_N$.

For the Dirichlet boundary conditions, the flux is calculated as follows:

$$\hat{\boldsymbol{F}}_D = \hat{\boldsymbol{F}}_{\boldsymbol{n}}(\boldsymbol{U}_h, \boldsymbol{U}'_h) - \boldsymbol{F}_{\boldsymbol{n}}(\boldsymbol{U}) = \begin{pmatrix} \mathbf{0} \\ (v_h - v_D).\boldsymbol{n} \end{pmatrix} - \frac{1}{2}\begin{pmatrix} z_n^-\boldsymbol{n}.(v_h - v_D)\boldsymbol{n} \\ \mathbf{0} \end{pmatrix} \tag{2.96}$$

and for the Neumann boundary condition:

$$\hat{\boldsymbol{F}}_N = \hat{\boldsymbol{F}}_{\boldsymbol{n}}(\boldsymbol{U}_h, \boldsymbol{U}'_h) - \boldsymbol{F}_{\boldsymbol{n}}(\boldsymbol{U}) = \begin{pmatrix} p_h\boldsymbol{n} - p_D\boldsymbol{n} \\ \mathbf{0} \end{pmatrix} - \frac{1}{2}\begin{pmatrix} \mathbf{0} \\ \frac{1}{z_n^-}(p_h - p_D) \end{pmatrix} \tag{2.97}$$

So the flux on the external boundaries where $\partial\Omega_{Ext} = \partial\Omega_D \cup \partial\Omega_N$ and $\partial\Omega_D \cap \partial\Omega_N = \phi$, is calulated as following:

$$\begin{aligned} < \hat{\boldsymbol{F}}_{ext}, W_h >_{\partial\Omega\cap\partial E} = & < \hat{\boldsymbol{F}}_D, \boldsymbol{W}_h >_{\partial\Omega_D\cap\partial E} + < \hat{\boldsymbol{F}}_N, \boldsymbol{W}_h >_{\partial\Omega_N\cap\partial E} = \frac{1}{2} < z_n^-\boldsymbol{n}.(\boldsymbol{v}_h)\boldsymbol{n}, \boldsymbol{w} >_{\partial\Omega_D\cap\partial E} \\ & - \frac{1}{2} < z_n^-\boldsymbol{n}.(\boldsymbol{v}_D)\boldsymbol{n}, \boldsymbol{w} >_{\partial\Omega_D\cap\partial E} + < \boldsymbol{n}.\boldsymbol{v}_h \ , \ q >_{\partial\Omega_D\cap\partial E} - < \boldsymbol{n}.\boldsymbol{v}_D \ , \ q >_{\partial\Omega_D} \\ & + < p_h\boldsymbol{n}, \boldsymbol{w} >_{\partial\Omega_N\cap\partial E} - < p_D\boldsymbol{n}, \boldsymbol{w} >_{\partial\Omega_N\cap\partial E} + \frac{1}{2} < \frac{1}{z_n^-}p_h, q >_{\partial\Omega_N\cap\partial E} - \frac{1}{2} < \frac{1}{z_n^-}p_D, q >_{\partial\Omega_N\cap\partial E} \end{aligned} \tag{2.98}$$

2.4 Validation of the numerical scheme: analytical/numerical comparison

This section aims to validate the proposed upwind numerical fluxes, particularly on the acoustic-elastic interface, and demonstrate the performance of the coupled dG solver. For this purpose, a numerical/analytical comparison is carried out by considering an example with a circular acoustic-elastic interface for which analytical solutions are available [54].

We consider $\Omega = \Omega_1 \cup \Omega_2$, with Ω_1 a square fluid domain $[0, L_x] \times [0, L_y]$ with $L_x = L_y = 600$m, inside which there is a circular solid inclusion Ω_2 centered at $(x_0, y_0) = (330, 299)$m and with radius $a = 119$m (see Figure 2.4a). The acoustic wave speed in the fluid domain Ω_1 with the density of $\rho_1 = 1000\frac{kg}{m^3}$ is $c = 1500$m/s, while the speeds of the pressure and shear waves in the solid domain Ω_2 with the density of $\rho_2 = 2600\frac{kg}{m^3}$ are $c_p = 4000$m/s and $c_s = 2000$m/s respectively.

An external loading, a uniformly distributed pressure, is applied to the left side of Ω_1. Its time dependence is a sinusoid signal defined by the following function (Figure 2.4b):

$$f(t) = sin(\omega_c t) - \frac{1}{2}sin(2\omega_c t), \qquad t \in [0, 0.025\text{s}] \tag{2.99}$$

The frequency content of the signal is centered at 40Hz (Figure 2.4c), and a cutoff frequency $f_c = 150$Hz can be defined, which gives rise to the shortest involved wavelength $\lambda_{min} = \min\{c, c_p, c_s\}/f_c = 10$m.

Finite element meshes with the 4-node quadrilateral (Q4) elements are used in the present work. It is noteworthy that the element size h^E is chosen with respect to λ_{min}. Herein, four different element sizes are considered: $h_1^E = 4$m, $h_2^E = 2$m, $h_3^E = 1$m and $h_4^E = 0.5$m, which correspond respectively to 2.5, 5, 10, and 20 elements per shortest wavelength.

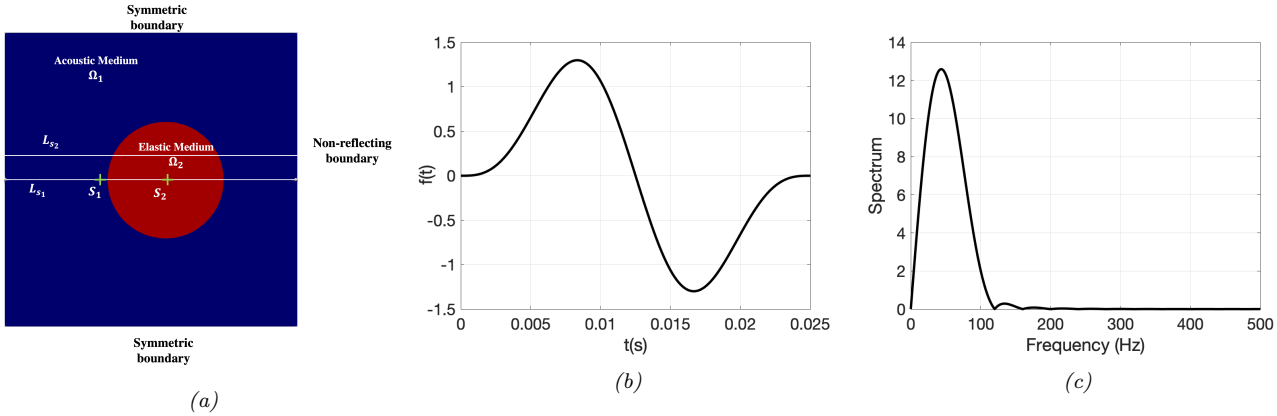

(a) *(b)* *(c)*

Figure 2.4. (a) Considered geometry with a circular acoustic-elastic interface and boundary conditions; (b) Initial sinusoid pulse placed over the left edge of the fluid medium, and (c) its frequency content

The total simulation time is chosen to equal $0.3s$, so the incident wavefront passes entirely through the circular inclusion. For the choice of time steps, in the present work, the time integration is performed by using the fourth-order Runge-Kutta iterative method, which is explicit and conditionally stable. Hence, it is necessary to respect the following stability condition [82]:

$$\Delta t \leq \frac{CFL}{2N_p + 1} \min_E \left\{ \frac{h^E}{c_{max}} \right\} \tag{2.100}$$

where N_p is the order of FE basis function and $N_p = 1$ with the use of the Q4 elements, h^E is the size of element E, c_{max} is the fastest wave speed in E, and CFL is the Courant-Friedrichs-Levy number. Our numerical experiences demonstrate that $CFL = 0.6$ guarantees the stability of our space DG solver.

2.4.1 Convergence analysis and analytical/numerical comparison

First of all, a convergence analysis is performed using previously defined six element sizes, and time signals in velocity, pressure, and stress are output and compared at two sampling points $S_1 = (200, 300)\text{m} \in \Omega_1$ and $S_2 = (330, 300)\text{m} \in \Omega_2$ (Figure 2.4a). Figure 2.5 shows that the convergence is reached for an element size less or equal to 1.5m, as suggested by the negligible differences between the obtained signals.

Then, the wave propagation phenomena are analyzed. For the numerical simulation using $h_4^E = 0.5\text{m}$ and $\Delta t = 2.5\mu\text{s}$, three snapshots of the evolving longitudinal (pressure) and transverse (shear) wavefronts are displayed in Figure 2.6 by means of the Helmholtz decomposition. By this method, in the case of isotropic and homogeneous elastic 2D medium, the scalar field $div(\boldsymbol{u})$ and the vector field $\boldsymbol{curl}(\boldsymbol{u})$ represent the longitudinal and transverse wavefronts, respectively. Expected wave phenomena are observed. The figures Figure 2.6(a-c) show the propagation of longitudinal waves in both media, which is faster in the solid inclusion, and wave reflection and transmission at the fluid-solid interface. Transverse waves are generated at the fluid-solid interface and only propagate inside the solid inclusion Ω_2 with a slower propagation speed than the longitudinal waves. Moreover, the minimum amplitude of the transverse waves is obtained along the horizontal diameter of the inclusion because no longitudinal to transverse wave conversion takes place due to the normal incidence of the incident wave at the fluid-solid interface (Figure 2.6(d-f)).

Finally, an analytical/numerical comparison is made using the analytical solution provided by

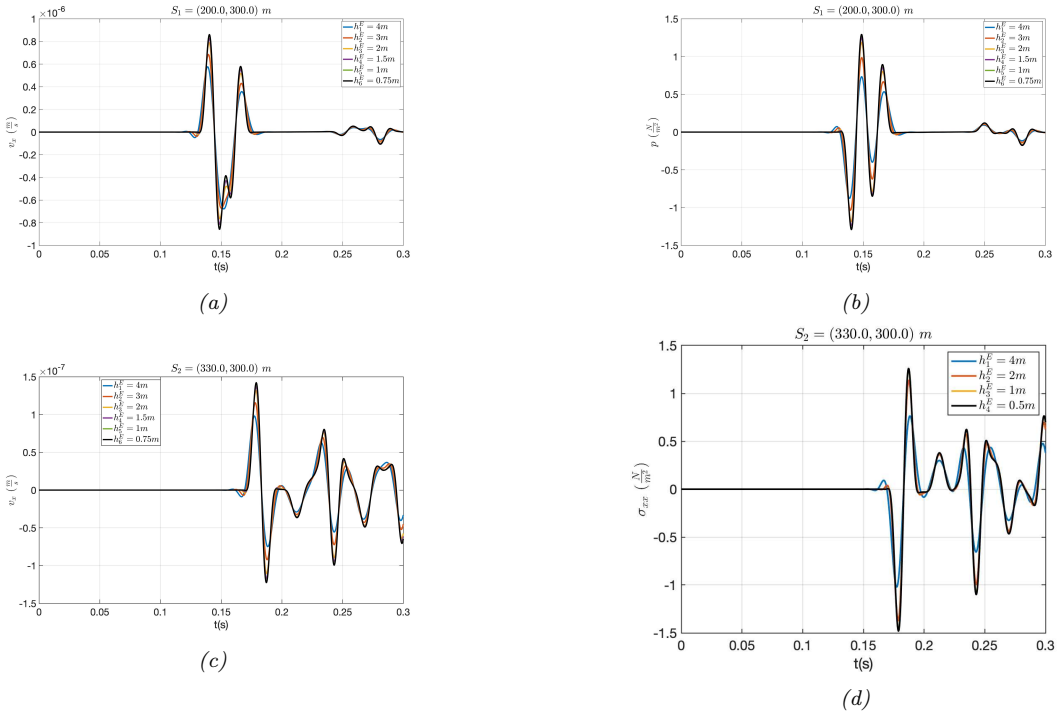

Figure 2.5. Convergence analysis of the space DG solver using six different element sizes by considering time signals output at $S_1 = (200, 300)\text{m} \in \Omega_1$ and $S_2 = (330, 300)\text{m} \in \Omega_2$. (a) v_x at S_1; (b) p at S_1; (c) v_x at S_2; (d) σ_{xx} at S_2

Lombard et al. [54]. Figure 2.7 presents the comparison along the horizontal line $L_{s_1} = \{(x, y)|y = 300\text{m}\}$ and $L_{s_2} = \{(x, y)|y = 344\text{m}\}$ (Figure 2.4a) of the numerical stress and pressure fields obtained using $h_4^E = 0.5m$ and the corresponding analytical solution. Figure 2.7a shows the pressure field over the line L_s at $t = 0.1380s$, which is before the arrival of the wavefront at the acoustic/elastic interface. It is noteworthy that the points with $x \in [0, 211[\cup]449, 600]$for L_{s_1} lie in the acoustic medium and the points with $x \in]211, 449[$ are in the elastic medium. Hence, the y-axis in Figure 2.7(b-d) reports either the pressure p or the σ_{xx} component of the stress tensor, normalized by the maximum amplitude incident pressure p_{max}. It can be seen there is a good agreement between the numerical results and the analytical solution. In addition, Figure 2.8 shows the comparison on L_{s_1} and L_{s_2} of the numerical results of different element sizes with the analytical solution, which shows the convergence when the mesh gets finer.

The proposed method, including the implemented numerical fluxes, seems to be working properly based on visual comparison of the spatial signals. However, these qualitative comparisons are not sufficient for precise quantification and characterization of the differences between the results. Therefore, a more rigorous approach is presented in the next section to quantify the mismatch between the numerical and analytical solutions.

2.4.2 Space-wavenumber misfit and goodness-of-fit criteria

Kristekova et al. proposed a criterion that quantifies and characterizes the misfit between two temporal signals using their time-frequency representations (TFR) [145, 146]. This criterion is shown to be able to detect envelope (or amplitude) and phase misfits and has a better performance compared to the standard Root-Mean-Squared (RMS) misfit criterion that overestimates the misfits up to 300% [145]. In the present work, we use a similar approach applied to spatial signals instead of temporal

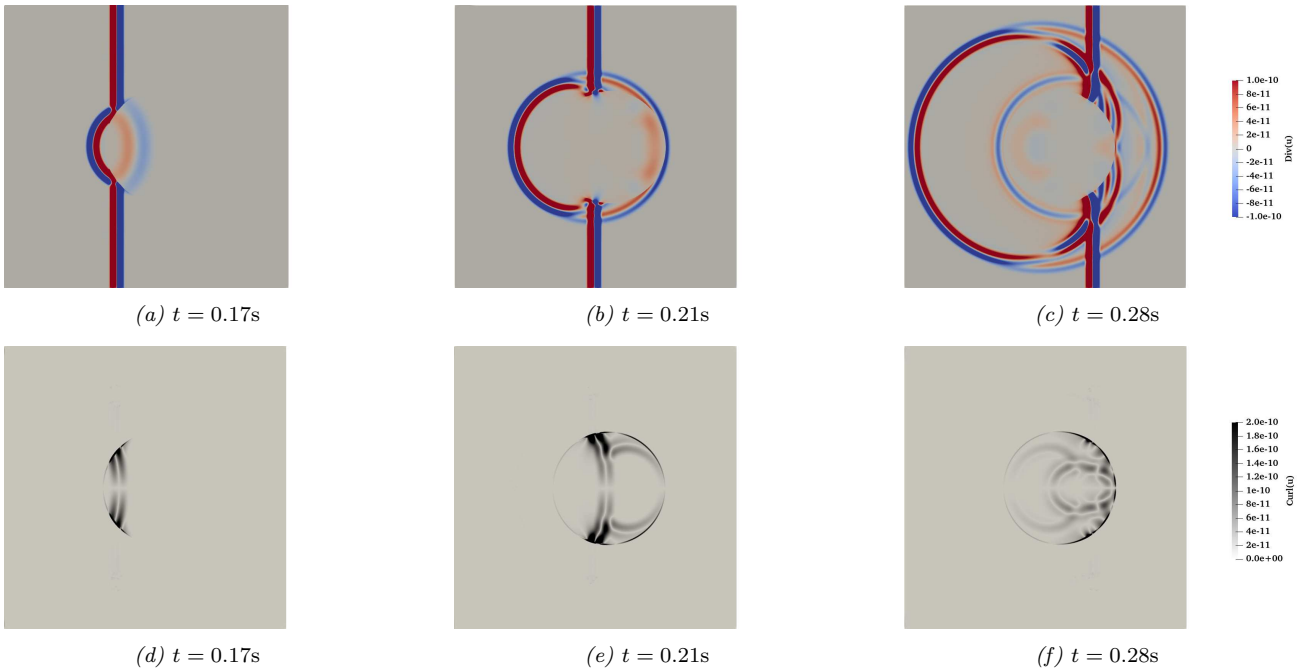

(a) $t = 0.17$s *(b)* $t = 0.21$s *(c)* $t = 0.28$s

(d) $t = 0.17$s *(e)* $t = 0.21$s *(f)* $t = 0.28$s

Figure 2.6. Wave propagation in the fluid-solid domain at different time instances; (a), (b) and (c): Longitudinal (pressure) wavefronts; (d), (e) and (f): Transverse (shear) wavefronts

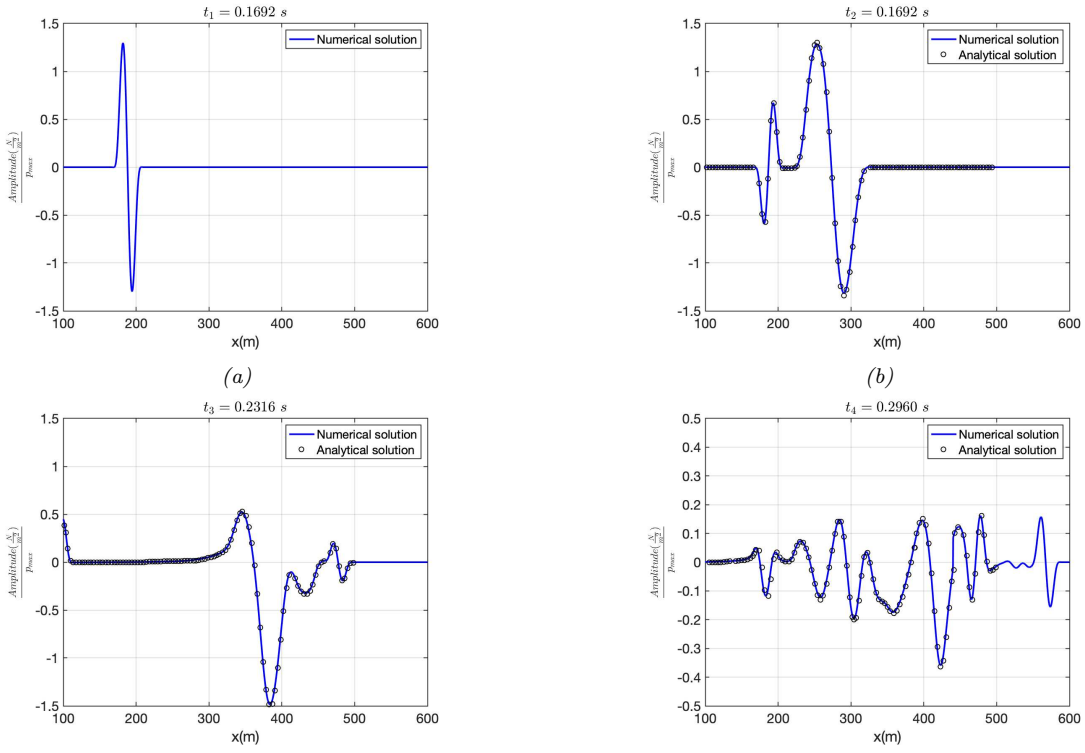

(a) *(b)* *(c)* *(d)*

Figure 2.7. (a) Pressure wavefront in the acoustic medium Ω_1 before its interaction with the acoustic/elastic interface; (b)-(c) Numerical/analytical comparison along the horizontal line $L_{s_1} = \{(x, y)|y = 300\text{m}\}$; (d) Numerical/analytical comparison along the horizontal line $L_{s_2} = \{(x, y)|y = 344\text{m}\}$

;

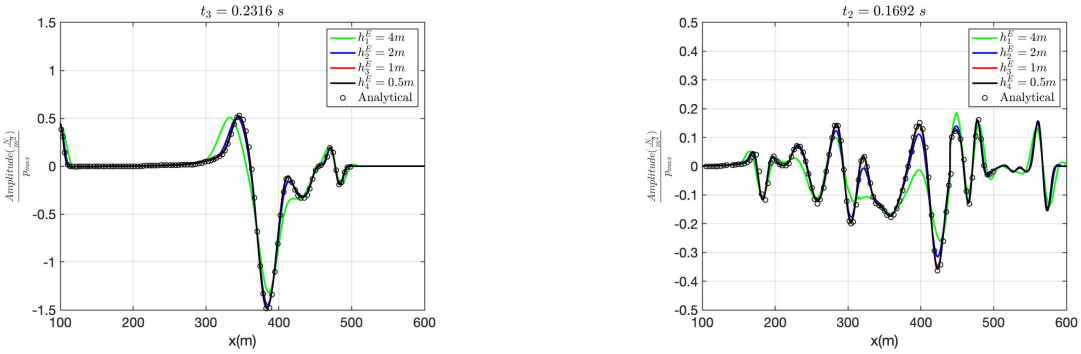

(a) *(b)*

Figure 2.8. (a) Numerical/analytical comparison along (a) L_{s_1} and (b) L_{s_2} for different element sizes

signals.

For this purpose, the Continuous Wavelet Transform (CWT) is used to obtain the space-wavenumber representation (SWR) of a 1-D spatial signal, denoted $g(x)$ below [145, 147]:

$$CWT(\xi, \ell)\{g\} = \frac{1}{\sqrt{\ell}} \int_{-\infty}^{+\infty} g(x)\psi^* \left(\frac{x - \xi}{\ell} \right) dx \tag{2.101}$$

Where ξ is the translational parameter, ℓ is the scale parameter inversely proportional to wavenumber k, ψ is the analyzing wavelet (or basic wavelet), and $(\cdot)^*$ is the complex conjugate operator. Using ℓ, the analyzing wavelet is stretched in space at different scales.

Among plenty of signals that can be used as the analyzing wavelet, the Morlet wavelet is selected for the rest of the calculations in this work. It is an analytical signal whose spectrum has zero amplitudes at negative frequencies and is written as follows:

$$\psi(\eta) = \pi^{-1/4} e^{i\chi\eta - 0.5\eta^2} \tag{2.102}$$

where χ is dimensionless wavenumber, and η is dimensionless space length. By choosing the appropriate ℓ and ξ, with a relation $k = \chi/\ell$ between the scale parameter ℓ and the wavenumber k, the SWR of the spatial signal $g(x)$ is defined as:

$$W(x, k)\{g\} = CWT(x, \frac{\chi}{k})\{g\} \tag{2.103}$$

The SWRs are obtained using the "cwt" function in MATLAB® with the parameter $\chi = 6$. Then a local SW envelope difference ΔE and a local SW phase difference ΔP with respect to a reference signal $g_{ref}(x)$ are defined for $g(x)$ as follows:

$$\Delta E(x, k) = |W(x, k)\{g\}| - |W(x, k)\{g_{ref}\}| \tag{2.104a}$$

$$\Delta P(x, k) = |W(x, k)\{g_{ref}\}| \frac{\mathrm{Arg}[W(x, k)\{g\}] - \mathrm{Arg}[W(x, k)\{g_{ref}\}]}{\pi} \tag{2.104b}$$

Afterward space-wavenumber envelope misfit (SWEM), and space-wavenumber phase misfit (SWPM)

are defined as follows:

$$\mathrm{SWEM}(x,k) = \frac{\Delta E(x,k)}{\max_{(x',k')}(|W(x',k')\{g_{ref}\}|)} \tag{2.105a}$$

$$\mathrm{SWPM}(x,k) = \frac{\Delta P(x,k)}{\max_{(x',k')}(|W(x',k')\{g_{ref}\}|)} \tag{2.105b}$$

We present the local envelope and phase misfits of the spatial signals recorded on the previously defined line L_s. In Figure 2.9, the x-axis of each subfigure is the horizontal position of the points on the sampling line, the y-axis is the wavenumber, and the corresponding numerical signal and the analytical solution are also shown below the x-axis of each subfigure. It is noteworthy that the maximum wavenumber range is $k \in [0, 0.65]$ where the maximum wavenumber is obtained as $k_{max} = \frac{2\pi f_c}{c}$ in the acoustic domain. A general decreasing trend is observed in the local envelope, and phase misfits as the element size is reduced. In addition, we note that the phase misfit is smaller than the envelope misfit for a given element size.

Figure 2.9 presents the local envelope and phase misfits SWEM and SWPM of the spatial signals recorded on the previously defined line L_{s_1} and L_{s_2}. In each subfigure, the x-axis is the horizontal position of the points on the sampling line, the y-axis is the wavenumber, and the corresponding numerical signal and the analytical solution are also shown below the x-axis. It is noteworthy that the investigated wavenumber range is $k \in [0, 0.65]$ where the maximum wavenumber is obtained as $k_{max} = \frac{2\pi f_c}{c}$ in the acoustic domain. A general decreasing trend is observed in the local envelope and phase misfits as the element size is reduced. In addition, we note that the phase misfit is smaller than the envelope misfit for a given element size.

On the other hand, Figure 2.10 shows the envelope and phase misfits on L_s at different time instances for the finest element size of $h_4^E = 0.5m$. Similar to Figure 2.9, here again, the phase misfit is smaller compared to the envelope misfit at a given time. Moreover, both the envelope and phase misfit are bigger in the elastic domain compared to the acoustic domain. According to [146], a fit is considered as a "good" one if the envelope and phase misfits are less than 0.41 and 0.35, and an "excellent" one if the envelope and phase misfits are less than 0.16 and 0.15, respectively. Based on this Goodness-of-Fit criterion, there is an excellent match between the numerical result and the analytical solution all over the sampling lines L_{s_1} and L_{s_2}, for the element sizes of $h_3^E = 1m$ and $h_4^E = 0.5m$.

In addition to the preceding local misfit criteria, there is also a useful single-valued measure of envelope and phase misfit proposed in [145], which is defined as follows:

$$\mathrm{EM} = \sqrt{\frac{\sum_{x,k} |\Delta E(x,k)|}{\sum_{x,k} |W(x,k)\{g_{ref}\}|}} \tag{2.106a}$$

$$\mathrm{PM} = \sqrt{\frac{\sum_{x,k} |\Delta P(x,k)|}{\sum_{x,k} |W(x,k)\{g_{ref}\}|}} \tag{2.106b}$$

Figure 2.11 shows the average single-valued envelope and phase misfits over different time instances

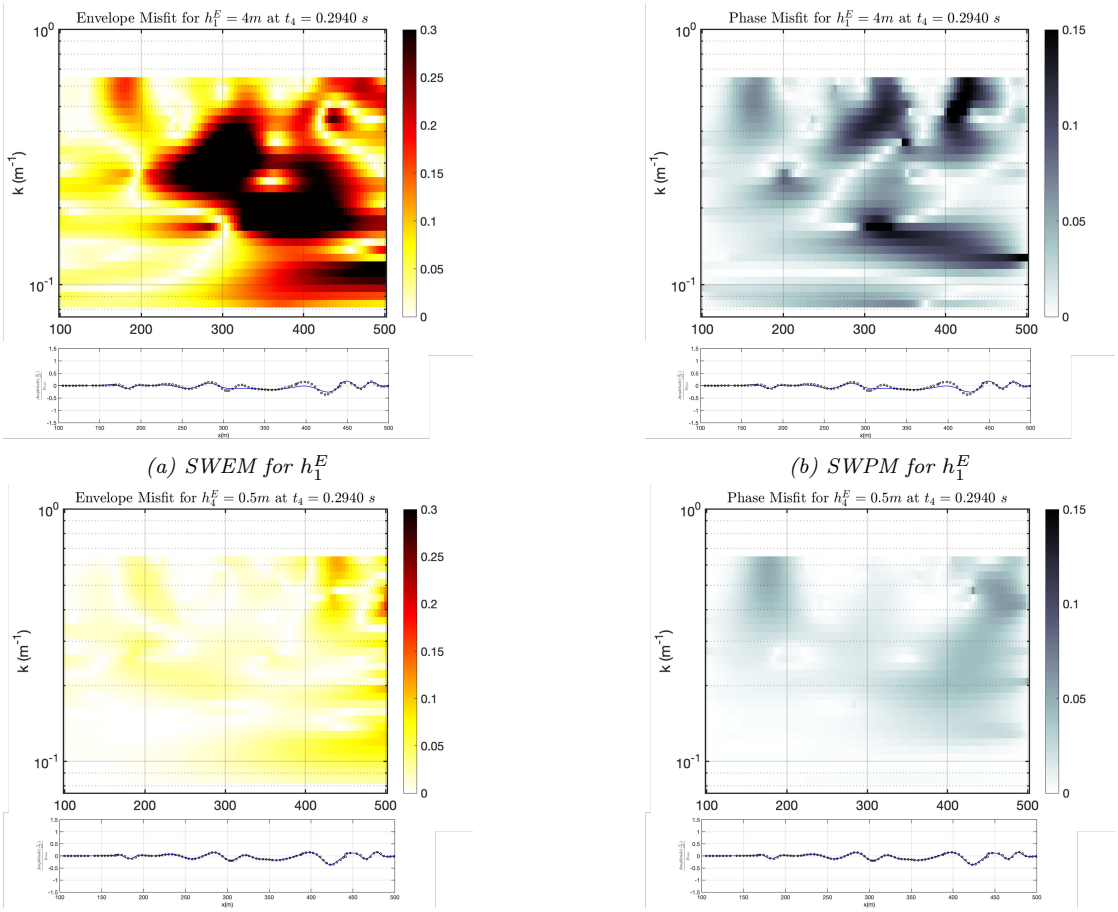

(a) SWEM for h_1^E *(b) SWPM for h_1^E*

(c) SWEM for h_4^E *(d) SWPM for h_4^E*

Figure 2.9. Space-wavenumber misfits between the numerical signal and the analytical solution on the sampling line L_{s_2} with different element sizes at $t_6 = 0.2940\ s$

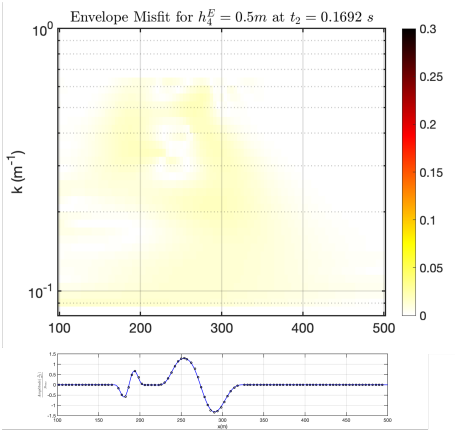

(a) SWEM at $t_2 = 0.1692$s

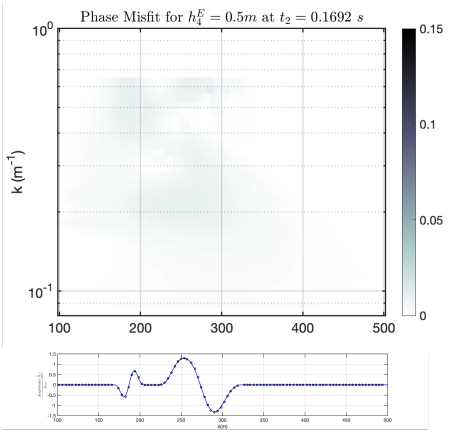

(b) SWPM at $t_2 = 0.1692$s

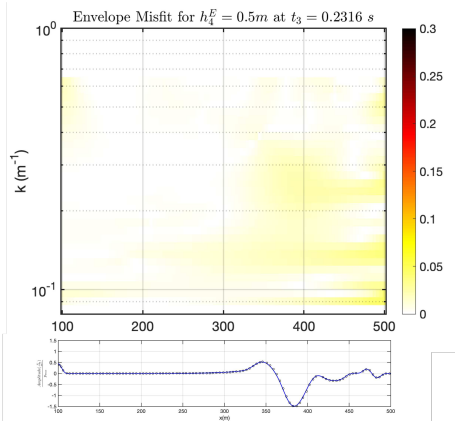

(c) SWEM at $t_3 = 0.2316$s

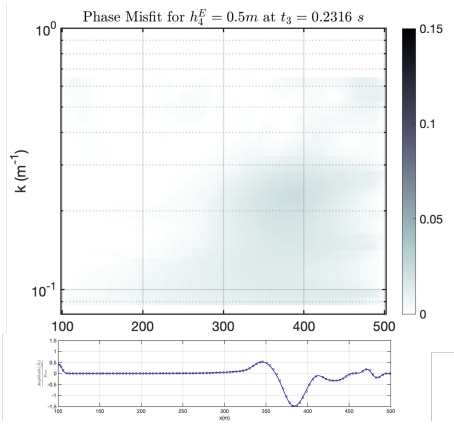

(d) SWPM at $t_3 = 0.2316$s

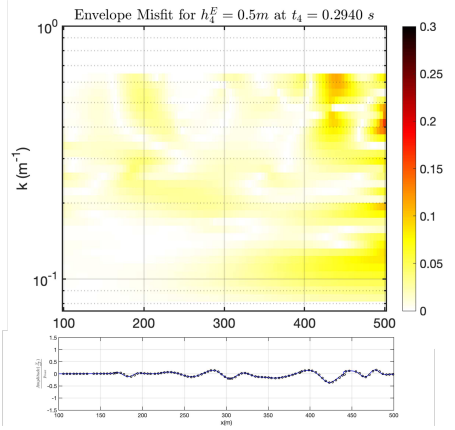

(e) SWEM at $t_4 = 0.2940$s

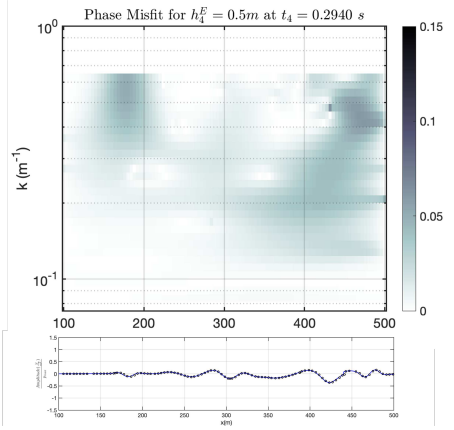

(f) SWPM at $t_4 = 0.2940$s

Figure 2.10. Space-wavenumber misfits between the numerical signal and the analytical solution on the sampling line L_{s_1} and L_{s_2} at different time instances for the element size $h_4^E = 0.5m$

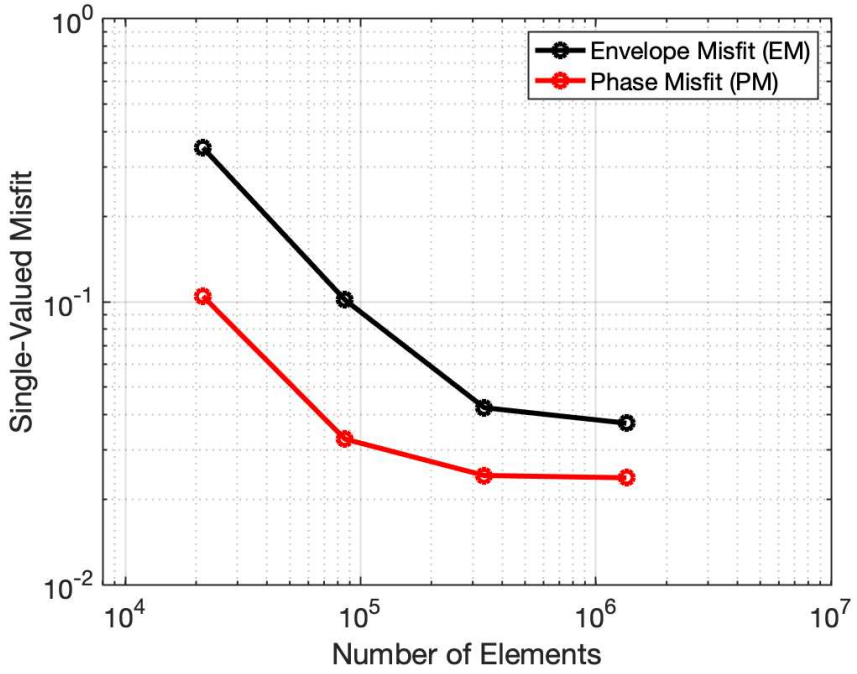

Figure 2.11. Convergence with respect to the number of elements, over time, instances t_2 to t_6, of the single-valued envelope and phase misfits

(t_2 to t_4) for different numbers of elements. However, we observe an unexpected deterioration of the convergence rate. Significant insights could have enriched this study if the analytical solutions over the entire domain was available to consider the L^2- or H^1- error norms. Nonetheless, obtaining the analytical solution over the entire domain has a high, even prohibitive, numerical cost.

2.5 Conclusions

The derivation of the upwind numerical fluxes for the space discontinuous Galerkin finite element method was first proposed, for numerical modeling of the coupled acoustic-elastic wave propagation in multidimensional media with arbitrary anisotropic solid and acoustic fluid. The upwind numerical fluxes were derived at the acoustic-elastic interfaces are original within the frameworks of the first order velocity-pressure and the first order velocity-stress formulation governing the domains composed of acoustic and elastic subdomains. The proposed fluxes were developed by analytically solving the Riemann problem and expressed in explicit closed-forms presented within a compact and intrinsic tensorial framework. Hence, the coupled numerical fluxes are implemented in our code, and they are computed once at the beginning of the calculation and used later at each time step. Their calculation does not add much to the total computational cost. Then, it was shown that the proposed numerical fluxes provide very good results for a problem with a circular acoustic-elastic interface, by analytical/numerical comparison. Indeed, the mismatch between the numerical and analytical solution was quantified using local misfit criteria. The difference between two signals were decomposed into the envelope (amplitude) and phase misfits and provided more information on the numerical errors. However, it is necessary to compare the performance of the proposed method to the other methods of developing the numerical flux (e.g. the penalty flux method) in terms of accuracy and convergence

rate, which is yet to be studied in detail in the future works.

Chapter 3
Ultrasonic wave scattering in matrix-inclusion composites

Contents

This chapter aims to enhance our understanding of the scattering characteristics exhibited by the matrix-inclusion microstructure of tissue-mimicking 3D-printed materials when subjected to ultrasonic waves. To achieve this, we employ a numerical approach based on finite element analysis to validate the analytical formulas proposed by Willis *et al.* for the scattering-induced attenuation coefficient of matrix-inclusion composites. The phase velocity and the attenuation coefficient of the compression wave in a two-dimensional two-phase composite with randomly distributed embedded circular inclusions are considered. The advantage of the finite element method is that the microstructure can be accurately represented, and all scattering phenomena can be fully simulated without any simplifying assumptions. In this chapter, we aim to achieve three objectives by considering both analytical and numerical approaches in parallel. First, the numerical approach is validated by an analytical/numerical comparison of the phase velocity and the attenuation coefficient in the case of a relatively low inclusion area fraction (2%). Second, the validated numerical approach is used to perform a parametric study for different inclusion area fractions and different inclusion sizes to study the limits of the analytical formula. Lastly, the validated numerical approach is applied to calculate the phase velocity and the

attenuation coefficient for the case in our target 3D-printed tissue-mimicking composite material with GLM material as the matrix. The reason is that according to [133], the analytical solution is valid for the wavelengths down to the diameter of the inclusion. In quasi-incompressible materials such as GLM, the propagation speed of the shear wave is substantially slower than the compression wave, so the shear wave's wavelength is much shorter than the compression wave's. Therefore, for the frequency range of ultrasonic imaging, the wavelength of the shear wave is considerably smaller than the size of the 3D-printed inclusions, and the analytical framework considered here cannot be used.

3.1 Willis analytical self-consistent homogenization approach

In the analytical framework developed in the literature by Willis and Sabina [130, 133], the composite is replaced with an effective homogeneous material. Therefore, the propagating wave in the composite, including the incident wave and the scattered wave from the inclusion, is approximated by effective harmonic wave propagation in an effective medium. This approximation is based on the description of the scattering of a harmonic wave by a single inclusion placed in a homogeneous matrix. Therefore, the simplifying assumption of single-scattering exists in the approximation. The elastic properties of the effective material are calculated using the self-consistent scheme used by Hills [148], and [149].

3.1.1 Self-consistent scheme

We still consider a domain Ω of space dimension d ($d = 1, 2, 3$) which is now a composite $\Omega = \Omega_m \cup (\cup_{r=1}^{n} \Omega_r) \subset \mathbb{R}^d$, made of a matrix Ω_m with the fourth-order elasticity tensor $\boldsymbol{C}_m$, and the density ρ_m, with n different types of inclusions $\Omega_r = \cup_{j=1}^{n_r} \Theta_j^r$, which are embedded in the matrix. The n_r inclusions Θ^r of type r ($r = 1, \cdots, n$) are the same size and shape, with the fourth-order elasticity tensor $\boldsymbol{C}_r$ and the density ρ_r. The volume fraction of Ω_m the matrix phase and Ω_r each inclusion phase of type r are respectively denoted ϕ_m and ϕ_r, and it is trivial that:

$$\phi_m + \sum_{r=1}^{n} \phi_r = 1 \tag{3.1}$$

Then, the harmonic wave equation in Ω is written in terms of $\boldsymbol{\sigma}$ the stress tensor and $\boldsymbol{p}$ the momentum density vector in the following form:

$$\mathbf{Div}_{\boldsymbol{x}}\, \boldsymbol{\sigma}(\boldsymbol{x}) = -i\omega \boldsymbol{p}(\boldsymbol{x}),\ \forall \boldsymbol{x} \in \Omega \tag{3.2}$$

with

$$\boldsymbol{\sigma}(\boldsymbol{u}) = \boldsymbol{C} : \boldsymbol{\varepsilon}(\boldsymbol{u})\ ,\ \boldsymbol{p} = -i\omega\rho\boldsymbol{u} \tag{3.3}$$

The equation (3.3) gives Hooke's law of elasticity and the definition of the momentum density, with $\boldsymbol{u}$ the displacement field, and ":" the usual double dot product between two tensors defined as $(\boldsymbol{C} : \boldsymbol{\varepsilon})_{ij} = C_{ijkl}\varepsilon_{kl}$.

To define the macroscopic behavior of the composite with randomly distributed inclusions, the ensemble average of the governing equation (3.2) is taken by denoting the ensemble mean operator by $\langle \bullet \rangle$:

$$\mathbf{Div}_{\boldsymbol{x}} \langle \boldsymbol{\sigma} \rangle = -i\omega \langle \boldsymbol{p} \rangle \tag{3.4}$$

Indeed, the given composite Ω is considered as one sample with an assigned probability density from a family, and we are interested in finding the expectation value $\langle \boldsymbol{u} \rangle$. In the presented framework, the uniform probability density function is used to generate the position of inclusions.

To solve (3.4), one needs effective constitutive equations similar to (3.3) relating $\langle \boldsymbol{\sigma} \rangle$ and $\langle \boldsymbol{p} \rangle$ to $\boldsymbol{\varepsilon}(\langle \boldsymbol{u} \rangle)$ and $\langle \boldsymbol{u} \rangle$. For that purpose, we intoduce the effective stiffness tensor $\boldsymbol{C}_{\text{eff}}$ and the effective

density tensor $\boldsymbol{\rho}_{\text{eff}}$, such that:

$$\langle \boldsymbol{\sigma} \rangle = \boldsymbol{C}_{\text{eff}} : \boldsymbol{\varepsilon}(\langle \boldsymbol{u} \rangle) \ , \ \langle \boldsymbol{p} \rangle = -i\omega \boldsymbol{\rho}_{\text{eff}} \cdot \langle \boldsymbol{u} \rangle \tag{3.5}$$

In the general case, $\boldsymbol{C}_{\text{eff}}$ is a fourth-order tensor, and $\boldsymbol{\rho}_{\text{eff}}$ is a second-order tensor, and they are generally complex-valued and frequency dependent.

For any $\boldsymbol{x} \in \Omega$, let $\langle \boldsymbol{u} \rangle_r(\boldsymbol{x})$ be the ensemble average of the $\boldsymbol{u}(\boldsymbol{x})$ over all $\boldsymbol{x} \in \Omega_r$, and defined as :

$$\langle \boldsymbol{u}_r \rangle(\boldsymbol{x}) = \frac{1}{|U_r(\boldsymbol{x})|} \int_{U_r(\boldsymbol{x})} \boldsymbol{u}(\boldsymbol{x}; \boldsymbol{x}') d\boldsymbol{x}' \tag{3.6}$$

In (3.6), $U_r(\boldsymbol{x}) = \{\boldsymbol{x}' : \boldsymbol{x} \in \Theta^r(\boldsymbol{x}')\}$ with $\Theta^r(\boldsymbol{x}')$ denoting the inclusion of type r centered at $\boldsymbol{x}'$ (see [131]). It can be shown that $|U_r(\boldsymbol{x})| = |\Theta^r|$, *i.e.*, the volume of the set $U_r(\boldsymbol{x})$, is equal to the volume of one r-type inclusion.

Afterward, the average displacement $\langle \boldsymbol{u} \rangle$ is obtained:

$$\langle \boldsymbol{u} \rangle = \phi_m \langle \boldsymbol{u}_m \rangle + \sum_{r=1}^{n} \phi_r \langle \boldsymbol{u}_r \rangle \tag{3.7}$$

Then, for the other fields:

$$\boldsymbol{\varepsilon}\left(\langle \boldsymbol{u} \rangle\right) = \phi_m \boldsymbol{\varepsilon}\left(\langle \boldsymbol{u}_m \rangle\right) + \sum_{r=1}^{n} \phi_r \boldsymbol{\varepsilon}\left(\langle \boldsymbol{u}_r \rangle\right) \tag{3.8a}$$

$$\langle \boldsymbol{\sigma} \rangle = \phi_m \boldsymbol{C}_m : \boldsymbol{\varepsilon}\left(\langle \boldsymbol{u}_m \rangle\right) + \sum_{r=1}^{n} \phi_r \boldsymbol{C}_r : \boldsymbol{\varepsilon}\left(\langle \boldsymbol{u}_r \rangle\right) \tag{3.8b}$$

$$\langle \boldsymbol{p} \rangle = -i\omega \phi_m \rho_m \langle \boldsymbol{u}_m \rangle - i\omega \sum_{r=1}^{n} \phi_r \rho_r \langle \boldsymbol{u}_r \rangle \tag{3.8c}$$

By eliminating $\phi_m \boldsymbol{\varepsilon}\left(\langle \boldsymbol{u}_m \rangle\right)$ between (3.8a) and (3.8b), and $\phi_m \langle \boldsymbol{u}_m \rangle$ between (3.7) and (3.8c), we obtain:

$$\langle \boldsymbol{\sigma} \rangle = \boldsymbol{C}_m : \boldsymbol{\varepsilon}\left(\langle \boldsymbol{u} \rangle\right) + \sum_{r=1}^{n} \phi_r (\boldsymbol{C}_r - \boldsymbol{C}_m) : \boldsymbol{\varepsilon}\left(\langle \boldsymbol{u}_r \rangle\right) \tag{3.9a}$$

$$\langle \boldsymbol{p} \rangle = -i\omega \rho_m \langle \boldsymbol{u} \rangle - i\omega \sum_{r=1}^{n} \phi_r (\rho_r - \rho_m) \langle \boldsymbol{u}_r \rangle \tag{3.9b}$$

Then, in order to obtain the effective properties (3.5), the basic idea is to develop $\boldsymbol{\varepsilon}\left(\langle \boldsymbol{u}_r \rangle\right)$ and $-i\omega \langle \boldsymbol{u}_r \rangle$ in terms of $\boldsymbol{\varepsilon}\left(\langle \boldsymbol{u} \rangle\right)$ and $-i\omega \langle \boldsymbol{u} \rangle$. To do this approximately, one can consider an auxiliary problem of one inclusion of type r centered at $\boldsymbol{x}'$ and embedded in a homogeneous material, whose properties are assumed to be those of the effective medium, according to the self-consistent assumption. In other words, it is a single scatterer scattering problem for which the field far from the scatterer is equal to the mean field $\langle \boldsymbol{u} \rangle$.

Even though the original problem is reduced to solving a single scatterer problem, this approach still accounts for some degree of multiple scattering due to the self-consistent assumption. Indeed, the scatterer being embedded in the effective medium and its interaction with all the other scatter-

ers is considered on average. However, if the distance between the scatterers becomes small, such consideration is no longer relevant, and the approach should give poor predictions.

3.1.2 Scattering problem of a single inclusion

Now, we consider the scattering problem of a single inclusion of type r centered at $\boldsymbol{x}'$ and embedded in the effective medium. So, we have $n = 1$, and $\Omega_r = \Theta^r(\boldsymbol{x}')$. We can write:

$$\boldsymbol{\sigma}(\boldsymbol{u}) = (\boldsymbol{C}_{\text{eff}} + \chi_r \delta \boldsymbol{C}_r) : \boldsymbol{\varepsilon}(\boldsymbol{u}) = \boldsymbol{C}_{\text{eff}} : \boldsymbol{\varepsilon}(\boldsymbol{u}) + \chi_r \boldsymbol{\tau}^{(r,\boldsymbol{x}')}(\boldsymbol{u}) \tag{3.10a}$$

$$\boldsymbol{p}(\boldsymbol{u}) = -i\omega(\boldsymbol{\rho}_{\text{eff}} + \chi_r \delta \boldsymbol{\rho}_r) \cdot \boldsymbol{u} = -i\omega \boldsymbol{\rho}_{\text{eff}} \cdot \boldsymbol{u} + \chi_r \boldsymbol{\pi}^{(r,\boldsymbol{x}')}(\boldsymbol{u}) \tag{3.10b}$$

with $\chi_r(\boldsymbol{x})$ the characteristic function of $\Theta^r(\boldsymbol{x}')$, i.e., $\chi_r(\boldsymbol{x})$ is equal to 1 when $\boldsymbol{x} \in \Theta^r(\boldsymbol{x}')$, and equal to 0 elsewhere, $\delta \boldsymbol{C}_r = \boldsymbol{C}_r - \boldsymbol{C}_{\text{eff}}$, $\delta \boldsymbol{\rho}_r = \rho_r \boldsymbol{I}^{(2)} - \boldsymbol{\rho}_{\text{eff}}$, and $\boldsymbol{I}^{(2)}$ the second order identity tensor.

In (3.10),

$$\boldsymbol{\tau}^{(r,\boldsymbol{x}')}(\boldsymbol{u}) = \delta \boldsymbol{C}_r : \boldsymbol{\varepsilon}(\boldsymbol{u}) \tag{3.11a}$$

$$\boldsymbol{\pi}^{(r,\boldsymbol{x}')}(\boldsymbol{u}) = -i\omega \delta \boldsymbol{\rho}_r \cdot \boldsymbol{u} \tag{3.11b}$$

are respectively called the stress and momentum polarizations defined in Willis's work [131]. They have the particularity of being non-zero only on the inclusion.

By substituting (3.10) in the wave equation (3.2), one can see that the displacement $\boldsymbol{u}$ could be estimated in the effective homogeneous medium as if it were excited by a body force $\boldsymbol{f}(\boldsymbol{\tau}^{(r,\boldsymbol{x}')}, \boldsymbol{\pi}^{(r,\boldsymbol{x}')}) = \chi_r \left(\mathbf{Div}_{\boldsymbol{x}} \boldsymbol{\tau}^{(r,\boldsymbol{x}')} + i\omega \boldsymbol{\pi}^{(r,\boldsymbol{x}')} \right)$:

$$\mathbf{Div}_{\boldsymbol{x}} \left(\boldsymbol{C}_{\text{eff}} : \boldsymbol{\varepsilon}(\boldsymbol{u}) \right) + \boldsymbol{f}(\boldsymbol{\tau}^{(r,\boldsymbol{x}')}(\boldsymbol{u}), \boldsymbol{\pi}^{(r,\boldsymbol{x}')}(\boldsymbol{u})) = -\omega^2 \boldsymbol{\rho}_{\text{eff}} \cdot \boldsymbol{u} \tag{3.12}$$

Therefore, it is possible to get an implicit expression of $\boldsymbol{u}$ using Green's function. Indeed, recalling the definition of the Green's tensor $\boldsymbol{G}$ for a homogeneous material, the displacement field $\boldsymbol{u}$ can be symbolically developed as:

$$\boldsymbol{u} = \boldsymbol{u}_0 + \boldsymbol{G} * \boldsymbol{f}(\boldsymbol{\tau}^{(r,\boldsymbol{x}')}(\boldsymbol{u}), \boldsymbol{\pi}^{(r,\boldsymbol{x}')}(\boldsymbol{u})) = \boldsymbol{u}_0 + \boldsymbol{G} * \mathbf{Div}_{\boldsymbol{x}} \boldsymbol{\tau}^{(r,\boldsymbol{x}')} + i\omega \boldsymbol{G} * \boldsymbol{\pi}^{(r,\boldsymbol{x}')} \tag{3.13}$$

where $\boldsymbol{u}_0$ is the solution of the problem (3.12) without any body force. In addition, by taking into account the previous reasoning, we have $\boldsymbol{u}_0 = \langle \boldsymbol{u} \rangle$.

We recall that Green's tensor is of second order and can be written as $\boldsymbol{G}(\boldsymbol{x}''; \boldsymbol{x}) = \sum_{k=1,d} \boldsymbol{g}_k(\boldsymbol{x}''; \boldsymbol{x}) \otimes \boldsymbol{e}_k$ with $\boldsymbol{g}_k(\boldsymbol{x}''; \boldsymbol{x})$ the solution of the following Helmholtz wave equation in the infinite homogeneous domain submitted to a Dirac point load in the $\boldsymbol{e}_k$ direction at the point $\boldsymbol{x}''$:

$$\mathbf{Div}_{\boldsymbol{x}}(\boldsymbol{\sigma}(\boldsymbol{g}_k)) + \delta(\boldsymbol{x} - \boldsymbol{x}'')\boldsymbol{e}_k = -\omega^2 \boldsymbol{g}_k \tag{3.14}$$

The frequency dependence of $\boldsymbol{G}$ is not mentioned here to simplify the notations. We also recall that the far-field assumption makes it possible to use $\boldsymbol{G}(\boldsymbol{x} - \boldsymbol{x}'') \equiv \boldsymbol{G}(\boldsymbol{0}, \boldsymbol{x} - \boldsymbol{x}'')$ instead of $\boldsymbol{G}(\boldsymbol{x}''; \boldsymbol{x})$ with $\boldsymbol{x}''$ as a source point. This assumption can be applied if the homogenous domain is large enough compared to the inclusion size.

Using this notation of $\boldsymbol{G}$, the following operators are defined:

$$\begin{aligned}(\boldsymbol{G} * \mathbf{Div}_{\boldsymbol{x}}\, \boldsymbol{\tau}^{(r,\boldsymbol{x}')})(\boldsymbol{x}) &= \int_{\Theta^r(\boldsymbol{x}')} \boldsymbol{G}(\boldsymbol{x}-\boldsymbol{x}'') \cdot \mathbf{Div}_{\boldsymbol{x}'}\, \boldsymbol{\tau}^{(r,\boldsymbol{x}')}(\boldsymbol{x}'')\mathrm{d}\boldsymbol{x}'' \\ (\boldsymbol{S} * \boldsymbol{\tau}^{(r,\boldsymbol{x}')})(\boldsymbol{x}) &= \int_{\Theta^r(\boldsymbol{x}')} \boldsymbol{S}(\boldsymbol{x}-\boldsymbol{x}'')(\boldsymbol{\tau}^{(r,\boldsymbol{x}')}(\boldsymbol{x}''))\mathrm{d}\boldsymbol{x}''\end{aligned} \tag{3.15}$$

with:

$$(\boldsymbol{S}(\boldsymbol{\tau}^{(r,\boldsymbol{x}')}))_i = S_{ikl}\tau^{(r)}_{kl}\ ,\ S_{ikl} = -\frac{1}{2}\left(\frac{\partial G_{ik}}{\partial x_l} + \frac{\partial G_{il}}{\partial x_k}\right) = -\frac{1}{2}\left(\frac{\partial (\boldsymbol{g}_k)_i}{\partial x_l} + \frac{\partial (\boldsymbol{g}_l)_i}{\partial x_k}\right) \tag{3.16}$$

We note that in (3.16) symmetrization is applied since $\boldsymbol{\tau}^{(r,\boldsymbol{x}')}$ is symmetric.

Then, by denoting $\boldsymbol{M} = -i\omega\boldsymbol{G}$ and using an integration-by-part argument, the displacement equation (3.13) finally becomes:

$$\boldsymbol{u} = \langle \boldsymbol{u} \rangle - \boldsymbol{S} * \boldsymbol{\tau}^{(r,\boldsymbol{x}')} - \boldsymbol{M} * \boldsymbol{\pi}^{(r,\boldsymbol{x}')} \tag{3.17}$$

The strain is obtained by differentiating the displacement field (3.17). By eliminating the strain $\boldsymbol{\varepsilon}(\boldsymbol{u})$ using (3.11), we obtain over the inclusion $\Theta^r(\boldsymbol{x}')$:

$$\begin{aligned}\boldsymbol{\varepsilon}(\langle \boldsymbol{u} \rangle) &= (\delta \boldsymbol{C}_r)^{-1} : \boldsymbol{\tau}^{(r,\boldsymbol{x}')} + \boldsymbol{\varepsilon}(\boldsymbol{S} * \boldsymbol{\tau}^{(r,\boldsymbol{x}')}) + \boldsymbol{\varepsilon}(\boldsymbol{M} * \boldsymbol{\pi}^{(r,\boldsymbol{x}')}) \\ -i\omega\langle \boldsymbol{u} \rangle &= (\delta \boldsymbol{\rho}_r)^{-1} \cdot \boldsymbol{\pi}^{(r,\boldsymbol{x}')} - i\omega(\boldsymbol{S} * \boldsymbol{\tau}^{(r,\boldsymbol{x}')}) - i\omega(\boldsymbol{M} * \boldsymbol{\pi}^{(r,\boldsymbol{x}')})\end{aligned} \tag{3.18}$$

The above system will finally make it possible to obtain the stress and momentum polarizations $(\boldsymbol{\tau}^{(r,\boldsymbol{x}')}, \boldsymbol{\pi}^{(r,\boldsymbol{x}')})$ in terms of $\langle \boldsymbol{u} \rangle$, and (3.9) will give properties of the effective medium (3.5).

The last hypothesis assumes that the two polarization fields, $\boldsymbol{\tau}^{(r,\boldsymbol{x}')}$, and $\boldsymbol{\pi}^{(r,\boldsymbol{x}')}$, are constant over the inclusion. This makes it possible to obtain the following explicit calculation formulas. Indeed, as $\boldsymbol{\tau}^{(r,\boldsymbol{x}')}$, and $\boldsymbol{\pi}^{(r,\boldsymbol{x}')}$ are constant over $\Theta^r(\boldsymbol{x}')$, the strain and velocity equations (3.18) becomes:

$$\begin{aligned}\boldsymbol{\varepsilon}(\langle \boldsymbol{u} \rangle) &= (\delta \boldsymbol{C}_r)^{-1} : \boldsymbol{\tau}^{(r,\boldsymbol{x}')} + \boldsymbol{S}_{\boldsymbol{x}} * \boldsymbol{\tau}^{(r,\boldsymbol{x}')} + \boldsymbol{M}_{\boldsymbol{x}} * \boldsymbol{\pi}^{(r,\boldsymbol{x}')} \\ -i\omega\langle \boldsymbol{u} \rangle &= (\delta \boldsymbol{\rho}_r)^{-1} \cdot \boldsymbol{\pi}^{(r,\boldsymbol{x}')} + \boldsymbol{S}_{\omega} * \boldsymbol{\tau}^{(r,\boldsymbol{x}')} + \boldsymbol{M}_{\omega} * \boldsymbol{\pi}^{(r,\boldsymbol{x}')}\end{aligned} \tag{3.19}$$

In (3.19), the different operators are defined as follows:

$$\begin{aligned}(\boldsymbol{S}_{\boldsymbol{x}}(\boldsymbol{\tau}^{(r,\boldsymbol{x}')}))_{ij} &= (\boldsymbol{S}_{\boldsymbol{x}})_{ijkl}\tau^{(r)}_{kl}\ ,\ (\boldsymbol{S}_{\boldsymbol{x}})_{ijkl} = -\frac{1}{4}\left(\frac{\partial^2 G_{ik}}{\partial x_j \partial x_l} + \frac{\partial^2 G_{il}}{\partial x_j \partial x_k} + \frac{\partial^2 G_{jk}}{\partial x_i \partial x_l} + \frac{\partial^2 G_{jl}}{\partial x_i \partial x_k}\right) \\ (\boldsymbol{M}_{\boldsymbol{x}}(\boldsymbol{\pi}^{(r,\boldsymbol{x}')}))_{ij} &= (\boldsymbol{M}_{\boldsymbol{x}})_{ijk}\pi^{(r)}_{k}\ ,\ (\boldsymbol{M}_{\boldsymbol{x}})_{ijk} = -\frac{1}{2}\left(\frac{\partial G_{ik}}{\partial x_j} + \frac{\partial G_{jk}}{\partial x_i}\right) \\ \boldsymbol{S}_{\omega} &= -i\omega\boldsymbol{S}\ ,\ \boldsymbol{M}_{\omega} = -i\omega\boldsymbol{M} = -\omega^2\boldsymbol{G}\end{aligned} \tag{3.20}$$

Hereafter, the mean value over a subdomain $V \subset \Omega$ of a field $w(\boldsymbol{x})$ is denoted $\overline{w}^V = \frac{1}{|V|}\int_V w(\boldsymbol{x})d\boldsymbol{x}$. Then the integration over the inclusion $\Theta_r(\boldsymbol{x}')$ of (3.19) give the following equations that $\boldsymbol{\tau}^{(r,\boldsymbol{x}')}$ and

$\boldsymbol{\pi}^{(r,\boldsymbol{x}')}$ should verify:

$$\begin{aligned}\overline{\boldsymbol{\varepsilon}(\langle\boldsymbol{u}\rangle)}^{\Theta^r(\boldsymbol{x}')} &= \left((\delta\boldsymbol{C}_r)^{-1} + \overline{\boldsymbol{S}_{\boldsymbol{x}}^{(r)}}^{\Theta^r(\boldsymbol{x}')}\right) : \boldsymbol{\tau}^{(r,\boldsymbol{x}')} + \overline{\boldsymbol{M}_{\boldsymbol{x}}^{(r)}}^{\Theta^r(\boldsymbol{x}')} \cdot \boldsymbol{\pi}^{(r,\boldsymbol{x}')} \\ -i\omega\overline{\langle\boldsymbol{u}\rangle}^{\Theta^r(\boldsymbol{x}')} &= \overline{\boldsymbol{S}_{\omega}^{(r)}}^{\Theta^r(\boldsymbol{x}')}(\boldsymbol{\tau}^{(r,\boldsymbol{x}')}) + \left((\delta\boldsymbol{\rho}_r)^{-1} + \overline{\boldsymbol{M}_{\omega}^{(r)}}^{\Theta^r(\boldsymbol{x}')}\right) \cdot \boldsymbol{\pi}^{(r,\boldsymbol{x}')}\end{aligned} \tag{3.21}$$

where $\overline{\boldsymbol{S}_{\boldsymbol{x}}^{(r)}}^{\Theta^r(\boldsymbol{x}')}$, $\overline{\boldsymbol{M}_{\boldsymbol{x}}^{(r)}}^{\Theta^r(\boldsymbol{x}')}$, $\overline{\boldsymbol{S}_{\omega}^{(r)}}^{\Theta^r(\boldsymbol{x}')}$, and $\overline{\boldsymbol{M}_{\omega}^{(r)}}^{\Theta^r(\boldsymbol{x}')}$ are the average of convolution operators over the volume of the inclusion $\Theta^r(\boldsymbol{x}')$. $\overline{\boldsymbol{S}_{\boldsymbol{x}}^{(r)}}^{\Theta^r(\boldsymbol{x}')}$ and $\overline{\boldsymbol{M}_{\omega}^{(r)}}^{\Theta^r(\boldsymbol{x}')}$ are respectively called the stress and momentum depolarisation tensors [133]. They respectively have the dimension of a compliance tensor and an inverse mass-density tensor and are defined as:

$$\begin{aligned}\overline{\boldsymbol{S}_{\boldsymbol{x}}^{(r)}}^{\Theta^r(\boldsymbol{x}')} &= -\frac{1}{|\Theta^r|}\iint_{\Theta^r(\boldsymbol{x}')\times\Theta^r(\boldsymbol{x}')} \boldsymbol{S}_{\boldsymbol{x}}(\boldsymbol{x}-\boldsymbol{x}'')d\boldsymbol{x}d\boldsymbol{x}'' \\ \overline{\boldsymbol{M}_{\omega}^{(r)}}^{\Theta^r(\boldsymbol{x}')} &= -\frac{\omega^2}{|\Theta^r|}\iint_{\Theta^r(\boldsymbol{x}')\times\Theta^r(\boldsymbol{x}')} \boldsymbol{G}(\boldsymbol{x}-\boldsymbol{x}'')d\boldsymbol{x}d\boldsymbol{x}''\end{aligned} \tag{3.22}$$

Notably, both tensors are independent of $\boldsymbol{x}'$, so $\boldsymbol{x}'$ will be dropped for them in the following.

Now we restrict the study to the case where the inclusion has a center of symmetry. In this case, it can be shown that, $\overline{\boldsymbol{M}_{\boldsymbol{x}}^{(r)}}^{\Theta^r} = \boldsymbol{0}$ and $\overline{\boldsymbol{S}_{\omega}^{(r)}}^{\Theta^r} = \boldsymbol{0}$, because $\boldsymbol{M}_{\boldsymbol{x}}$ and $\boldsymbol{S}_{\omega}$ are odd functions of $\boldsymbol{x}$. Finally, (3.21) leads to:

$$\begin{aligned}\boldsymbol{\tau}^{(r,\boldsymbol{x}')} &= \left((\delta\boldsymbol{C}_r)^{-1} + \overline{\boldsymbol{S}_{\boldsymbol{x}}^{(r)}}^{\Theta^r}\right)^{-1} : \overline{\boldsymbol{\varepsilon}(\langle\boldsymbol{u}\rangle)}^{\Theta^r(\boldsymbol{x}')} \\ \boldsymbol{\pi}^{(r,\boldsymbol{x}')} &= -i\omega\left((\delta\boldsymbol{\rho}_r)^{-1} + \overline{\boldsymbol{M}_{\omega}^{(r)}}^{\Theta^r}\right)^{-1} \cdot \overline{\langle\boldsymbol{u}\rangle}^{\Theta^r(\boldsymbol{x}')}\end{aligned} \tag{3.23}$$

As we are interested in analyzing the scattering-induced attenuation, we concentrate on a solution of the ensemble average displacement field under the form of a harmonic plane wave:

$$\langle\boldsymbol{u}\rangle(\boldsymbol{x}) = \boldsymbol{U}\,\mathrm{e}^{i\boldsymbol{k}\cdot\boldsymbol{x}} \tag{3.24}$$

where $\boldsymbol{U}$ is the unit polarization vector, $\boldsymbol{k}$ is the wave vector that may be complex. Taking into account (3.24) the harmonic plane wave form of the ensemble average displacement $\langle\boldsymbol{u}\rangle$, we get $\boldsymbol{\varepsilon}(\langle\boldsymbol{u}\rangle) = \boldsymbol{U}\otimes_s(i\boldsymbol{k})\,\mathrm{e}^{i\boldsymbol{k}\cdot\boldsymbol{x}}$, it can be thus shown that:

$$\begin{aligned}\boldsymbol{\tau}^{(r,\boldsymbol{x}')} &= h_r(\boldsymbol{k})\left((\delta\boldsymbol{C}_r)^{-1} + \overline{\boldsymbol{S}_{\boldsymbol{x}}^{(r)}}^{\Theta^r}\right)^{-1} : \boldsymbol{\varepsilon}(\langle\boldsymbol{u}\rangle(\boldsymbol{x}')) \\ \boldsymbol{\pi}^{(r,\boldsymbol{x}')} &= -i\omega h_r(\boldsymbol{k})\left((\delta\boldsymbol{\rho}_r)^{-1} + \overline{\boldsymbol{M}_{\omega}^{(r)}}^{\Theta^r}\right)^{-1} \cdot \langle\boldsymbol{u}\rangle(\boldsymbol{x}')\end{aligned} \tag{3.25}$$

with

$$h_r(\boldsymbol{k}) = \frac{1}{|\Theta^r|}\int_{\Theta^r(\boldsymbol{0})} \mathrm{e}^{i\boldsymbol{k}\cdot\boldsymbol{x}}d\boldsymbol{x} \tag{3.26}$$

Using (3.11), we get on the inclusion $\Theta^r(\boldsymbol{x}')$:

$$\begin{aligned}\boldsymbol{\varepsilon}(\boldsymbol{u}_r) &= h_r(\boldsymbol{k})\left(\boldsymbol{I}^{(4)} + \overline{\boldsymbol{S}_{\boldsymbol{x}}^{(r)}}^{\Theta^r} : \delta\boldsymbol{C}_r\right)^{-1} : \boldsymbol{\varepsilon}(\langle\boldsymbol{u}\rangle(\boldsymbol{x}')) \\ \boldsymbol{u}_r &= h_r(\boldsymbol{k})\left(\boldsymbol{I}^{(2)} + \overline{\boldsymbol{M}_{\omega}^{(r)}}^{\Theta^r} \cdot \delta\boldsymbol{\rho}_r\right)^{-1} \cdot \langle\boldsymbol{u}\rangle(\boldsymbol{x}')\end{aligned} \tag{3.27}$$

where $\boldsymbol{I}^{(4)}$ is the 4-th order identity tensor.

3.1.3 General equations of effective stiffness and density tensors and self-consistent effective properties of 2D/3D composites with spherical/circular inclusions

To obtain the effective stiffness and density tensors, the equations (3.9) are used. Therefore, it is necessary to calculate the ensemble average field $\langle\boldsymbol{u}_r\rangle$ defined by (3.6). Always by taking into account (3.24) the harmonic plane wave form of the ensemble average displacement $\langle\boldsymbol{u}\rangle$, we get:

$$\begin{aligned}\langle\boldsymbol{u}_r\rangle(\boldsymbol{x}) &= h_r(\boldsymbol{k})\left(\boldsymbol{I}^{(2)} + \overline{\boldsymbol{M}_{\omega}^{(r)}}^{\Theta_r} \cdot \delta\boldsymbol{\rho}_r\right)^{-1} \cdot \boldsymbol{U}\left(\frac{1}{|U_r(\boldsymbol{x})|}\int_{U_r(\boldsymbol{x})} \mathrm{e}^{i\boldsymbol{k}\cdot\boldsymbol{x}'}d\boldsymbol{x}'\right) \\ &= h_r^2(\boldsymbol{k})\left(\boldsymbol{I}^{(2)} + \overline{\boldsymbol{M}_{\omega}^{(r)}}^{\Theta_r} \cdot \delta\boldsymbol{\rho}_r\right)^{-1} \cdot \langle\boldsymbol{u}\rangle(\boldsymbol{x})\end{aligned} \tag{3.28}$$

Substituting (3.28) in (3.9), we finally obtain the following equation of the properties of the effective medium:

$$\begin{aligned}\boldsymbol{C}_{\text{eff}} &= \boldsymbol{C}_m + \sum_{r=1}^{n}\phi_r h_r^2(\boldsymbol{k})(\boldsymbol{C}_r - \boldsymbol{C}_m) : \left(\boldsymbol{I}^{(4)} + \overline{\boldsymbol{S}_{\boldsymbol{x}}^{(r)}}^{\Theta_r} : (\boldsymbol{C}_r - \boldsymbol{C}_{\text{eff}})\right)^{-1} \\ \boldsymbol{\rho}_{\text{eff}} &= \rho_m\boldsymbol{I}^{(2)} + \sum_{r=1}^{n}\phi_r h_r^2(\boldsymbol{k})(\rho_r - \rho_m)\left(\boldsymbol{I}^{(2)} + \overline{\boldsymbol{M}_{\omega}^{(r)}}^{\Theta_r} \cdot (\rho_r\boldsymbol{I}^{(2)} - \boldsymbol{\rho}_{\text{eff}})\right)^{-1}\end{aligned} \tag{3.29}$$

Until now, the equations (3.29) are developed for a general case in which there are no simplifying assumptions on the materials' mechanical properties nor the inclusions' shape.

Both self-consistent equations (3.29) are coupled and implicit, because the wave vector $\boldsymbol{k}$ is obtained from the solution of the equation of motion of the harmonic plane wave in the effective medium, and $\boldsymbol{C}_{\text{eff}}$ and $\boldsymbol{\rho}_{\text{eff}}$ are on the right-hand side of the equations, and h_r, $\overline{\boldsymbol{S}_{\boldsymbol{x}}^{(r)}}^{\Theta_r}$ and $\overline{\boldsymbol{M}_{\omega}^{(r)}}^{\Theta_r}$ also on the right-hand side of the equations are calculated with $\boldsymbol{G}$ the Green's tensor of the effective-medium.

In (3.29), inverting the 4th-order tensor can be difficult. However, in the case of spherical (*resp.* circular) inclusions inside a 3D (*resp.* 2D) isotropic matrix, both stress and momentum depolarisation tensors $\overline{\boldsymbol{S}_{\boldsymbol{x}}^{(r)}}^{\Theta_r}$ and $\overline{\boldsymbol{M}_{\omega}^{(r)}}^{\Theta_r}$ are also isotropic. In this case, we have, $\boldsymbol{\rho}_{\text{eff}} = \rho_{\text{eff}}\boldsymbol{I}^{(2)}$ and $\overline{\boldsymbol{M}_{\omega}^{(r)}}^{\Theta_r} = \rho_{M^{(r)}}\boldsymbol{I}^{(2)}$, and inverting the 4-th order tensor becomes easy. Indeed, in the isotropic case, by decomposing the stress and the strain tensors into volumetric and deviatoric parts:

$$\begin{aligned}\boldsymbol{\sigma} &= \sigma_v\boldsymbol{I}^{(2)} + \boldsymbol{\sigma}^D \equiv \gamma\,\mathrm{tr}(\boldsymbol{\sigma})\boldsymbol{I}^{(2)} + (\boldsymbol{\sigma} - \gamma\,\mathrm{tr}(\boldsymbol{\sigma})\boldsymbol{I}^{(2)}) \\ \boldsymbol{\varepsilon} &= \varepsilon_v\boldsymbol{I}^{(2)} + \boldsymbol{\varepsilon}^D \equiv \gamma\,\mathrm{tr}(\boldsymbol{\varepsilon})\boldsymbol{I}^{(2)} + (\boldsymbol{\varepsilon} - \gamma\,\mathrm{tr}(\boldsymbol{\varepsilon})\boldsymbol{I}^{(2)})\end{aligned} \tag{3.30}$$

where γ is a space dimension dependent parameter, such that $\gamma = \frac{1}{3}$ in 3D and $\gamma = \frac{1}{2}$ in 2D. The

constitutive equation (3.3) and its inverted form are written as follows:

$$\begin{aligned}\sigma_v \boldsymbol{I}^{(2)} + \boldsymbol{\sigma}^D &= \frac{\kappa}{\gamma}\varepsilon_v \boldsymbol{I}^{(2)} + 2\mu\boldsymbol{\varepsilon}^D \\ \varepsilon_v \boldsymbol{I}^{(2)} + \boldsymbol{\varepsilon}^D &= \frac{\gamma}{\kappa}\sigma_v \boldsymbol{I}^{(2)} + \frac{1}{2\mu}\boldsymbol{\sigma}^D\end{aligned} \tag{3.31}$$

where the trace operator $\mathrm{tr}(\bullet)$ is defined as $\mathrm{tr}(\boldsymbol{\sigma}) = \sum_{i=1}^{3}\sigma_{ii}$. In (3.31), $\kappa = \lambda + \gamma(2\mu)$ and μ are respectively the bulk modulus and the shear modulus of an isotropic elastic medium with (λ, μ) the Lamé parameters.

Owing to (3.31), the following equations of the properties of the effective medium for both 2D and 3D cases are obtained:

$$\begin{aligned}\kappa_{\text{eff}} &= \kappa_m + \sum_{r=1}^{n}\phi_r \frac{h_r^2(\boldsymbol{k})(\kappa_r - \kappa_m)}{1 + \frac{\kappa_{S^{(r)}}}{\gamma^2}(\kappa_r - \kappa_{\text{eff}})} \\ \mu_{\text{eff}} &= \mu_m + \sum_{r=1}^{n}\phi_r \frac{h_r^2(\boldsymbol{k})(\mu_r - \mu_m)}{1 + 4\mu_{S^{(r)}}(\mu_r - \mu_{\text{eff}})} \\ \rho_{\text{eff}} &= \rho_m + \sum_{r=1}^{n}\phi_r \frac{h_r^2(\boldsymbol{k})(\rho_r - \rho_m)}{1 + \rho_{M^{(r)}}(\rho_r - \rho_{\text{eff}})}\end{aligned} \tag{3.32}$$

where $\kappa_{S^{(r)}}$ and $\mu_{S^{(r)}}$ are the bulk and shear moduli characterizing the isotropic tensor $\overline{\boldsymbol{S}_{\boldsymbol{x}}^{(r)}}^{\Theta_r}$.

This work aims to compare the analytical and numerical solution in a 2D matrix-inclusion composite with randomly distributed circular inclusions. Therefore, the calculation of the effective parameters in the 2D plane strain case is detailed hereafter.

Of course, the factor $h(\boldsymbol{k})$, a function of the wave vector $\boldsymbol{k}$ defined by (3.26), depends upon the space dimension. In the following, we will denote $\boldsymbol{k} = k\boldsymbol{e_k}$, with k the wavenumber and $\boldsymbol{e_k}$ the unit direction vector of $\boldsymbol{k}$. In the 2D case with circular inclusions, the radius of an r-type circular inclusion being denoted by a_r, $h_r(\boldsymbol{k})$ only depends on the wave number k and is calculated as:

$$h_r(\boldsymbol{k}) \equiv \frac{1}{\Theta^r}\int_{\Theta^r(\boldsymbol{0})} \mathrm{e}^{i\boldsymbol{k}.\boldsymbol{x}}\mathrm{d}\boldsymbol{x} = \frac{2}{ka_r}J_1(ka_r) \tag{3.33}$$

where J_1 is the first-order Bessel function of the first kind.

The last step in analytical development is to obtain $(\kappa_{S^{(r)}}, \mu_{S^{(r)}}, \rho_{M^{(r)}})$ from the Green's tensor. As in the 2D isotropic case, the Green tensor is known, the following formulas of $(\kappa_S^{\text{2D}}, \mu_{S^{(r)}}, \rho_{M^{(r)}})$ can be obtained (see the Appendix of [133] for more details):

$$\begin{aligned}\kappa_{S^{(r)}} &= \frac{1}{4} + \frac{I(k_{p,\text{eff}}a_r) + 1}{\rho_{\text{eff}}c_{p,\text{eff}}^2} \\ \mu_{S^{(r)}} &= \frac{1}{8}\left(\frac{I(k_{p,\text{eff}}a_r) + 1}{\rho_{\text{eff}}c_{p,\text{eff}}^2} + \frac{I(k_{s,\text{eff}}a_r) + 1}{\rho_{\text{eff}}c_{s,\text{eff}}^2}\right) \\ \rho_{M^{(r)}} &= -\frac{1}{2}\left(\frac{I(k_{p,\text{eff}}a_r) + I(k_{s,\text{eff}}a_r)}{\rho_{\text{eff}}}\right)\end{aligned} \tag{3.34}$$

where $k_{p,\text{eff}}$ and $k_{s,\text{eff}}$ are the wavenumbers of respective compression and shear waves in the effective

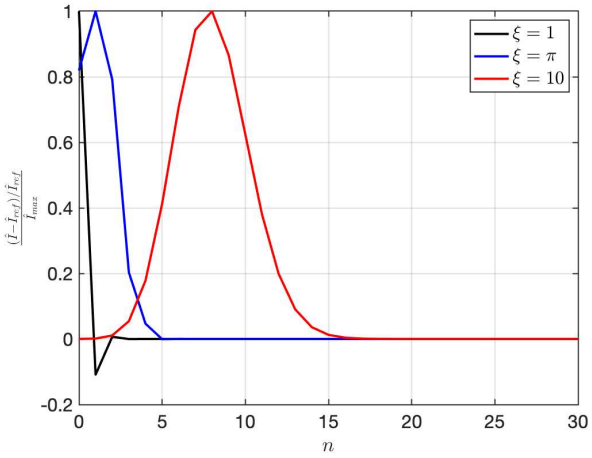

Figure 3.1. Convergence of the $I(\xi)$ for different values of ξ

medium:

$$k_{p,\text{eff}} = \frac{\omega}{c_{p,\text{eff}}} \ , \ k_{s,\text{eff}} = \frac{\omega}{c_{s,\text{eff}}} \tag{3.35}$$

with:

$$c_{p,\text{eff}} = \sqrt{\frac{\kappa_{\text{eff}} + \mu_{\text{eff}}}{\rho_{\text{eff}}}} \ , \ c_{s,\text{eff}} = \sqrt{\frac{\mu_{\text{eff}}}{\rho_{\text{eff}}}} \tag{3.36}$$

The function $I(\bullet)$ in (3.34) is given by:

$$I(\xi) = \frac{i\pi\xi^2}{2} \sum_{n=0}^{\infty} \frac{(-1)^n (2n+1)!}{(n+2)(n!(n+1)!)^2} \left(\frac{\xi}{2}\right)^{2n} \left(1 + \frac{2i}{\pi}\left(\psi(2n+2) - \psi(n+2) - \psi(n+1) + ln(\frac{\xi}{2}) - \frac{1}{2n+4}\right)\right) \tag{3.37}$$

with ψ, the logarithmic derivative of the Gamma function. ψ can be evaluated as:

$$\psi(n) = -\gamma + \sum_{m=1}^{n-1} \frac{1}{m} \tag{3.38}$$

with Euler's constant $\gamma = 0.57721566\ldots$.

According to the statement in [133], the series expansion (3.37) converges rapidly $\forall \xi > 0$. Moreover, the convergence rate of the series varies with the value of ξ; the smaller the ξ is, the faster the series converges. Figure 3.1 shows the convergence of the series for three different ξ. The vertical axis shows the normalized norm of the relative error for this complex-valued series: $\frac{(\hat{I}-\hat{I}_{ref})/\hat{I}_{ref}}{\hat{I}_{max}}$. where $\hat{I}_{ref}$ is the value of the series for $n = 84$ and $\hat{I}_{max}$ is the maximum value of the series for each ξ. We cannot use $n > 84$ since the term $(2n+1)!$ exceeds the maximum possible double precision number stored in a variable (1.7×10^{308}) in Matlab software.

Now by using (3.32) the self-consistent equations, the effective isotropic moduli can be calculated for the 2D matrix-inclusion composite with random distributed circular inclusions. However, as previously stated, the equations in (3.32) are implicit, and the effective properties can only be calculated iteratively. Taking the example of an incident compression wave, the iterative solving algorithm is defined as follows:

In the case of an incident shear wave, $h_r(\boldsymbol{k}_s)$ is calculated in step (5) of the previous algorithm.

Algorithm 1 Effective properties calculation

1: Initialize all the effective properties κ_{eff}, μ_{eff} and ρ_{eff}, consequently $c_{p,\text{eff}}$ and $c_{s,\text{eff}}$, with the matrix's properties.
2: **repeat**
3: Calculate the wavenumbers $k_{p,\text{eff}}$ and $k_{s,\text{eff}}$ for the desired frequency ω using (3.35).
4: Calculate $I(k_{p,\text{eff}}a_r)$ and $I(k_{s,\text{eff}}a_r)$ using (3.37).
5: Calculate $\kappa_{S^{(r)}}$, $\mu_{S^{(r)}}$, and $\rho_{M^{(r)}}$ using (3.34), and $h_r(\boldsymbol{k}p)$ using (3.33).
6: Update the effective properties κeff, μ_{eff} and ρ_{eff} using (3.32), and consequently $c_{p,\text{eff}}$ and $c_{s,\text{eff}}$ using (3.36).
7: **until** convergence is achieved
8: Calculate the complex-valued wavenumber $k_{p,\text{eff}}(\omega)$ using (3.35).
9: Calculate, for the compression waves, the effective phase velocity $V_{p,\text{eff}}(\omega) = \dfrac{\omega}{\mathfrak{Re}(k_{p,\text{eff}})}$ and the attenuation coefficient $\alpha_{p,\text{eff}}(\omega)$ with respectively the real part $\mathfrak{Re}(k_{p,\text{eff}})$ and the imaginary part $\mathfrak{Im}(k_{p,\text{eff}})$ of the effective wavenumber.

Then, in the step (9), the converged value of $k_{s,\text{eff}}(\omega)$ gives the effective phase velocity $V_{s,\text{eff}}(\omega)$ and the attenuation coefficient $\alpha_{s,\text{eff}}(\omega)$ for the shear waves.

3.1.4 Analytical attenuation coefficient: an epoxy-lead composite

As an example, the introduced self-consistent method is applied to a composite material made of epoxy matrix and lead inclusions, whose material properties are shown in Table 3.1. In this example, the ξ is always less than 4 for both compression and shear waves, and it is observed the convergence of equation (3.37) is obtained with $n = 20$ with relative error criterion $\varepsilon = 10^{-15}$.

Table 3.1. Material properties of the epoxy matrix and the lead inclusions

Material	ρ(kg/m^3)	κ(GPa)	μ(GPa)	c_p(m/s)	c_s(m/s)
Epoxy (matrix)	1200	6.61	1.73	2720	1200
lead (inclusion)	11300	49.6	8.36	2320	860

In the present work, we focus on the phase velocity and attenuation of the compression waves. The phase velocity and dimensionless attenuation coefficient $\mathfrak{Im}(k_{p,\text{eff}})a$ are illustrated for different area fractions of the inclusion phase with respect to the dimensionless wavenumber $x_0 = k_{p,m}a/\pi = 2a/\lambda_{p,m}$ (see Figure 3.2), with a denoting the radius of inclusion. This definition of the dimensionless wavenumber gives the ratio between the inclusion's diameter and the wavelength of compression waves.

According to [133], the theoretical model presented in the previous section is validated for large wavelengths down to the diameter of the inclusion, *i.e.,* $\lambda \geq 2a$. Therefore, the validated frequency range of the theory is determined by the shortest wavelength, which is the wavelength of shear waves. Using the definition of the wavenumber (3.35) and the definition of x_0, this velocity range can be written as $x_0 \leq c_{s,m}/c_{p,m}$. Hence, the proposed dimensionless wavenumber x_0 helps to directly see the validated frequency range on the figures, which is $x_0 = 0.44$ for the composite defined in Table 3.1.

In Figure 3.2, it is observed that the phase velocity and the attenuation coefficient are frequency-dependent, meaning that the effective medium is dispersive. As expected, the attenuation coefficient shows an increasing trend when the area fraction increases. The phase velocity, on the other hand,

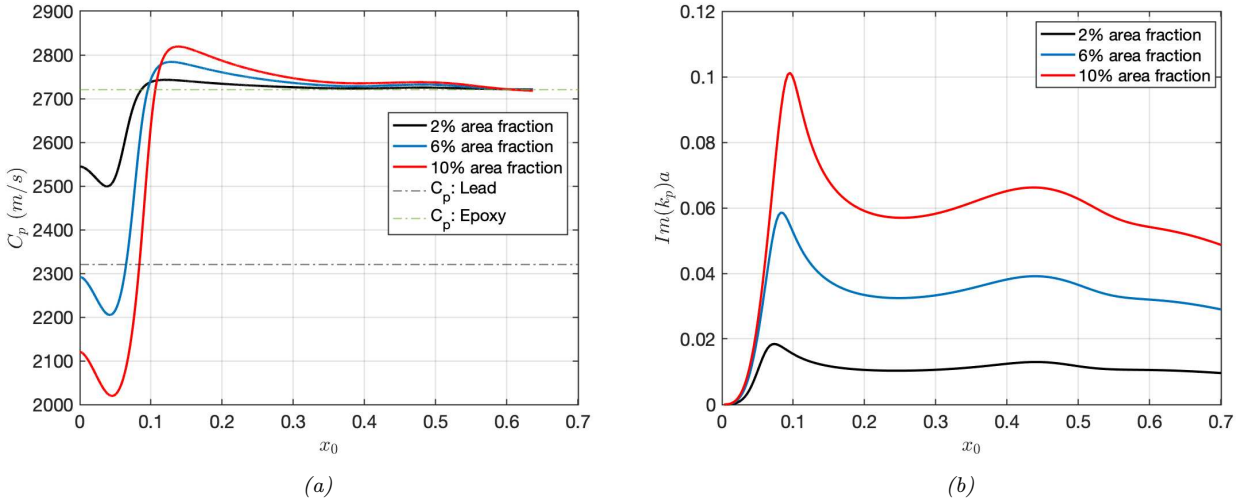

Figure 3.2. Analytical (a) phase velocity and (b) attenuation coefficient ($\Im\mathfrak{m}(k)a$) of the compression with respect to the dimensionless wavenumber $x_0 = k_{p,m}a/\pi = 2a/\lambda_{p,m}$ for different area fractions of the inclusion phase. These results are similar to those of [133], with a slight modification in the material properties.

converges to the propagation speed of the compression wave in the pure matrix when the frequency is increased for any area fraction. It is also observed in Figure 3.2a that the phase velocity is outside of the range bounded by the phase velocities of the matrix and inclusion, which are shown with horizontal dashed lines. Notably, the same phenomenon is observed in the numerical results later in Figure 3.8.

By increasing the area fraction of the inclusions, the scattered displacement fields of each inclusion influence the others, and from a certain point, the single-scattering assumption is no longer valid. However, there is no criterion to verify whether the single-scattering assumption is valid just by relying on the analytical solution. Hence, we use the numerical simulation to compare and determine a more rigorous range for validity of the introduced effective medium with the single-scattering assumption.

3.2 FE-based method for estimation of phase velocity and attenuation

This section introduces a finite element-based numerical approach to numerically evaluate the phase velocity and the attenuation coefficient for a matrix-inclusion composite. This approach is similar to the numerical method used to estimate the attenuation coefficient for polycrystalline materials proposed in [126–128]. Compared to the analytical analysis presented previously, the finite element approach has the advantage of modeling exactly the microstructure of matrix-inclusion composites without any simplifying assumptions. Hence, by comparing the numerically evaluated phase velocity and attenuation coefficient with their analytically predicted values, we can mutually validate both approaches for microstructures that comply with the analytical hypotheses. The validated numerical approach can also be extended to characterize other microstructures that do not conform to these hypotheses. This would enable us to expand the scope of the analysis beyond the analytical regime.

3.2.1 FE model and the numerical setup

Concerning the numerical models, the considered domain consists of a 2D square $\Omega = [0, L_x] \times [0, L_y]$ with $L_x = L_y = 4$mm (Figure 3.3). Inside Ω, there is a random distribution of an ensemble of N circular

inclusions Θ_n of the same type: $\Omega_{inc} = \cup_{n=1}^{N} \Theta_n$. The numerical simulation is performed for various area fractions of $\phi = 2\%$ 4%, 6%, and 8%. For each chosen area fraction, calculations are performed for different inclusion radii of $a = 100\mu$m, 150μm, 200μm, and 250μm. The domain $\Omega_m = \Omega \setminus \Omega_{inc}$ is considered as the matrix subdomain. The upper boundary of Ω is subjected to a time-varying vertical pressure loading, while the free boundary condition is applied to the lower boundary. The symmetry boundary condition is applied to both vertical edges to ensure that a plane wave propagates "macroscopically" in the domain.

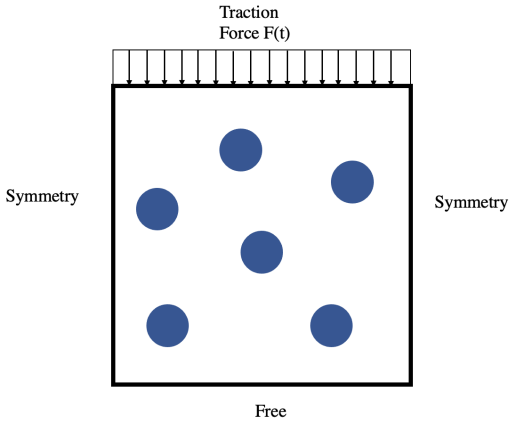

Figure 3.3. Geometry, loading, and boundary conditions considered for the problem

The temporal variation of the pressure loading is prescribed as a Ricker wavelet whose frequency content is centered at f_{max} with a cutoff frequency $f_c = 2.5 f_{max}$. In this study, two Ricker signals, LFR and HFR, with different f_{max} are considered:

- *LFR*: ricker signal with $f_{max} = 1$MHz,
- *HFR*: ricker signal with $f_{max} = 3$MHz,.

The element size h in the numerical setup is chosen based on the smallest wavelength in the domain $\lambda_{min} = min\{cp_{mat}, cs_{mat}, cp_{inc}, cs_{inc}\}/fc$, where $fc = 7.5$Hz. All the numerical results presented hereafter are calculated using 15 elements per smallest wavelength of $h = \lambda_{min}/15$. For the choice of time steps, the same approach as section 2.4 is used to ensure the stability of the solver.

Figure 3.4 shows both Ricker signals as a function of the time and frequency. The element size h in the numerical setup is chosen based on the smallest wavelength in the domain $\lambda_{min} = min\{c_{p,m}, c_{s,m}, c_{p,inc}, c_{s,inc}\}/fc$, where $f_c = 7.5$Hz. This chapter's numerical results are calculated using 15 elements per smallest wavelength of $h = \lambda_{min}/15 = 8.6\mu$m. This element size h gives the ratio of $\frac{2a}{h} = 23$ for the smallest modeled scatterer of radius $a = 100\mu$m.

3.2.2 Post-processing of the ultrasonic signal

To calculate the attenuation coefficient for the introduced configuration, the vertical component of the velocity signal provided by the finite element solution is recorded at $N^{points} = 150$ sampling points, which are placed equally distant on the top line of the domain Ω. This vertical component is called $V(t)$ hereafter. For each pair (ϕ, a), the numerical calculation is repeated over a batch of 30 samples with a different random inclusion distribution. The random position of the inclusions is generated using a

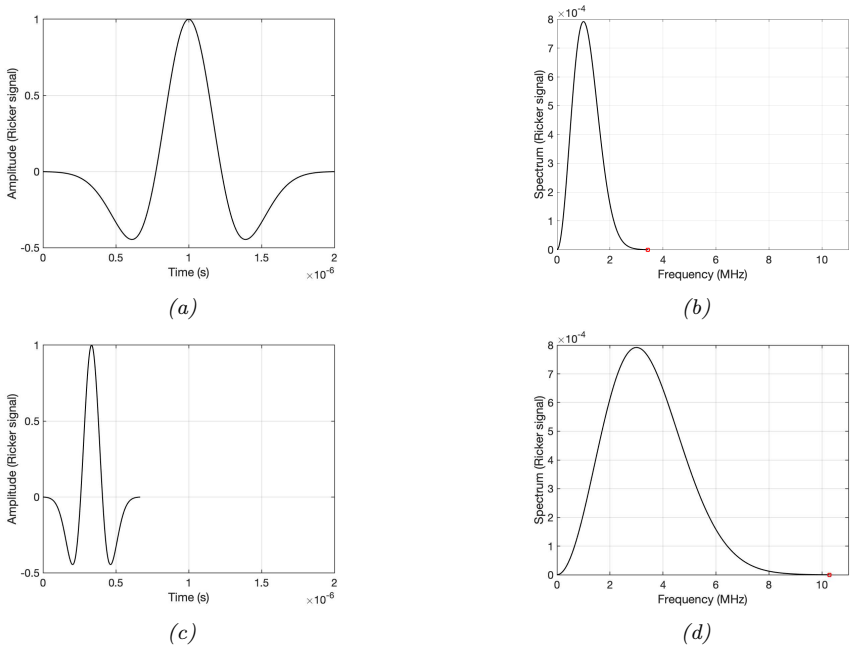

Figure 3.4. Ricker signals used for the numerical simulation. LFR signal (a) and its frequency content (b); HFR signal (c) and its frequency content (d).

uniform distribution function. We always verify that the inclusions with the generated distribution do not interfere with each other. Otherwise, one of the points is removed and placed in another random position. This recorded signal $V(t)$ is then averaged twice: first over the 150 sampling points to get each configuration's average signal and second over the 30 different random configurations. Eventually, for each pair of (ϕ, a), we get a single averaged signal. Afterward, the echo signal of the incident signal, reflected by the bottom boundary of Ω, is detected according to its maximum amplitude V_{max}^{refl}, along with the corresponding time T_{max}^{refl} at which the echo signal reaches the transducer. Indeed, the echo signal is obtained by using a time window defined as $[T_{max}^{refl} - \frac{T_r}{2}, T_{max}^{refl} + \frac{T_r}{2}]$, where T_r is the duration of Ricker signals. Finally, using this windowed echo signal and the reference signal, which in this case is the incident velocity signal, the attenuation coefficient is calculated as:

$$\alpha\left(f\right) = \frac{1}{D} \ln\left(\frac{|\widehat{V}^{refl}(f)|}{|\widehat{V}^{inc}(f)|}\right) \tag{3.39}$$

where D is the propagation distance, $\widehat{V}^{refl}$ and $\widehat{V}^{inc}$ are the complex-valued discrete Fourier transform of the vertical velocity component of the reflected and incident wave, respectively.

On the other hand, the phase velocity is obtained as follows:

$$c_{p,num}\left(f\right) = \frac{D \times f}{\Delta\phi} \tag{3.40}$$

where $\Delta\phi$ is the phase shift of the incident signal V^{inc} and reflected signal V^{refl}, calculated as following:

$$\Delta\phi(f) = tan^{-1}\left(\frac{Im(SC(f))}{Re(SC(f)}\right) + k\pi \tag{3.41}$$

where SC is the spectral intercorrelation of the two complex-valued signals and is obtained as follows:

$$SC(f) = \frac{\widehat{V}^{inc}(f)\overline{\widehat{V}^{refl}(f)}}{|\widehat{V}^{inc}(f)||\widehat{V}^{refl}(f)|} \tag{3.42}$$

3.2.3 Convergence study: number of samples with different random distributions

A primary convergence study is performed to show that 30 samples are enough to estimate the phase velocity and attenuation coefficient numerically. The following L^2 relative error norm of the attenuation coefficient is used as the convergence criterion:

$$e_\alpha = \sqrt{\frac{\sum_f (\alpha(f) - \alpha_{ref}(f))^2}{\sum_f \alpha_{ref}(f)^2}} \tag{3.43}$$

As an example, for the case corresponding to $(\phi, a) = (2\%, 200\mu\text{m})$, Figure 3.5 shows the attenuation coefficient obtained from the average reflected signal for different numbers of samples over the corresponding numerical valid range of frequency (*cf.* section 3.2.3). Taking the attenuation coefficient evaluated by averaging over 30 samples as α_{ref} the reference value, Table 3.2 shows e_α the L^2 relative error for 25 samples with $\phi = 2\%$ for all the considered values of the radius a. All the reported error values in Table 3.2 are less than 6%, showing that a batch of 25 samples is good enough. Our analysis shows that convergence is reached with fewer samples for the higher-frequency signal. For the area fraction of $\phi = 2\%$ and different inclusion sizes, the L^2 relative error norm is less than 5% with 15 samples for the high-frequency ricker signal. However, all the results presented in this paper are obtained with 30 samples with different random distributions of the inclusions.

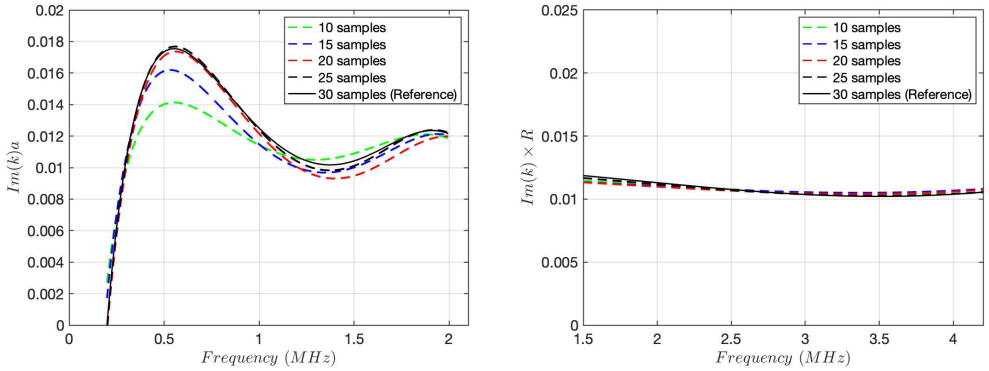

(a) (b)

Figure 3.5. Numerically evaluated attenuation coefficient w.r.t. the frequency in the case of $(\phi, a) = (2\%, 200\mu\text{m})$ *for different numbers of samples and (a) LFR, and (b) HFR signals*

Taking the attenuation coefficient evaluated by averaging over 30 samples as α_{ref} the reference value, Table 3.2 shows e_α the L^2 relative error for 25 samples with $\phi = 2\%$ for all the considered values of the radius a. All the reported error values in Table 3.2 are less than 6%, showing that a batch of 25 samples is good enough. However, all the results presented in this paper are obtained with 30 samples with different random distributions of the inclusions.

Table 3.2. The L^2 relative error (e_α) for 25 samples in the case of $\phi = 2\%$

	$a = 100\mu$m	$a = 150\mu$m	$a = 200\mu$m	$a = 250\mu$m
Lower Frequency (%)	3.1	1.9	1.5	6.0
Higher Frequency (%)	2.6	1.9	1.1	1.8

Valid frequency range of the ricker signal

In this section, we intend to determine a frequency range for different ricker signals in which the presented results are valid. Looking at the frequency content of the two ricker signals used in this study (Figure 3.4b and Figure 3.4d), we expect the best solution around the f_{max}. As we move toward left or right, the quality of the results would be degraded. The goal is to find the broadest range in which the discrepancy between the analytical and numerical results is still acceptable. To achieve this, we have employed e_α the L^2 relative error norm (3.43) as a measure, where this time $\alpha_{ref}(f)$ is the analytical value. The frequency range in which e_α is less than 15% for all inclusion sizes is identified as the acceptable range. Based on [128], we chose as a reference the frequency range in which the amplitude of the spectrum is more than 50% of the peak amplitude, as it is shown in Figure 3.6(a)-(b).

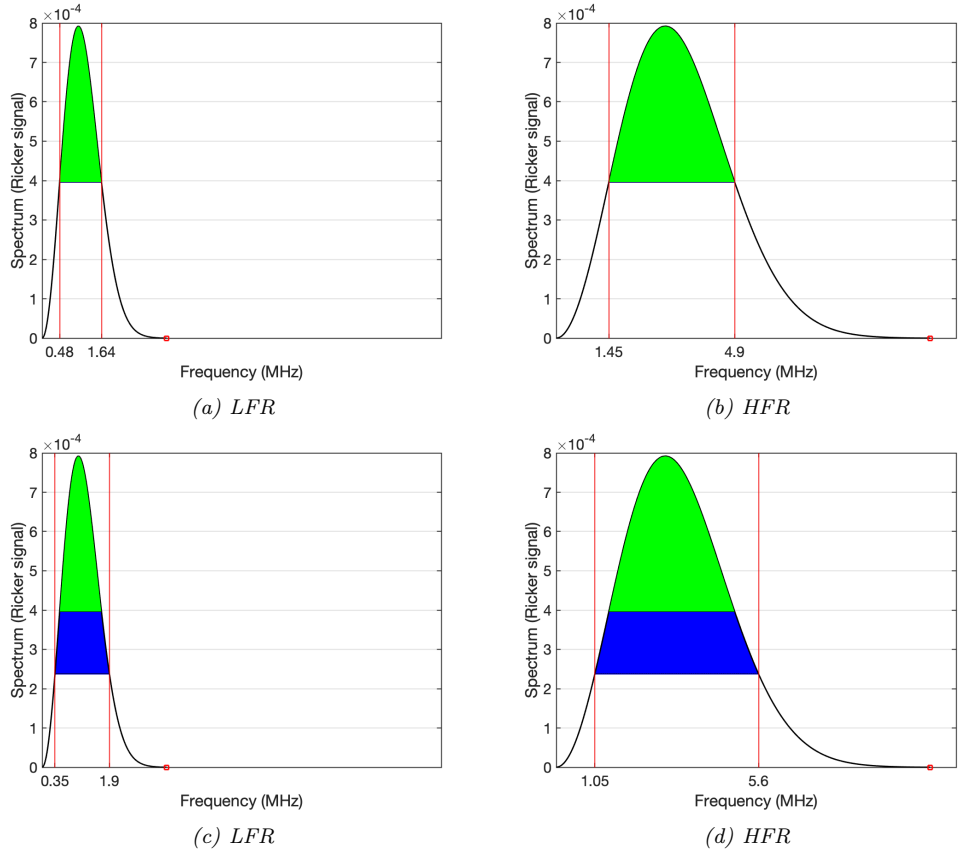

(a) LFR *(b) HFR*

(c) LFR *(d) HFR*

Figure 3.6. Considered frequency ranges of the ricker signals. (a)-(b) reference range defined with 50% of the peak amplitude; (c)-(d) larger range defined with 30% of the peak amplitude

Therefore, the reference numerical valid frequency range for two ricker signals are as follows:

- *LFR*: signal with $f_{max} = 1$MHz, for which the valid frequency of $[0.48, 1.64]$MHz leading to a range of $[1.7, 5.7]$mm for the wavelength of the compression wave in the matrix;

- *HFR*: signal with $f_{max} = 3$MHz, for which the valid frequency of $[1.45, 4.90]$MHz leading to a range of $[0.5, 1.9]$mm for the wavelength of the compression wave in the matrix.

For the sake of simplicity, the results are plotted for a modified range of $[0.48, 1.55]$MHz and $[1.55, 4.90]$MHz, to avoid the slight overlap of the valid range of the two ricker signals. Our observations indicate that the phase velocity and attenuation coefficient values do not necessarily correspond at the joint frequency of the LFR and HFR signals, where $f = 1.55$MHz. As a result, we used a moving average filter to effectively smooth out the curve discontinuity at this frequency.

Figure 3.7 compares the analytical and numerical attenuation coefficient for three different inclusion sizes. The numerical attenuation coefficient is plotted in the reference valid frequency range with respect to the dimensionless wavenumber x_0 (bottom horizontal axis) and the actual frequency (top horizontal axis). The L^2 relative error for each plot is reported in Table 3.3. It should be noted that the analytical/numerical comparison shows the highest L^2 relative error of 13% for the smallest inclusion size of $a = 150\mu$m.

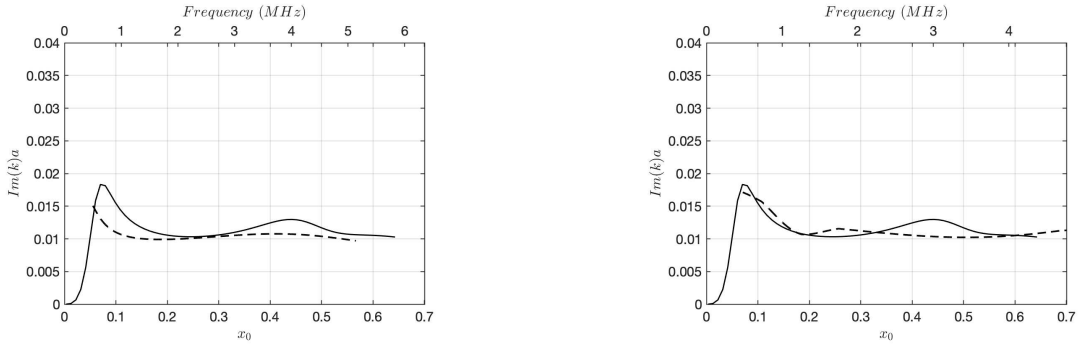

(a) $a = 150\mu$m *(b)* $a = 200\mu$m

Figure 3.7. Analytical (solid lines –) and numerical (dashed lines - -) area fraction w.r.t. the frequency for area fraction $\phi = 2\%$

Table 3.3. The L^2 *relative error* (e_α) *in the extended frequency range for the case of* $\phi = 2\%$

	$a = 150\mu$m	$a = 200\mu$m	$a = 250\mu$m
$e_\alpha(\%)$	13.0	5.4	7.0
$e_\alpha(\%)$ in extended low frequency range $[0.35, 0.48]$MHz for LFR signal	25	6.5	17
$e_\alpha(\%)$ in extended high frequency range $[1.64, 1.90]$MHz for LFR signal	22	14	8
$e_\alpha(\%)$ in extended low frequency range $[1.05, 1.45]$MHz for HFR signal	19	12	13
$e_\alpha(\%)$ in extended high frequency range $[4.90, 5.60]$MHz for HFR signal	12	NA	NA

Now, we consider a frequency range defined by 30% of the peak amplitude of the frequency content instead of 50%. In that case, we obtain a more extensive frequency range ($[0.35, 1.90]$MHz for the lower frequency signal and $[1.05, 5.60]$MHz for the higher frequency signal). The L^2 relative error obtained in these extended frequency ranges is also shown in the Table 3.3. One observes that the L^2

relative error increases significantly in the extended frequency region for the case of $a = 150\mu$m and $a = 250\mu$m. For the other inclusion sizes, the error also gets larger for specific extended regions. In addition, extending the high-frequency range for the HFR signal is also unnecessary because there is no valid analytical solution to compare the results. Therefore, For the subsequent parametric studies, we use the reference valid frequency range defined by 50% of the peak amplitude of the frequency content, *i.e.*, all the results are presented for the frequency range of $[0.5, 4.90]$MHz shown in Figure 3.6a and Figure 3.6b. It is worth noticing that this valid frequency range translates into a different range of the dimensionless wavenumber for different inclusion sizes. For instance, for an inclusion size of $a = 150\mu$m, the dimensionless wavenumber range is $[0.05, 0.57]$, while for an inclusion size of $a = 200\mu$m, it is $[0.07, 0.72]$.

3.2.4 Analytical/numerical comparison: effect of the area fraction and inclusion size

The effects of two microstructure parameters, the area fraction of inclusions and the inclusion size, are studied in the present work. Figure 3.8 illustrates the analytical/numerical comparison of the phase velocity and attenuation coefficient for different area fractions of inclusions with various sizes. Each plot contains the target parameter (either phase velocity or dimensionless attenuation coefficient) with respect to both the dimensionless frequency $x_0 = ka$ (bottom x-axis) and frequency in *Hertz* (top x-axis).

Looking at the results presented in Figure 3.8, one observes a good agreement between the analytical and numerical results for $\phi = 2\%$ and $\phi = 4\%$ regardless of the inclusion size. However, discrepancies appear among the analytical and numerical attenuation coefficients for higher area fractions. This disagreement is expected because increasing the area fraction makes the interaction among the inclusions no longer negligible. In other words, the single-scattering assumption, the principle assumption for obtaining the analytical attenuation coefficient, is no longer respected.

Moreover, looking at the Figure 3.8e and Figure 3.8f for the case of $a = 150\mu$m and $\phi = 8\%$, one can observe that the numerical phase velocity and attenuation coefficient are not shown for the low-frequency ricker signal. The reason is due to the inability of the post-processing approach to accurately identify the reflected signal from the bottom edge. Therefore, the corresponding phase velocity and numerical attenuation coefficient are not correct. The phase velocity and attenuation coefficient for $a = 100\mu$m are presented in Figure 3.8g and Figure 3.8h. Again, the numerical solution is not depicted for the area fractions $\phi = 6\%$ and $\phi = 8\%$ due to the same limitation of the post-processing approach. This point will be discussed later in this section.

To obtain a more precise quantitative analysis of the discrepancy between analytical and numerical attenuation coefficients, we present the relative error norm in Table 3.4. As the value of the attenuation coefficient changes with the volume fraction ϕ, the normalization of error presented in Table 3.4 is done with the analytical attenuation curve for $\phi = 8\%$. The error exhibits a general upward trend as the area fraction increases for LFR and HFR. However, the rate of increase varies for different inclusion sizes. Additionally, while raising ϕ from 6% to 8%, we do not always observe a corresponding elevation in error. As expected, the errors reported in the table indicate that the discrepancy among the results is greater for the HFR.

As demonstrated earlier, the dimensionless attenuation coefficient has an analytical master curve as a function of the dimensionless wavenumber, independently of the inclusion size (see the equation

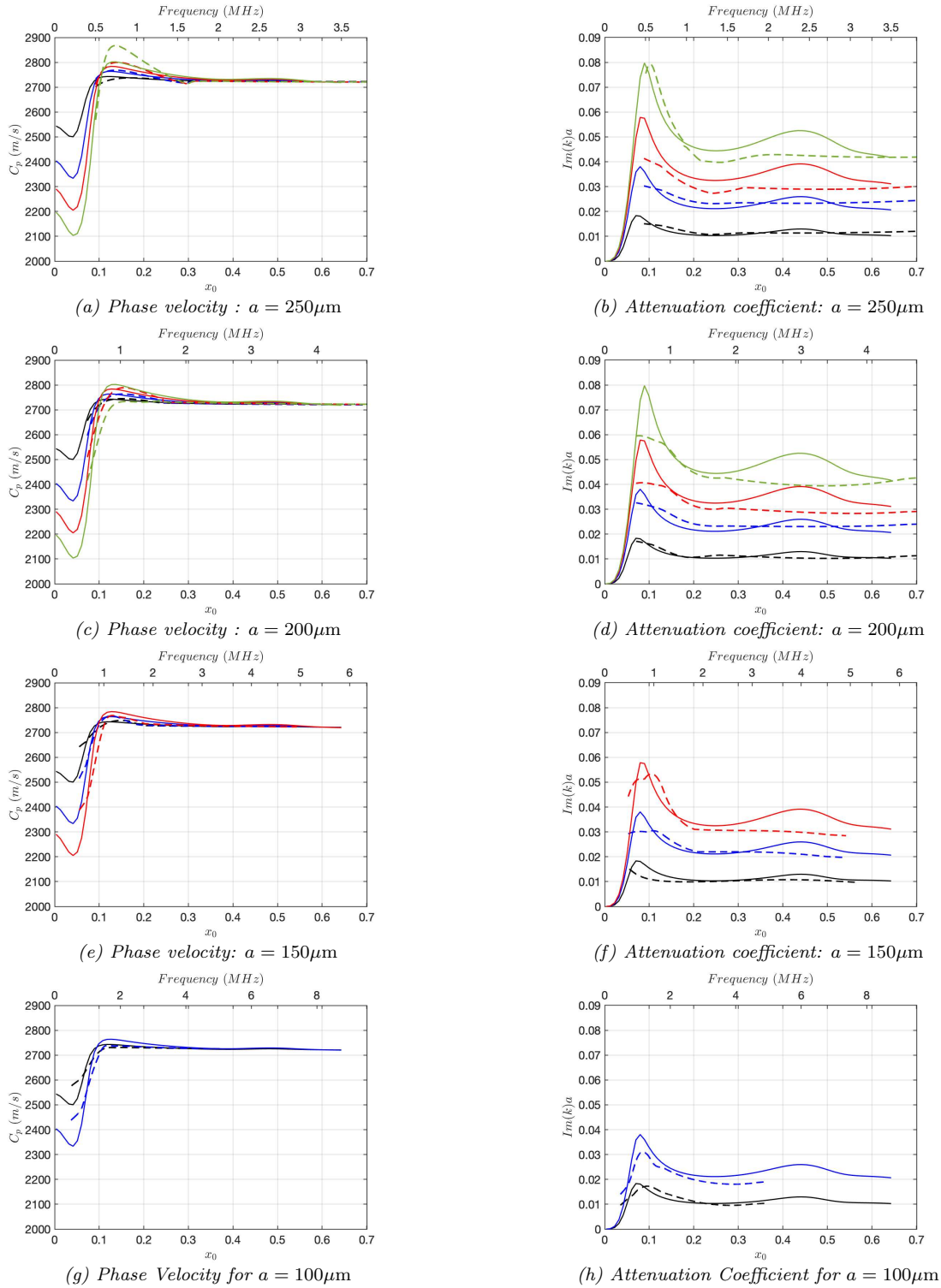

(a) Phase velocity : $a = 250\mu$m

(b) Attenuation coefficient: $a = 250\mu$m

(c) Phase velocity : $a = 200\mu$m

(d) Attenuation coefficient: $a = 200\mu$m

(e) Phase velocity: $a = 150\mu$m

(f) Attenuation coefficient: $a = 150\mu$m

(g) Phase Velocity for $a = 100\mu$m

(h) Attenuation Coefficient for $a = 100\mu$m

Figure 3.8. Analytical (solid lines –) and numerical (dashed lines - -) phase velocity and attenuation coefficient w.r.t. the frequency for different area fractions: $\phi = 2\%$ (black), $\phi = 4\%$ (blue), $\phi = 6\%$ (red), and $\phi = 8\%$ (green)

(3.34) and Figure 3.2). Nevertheless, it has been observed on the numerical side that when plotting the dimensionless attenuation coefficients for various inclusion sizes of the same area fraction, discrepancies arise as the area fraction increases (Figure 3.9). This can be considered as another indicator showing that the theoretical model gradually diverges from the actual attenuation coefficient with increasing

Table 3.4. L^2 relative error (%) for different area fractions and inclusion sizes

	Low-frequency Ricker (LFR)				High-frequency Ricker (HFR)			
	$\phi = 2\%$	$\phi = 4\%$	$\phi = 6\%$	$\phi = 8\%$	$\phi = 2\%$	$\phi = 4\%$	$\phi = 6\%$	$\phi = 8\%$
$a = 250\mu m$	1.5	3.2	9.4	9.0	2.0	4.0	13.7	12.7
$a = 200\mu m$	1.2	4.3	13.0	12.7	3.4	4.7	15.8	19.3
$a = 150\mu m$	3.2	5.1	8.8	NA	3.5	7.5	16.0	19.8
$a = 100\mu m$	3.8	9.5	NA	NA	3.8	8.1	15.2	31.8

volume fraction. To better show the challenge of the post-processing approach, the velocity signals at

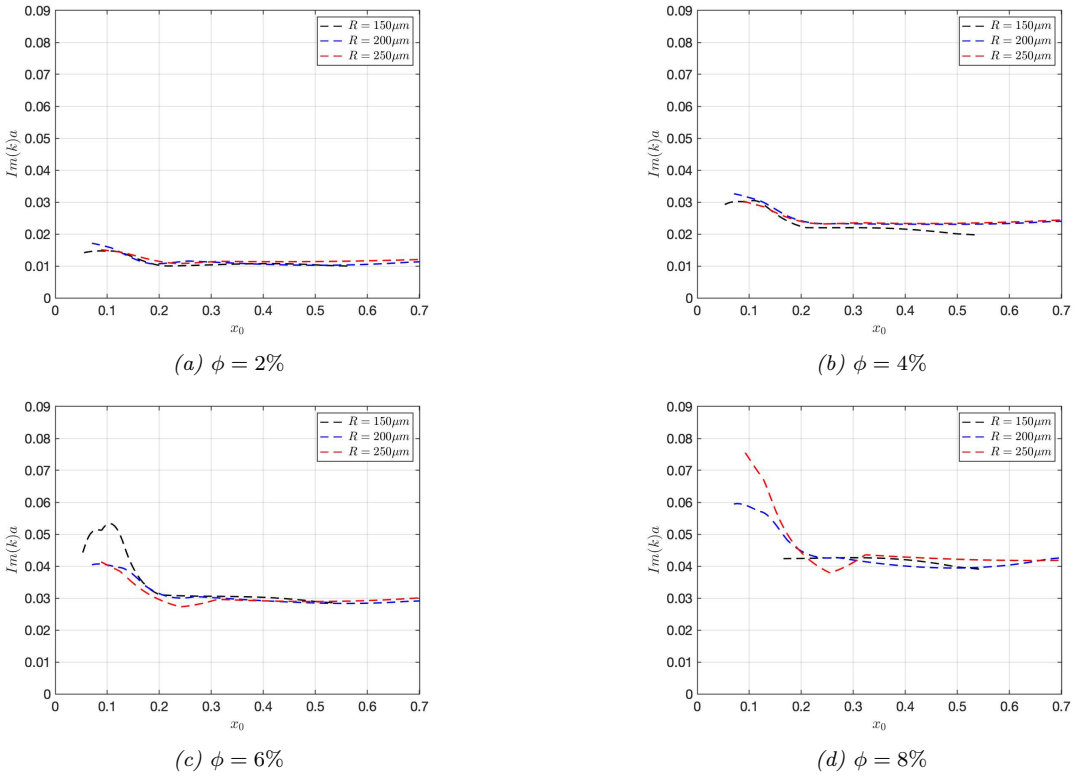

(a) $\phi = 2\%$ *(b) $\phi = 4\%$*

(c) $\phi = 6\%$ *(d) $\phi = 8\%$*

Figure 3.9. Numerically computed attenuation coefficient w.r.t. the frequency for each area fraction with different inclusion sizes

the top boundary are presented in Figure 3.10 for two different area fractions: $\phi = 2\%$ and $\phi = 8\%$. For the first case, the echo of the bottom boundary can be easily detected due to its maximum amplitude during the post-processing stage. However, for $\phi = 8\%$, the echo amplitude is comparable to the backscattered noise from the microstructure, making it undetectable during the post-processing stage.

As a primary analysis, we investigate the potential correlation between the minimum distance between inclusions and the failure of the post-processing stage. Increasing the area fraction of the inclusions or reducing their diameter will increase the number of inclusions in the domain. Therefore, We expect the minimum distance of the inclusions to decrease in a domain with more inclusions. Figure 3.11 shows the average of minimum distances over 10000 samples with different area fractions and sizes of the inclusions. It is observed that the minimum distance decreases for a certain size of inclusion by raising the area fraction or for a certain area fraction by decreasing the size of inclusion. We also depicted the three configurations where the numerical approach failed to capture the echo

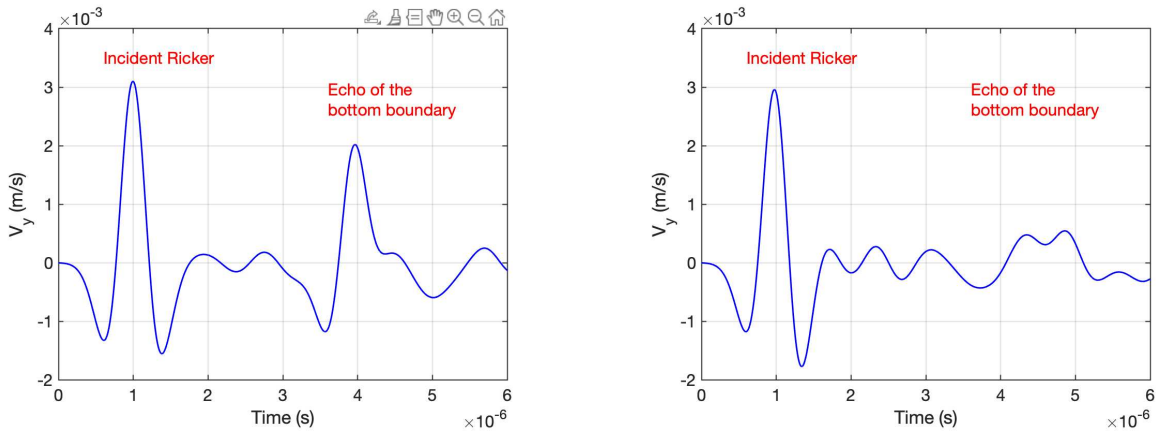

(a) $\phi = 2\%$ (b) $\phi = 8\%$

Figure 3.10. Case of inclusion size $a = 100\mu m$. Average velocity signal on the top boundary for two different area fractions

signal reflected from the boundary with a cross marker. For all these cases, which are (1) $\phi = 8\%$ and $a = 100\mu m$, (2) $\phi = 6\%$ and $a = 100\mu m$ and $\phi = 8\%$ and $a = 150\mu m$, the average minimum distance is less than $40\mu m$ (the horizontal red line in Figure 3.11).

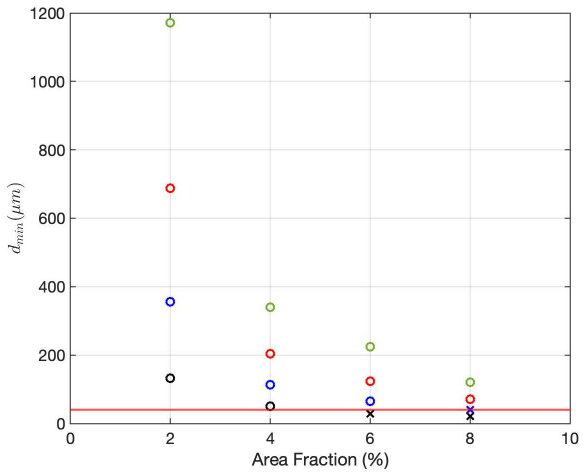

Figure 3.11. The average minimum distances between the inclusions for different area fractions ($a = 100\mu m$, $a = 150\mu m$, $a = 200\mu m$ and $a = 250\mu m$)

This primary analysis is also consistent with the observation that the analytical/numerical discrepancy increases with increasing surface fraction and decreasing inclusion size. Indeed, with the decrease of the minimum distance between inclusions, the single-scattering assumption becomes less valid, and the analytical formulas become consequently less relevant.

3.3 3D-printed tissue-mimicking composite: numerically calculated phase velocity and attenuation

This section presents the phase velocities and attenuation coefficients for a 3D-printed composite with a quasi-incompressible 3D-printed GLM as the matrix and 3D-printed RTOP material whose

properties are shown in Table 3.5. Here we use a Ricker wavelet with $f_{max} = 5$MHz and a valid frequency range of $[2.4, 8.2]$MHz, which includes the frequency range of ultrasonic imaging. For this specific frequency range, the corresponding wavelengths of the compression and shear waves are shown in Table 3.5.

Table 3.5. Material properties of the quasi-incompressible GLM (matrix) and RTOP (inclusions)

Material	$\rho(kg/m^3)$	$\kappa(GPa)$	$\mu(MPa)$	$c_p(m/s)$	$c_s(m/s)$	$\lambda_p(\mu\text{m})$	$\lambda_s(\mu\text{m})$
GLM	1100	3.10	0.3	1620	17	$[200-675]$	$[2-7]$
RTOP	1150	6.78	1830	2680	1235	$[330-1100]$	$[150-520]$

The analytical model does not apply to this particular application for the frequency range of interest defined by ultrasonic imaging since the wavelength of the shear wave is considerably smaller than the diameter of the inclusion. Recalling the definition of the valid frequency range already discussed in section 3.1.4, the valid frequency range of the analytical framework for this particular composite is $x_0 \leq c_{s,m}/c_{p,m} = 0.01$. Hence, the analytical framework is just valid for a very small range of frequencies which does not cover the frequency range of ultrasonic imaging. Therefore, the numerical approach is used alternatively to obtain the phase velocity and attenuation coefficient.

The considered domain always consists of a 2D rectangular domain $\Omega = [0, L_x] \times [0, L_y]$ with $L_x =$ 5mm and $L_y = 3$mm (Figure 3.3). The phase velocity and the attenuation coefficient are calculated using the method presented in section 3.2 for three different area fractions of inclusions: $\phi_1 = 1\%$, $\phi_2 = 3\%$, and $\phi_3 = 5\%$. We also consider three different sizes for the inclusions: $a = 100\mu\text{m}, 150\mu\text{m}$, and 200μm (see Figure 3.12).

One observes from Figure 3.12 that the phase velocity slightly increases for the higher area fractions of inclusions since the compression wave propagates faster in the inclusion. However, the phase velocities converge to the phase velocity of the homogeneous matrix as we increase the frequency. On the other hand, the dimensionless attenuation coefficient increases for a higher area fraction of the inclusions, as anticipated.

As the final result, Figure 3.13 shows the comparison of attenuation coefficients for the epoxy-lead and the 3D-printed composites for the same area fraction$\phi = 2\%$ and the same inclusion size $a = 100\mu$m. One can see that the attenuation coefficient is bigger for the 3D-printed composite since the gap in the propagation speeds, in this case, is higher than the epoxy-lead composite. Moreover, it is observed that, unlike the epoxy-lead composite, the attenuation coefficient curves of the 3D-printed composite do not overlap to form a master curve. Since here the numerical approach is used to estimate the attenuation coefficient, it is important to note that the assumption of having a diameter smaller than the wavelength does not apply. Therefore, one may notice that the results for the 3D-printed material are presented over a broader range of dimensionless wavenumber in Figure 3.13 (see the horizontal axes).

As another important characteristic of the microstructure, the impact of the material properties of the inclusion phase is investigated. Indeed, as detailed in section 1.1.1, the constituent materials of a 3D printer can be mixed to create digital materials with varying properties. While GLM is the material that best approximates cardiac tissue and is suitable for use as the matrix, RTOP can be substituted with any digital material to achieve the desired attenuation coefficient. Given a large

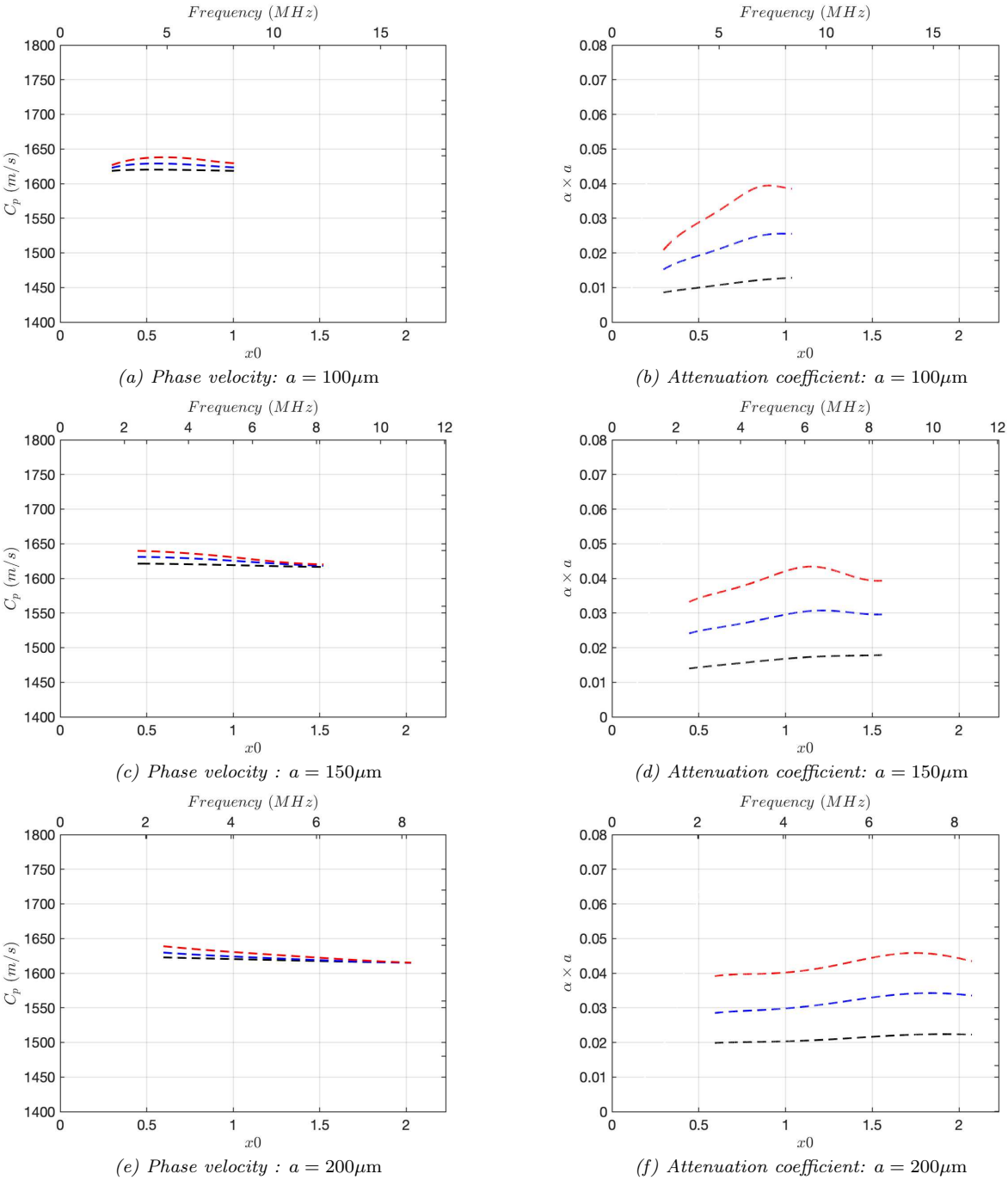

(a) Phase velocity: $a = 100\mu$m (b) Attenuation coefficient: $a = 100\mu$m

(c) Phase velocity : $a = 150\mu$m (d) Attenuation coefficient: $a = 150\mu$m

(e) Phase velocity : $a = 200\mu$m (f) Attenuation coefficient: $a = 200\mu$m

Figure 3.12. Numerical phase velocity and attenuation coefficient for the 3D-printed composite material with the RTOP inclusion with different area fractions: $\phi = 1\%$ (black), $\phi = 3\%$(blue), $\phi = 5\%$ (red)

number of potential digital materials, with over 50 available options, and a lack of available acoustic property data for each material, we have selected four digital materials with P-wave propagation speeds of $C_p^{DM1} = 2400\ m/s$, $C_p^{DM2} = 2200\ m/s$, $C_p^{DM3} = 2000\ m/s$, and $C_p^{DM4} = 1800\ m/s$ for our analysis. Figure 3.14 to Figure 3.16 shows the phase velocity and attenuation speed of these materials. One can observe that the phase velocity in the target frequency range is very similar to the P-wave propagation speed in GLM. The difference reduces as we use inclusions with smaller C_p, which is expected since the degree of inhomogeneity decreases. Moreover, the attenuation coefficient will decrease when we replace the RTOP material with digital materials with lower propagation speed (i.e., softer materials).

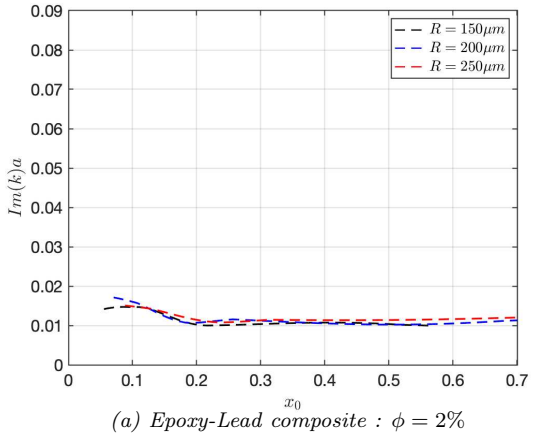

(a) Epoxy-Lead composite : $\phi = 2\%$

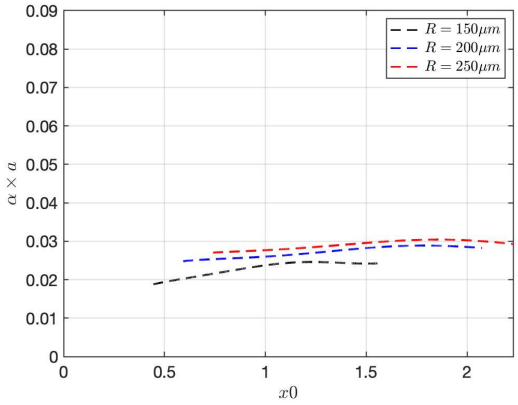

(b) 3D-printed composite : $\phi = 2\%$

Figure 3.13. Comparison of the attenuation coefficients for the epoxy-lead and the 3D-printed composites for the same area fraction $\phi = 2\%$

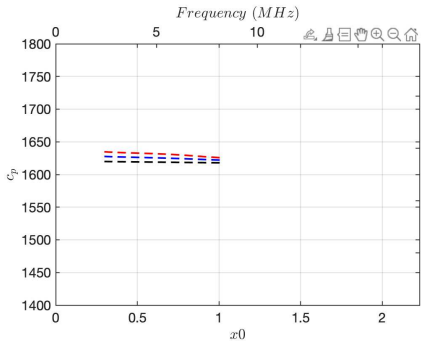

(a) Phase velocity: DM1 inclusion ($C_p^{DM1} = 2400\ m/s$)

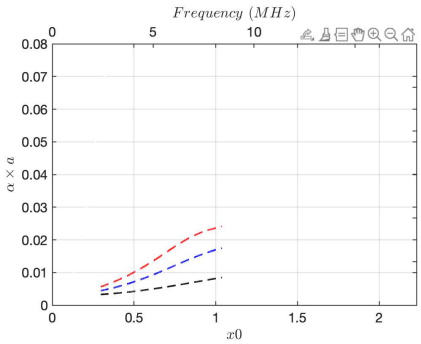

(b) Attenuation coefficient: DM1 inclusion ($C_p^{DM1} = 2400\ m/s$)

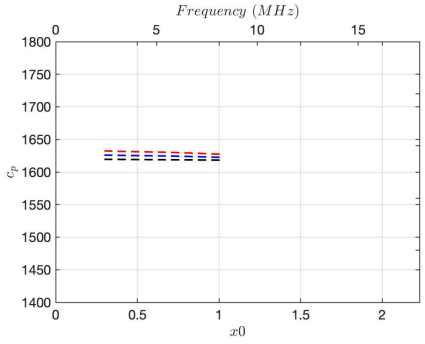

(c) Phase velocity: DM2 inclusion ($C_p^{DM2} = 2200\ m/s$)

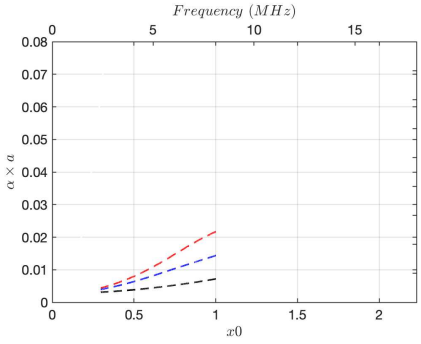

(d) Attenuation coefficient: DM2 inclusion ($C_p^{DM2} = 2200\ m/s$)

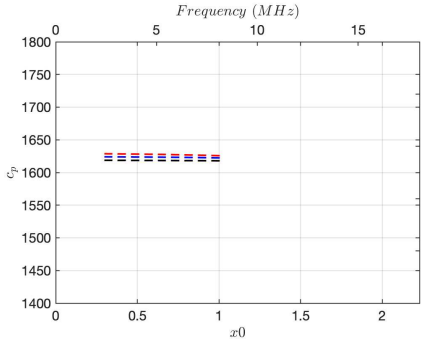

(e) Phase velocity: DM3 inclusion ($C_p^{DM3} = 2000\ m/s$)

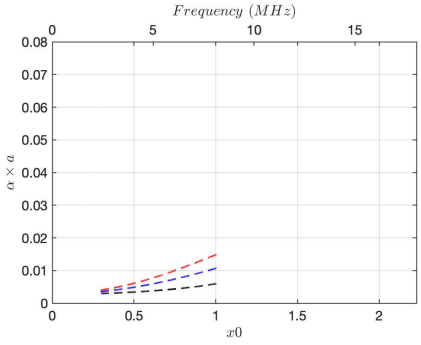

(f) Attenuation coefficient: DM3 inclusion ($C_p^{DM3} = 2000\ m/s$)

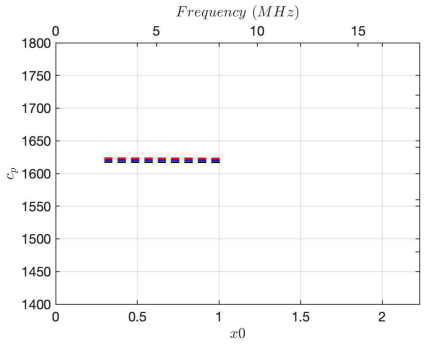

(g) Phase velocity: DM4 inclusion ($C_p^{DM4} = 1800\ m/s$)

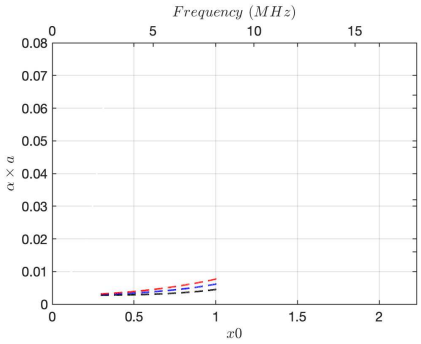

(h) Attenuation coefficient: DM4 inclusion ($C_p^{DM4} = 1800\ m/s$)

Figure 3.14. Numerical phase velocity and attenuation coefficient for the 3D-printed composite material with the radius size of $a = 100\mu$m, with different area fractions: $\phi = 1\%$ (black), $\phi = 3\%$(blue), $\phi = 5\%$ (red)

3.4 Conclusions

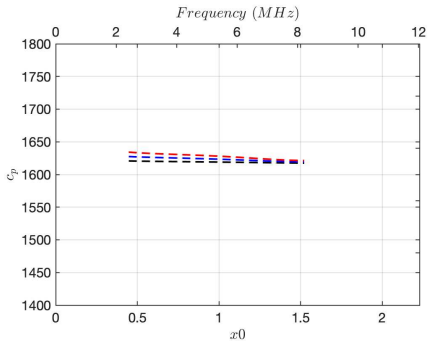

(a) Phase velocity : DM1 inclusion ($C_p^{DM1} = 2400\ m/s$)

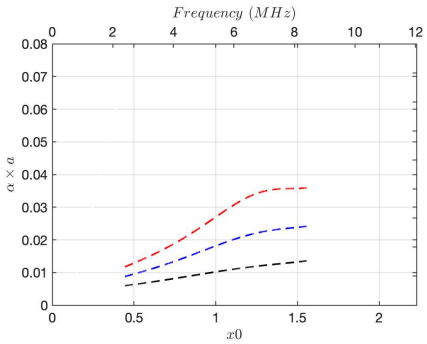

(b) Attenuation coefficient: DM1 inclusion ($C_p^{DM1} = 2400\ m/s$)

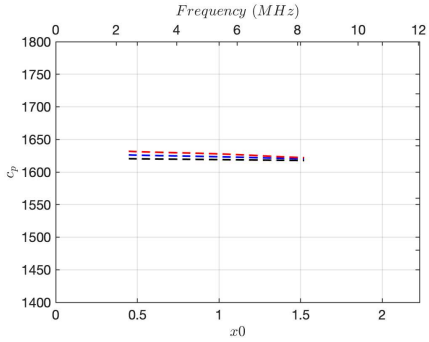

(c) Phase velocity : DM2 inclusion ($C_p^{DM2} = 2200\ m/s$)

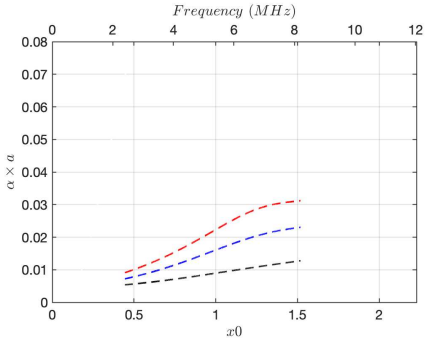

(d) Attenuation coefficient: DM2 inclusion ($C_p^{DM2} = 2200\ m/s$)

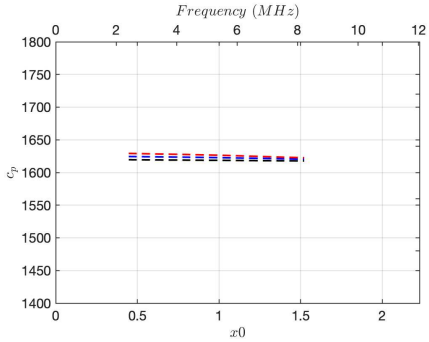

(e) Phase velocity : DM3 inclusion ($C_p^{DM3} = 2000\ m/s$)

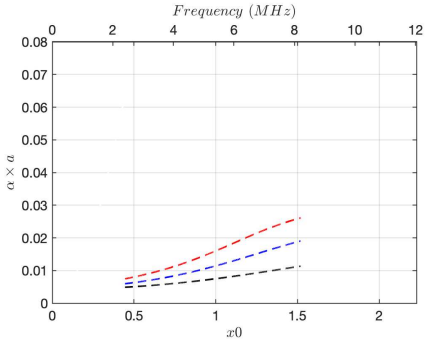

(f) Attenuation coefficient: DM3 inclusion ($C_p^{DM3} = 2000\ m/s$)

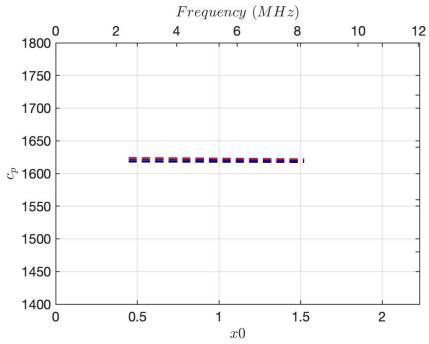

(g) Phase velocity : DM4 inclusion ($C_p^{DM4} = 1800\ m/s$

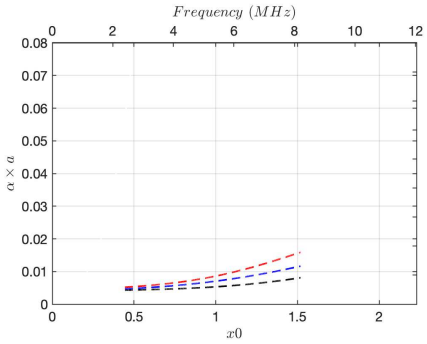

(h) Attenuation coefficient: DM4 inclusion ($C_p^{DM4} = 1800\ m/s$

Figure 3.15. Numerical phase velocity and attenuation coefficient for the 3D-printed composite material with the radius size of $a = 150\mu$m*, with different area fractions:* $\phi = 1\%$ *(black),* $\phi = 3\%$*(blue),* $\phi = 5\%$ *(red)*

The objective of this chapter was to better understand the scattering characteristics exhibited by the matrix-inclusion microstructure of tissue-mimicking 3D-printed materials when subjected to ultrasonic waves. An analytical framework has been recalled for the elastic wave propagation in a matrix-

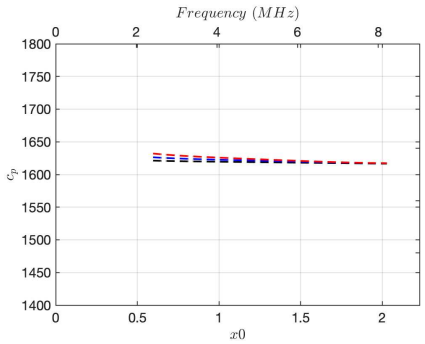

(a) Phase velocity : DM1 inclusion ($C_p^{DM1} = 2400\ m/s$)

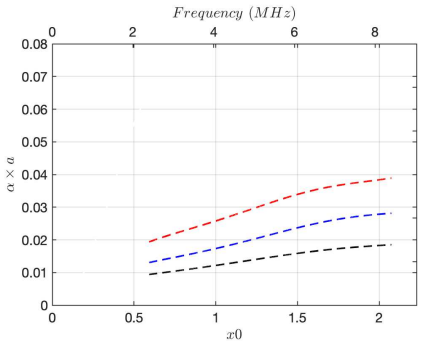

(b) Attenuation coefficient: DM1 inclusion ($C_p^{DM1} = 2400\ m/s$)

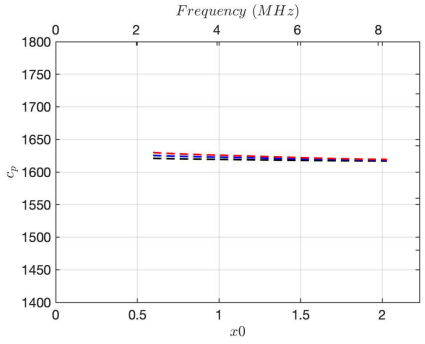

(c) Phase velocity : DM2 inclusion ($C_p^{DM2} = 2200\ m/s$)

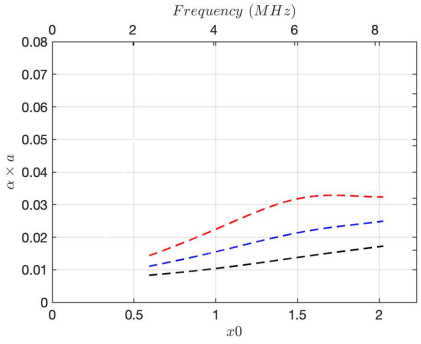

(d) Attenuation coefficient: DM2 inclusion ($C_p^{DM2} = 2200\ m/s$)

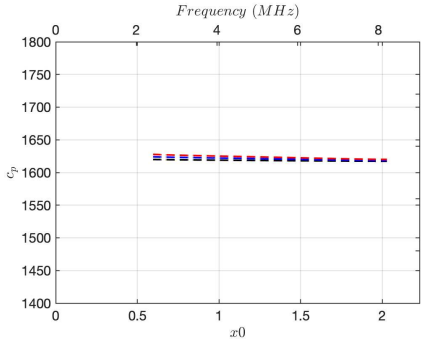

(e) Phase velocity : DM3 inclusion ($C_p^{DM3} = 2000\ m/s$)

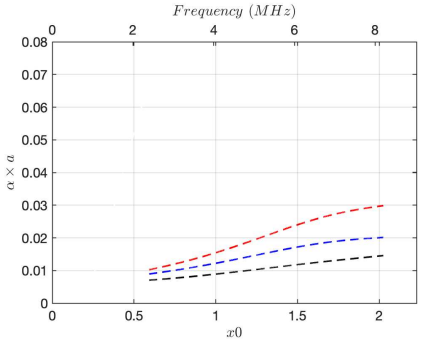

(f) Attenuation coefficient: DM3 inclusion ($C_p^{DM3} = 2000\ m/s$)

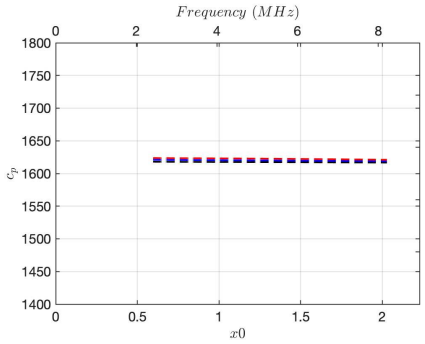

(g) Phase velocity : DM4 inclusion ($C_p^{DM4} = 1800\ m/s$

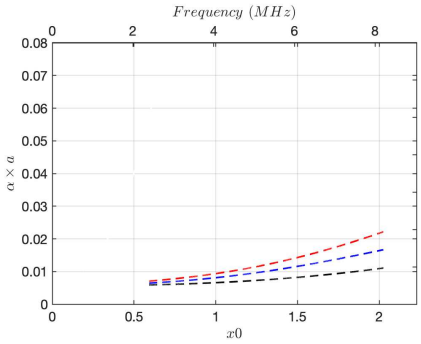

(h) Attenuation coefficient: DM4 inclusion ($C_p^{DM4} = 1800\ m/s$

Figure 3.16. Numerical phase velocity and attenuation coefficient for the 3D-printed composite material with the radius size of $a = 200\mu$m, with different area fractions: $\phi = 1\%$ (black), $\phi = 3\%$(blue), $\phi = 5\%$ (red)

inclusion composite with randomly distributed circular/spherical inclusions. Within this framework, the composite is replaced with an effective homogeneous material, and an effective harmonic wave solution approximates the scattering of the wave caused by inclusions. This approximation is based

on a single scattering assumption. The elastic properties of the effective medium were obtained within this analytical framework, as well as the phase velocity and attenuation coefficient. Regarding numerical modeling, a finite element-based numerical approach has been introduced to calculate the phase velocity and attenuation coefficient of the considered matrix-inclusion composites. Both analytical and numerical results were given, studied, and compared for different area fractions and sizes of inclusions. A good agreement was observed for area fractions less than 10%. However, it was observed that the analytical/numerical discrepancy increases with increasing area fraction and decreasing inclusion size. By reducing the size or increasing the area fraction of the inclusions, it is more challenging for the numerical post-processing tool is not able to estimate the attenuation coefficient correctly. A first quantitative study has been given based on the average minimum distances between inclusions, highlighting the need to add statistical data other than the volume fraction in the analytical models when the volume fraction increases, or the inclusion size decreases. Finally, the numerical method was used to calculate the attenuation coefficient for a 3D-printed composite with a quasi-incompressible matrix. The analytical framework cannot be used since the wavelength of the propagating shear wave is considerably smaller than the printed inclusions. The phase velocity and attenuation curves of the 3D-printed composite as a function of the frequency have been obtained numerically for composites with various area fractions, diameter sizes, and material properties of the inclusion phase.

Chapter 4
Ultrasonic imaging of the synthetic 3D-printed material

Contents

This chapter examines how the microstructure's characteristics affect the echogenicity of 3D-printed tissue-mimicking materials. The first section introduces a simplified numerical model of the ultrasonic transducer to initiate the wave in the numerical simulation. Then, the developed coupled acoustic-elastic solver is used to perform the numerical simulation and investigate the impact of the microstructure, such as the area fraction and diameter size of the inclusion, on the resulting B-mode image. The resulting B-mode images are quantitatively studied and compared to each other.

The second section is dedicated to an approach for numerical modeling of the phased array transducer using the time delays introduced in the first chapter. A preliminary study is also performed to consider the curvature of the structure and reconstruct sector B-mode images.

The third section of the chapter is dedicated to a morphological study of the shape of the microstructure and the deviation of the final printed inclusions from the input spherical shape delivered to the 3D printer. The actual shape of the inclusions is significant in the scattering of the ultrasonic wave and the echogenicity of the printed material. The micro-CT, 2D, and 3D images of the 3D-printed inclusions are obtained, and image segmentation is employed to acquire binary images containing the matrix and inclusion phases. In the final chapter, we incorporate the actual shape of the inclusion in

the numerical simulations. Then the circular shape of the inclusion is replaced with the image of different sections of the acquired 3D image of the inclusion, and the numerical simulation with structured mesh is launched to obtain the corresponding phase velocity and attenuation coefficient.

4.1 Echogenicity of the 3D-printed microstructure: a multiparametric study

The proposed coupled acoustic-elastic solver is used here to simulate ultrasonic wave propagation in the simplified 2D representation of the 3D-printed material's microstructure. The objective is to examine the influence of two key microstructure parameters: the area fraction and size of inclusion, on the echogenicity of the resulting ultrasonic imaging.

For that purpose, a simplified model of the printed microstructure already explained in section 1.1.2 is considered here. This model consists of a rectangular domain made of a matrix with circular inclusions (see Figure 4.1a). In this configuration, we neglect the presence of the surrounding shell of RTOP material on the top and bottom of the composite material. Furthermore, the 3D-printed microstructure is assumed to be submerged in water, just as in the actual ultrasonic imaging process, where tissues are usually surrounded by a fluid (blood or water). Hence, a water layer is added above and below the solid material layer (Figure 4.1a). The geometry size of the modeled domain is 6mm $\times$ 4.5mm, of which the thickness of each water layer is 1mm, and the thickness of the 3D-printed material is 2.5mm. As depicted in Figure 4.1a, a non-reflecting boundary condition is applied to the sides and bottom edge of the rectangular geometry.

The ultrasonic wave is initiated in the domain with a simple sequential linear array transducer model, whose working principle is elaborated in section 1.2.2. To simplify the process, it is assumed that the aperture size is that of a single piezoelectric element, meaning that the ultrasonic wave each transmitted and received by just a single piezoelectric element at each transmit/receive cycle. Hence, the total length of the image is equivalent to the size of the transducer. The final image is composed of n different lines, with n corresponding to the total number of elements in the transducer. In the examples presented in this section, the transducer is assumed to have a length of $5.6mm$ and is composed of $n = 28$ piezoelectric elements, each with a size of 200µm. We have also used the vertical component of the velocity signal recorded on the transducer to post-process and reconstruct the final B-mode image.

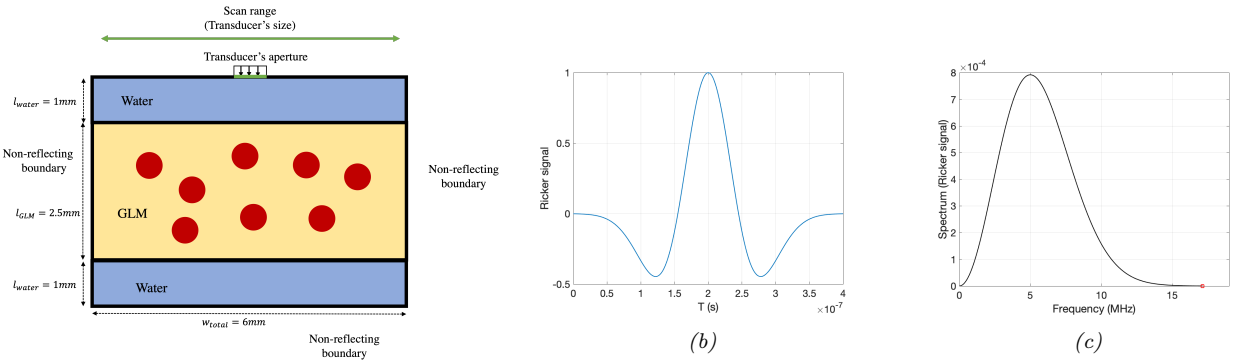

(a) *(b)* *(c)*

Figure 4.1. (a) 2D representative geometry of the 3D-printed microstructure, submerged in water and boundary conditions; (b) Initial Ricker pulse generated by the transducer's piezoelectric element, and (c) its frequency content

The ultrasonic pulse generated at the transducer is chosen to be a Ricker wavelet with the frequency content centered at $f_{max} = 5MHz$, and a cutoff frequency of $f_c = 17MHz$ (Figure 4.1b and .Figure 4.1c). The material properties and corresponding wavelengths of the ultrasonic wave in the

ultrasonic imaging frequency range $(3-7MHz)$ are presented in Table 4.1. One can observe that in the GLM matrix, which is a quasi-compressible material, the propagation speed of the shear wave is two orders of magnitude smaller than that of the compression wave. Therefore, an extremely small element size is required to capture the shear wave in the matrix, making the numerical simulation extremely computationally expensive. In addition, the shear wave generated at the matrix/inclusion interface propagates very slowly in the matrix and needs much more time to reach the transducer. As a result, we argue that its propagation in the matrix has a negligible impact on the velocity signal recorded by the transducer compared to the compression wave so it can be disregarded. Therefore, the finite element size in the numerical simulations is chosen based on the next shortest wavelength in the domain, the one determined by the shear wave in the inclusion. By selecting the element size of $h = 10\mu$m, we have respectively 10 and 18 elements per this shortest wavelength at the cutoff frequency 12.5MHz of the ricker signal and the maximum frequency 7MHz of the ultrasonic imaging frequency range considered in this work. The time step $\Delta t = 0.7\mu$s is chosen to ensure the stability, regarding the stability condition presented in equation (2.100).

Table 4.1. Material properties of the water, quasi-incompressible GLM (matrix), and RTOP (inclusions)

Material	$\rho(kg/m^3)$	$\kappa(GPa)$	$\mu(MPa)$	$c_p(m/s)$	$c_s(m/s)$	$\lambda_p(\mu\text{m})$	$\lambda_s(\mu\text{m})$
Water	1000	2.10	–	1500	–	$[215-500]$	–
GLM	1150	3.10	0.3	1620	17	$[230-540]$	$[2.4-5.6]$
RTOP	1200	6.78	1830	2680	1235	$[380-890]$	$[175-410]$

For the following first example, the quasi-incompressible GLM matrix in the composite is modeled using an equivalent acoustic material, i.e., both quasi-incompressible elastic material and acoustic material have the same compression wave speed (see Table 4.2). The objective is to see whether this modification impacts the velocity signal recorded on the transducer and evaluate the performance of the developed coupled acoustic-elastic solver compared to the pure elastic solver In this precise case. For this purpose, the layer of water is removed, and the transducer is placed directly in contact with the matrix over the entire top boundary (see Figure 4.2a).

Table 4.2. Material properties of the quasi-incompressible GLM matrix, using acoustic and elastic models

Material	$\rho(kg/m^3)$	$\kappa(GPa)$	$\mu(MPa)$	$c_p(m/s)$	$c_s(m/s)$	$\lambda_p(\mu\text{m})$	$\lambda_s(\mu\text{m})$
GLM (acoustic)	1150	3.03	–	1620	–	$[230-540]$	–
GLM (elastic)	1150	3.10	0.3	1620	17	$[230-540]$	$[2.4-5.6]$

Figure 4.2b shows the vertical component of velocity recorded on the transducer using two different models, and there is an excellent agreement in the results. However, it was observed that by using the coupled solver, the total calculation time is decreased by 19%. The reason is that for the acoustic element in a 2D problem, we have 3 degrees of freedom per node (2 for velocity and 1 for pressure, while for the elastic problem, we have 5 degrees of freedom per node (2 for velocity and 3 for stress). Moreover, the size of the flux matrices on an acoustic-elastic interface is smaller than those on an elastic-elastic interface (see chapter 2). Therefore the coupled acoustic-elastic is faster and less expensive in memory than the elastic solver. This advantage is more pronounced in 3D because, for 3D problems, we have for the acoustic case 4 degrees of freedom per node (3 for velocity and 1 for pressure), whereas

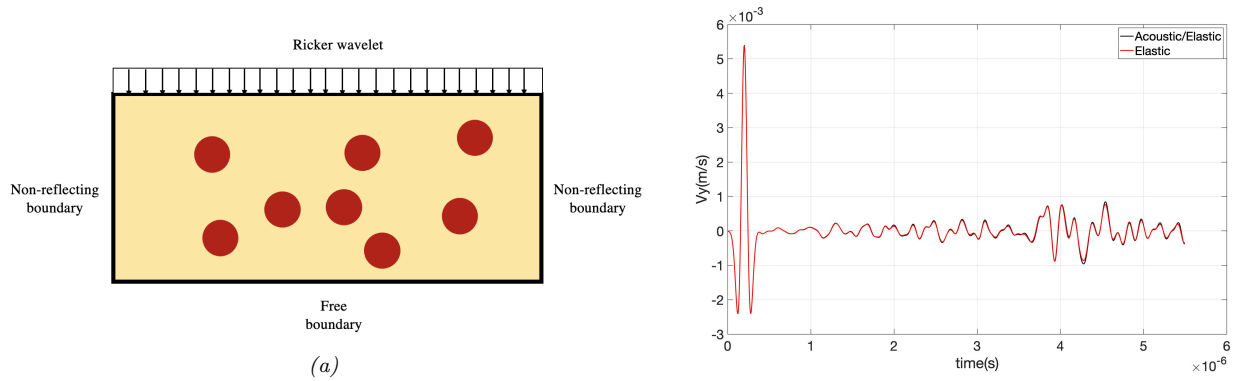

Figure 4.2. (a) Considered geometry and boundary conditions for comparing the elastic and acoustic model of the quasi-incompressible matrix, (b) Comparison of the vertical component of the velocity signal recorded on the transducer, obtained by coupled acoustic-elastic and pure elastic solver

for the elastic case, 9 degrees of freedom per node (3 for velocity and 6 for stress). Hence, we chose to model the quasi-incompressible matrix by its equivalent acoustic medium for all the results presented hereafter.

4.1.1 Reconstructed B-mode images for the 2-phase matrix-inclusion composite

The B-mode images are obtained by a simple post-processing procedure on the vertical component of the velocity signal recorded on the transducer. The amplitude of the reflected echoes is then used to generate an image, with the brightness of each pixel representing the object's reflectivity at that location. The image is displayed in a cartesian format, with parallel scan lines perpendicular to the direction of the ultrasound beam. The gray levels in the presented B-mode images are represented by an 8-bit scale (0-255), where higher values correspond to brighter pixels and lower values correspond to darker pixels.

Here we investigate the impact of the area fraction (ϕ) and the diameter (D) of circular inclusions on the echogenicity of a single layer of 3D-printed composites (Figure 4.1a). For that purpose, the B-mode images are obtained for four different area fractions of inclusions: $\phi_1 = 1\%, \phi_2 = 3\%, \phi_3 = 5\%$ and $\phi_4 = 10\%$ and three different inclusion diameters $D_1 = 200\mu$m, $D_2 = 300\mu$m and $D_3 = 400\mu$m.

In the reconstruction of B-mode images, a series of post-processing steps are applied to the raw received signal from each piezoelectric element:

- Obtain the envelope of the received signal;
- Convert the amplitude to gray levels (G), with higher amplitudes resulting in brighter points;
- Convert the time to the distance of the reflector from the transducer by multiplying the time by the propagation speed of the compression wave in water, $c_{p,water} = 1500m/s$, and dividing by two. This is done to account for the wave traveling to the object and back to the transducer.

Figure 4.3 shows these steps applied to the raw signal obtained for a piezoelectric element for the case of $\phi = 10\%$ and $D = 200\mu$m. The final image is obtained by assembling all the gray level vectors, where the vertical axis shows the distance of the reflector from the transducer, and the lateral axis shows the total scan range, which in this paper is the size of the transducer.

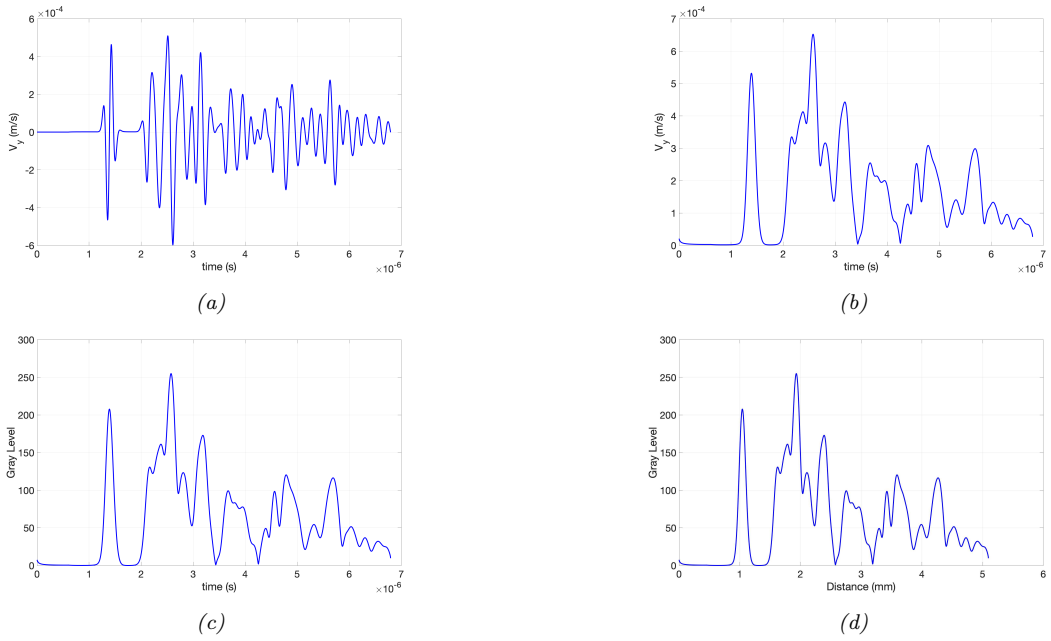

Figure 4.3. Post-processing steps for reconstruction of the B-mode medical image applied to a signal obtained for a single piezoelectric element for the case of $\phi = 10\%$ and $D = 200\mu$m (a) raw received signal, (b) extracted envelope, (c) converted to gray levels ranging from 0 to 255, and (d) converting time to distance of the reflector from the transducer.

As an example, Figure 4.4 depicts two different geometries and the corresponding B-mode images (all the numbers are in millimeters). One can observe that the water-matrix interface at the distance of 1mm is perfectly depicted. A horizontal dashed red line is also added to the B-mode image to show the ideal location of the matrix-water interface at the distance of 3.5mm. This interface might not be easily distinguishable in some cases, but it is very important to obtain precisely the thickness of the imaged layer. Figure 4.5 presents the reconstructed B-mode images for all the mentioned area fractions and sizes of inclusions. It can be observed that as the area fraction of the inclusion decreases, the matrix-water interface becomes more visible. Nonetheless, the interface seems nearer to the transducer than its actual position. This is because the post-processing steps assume the medium in which the wave is propagating is water and therefore calculate distances based on the speed of sound in water. Since the speed of sound in the matrix is faster than that of water, the wave travels faster in the matrix and appears thus closer to the transducer.

Upon analyzing the B-mode images, it can be observed that an increase in the area fraction of the inclusions and a decrease in the size of the inclusion leads to an improvement in the material's echogenicity to ultrasound waves. However, this makes it more challenging to distinguish the matrix-water interface, located at a distance of $3.5mm$ from the transducer. Therefore, it is difficult to see the material's actual thickness, which is an important objective.

To have a more precise quantitative measure of echogenicity, the average gray level over the region of interest (ROI), which corresponds to the actual thickness of the material, is chosen as a parameter to measure the reflectivity of the material to ultrasound waves, which is defined as follows:

$$\overline{G}_{ROI} = \frac{1}{N_{piezo} \times (d_{bottom} - d_{top})} \sum_{i=1}^{N_{piezo}} \int_{d_{top}}^{d_{bottom}} G(x_i, y) dy \tag{4.1}$$

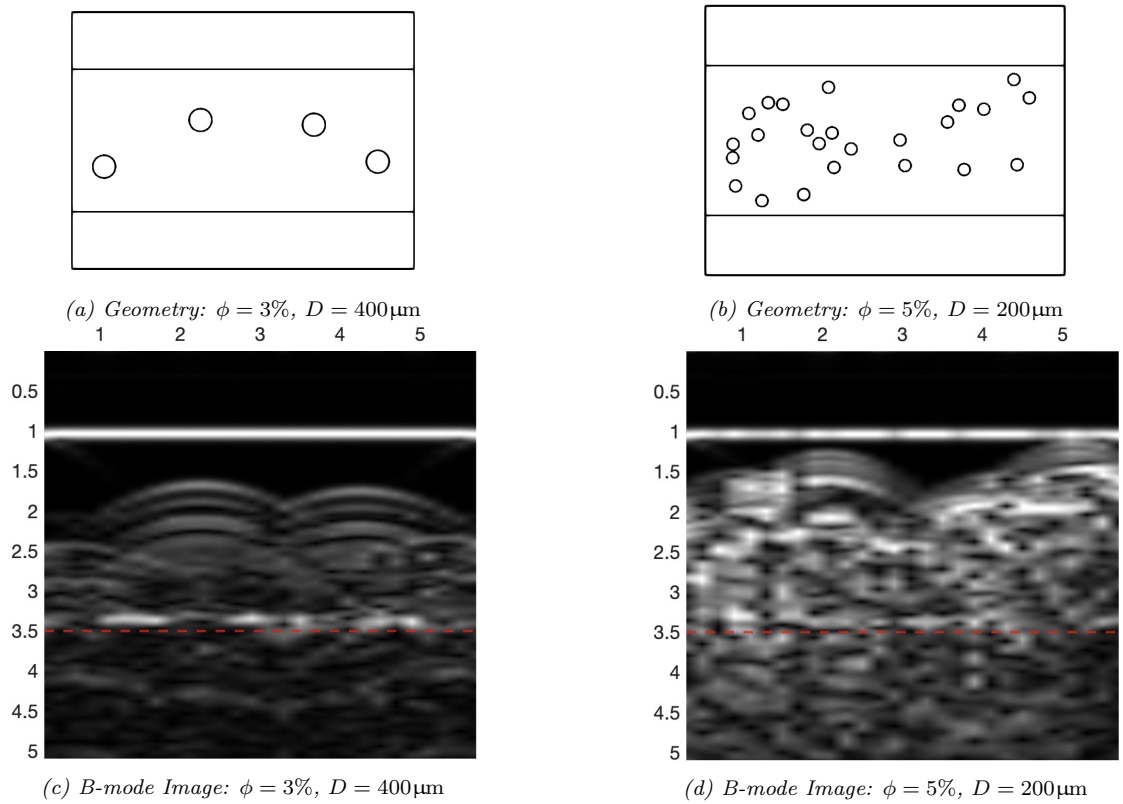

(a) Geometry: $\phi = 3\%$, $D = 400\mu m$

(b) Geometry: $\phi = 5\%$, $D = 200\mu m$

(c) B-mode Image: $\phi = 3\%$, $D = 400\mu m$

(d) B-mode Image: $\phi = 5\%$, $D = 200\mu m$

Figure 4.4. Two different configurations with various area fractions and diameter sizes of the inclusions and corresponding B-mode images (all the sizes are in millimeters)

where $d_{top} = 1$mm and $d_{bottom} = 3.5$mm are respectively the distance from the transducer to the top water-matrix interface and the bottom matrix-water interface. Moreover, the average gray level of the region below the bottom matrix-water interface, hereafter named the region of the residual signal (RORS), is calculated as follows:

$$\overline{G}_{RORS} = \frac{1}{N_{piezo} \times (d_{total} - d_{bottom})} \sum_{i=1}^{N_{piezo}} \int_{d_{bottom}}^{d_{total}} G(x_i, y) dy \tag{4.2}$$

where the total distance is $d_{total} = T_{total} \times c_{p,water}/2$. The ratio of $\overline{G}_{RORS}$ to $\overline{G}_{ROI}$ is used as another important metric to indicate how well the thickness of the material can be distinguished.

Figure 4.6a and Figure 4.6b show the average of the gray levels $\overline{G}_{ROI}$ with respect to the area fraction of the inclusions and the diameter size, respectively. These figures show an increasing trend in the average gray level when the area fraction is increased for all three sizes. It also indicates that for a given area fraction of inclusion, the average gray level increases as the size of the inclusions decreases. However, the same behavior is observed for the $\overline{G}_{RORS}$ as illustrated in Figure 4.6c and Figure 4.6d, which is not desirable.

Looking at the ratio of the $\overline{G}_{RORS}$ to the $\overline{G}_{ROI}$, we notice that it increases for $D = 200\mu m$ and $D = 300\mu m$ as the area fraction is raised. On the other hand, for $D = 400\mu m$, the ratio decreases when we increase the area fraction from 5 to 10, which means that the actual thickness of the material is more recognizable. This behavior could be observed in Figure 4.6e and Figure 4.6f.

The same calculations are repeated for another batch of samples with $\phi = 10\%$, and the results

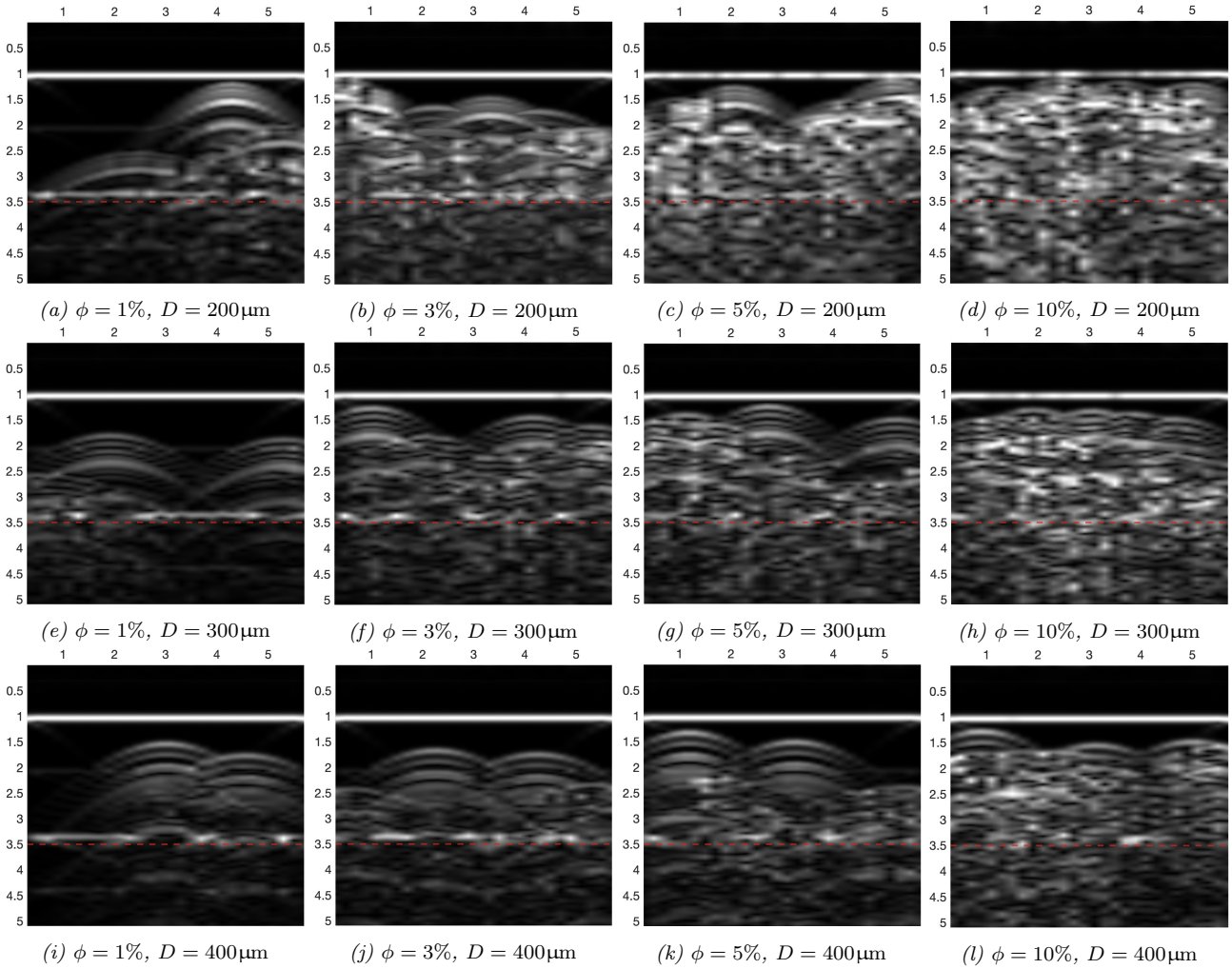

(a) $\phi = 1\%$, $D = 200\mu m$ *(b)* $\phi = 3\%$, $D = 200\mu m$ *(c)* $\phi = 5\%$, $D = 200\mu m$ *(d)* $\phi = 10\%$, $D = 200\mu m$

(e) $\phi = 1\%$, $D = 300\mu m$ *(f)* $\phi = 3\%$, $D = 300\mu m$ *(g)* $\phi = 5\%$, $D = 300\mu m$ *(h)* $\phi = 10\%$, $D = 300\mu m$

(i) $\phi = 1\%$, $D = 400\mu m$ *(j)* $\phi = 3\%$, $D = 400\mu m$ *(k)* $\phi = 5\%$, $D = 400\mu m$ *(l)* $\phi = 10\%$, $D = 400\mu m$

Figure 4.5. Reconstructed B-mode images for matrix-inclusion configuration without the surrounding RTOP shell, with area fractions of inclusions 1%, 3%, 5%, *and* 10%

are presented in Table 4.3. According to this table, the average gray levels are similar for two different batches, independent of the inclusions' distribution. However, a more rigorous statistical investigation is required to study different random distributions of inclusions for a given area fraction and size of inclusions.

Table 4.3. Comparison of average gray levels for two different batches of samples with $\phi = 10\%$

Diameter Size	$D = 200\mu m$		$D = 300\mu m$		400μm	
	1st batch	2nd batch	1st batch	2nd batch	1st batch	2nd batch
$\overline{G}_{ROI}$	101	100	81	81	70	73
$\overline{G}_{noise}$	71	72	58	58	42	43
$\frac{\overline{G}_{Noise}}{\overline{G}_{ROI}}$	0.70	0.72	0.72	0.72	0.60	0.59

4.1.2 Reconstructed B-mode images for the sandwich matrix-inclusion composite

Here, we investigate the echogenicity of the sandwich microstructure presented in section 1.1.2, as depicted in Figure 4.7. As discussed earlier in section 1.1.2, the outer and inner protective shells made of PolyJet materials (excluding GLM) are crucial to prevent the destruction of the composite

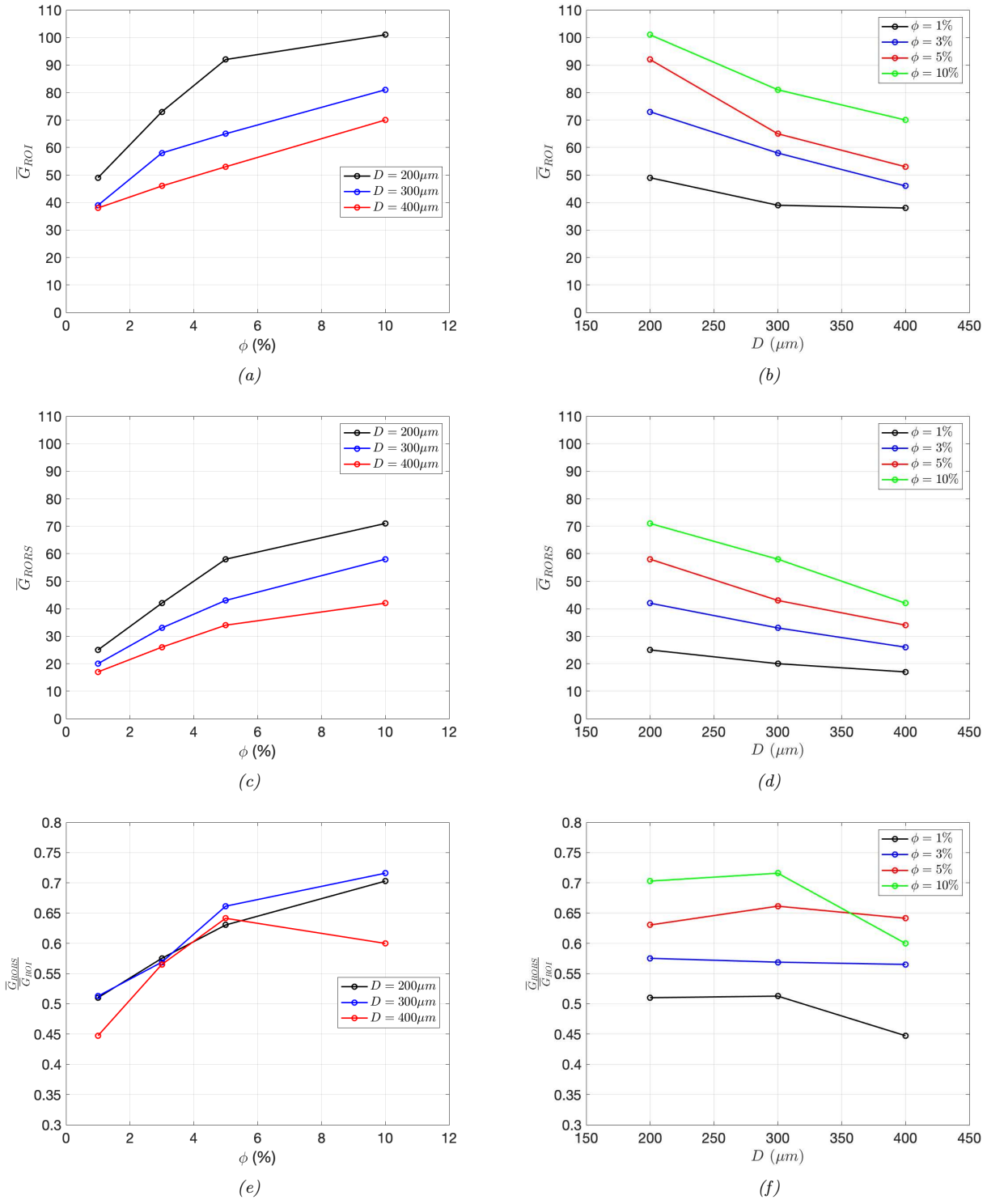

Figure 4.6. Quantitative analysis of the average gray levels for the matrix-inclusion composite: (a) $\overline{G}_{ROI}$, (c) $\overline{G}_{RORS}$, and (e) $\frac{\overline{G}_{RORS}}{\overline{G}_{ROI}}$ with respect to the area fraction ϕ; (b) $\overline{G}_{ROI}$, (d) $\overline{G}_{RORS}$, and (f) $\frac{\overline{G}_{RORS}}{\overline{G}_{ROI}}$ with respect to the inclusion's diameter D

microstructure. However, we require the softest possible material to maximize the energy transmitted through the water/PolyJet interface and into the interior microstructure by minimizing the difference in acoustic impedances. To achieve this, the top layer is made of Digital Material (DM) with a propagation speed of $C_p = 1865\ m/s$ and a density of $\rho = 1200\ kg/m^3$. The thickness of these added

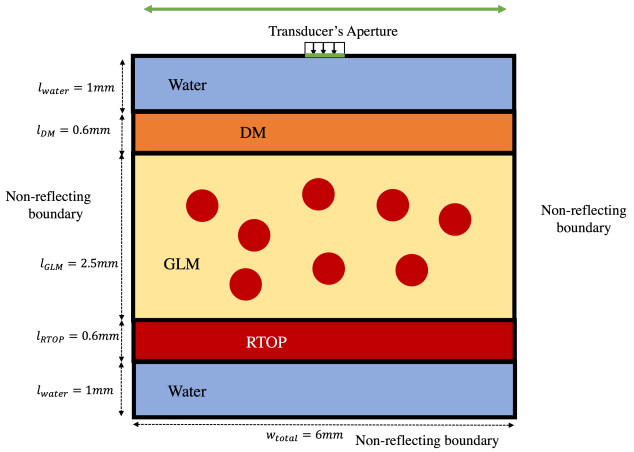

Figure 4.7. Schematic illustration of the sandwich configuration in the presence of water

layers is assumed to be 0.6mm. However, we have chosen to make the inclusions and the bottom layer of the protective shell using the RTOP material to enhance the echogenicity and to facilitate the differentiation of the second interface of the material with water.

The same model of the transducer is used in this section, as well as all the other numerical setups, including the thickness of the matrix and water layers, boundary conditions, element size, and the time step. Using the same B-mode image reconstruction algorithm, the resulting images for different area fractions and diameter sizes of the inclusions are illustrated in Figure 4.8. The dashed red lines in the figures illustrate the expected position of the different interfaces from the top: the water/DM, the DM/GLM, the GLM/RTOP, and the RTOP/water interfaces.

Once again, here we calculate the average gray level of the region of interest $\overline{G}_{ROI}$ according to the equation (4.1), where this time $d_{top} = 1$mm and $d_{bottom} = 4.2$mm. Similarly, $\overline{G}_{RORS}$ is also calculated based on the equation (4.2), and the ratio between these two parameters is also used as a metric to perform a quantitative comparison.

Similar to the previous section, Figure 4.9a and Figure 4.9b depicts the variation of the average gray levels ($\overline{G}ROI$) of the sandwich microstructure as a function of the area fraction and diameter size of the inclusions, respectively. The results indicate an increasing trend in the average gray level as the area fraction of the inclusions increases for all three sizes considered. Moreover, it is observed that for a given area fraction of inclusions, the average gray level increases with decreasing inclusion size. However, this behavior is also observed for $\overline{G}RORS$, as presented in Figure 4.9c and Figure 4.9d, which is not a desirable outcome.

In Figure 4.9e and Figure 4.9f, the ratio of the average gray levels $\overline{G}RORS$ to $\overline{G}ROI$ is examined. It can be observed that there is no clear trend for the ratio of average gray levels. For the inclusion diameter of $D = 200\mu$m, the ratio slightly increases when the area fraction is increased from 1% to 3% and remains constant for higher area fractions. However, for $D = 300\mu$m and $D = 400\mu$m, the ratio decreases after reaching 3% and 5% area fractions, respectively. This suggests that the thickness of the material becomes more distinguishable at higher area fractions. To obtain a more precise analysis, it may be necessary to perform simulations for more inclusion sizes and area fractions to achieve more reliable results.

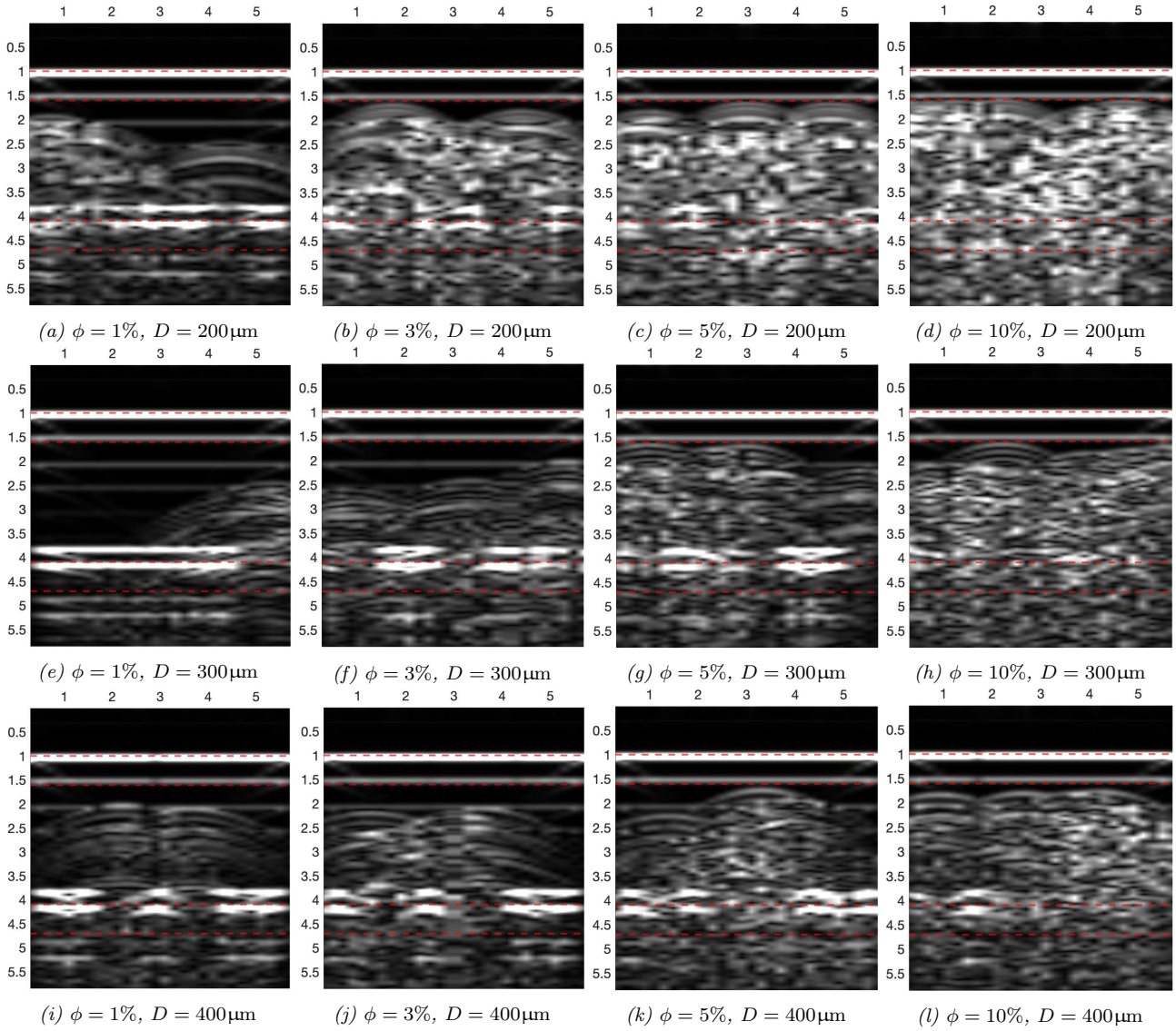

(a) $\phi = 1\%$, $D = 200\mu m$ *(b)* $\phi = 3\%$, $D = 200\mu m$ *(c)* $\phi = 5\%$, $D = 200\mu m$ *(d)* $\phi = 10\%$, $D = 200\mu m$

(e) $\phi = 1\%$, $D = 300\mu m$ *(f)* $\phi = 3\%$, $D = 300\mu m$ *(g)* $\phi = 5\%$, $D = 300\mu m$ *(h)* $\phi = 10\%$, $D = 300\mu m$

(i) $\phi = 1\%$, $D = 400\mu m$ *(j)* $\phi = 3\%$, $D = 400\mu m$ *(k)* $\phi = 5\%$, $D = 400\mu m$ *(l)* $\phi = 10\%$, $D = 400\mu m$

Figure 4.8. Reconstructed B-mode images for the sandwich matrix-inclusion configuration with the surrounding RTOP shell, with area fractions of inclusions 1%, 3%, 5%, *and* 10%

4.1.3 Real B-mode image of the sandwich microstructure

Now we intend to visually compare the actual B-mode image obtained from a Philips X7-2t TEE transducer with the reconstructed B-mode image of a tissue-mimicking microstructure. The Philips X7-2t TEE transducer is a phased array transducer that provides a sector B-mode image of the organs commonly used in cardiovascular interventions. However, by printing a $10 \times 10 \times 50 mm^3$ cube specimen containing the tissue-mimicking microstructure and placing it far from the transducer, we expect to diminish the effect of beam steering and have comparable B-mode images of the microstructure. The cross-section of the printed material, in the presence of water, is illustrated in Figure 4.10, with the water layer, RTOP shell, and GLM matrix having a thickness of 1mm, 0.6mm, and 3mm, respectively. The matrix contains 43 inclusions randomly distributed with a diameter of $D = 300\mu m$, providing an area fraction of $\phi = 10\%$. Figure 4.11a shows the actual geometry used for the numerical simulation, with the exact position and size of the inclusions. The numerical simulation and B-mode image reconstruction approach we used was applied again to obtain a virtual B-mode image, as shown in

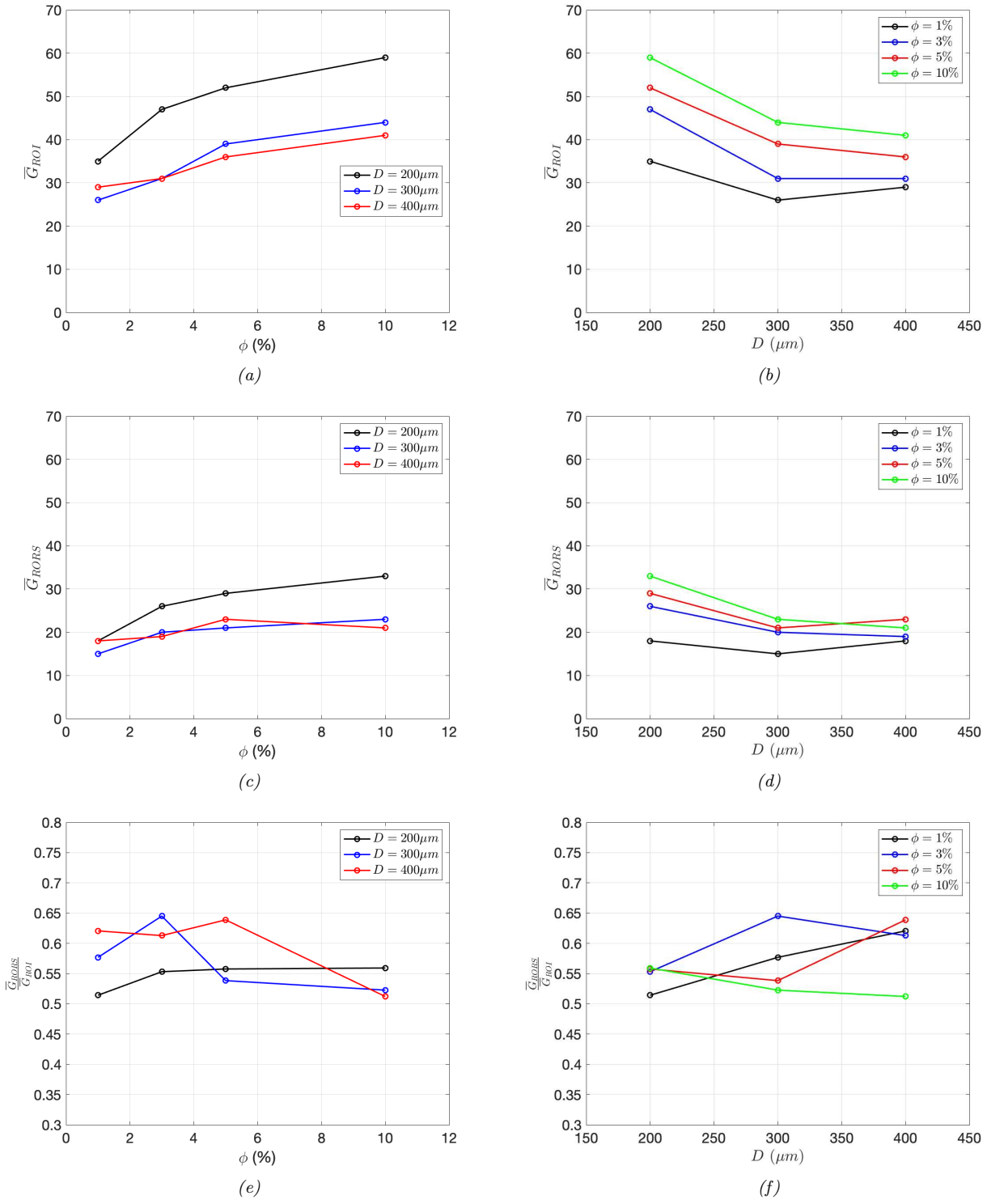

Figure 4.9. Quantitative analysis of the average gray levels for the sandwich microstructure: (a) $\overline{G}_{ROI}$, (c) $\overline{G}_{RORS}$, and (e) $\frac{\overline{G}_{RORS}}{\overline{G}_{ROI}}$ as a function of the area fraction ϕ; (b) $\overline{G}_{ROI}$, (d) $\overline{G}_{RORS}$, and (f) $\frac{\overline{G}_{RORS}}{\overline{G}_{ROI}}$ with respect to the inclusion's diameter D

Figure 4.11b. Meanwhile, we also acquired an actual sector B-mode image using a TEE transducer, as depicted in Figure 4.11c. The 3D-printed specimen is visible at the center of the image in this figure. To examine the specimen more closely, we zoomed in on it in Figure 4.11d, where horizontal red lines indicate the approximate positions of the specimen's interfaces with water. One can observe that in

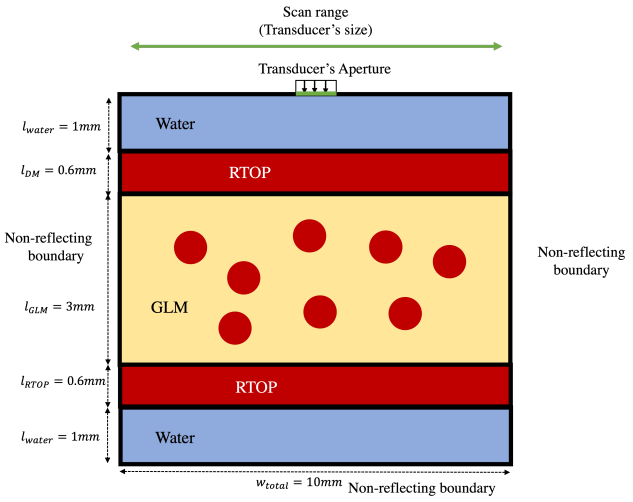

Figure 4.10. Schematic illustration of the cross-section of the 3D-printed sandwich configuration in presence of water

both images, the whole thickness of the material is visible, and the bottom interface with water is not distinguishable. Therefore, the actual thickness of the material could not be estimated either in the real or the virtual image.

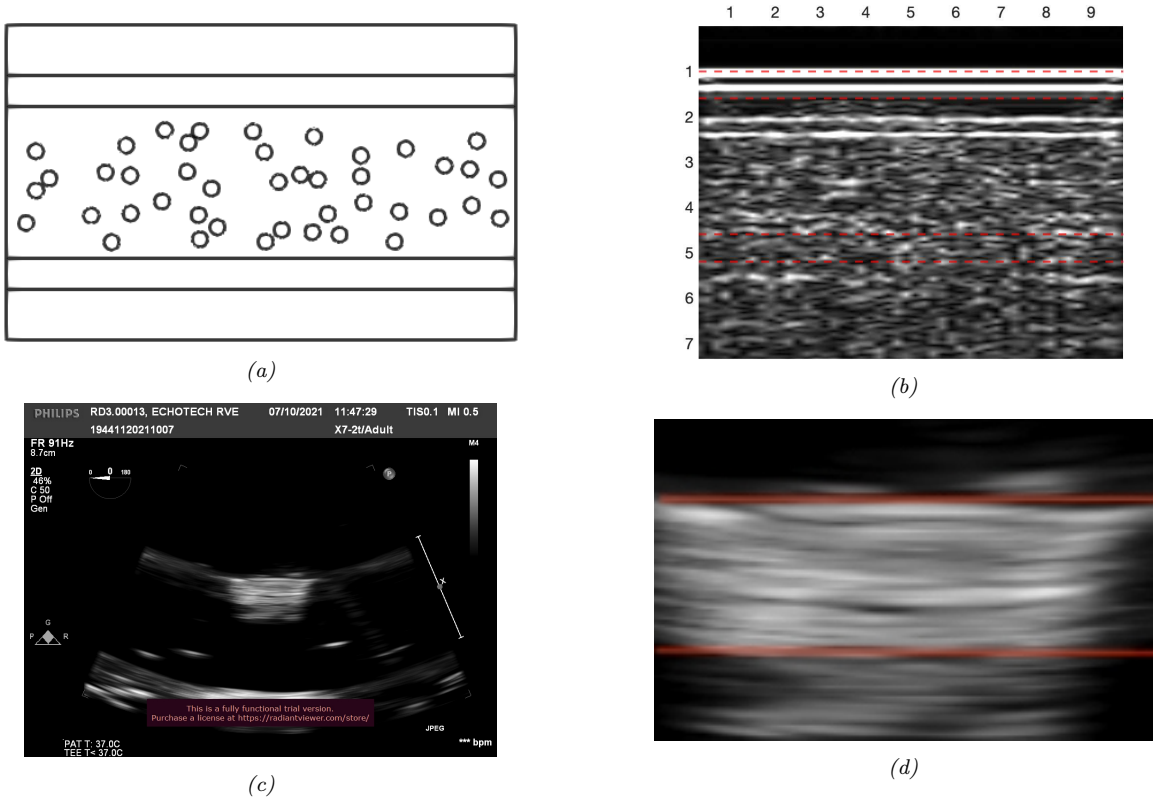

(a) *(b)* *(c)* *(d)*

Figure 4.11. (a) The cross-section of the 3D-printed microstructure with a random distribution of the inclusions for ultrasonic imaging with X7-2t TEE transducer, (b) The virtual B-mode image obtained from the numerical simulation with a simplified reconstruction algorithm, (c) The sector B-mode image obtained for the 3D-printed specimen with sandwich microstructure acquired by X7-2t TEE transducer. (d) More detailed view of the specimen with sandwich microstructure

4.2 Numerical study of the curved sandwich 3D-printed material

Here we perform a preliminary examination of the numerical simulation of ultrasonic wave propagation in curved sandwich composite materials using a numerical model of the phased array transducer.

With knowledge of the frequency range used in ultrasonic imaging and material properties, an estimate can be made of the dominant wavelengths and appropriate element size needed for accurate numerical simulation. However, the required element size is typically much smaller than the characteristic size of an actual organ, making it impossible to perform a 2D numerical simulation on a simplified model of an organ with the proper element size using the OOFE code. Therefore, here we try to reduce the problem size to a manageable extent which can be handled using our code. We also intend to use a numerical model of the phased array transducer instead of the sequential linear transducer. The working principle of the phased array transducer is explained in section 1.2.2. Using a calculated time delay, the transducer is able to steer and focus the ultrasonic wave.

The first step for this problem is to define the smallest representative geometry, starting from a sandwich composite in a circular shape with an outermost radius of $R_{oo} = 7$cm. An analytical study is conducted on the reflection and transmission coefficients in an oblique incidence problem, particularly the water-solid interface problem, to find the maximum incident angle that transmits energy inside the material. This angle is later used to create the geometry of the problem. The incidence angle (θ_i), reflected angle (θ_r), longitudinal transmitted angle (θ_d), and the transverse transmitted angle (θ_s) in an oblique incidence problem are shown in Figure 4.12. From Snell's law, we have :

$$\frac{\sin(\theta_i)}{c_f} = \frac{\sin(\theta_r)}{c_f} = \frac{\sin(\theta_d)}{c_p} = \frac{\sin(\theta_s)}{c_s} \tag{4.3}$$

The reflection coefficient (R), longitudinal transmission coefficient (T_d), and transverse transmission coefficient (T_s) are obtained by solving the following system of equations:

$$\begin{bmatrix} -\cos(\theta_i) & -\cos(\theta_d) & \sin(\theta_s) \\ -Z_f & Z_d\cos(2\theta_s) & -Z_s\sin(2\theta_s) \\ 0 & -Z_s\frac{c_s}{c_f}\sin(2\theta_d) & -Z_s\cos(2\theta_s) \end{bmatrix} \begin{bmatrix} R \\ T_d \\ T_s \end{bmatrix} = \begin{bmatrix} -cos(\theta_i) \\ Z_f \\ 0 \end{bmatrix} \tag{4.4}$$

where $Z_f = \rho_f c_f$, $Z_d = \rho_d c_p$ and $Z_s = \rho_s c_s$ are the acoustic impedances. After obtaining the reflection and transmission coefficients, the corresponding power reflection and transmission coefficients are obtained as follows:

$$R^{power} = R^2, \quad T_d^{power} = T_d^2 \frac{Z_d}{Z_f}\frac{\cos(\theta_d)}{\cos(\theta_i)}, \quad T_s^{power} = T_s^2 \frac{Z_s}{Z_f}\frac{\cos(\theta_s)}{\cos(\theta_i)} \tag{4.5}$$

The power reflection and transmission coefficients represent the rate of energy reflected from or transmitted through the interface at different angles. Figure 4.13 shows the coefficients for three different interfaces as a function of the incident angle: the water-cardiac tissue interface, water-RTOP interface, and water-DM interface. Since the difference in Z_f and Z_d of the water and cardiac tissue is very small, one can see in Figure 4.13a that the wave is almost entirely transmitted through the interface in the small incident angles. However, as the angle of incidence surpasses 40 degrees, the longitudinal

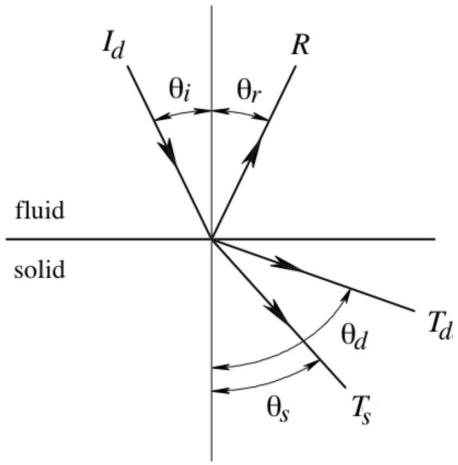

Figure 4.12. General acoustic wave interaction with a fluid-solid interface: reflection and transmission of waves

transmission coefficient begins to decline. At $\theta_i = asin(\frac{c_p^{water}}{c_p^{cardiac}}) = asin(\frac{1500}{1580}) = 70.7°$, the longitudinal transmission coefficient becomes zero for the cardiac tissue, and the reflection coefficient becomes one. This angle is called the "critical angle", denoted as θ_c hereafter. On the other hand, the water-RTOP interface has a different behavior (see Figure 4.13b), and the corresponding critical angle is significantly smaller $\theta_c = sin(\frac{c_p^{water}}{c_p^{cardiac}}) = asin(\frac{1500}{2680}) = 34.0°$ than the case of cardiac tissue. When the incident angle is greater than the critical angle θ_c, the wave undergoes a conversion to the shear wave at the interface, which is then transmitted. The water-DM interface follows a similar pattern to the water-cardiac tissue interface. Still, the difference in propagation speeds is more significant, resulting in a smaller critical angle of $\theta_c = 53.5°$. It can be inferred that using the 3D-printed materials, the material's behavior would be different at angles within the interval defined by the two critical angles: the water-cardiac tissue interface and the water-DM interface. Consequently, the differences in B-mode images obtained by phased array transducers become more significant.

Returning to our numerical problem, we consider a curved sandwich structure with a shell made of the RTOP material, where the GLM layer has a thickness of 3mm, and the RTOP shell has a thickness of 0.6mm. A phased array transducer with a total length of $l_{transducer} = 6$mm is placed on the top of the geometry at a distance of $d_{transducer} = 1$cm from the curved layer, with $n = 25$ piezoelectric element. The total length of the domain is $L_{total} = 4.5$cm, and the curved structure is a circle sector with an outermost radius of $R_{oo} = 7$cm. A Matlab script was developed to determine the points of the geometry using the layer thicknesses and the critical angle θ_c of the water-RTOP interface as input parameters. This is done by calculating the maximum steering angle ($\theta_{s_{max}}$) using the sine law: $\theta_{s_{max}} = \arcsin(\frac{R_{oo} \times \sin(\theta_c)}{R_{oo} + d_{transducer}})$. Then the intersection point of the radial axis of the outermost circle with the maximum steering angle line (yellow dashed line in Figure 4.14) is found. The geometry now can be built by determining the intersection of the maximum steering angle line with the other interfaces (RTOP-GLM, GLM-RTOP, and RTOP-Water), which provides all the necessary points. The schematic geometry of the curved 3D-printed sandwich structure is shown in Figure 4.14.

4.2.1 Numerical modeling of the phased-array transducers

The time delays explained in section 1.2.2 need to be implemented to the piezoelectric elements to simulate the phased array transducer. To steer the wave in a specific direction, such as the angle θ_s,

Table 4.4. Propagation speed and density of the materials used in the analysis of the oblique incidence on a fluid-solid interface

Material	$\rho(kg/m^3)$	$c_p(m/s)$	$c_s(m/s)$
Water	1000	1500	–
Cardiac Tissue	1060	1580	5
RTOP	1200	2630	1235
DM	1200	1865	5

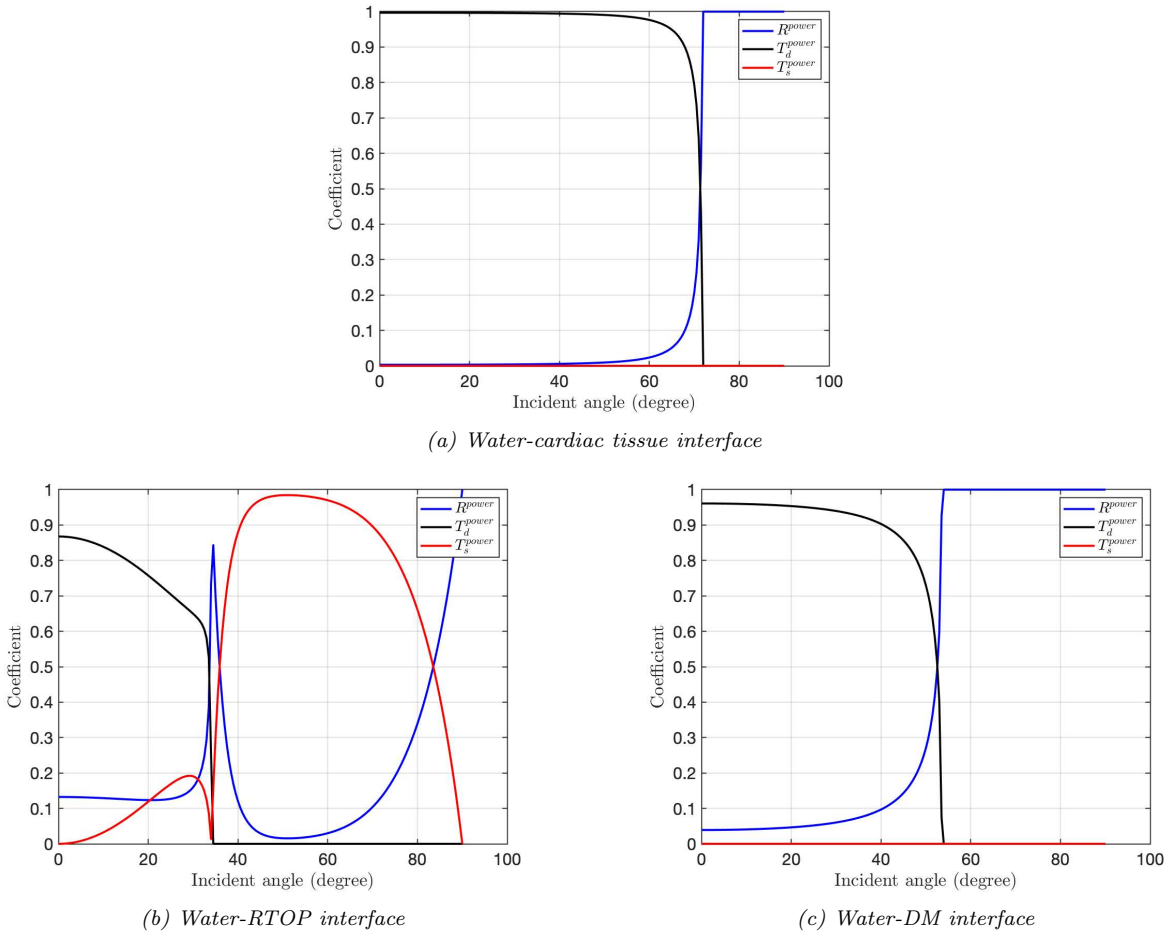

(a) Water-cardiac tissue interface

(b) Water-RTOP interface

(c) Water-DM interface

Figure 4.13. The power reflection and transmission coefficients as a function of the incident angle for three different fluid-solid interfaces

the time delay given by equation (1.1) must be applied to the transducer. The piezoelectric element on the transducer's left side is considered the first element. To illustrate, consider a steering angle of $\theta_s = 10$. At this angle, the first piezoelectric element in the phased array transducer does not require any time delay. However, the following elements require a linear increasing time delay until the last element on the right side of the transducer. Figure 4.15a shows the steering of the wavefront by the angle of $\theta_s = 10$ degree for a ricker signal with $f_{max} = 5$MHz.

Moreover, the focus and steer of the beam could be implemented using the equation (1.2). Unlike the pure steering of the wavefront, the time delay is not increasing linearly and has a more complex behavior. Figure 4.15b shows the focusing and steering of the wavefront by a fixed focal length of $F = 1$cm and the angle of $\theta_s = 10$ degree for a ricker signal with $f_{max} = 1.5$MHz.

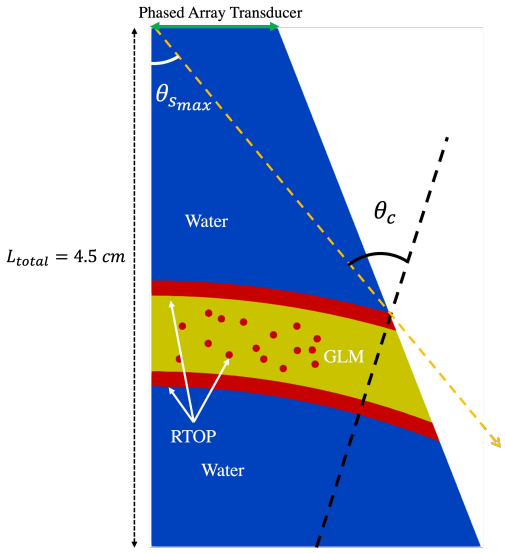

Figure 4.14. The schematic geometry of the curved 3D-printed sandwich structure designed based on the critical angle θ_s of water-RTOP

An initial attempt has been made to reconstruct a sector B-mode image from a numerical simulation by incorporating time delays in the receiving end. Each line of the final B-mode image corresponds to a specific steering angle θ_s and focal length (F), and requires a separate numerical simulation with specific time delays. When the steering angle is changed, the time delays for the new angle and focal length must be recalculated. Here are the steps taken to reconstruct the sector B-mode image:

- For each steering angle, the time delays corresponding to each piezoelectric element are subtracted from the received signal of that same element.
- Now that all the received signals of the piezoelectric elements are in phase, the average signal is calculated for each steering angle.
- The amplitude of the envelope of the average signal is converted to the gray levels, and the time is converted to the distance using the propagation speed for each steering angle.
- The vector of gray levels corresponding to each steering angle is put together in a polar coordinate to generate the sector image.
- A final geometrical correction is applied to move starting point of each vector of gray level from the center of the coordinates to the transducer

However, the obtained results lack precision and fail to represent the underlying structure accurately. The simulation considers a sandwich structure with a curved geometry and 2% area fraction of inclusions with a radius of $a = 150\mu$m (see Figure 4.16a). Figure 4.16b illustrates the interaction of the wavefront with the curved sandwich structure. The reconstructed B-mode image (Figure 4.16c) does not exhibit the desired curvature, and the noise level increases as the incident angle increases. Therefore, a more detailed investigation is necessary to obtain a more accurate sector B-mode image. Notably, the thickness of the layer is not visible in the reconstructed image due to the low maximum frequency of the used Ricker signal ($f_{max} = 1.5$MHz), which was chosen to reduce computational costs.

Once an appropriate reconstruction algorithm is developed, the numerical simulation can be repeated with the desired Ricker frequency.

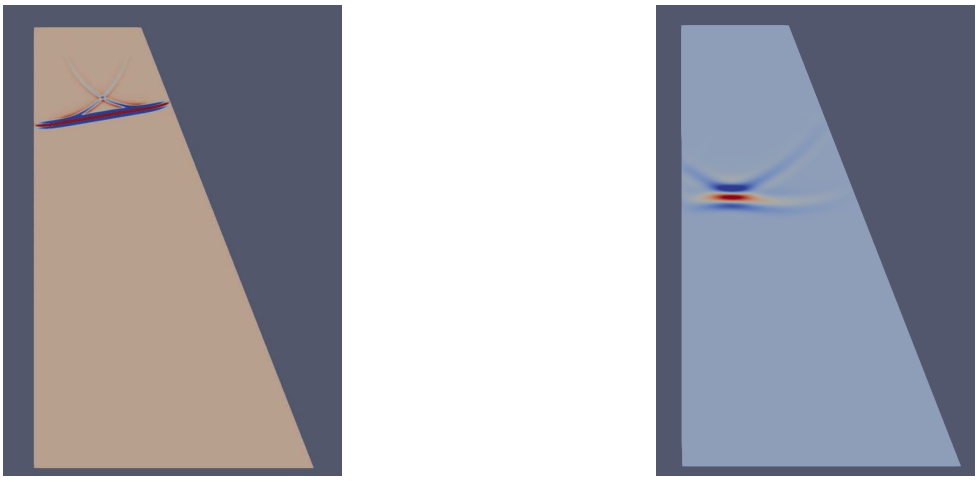

(a) (b)

Figure 4.15. (a) Steering of the wavefront by the angle of $\theta_s = 10$ degree for a ricker signal with $f_{max} = 5$MHz. (b) Focusing and steering of the wavefront by a focal length of $F = 1$cm and the angle of $\theta_s = 10$ degree for a ricker signal with $f_{max} = 1.5$MHz

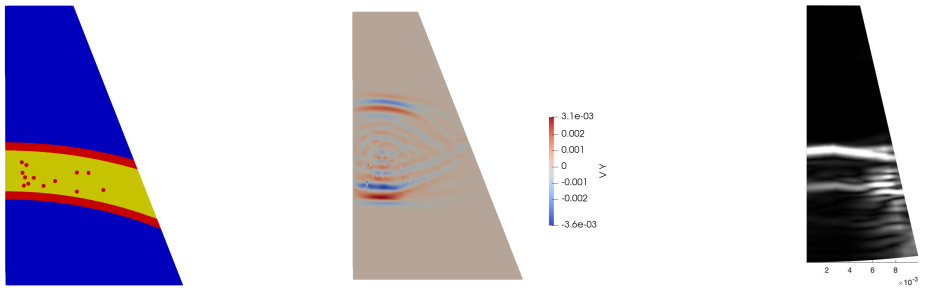

(a) (b) (c)

Figure 4.16. (a) Considered geometry for simulation of the wave generated by the phased array transducer with the curved sandwich structure with 2% area fraction of the inclusions and radius of $a = 150\mu$m(b) interaction of the wavefront with the curved sandwich structure (c) reconstructed sector B-mode image

4.3 The real microstructure of 3D-printed material: experimental study

Until now, all the numerical results have been obtained for the assumed perfect spherical shape inclusions within the matrix-inclusion composite. However, due to the inherent limitations of the 3D-printing process, it is expected that the inclusions are not in a perfectly spherical shape. The geometry of the inclusions may have a vital role in the ultrasonic wave scattering behavior of the microstructure, which impacts the acoustic properties (including phase velocity and attenuation coefficient) and the echogenicity of the 1D-printed synthetic material. As a result, a morphological analysis was undertaken to attain a more in-depth comprehension of inclusion morphology. Furthermore, the study aimed to observe and characterize potential porosities in the final printed microstructure. The porosities have the potential to significantly affect the attenuation coefficient and echogenicity of the material as they act as strong scatterers of ultrasonic waves.

Various microscopy devices, including optical microscopy, SEM (scanning electron microscopy), and TEM (transmission electron microscopy), can be used for 2D physical observations. Micro-CT has gained popularity in medical applications due to the widespread use of 3D printing and the complexity of organ shapes and internal bone structures. Its non-destructive nature, high resolution, and ability to characterize small structures, such as imperfections, porosity, microstructures, and interfaces, have all contributed to its current usage in investigating these features [150–155].

Table 4.5. Imaging techniques, advantages, and disadvantages

Imaging Technique	Resolution	Advantages	Disadvantages
Optical Microscopy	0.2 μm	• study almost anything in its natural colors • unaffected by electromagnetic fields • do not require radiation to operate • allows observing living organisms	• cannot provide three-dimensional rendering • make it challenging to view living internal structures
SEM	0.5 – 4.0 nm	• High resolution • The traceable standard for magnification • Chemical analysis with EDS (energy dispersive spectroscopy)	• Cannot provide 3D rendering • Sensible to the magnetic field
TEM	0.1 – 0.3 nm	• High-quality images • Highest magnification in microscope field • Chemical analysis with EDS	• Laborious sample preparation • Cannot provide 3D rendering
Micro-CT	1 – 150 μm	• High spatial resolution • 2D and 3D format	• Radiation damage • Poor contrast of soft tissues

In this study, we employed optical microscopy and micro-CT to conduct a morphological analysis of the 3D-printed inclusions and examine their actual shape. Optical microscopy provided an initial 2D image of the inclusions, while micro-CT delivered a more comprehensive 2D and 3D representation of the printed inclusions.

4.3.1 Optical microscopy

Using the Biomodex's 3D-printer, a $10 \times 10 \times 55\text{mm}^3$ cubic sample is printed containing a $6 \times 6 \times 9\text{mm}^3$ matrix of inclusions in the center (see Figure 4.17a). The outer shell and inclusions were printed using RTOP material, filling the box with GLM material. The shell was 0.6mm thick, and the inclusions were 300µm in diameter, with a center-to-center spacing of 1mm.

The observation is performed using the Optika B-159 optical microscope, with a magnification of x40 (ocular magnification x10 and achromatic objectives x4). Figure 4.18 shows the obtained 2D optical microscopy image for one of the inclusions. As one can see, the shape of the inclusion is far

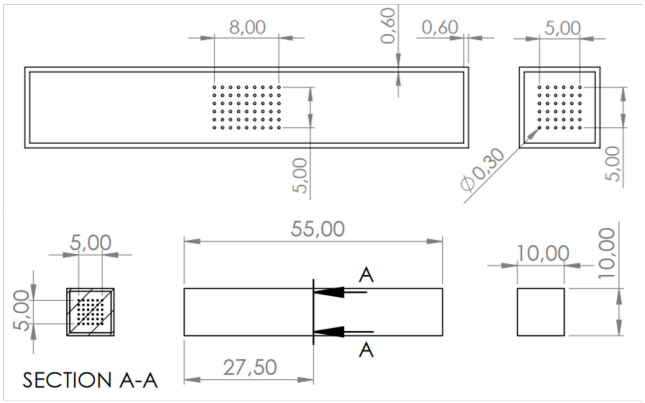

(a)

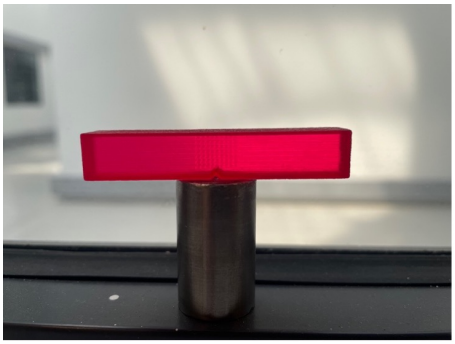

(b)

Figure 4.17. (a) Two-dimensional drawing of the 3D-printed specimen's CAD file used for observation with an optical microscope (b) The final 3D-printed specimen.

from the expected circular cross-section and more similar to an ellipse with a major diameter of D_1 and a minor diameter of D_2. By measuring these major and minor diameters and averaging over four different inclusions, we have obtained $\overline{D_1} = 295 \pm 13$mm and $\overline{D_2} = 231 \pm 8$mm. One can see that the major diameter is close to the input diameter of the inclusion in the CAD file 300µm, but the minor radius is 23% smaller. This image also illustrates the multilayered 3D-printing process, as the layers with a specific thickness are visible in the image. Notably, the layer thickness of 27µm was set as a printing parameter of the 3D printer.

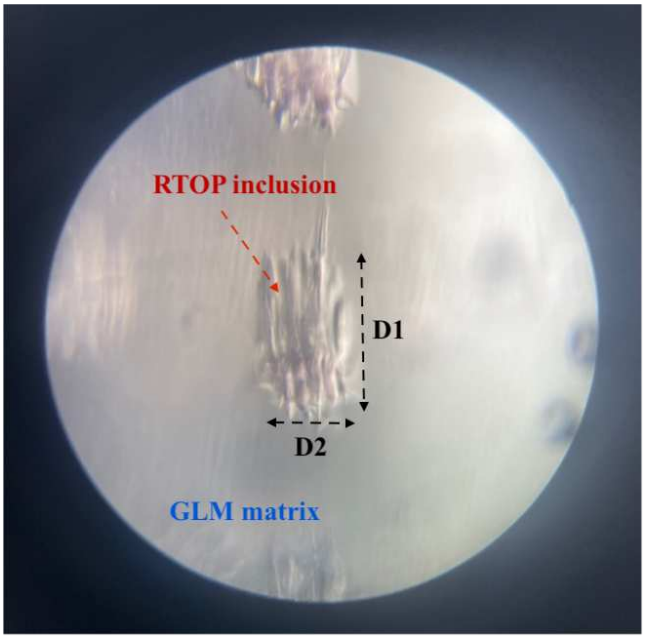

Figure 4.18. 2D optical microscopy image for an RTOP inclusion, with a magnification of x40

4.3.2 Micro-CT (Computed Tomography) scan

X-ray observation relies on differences in density between materials within a given sample. The material with a higher density will absorb more X-ray photons, resulting in a difference in absorption for the detector and a corresponding variation in the gray level on the resulting image. However, the

materials in the phantom 3D printer have similar densities (see Table 1.2); therefore, they could not be distinguished using this method. Injecting a contrast agent to highlight specific areas is common in medical applications, such as diagnosing blood vessels using CT scans. In this technique, contrast agents with a higher atomic number than blood, such as iodine, gadolinium, or barium, are used to partially increase the density of the target area [156]. To enhance the contrast between the RTOP inclusions and the surrounding GLM material, we employed a similar approach of introducing a contrast agent into the GLM matrix. The GLM material is more likely to absorb and diffuse the contrast agent and create adequate contrast to observe the RTOP inclusions. In this study, we used the iodine contrast agent Omnipaque 300mg Iode/mL by GE Healthcare to achieve the desired effect. The final contrast agent solution comprised 50% water and 50% Omnipaque.

We generated CT images of the printed sample using an X-ray microtomography X-View X50-CT, North Star Imaging in LMPS laboratory, which had a cooled open microfocus dual-head XWT240-XC190 tube operating in reflection mode and a flat-panel detector NSI Dexela 2923 (see Figure 4.19a). The X-ray source was used at an accelerating voltage of 120kV and a current of 80 μA, in reflection mode with a detail detectability of less than 1µm. The NSI in-house software efX-CT was used for CT image reconstruction. With the adopted magnification, we could generate CT images with a voxel size of approximately $3.2 \times 3.2 \times 3.2\mu m^3$, which is suitable for measuring the inclusion with a diameter of 300µm. This method provides us with 2D and 3D high-resolution images that can give a comprehensive insight into the morphology of the 3D-printed microstructure.

(a) *(b)*

Figure 4.19. (a) X-ray microtomograph X-View X50-CT, North Star Imaging in LMPS laboratory. (b) The specimen used for the Micro-CT observation of the inclusion shape.

The specimen designed for this observation is a cylindrical shell of RTOP material filled with GLM material, with three embedded columns of RTOP inclusions. The diameter of the cylinder is 4mm, and height of the cylinder is 5mm (see Figure 4.19b). To prepare for the observation, the specimen was submerged in a contrast agent solution. The solution was refilled twice daily, once in the morning and once in the afternoon, for 15 days. Figure 4.20 shows the 2D and 3D images obtained from the specimens. One can observe that the CT images approve that the shape of the printed RTOP material inclusions significantly deviates from the expected spherical shape and possess an ellipsoidal shape. The micro-CT output allows us to see the shape in XY, YZ, and XZ planes (see Figure 4.21) and

measure the size of the printed inclusion. We measured the major, minor, and intermediate diameters (D_1, D_2, and D_3, respectively) of 17 ellipsoidal inclusions from the observation. Segmentation of the images was performed using a gray level threshold of 107, and the resulting average diameters were $\overline{D_1} = 323 \pm 34\mu m$, $\overline{D_2} = 80 \pm 5\mu m$, and $\overline{D_3} = 237 \pm 20\mu m$. It is worth noting that changing the gray level threshold by 10, from 107 to 97, resulted in a less than 5% change in the measured diameters.

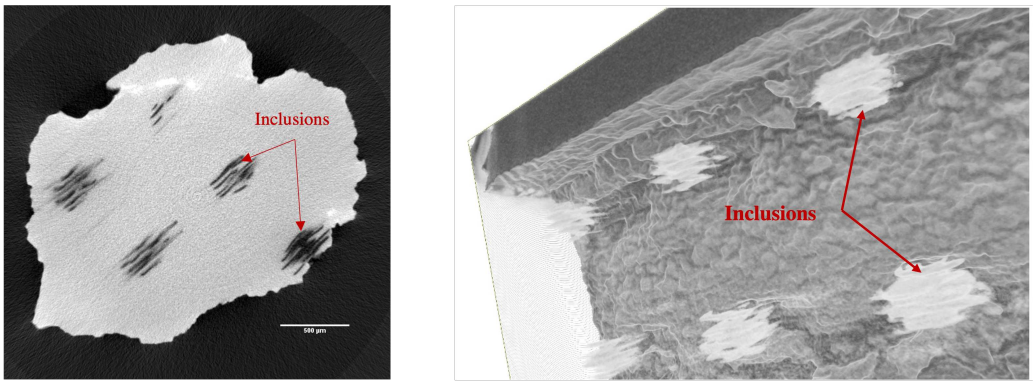

(a) (b)

Figure 4.20. (a) 2D and (b) 3D CT-scan images obtained from the cylindrical specimens with multiple columns of RTOP inclusions embedded in a GLM matrix, surrounded by an RTOP shell.

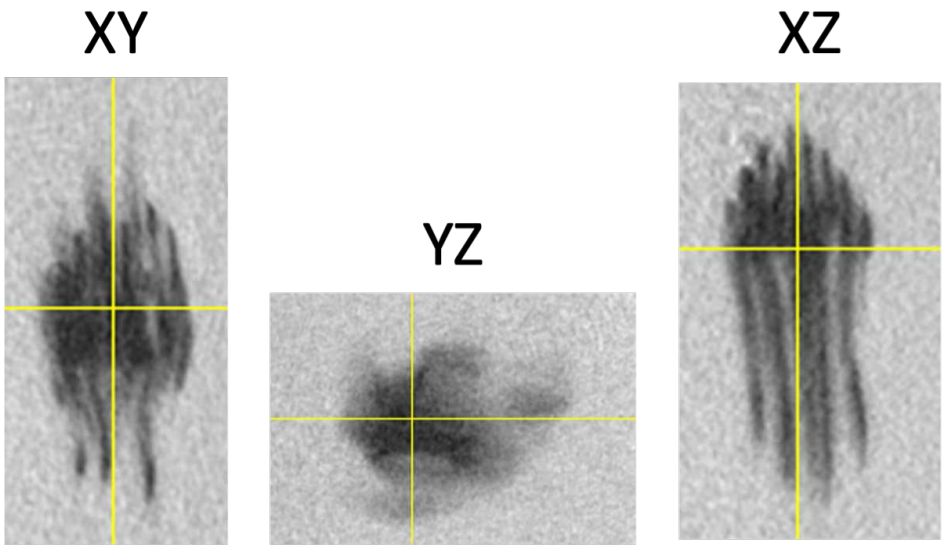

Figure 4.21. Observation of the RTOP inclusions in three planes

4.4 The real microstructure of 3D-printed material: numerical study

In this section, our goal is to incorporate the real shape of the inclusion, which was obtained through Micro-CT observation, into our numerical simulation. We aim to use this real inclusion shape to determine the phase velocity and attenuation coefficient of the matrix-inclusion composite. The purpose is to assess whether replacing the circular inclusion shape with the actual inclusion shape impacts the resulting phase velocity and attenuation coefficient.

To implement this approach, a structured grid is used for the simulation instead of an unstructured mesh with the same element size. The structured mesh has several advantages over the unstructured mesh, including easy implementation in the OOFE code, ensuring the numerical stability of the dG solver, and is faster and more memory efficient. Moreover, although the structured grid does not accurately represent the inclusion's geometry, this method is still appropriate because the image's resolution of the inclusion's shape is in the same order of magnitude as the element size. Consequently, the obtained image is approximated with the same precision as the element size. A pre-processing tool is developed in Matlab to generate the structured mesh for a 2D rectangular domain with a random distribution of the inclusions that provide the input mesh file of the OOFE software. As an illustration, we consider an inclusion with a $a = 150\mu$m radius. Figure 4.22a displays the circular inclusion with unstructured quadrilateral elements, while Figure 4.22a shows the same inclusion using a structured quladrilateral grid. Both simulations use the same element size of $h_e = 10\mu$m.

Using the same material properties and numerical setup discussed in section 3.3, a numerical simulation was conducted for a matrix-inclusion composite configuration with an area fraction $\phi = 5\%$ and inclusion size $a = 150\mu$m. Both unstructured and structured meshes were generated within the same geometry, using the same material properties and numerical setup. The resulting vertical wavefronts within the composite configurations for the unstructured and structured meshes are depicted in Figure 4.23a and Figure 4.23b, respectively. To enable a more precise comparison, the average of the vertical component of the velocity recorded on the top line of the geometry is presented in Figure 4.23c. It can be noticed that the signals obtained from the unstructured and structured mesh are comparable at the beginning, but differences become apparent as time progresses. Nonetheless, the section of the signal used for determining the phase velocity and attenuation coefficient, which is the echo from the bottom edge, is identical in both signals.

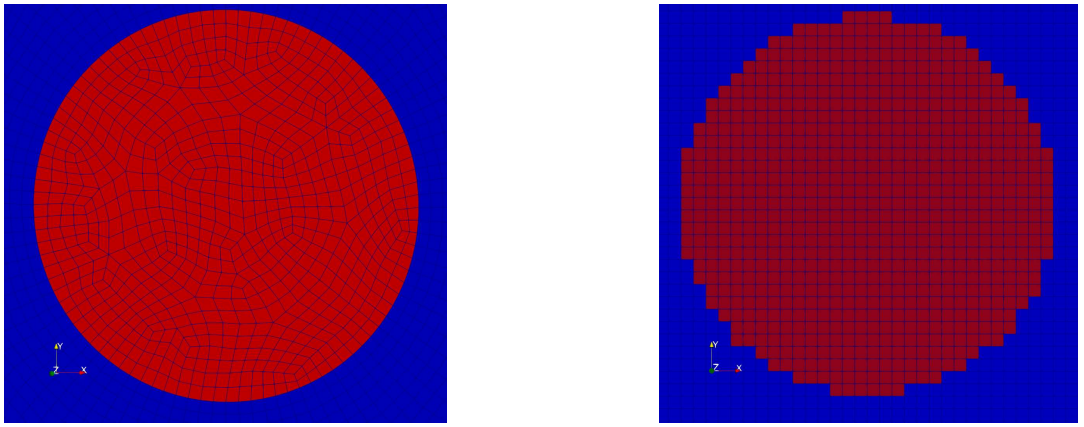

(a) *(b)*

Figure 4.22. Circular inclusion with a diameter of $a = 150\mu$m with (a) unstructured quadrilateral elements, and (b) structured quadrilateral grid. The element size in both cases is $h_e = 10\mu$m.

4.4.1 Matrix-inclusion composites with real shape of inclusion

To perform the numerical simulation on a composite with the actual microstructure of the inclusions, first, we obtain a 3D image of one of the inclusions and perform image segmentation to generate a binary image. The resulting 2D binary images of four arbitrary slices of a 3D-printed inclusion are

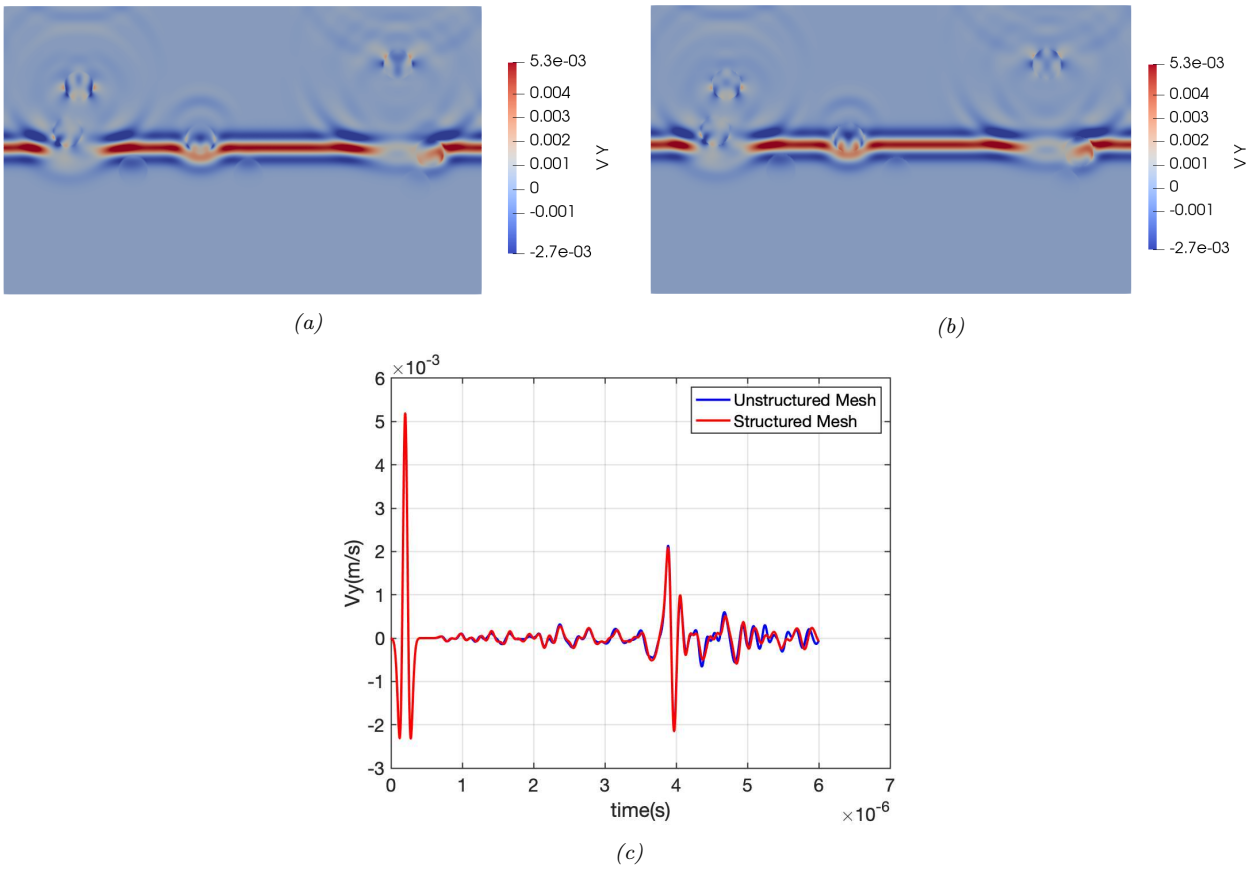

Figure 4.23. Illustration of the wave propagation in matrix-inclusion with circular inclusions, with area fraction of $\phi = 5\%$ and radius of $a = 150\mu m$, using (a) unstructured quadrilateral elements, and (b) structured quadrilateral elements. (c) Average vertical velocity V_y recorded on the top line of the geometry, with unstructured and structured meshes.

depicted in Figure 4.24. These images were captured from a single inclusion on the plane perpendicular to the printing direction (YZ plane). The idea is to replace the circular inclusions with a radius of $a = 150\mu m$ with a square shape of $400\mu m \times 400\mu m$, which contains the real shape of the inclusions. Two different shapes (as shown in Figure 4.24a and Figure 4.24b) are selected for this purpose and are called S1 and S2 hereafter. Initially, the size of each image is 400×400 pixels, with each pixel representing $1\mu m$ of the material. To match the element size of $10\mu m$, each element is represented by a 10×10 pixel box. If most pixels within an element are black, the entire element is considered as matrix material; otherwise, it is regarded as an inclusion. The structured mesh within the real shape of the inclusion, with an element size of $h_e = 10\mu m$, is presented in Figure 4.25. Two distinct shapes are randomly distributed within a rectangular matrix with a uniform probability function. The number of inclusions is adjusted to obtain the area fractions of $\phi = 3\%$ and $\phi = 5\%$. Four configurations of the composite with random distribution, comprising two distinct shapes and two area fractions, are shown in Figure 4.26.

In Figure 4.27, wave propagation in a composite material with two different inclusion shapes and area fraction of $\phi = 3\%$ is illustrated at $t_1 = 1.13\mu s$. The area fraction of the inclusion is calculated by counting the number of elements placed in the inclusion, devided by total number of the elements. Additionally, the average velocity signals recorded on the top line of the geometry are presented for both cases (see Figure 4.27b and Figure 4.27d). It is observed that the S1 inclusion shape scatters

the wavefront more strongly than the S2 shape, as evidenced by the smaller amplitude of the reflected wavefront from the bottom boundary in the case of S1.

The numerical attenuation coefficients obtained for these configurations are obtained similar to the third chapter, by averaging over 30 samples with different distribution of inclusions are shown in Figure 4.28.The blue dashed lines indicate the attenuation coefficients for the S1 shape, while the red dashed lines represent the results for the S2 shape. The black line corresponds to the composite's phase velocity and attenuation coefficients with circular inclusions with $a = 150\mu m$ radius. It is worth noting that the involved wavelengths of interest lie within the range $200\mu m < \lambda < 670\mu m$, and the characteristic size of the microstructure implies the "stochastic" scattering regime. Here, the average cross-sectional length of the inclusion determines the attenuation coefficient. Thus, it is expected that the S1 shape has a higher attenuation coefficient since its cross-section is larger than that of S2.

However, we believe the calculation must be repeated for more samples with different inclusion distributions to obtain more accurate and reliable results.

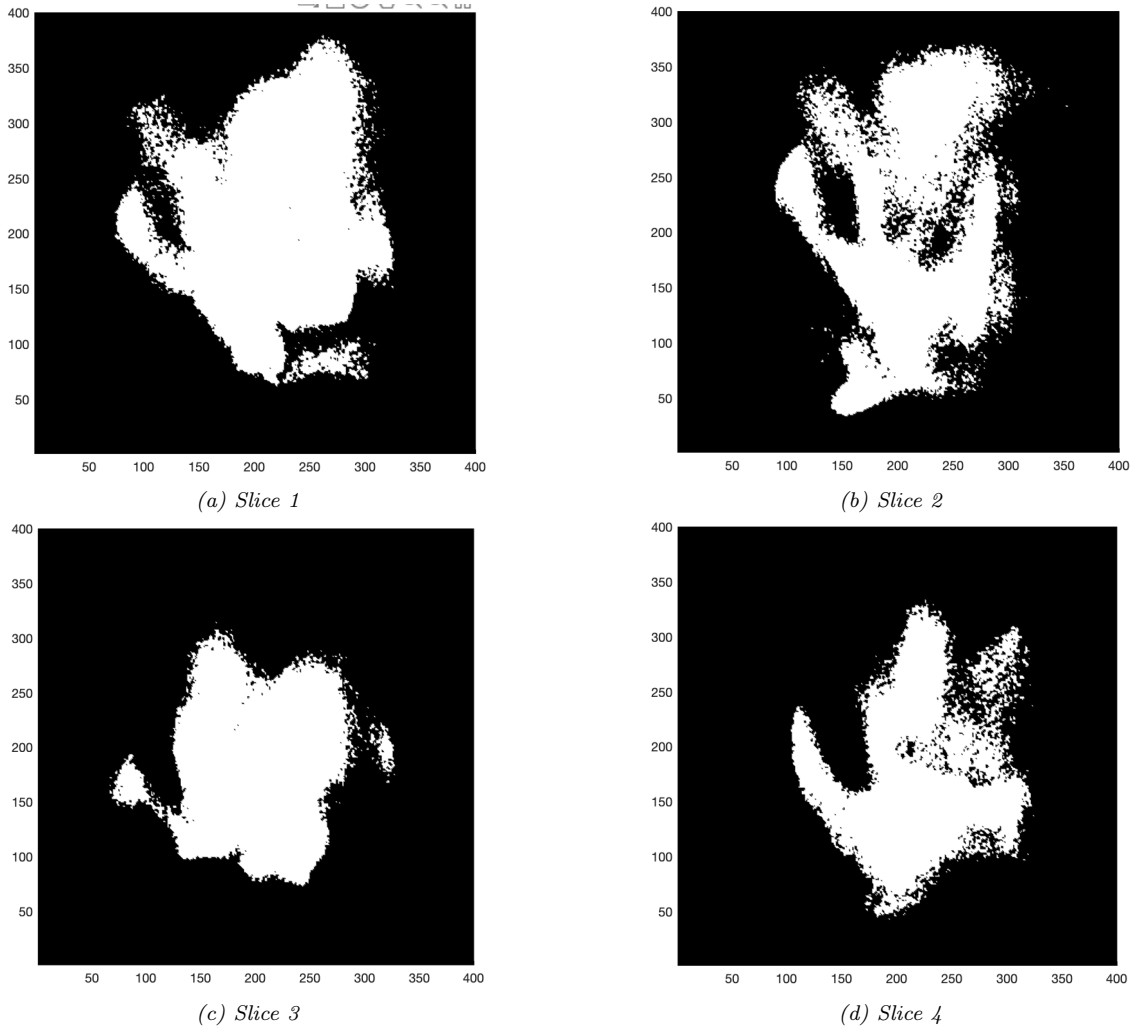

(a) Slice 1 *(b) Slice 2*

(c) Slice 3 *(d) Slice 4*

Figure 4.24. Two-dimensional binary images of various Slices of a 3D-printed inclusion

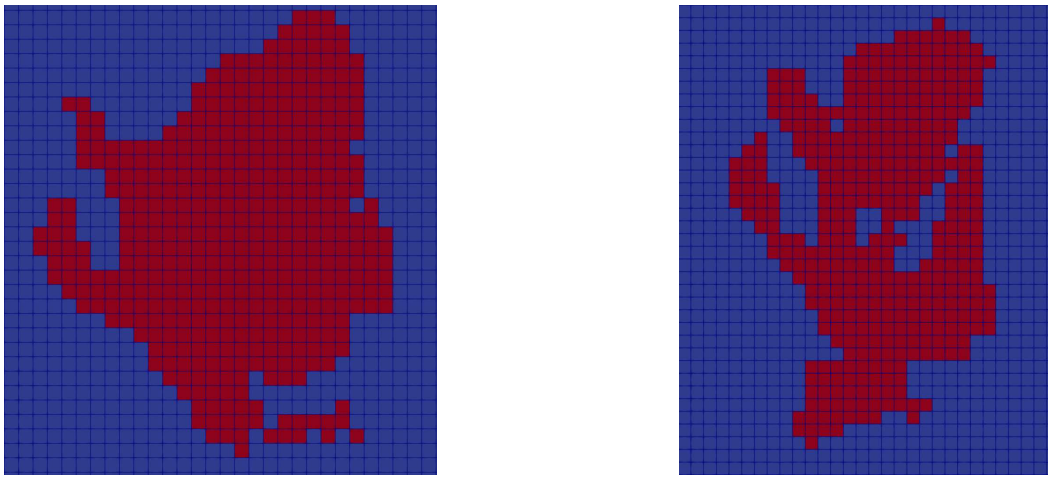

(a) *(b)*

Figure 4.25. The structured mesh within the real shape of the inclusion using the element size of $h_e = 10\mu m$

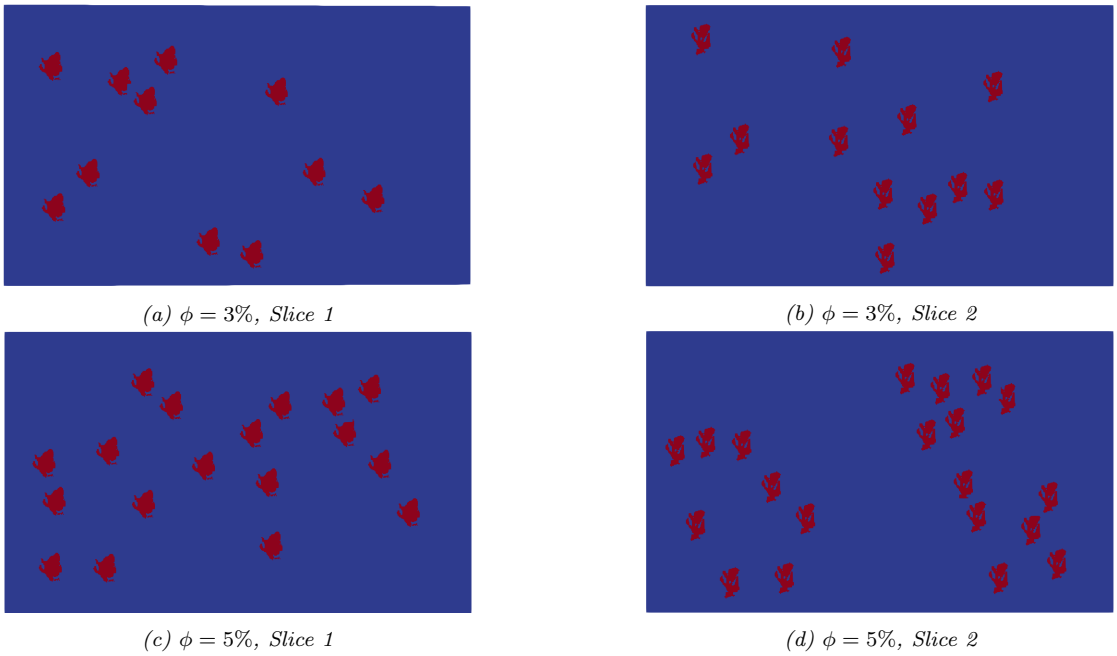

(a) $\phi = 3\%$*, Slice 1* *(b)* $\phi = 3\%$*, Slice 2*

(c) $\phi = 5\%$*, Slice 1* *(d)* $\phi = 5\%$*, Slice 2*

Figure 4.26. our configurations of the composite with random distribution, comprising two distinct shapes and two area fractions

4.5 Conclusions

The developed coupled acoustic-elastic space dG solver was used to simulate ultrasonic wave propagation in a simplified model of a 3D-printed matrix-inclusion composite microstructure and a sandwich composite microstructure designed to mimic the acoustic properties of the biological tissues. The reconstructed rectangular B-mode image was obtained using a simple algorithm. A parametric study investigated the effects of the area fraction and size of the inclusions on the average gray level of the reconstructed B-images. Results showed that increasing the area fraction of the circular inclusions and decreasing their size improved the echogenicity of the composite layer. However, this also made it more challenging to accurately determine the layer's thickness.

The study included a numerical model of the phased array transducer that used appropriate time

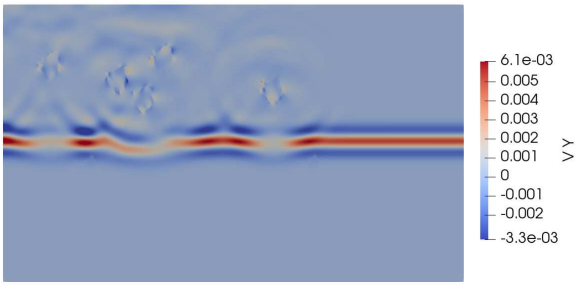

(a) Slice 1, $t_1 = 1.13\mu s$

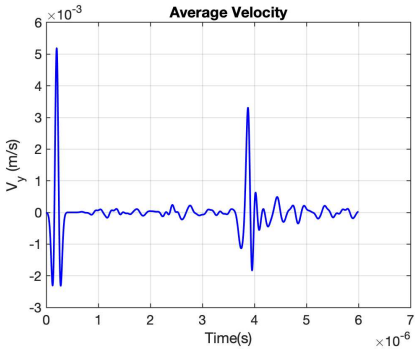

(b)

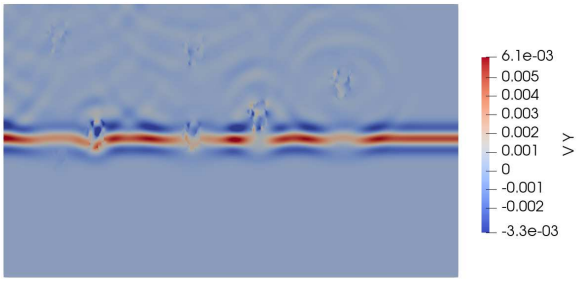

(c) Slice 2, $t_1 = 1.13\mu s$

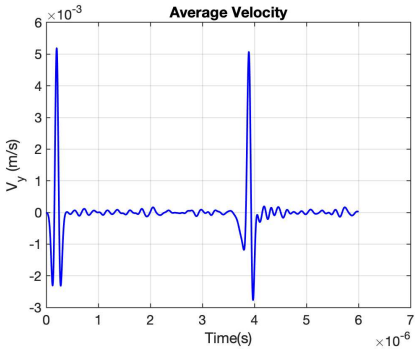

(d)

Figure 4.27. (a) Wave propagation in the composite for the inclusion shapes S1 and S2 with area fraction of $\phi = 3\%$, and the corresponding recorded average velocity on the top line of the geometry.

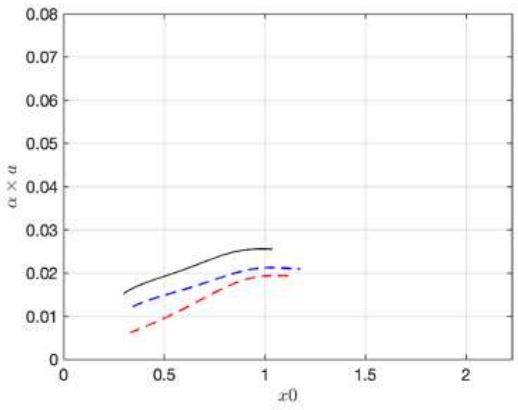

(a) Attenuation coefficient: $\phi = 3\%$

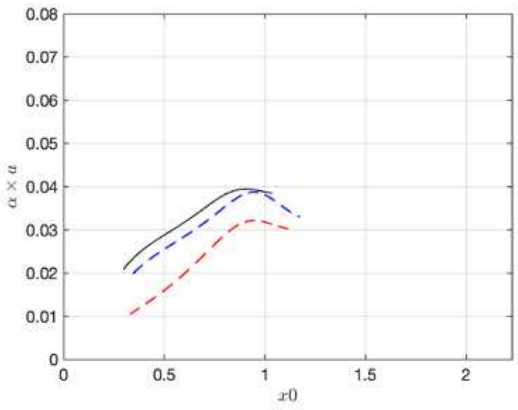

(b) Attenuation coefficient: $\phi = 5\%$

Figure 4.28. Numerical attenuation coefficient for the 3D-printed composite material with different shapes of S1 (blue), S2 (red) and circular inclusion (black), for different area fractions of $\phi = 3\%$ and $\phi = 5\%$.

delays applied to the piezoelectric elements to steer and focus the ultrasonic wave. While initial efforts were made to reconstruct B-mode images of a curved sandwich structure in sector format, further refinement of the reconstruction algorithm is needed to achieve an image that accurately represents the target material.

An experimental study was conducted to obtain the real shape of the 3D-printed inclusions. A preliminary observation was performed with an optical microscope. Subsequently, the inclusions' real 2D and 3D images were obtained using a Micro-CT scan. The acquired 2D and 3D images of the

inclusions were then used as input for the numerical simulation to estimate the phase velocity and attenuation coefficient of the composite microstructure with the real shape of the inclusions. The results were compared to those obtained using the simplified circular shape inclusion.

Conclusions and perspectives

This work was mainly focused on the numerical investigation of the tissue-mimicking 3D-printed material's acoustic properties at the microstructure level, with experiments providing additional insights.

The first contribution of this thesis consists of developing the mathematical framework of the space discontinuous Galerkin (dG) finite element (FE) approach for the numerical modeling of the coupled acoustic/elastic wave propagation in multidimensional media with arbitrary anisotropic solid and acoustic fluid. The unified strong form and variational frameworks for acoustic and elastic media are presented using an intrinsic tensorial notation within the first-order hyperbolic system of equations. After studying the eigenstructure of the equations, the upwind numerical fluxes were derived analytically by solving the Riemann problem at the acoustic-acoustic and coupled acoustic-elastic interfaces. Together with the numerical fluxes previously derived for the elastic-elastic interfaces and presented again in this work, the calculated upwind numerical fluxes provide closed-form expressions within a compact and intrinsic tensorial framework. This approach has been implemented in an in-house software called OOFE (Object-Oriented Finite Element), which allowed us to perform parallel numerical simulations of wave propagation in a multi-physics fluid-solid medium on a cluster, thanks to the MPI-implemented version. The numerical results from the coupled acoustic-elastic solver are compared to the analytical solution for a problem with a circular acoustic-elastic interface to validate the numerical fluxes. However, the performance of the proposed method in terms of accuracy and convergence rate needs to be compared to other numerical flux methods in future works. In this thesis, the simulation of ultrasonic wave propagation was performed entirely using the introduced discontinuous Galerkin FE approach.

Secondly, an FE-based numerical approach was proposed for estimating the phase velocity and attenuation coefficient for matrix inclusion composites with a random distribution of circular inclusions. To validate this approach, a comprehensive study of Willis' theoretical framework for the analytical calculation of the phase velocity and attenuation coefficient in the matrix-inclusion composites. This theory is based on a self-consistent scheme to replace the heterogeneous composite medium with an effective homogenized medium and a single scattering assumption. Using this approach, the elastic properties of the effective medium can be obtained analytically, as well as the phase velocity and attenuation coefficient. This theoretical framework has been presented synthetically in this work, and the limitations of this approach have been addressed. Both analytical and numerical results were given and compared for an epoxy lead with different area fractions and inclusion sizes, and the differences were quantified. However, since this theoretical approach did not apply to matrix-inclusion composites with a quasi-incompressible matrix, including our target 3D printed material, the validated numerical method is subsequently used to estimate the phase velocity and attenuation coefficient for 3D printed synthetic tissues, considering the area fraction of inclusions, size, and material properties. Nonetheless, it was observed that the numerical approach fails to provide reliable results when we increase the area

fraction and/or decrease the inclusion size. This could be a point of further studies, where different techniques could be employed to capture the signal better by reducing the level of backscattered noise and eventually estimating the phase velocity and the attenuation coefficient.

Third, the developed coupled dG solver was used to simulate ultrasonic wave propagation in a simplified two-dimensional model of a 3D-printed matrix-inclusion composite microstructure and a sandwich composite microstructure. A numerical model of a linear sequential transducer is used for initiating the ultrasonic pulse in the domain, and the corresponding cartesian B-mode image was obtained using a simple reconstruction algorithm. A parametric study was performed to investigate the effects of the area fraction and size of the inclusions on the average gray level of the reconstructed B-images, which is used as a metric to measure the echogenicity of the 3D-printed synthetic tissue. A numerical model of the phased array transducer was also presented, in which the steering and focusing of the ultrasonic wave were obtained by applying appropriate time delays to the piezoelectric elements of the transducer. An initial effort was made to reconstruct B-mode images of a curved sandwich structure in sector format. However, a more thorough refinement of the reconstruction algorithm is necessary to achieve a B-mode image that closely reflects reality.

An experimental study was conducted to obtain the real shape of the 3D-printed inclusions. Initially, a preliminary observation of the 3D printed inclusion was carried out using an optical microscope, which produced 2D images. 2D and 3D images of the printed microstructure were then acquired using micro-CT observation. These images were then used as input to the numerical simulation to determine the phase velocity and attenuation coefficient of the composite microstructure with the actual shape of the inclusions. The actual shape of the inclusions obtained from micro-CT was later incorporated into the matrix inclusion composite, replacing the circular shape inclusion, thanks to a structured mesh. This approach allowed the wave propagation simulation in matrix inclusion composites with arbitrarily shaped inclusions. The new composite's phase velocity and attenuation coefficient were calculated using the validated FE-based approach. The results were compared to those obtained using the simplified circular shape inclusion.

Thus far, this investigation could provide insights into the physical mechanisms underlying certain inconsistencies observed between the B-mode images of the 3D-printed synthetic organ and its corresponding actual organ. A comprehensive analytical/numerical study of the scattering behavior and scattering-induced attenuation of the matrix-inclusion microstructures, used in the 3D-printed synthetic tissue was presented. The study focused on a two-dimensional problem to gain insights into the underlying physical mechanisms involved. Willis's analytical framework presented in Chapter 2 could be used for a three-dimensional matrix-inclusion with spheroidal inclusions, which is an interesting avenue for future research. However, to tackle the problem numerically, it is necessary to improve the performance and scalability of the dG solver to solve the problems with a higher number of elements. By employing the structured mesh technique and the pre-processing tool developed for importing the geometry in the OOFE code, along with the post-processing tool for calculating the phase velocity and attenuation coefficient, it is feasible to extend this investigation to a three-dimensional matrix-inclusion composite with an arbitrary shape of the inclusion.

The study of echogenicity, which is the primary goal of the 3D-printed tissue mimicking materials used in the synthetic organs, was limited to the microstructure level and in two-dimensional problems

in this work. Future studies could focus on investigating the echogenicity of synthetic organs at a macroscopic level by considering the overall shape of the organ. Once again, here, the better scalability of the OOFE code is necessary to handle this computationally expensive problem. Additionally, while the post-processing tool used for reconstructing the cartesian B-mode image can potentially be applied to 2D or 3D simulations, more rigorous analysis is needed to generate reliable sector B-mode images. Future studies could incorporate the actual shape of inclusions within the microstructure to further investigate echogenicity.

Finally, reduced-order methods such as POD (Proper Orthogonal Decomposition) can be used in the future to step toward a multi-parametric optimization of the microstructure to achieve the desired echogenicity and better understand the physical properties of the system.

Bibliography

[1] Fabian Adams, Tian Qiu, Andrew Mark, Benjamin Fritz, Lena Kramer, Daniel Schlager, Ulrich Wetterauer, Arkadiusz Miernik, and Peer Fischer. Soft 3D-Printed Phantom of the Human Kidney with Collecting System. *Annals of Biomedical Engineering*, 45(4):963–972, April 2017.

[2] Adolf Müller, Kartik G. Krishnan, Eberhard Uhl, and Gerson Mast. The Application of Rapid Prototyping Techniques in Cranial Reconstruction and Preoperative Planning in Neurosurgery. *Journal of Craniofacial Surgery*, 14(6):899, November 2003.

[3] Geoffrey R. Wignall, John D. Denstedt, Glenn M. Preminger, Jeffrey A. Cadeddu, Margaret S. Pearle, Robert M. Sweet, and Elspeth M. McDougall. Surgical Simulation: A Urological Perspective. *Journal of Urology*, 179(5):1690–1699, May 2008. Publisher: WoltersKluwer.

[4] Geoff A. Bellingham and Philip W.H. Peng. A Low-Cost Ultrasound Phantom of the Lumbosacral Spine:. *Regional Anesthesia and Pain Medicine*, 35(3):290–293, May 2010.

[5] Jason R. Cook, Richard R. Bouchard, and Stanislav Y. Emelianov. Tissue-mimicking phantoms for photoacoustic and ultrasonic imaging. *Biomedical Optics Express*, 2(11):3193, November 2011.

[6] Giovanni Biglino, Claudio Capelli, Jo Wray, Silvia Schievano, Lindsay-Kay Leaver, Sachin Khambadkone, Alessandro Giardini, Graham Derrick, Alexander Jones, and Andrew M. Taylor. 3D-manufactured patient-specific models of congenital heart defects for communication in clinical practice: feasibility and acceptability. *BMJ Open*, 5(4):e007165, April 2015. Publisher: British Medical Journal Publishing Group Section: Communication.

[7] M. Kusaka, M. Sugimoto, N. Fukami, H. Sasaki, M. Takenaka, T. Anraku, T. Ito, T. Kenmochi, R. Shiroki, and K. Hoshinaga. Initial Experience With a Tailor-made Simulation and Navigation Program Using a 3-D Printer Model of Kidney Transplantation Surgery. *Transplantation Proceedings*, 47(3):596–599, April 2015.

[8] Xiangxue Kong, Lanying Nie, Huijian Zhang, Zhanglin Wang, Qiang Ye, Lei Tang, Wenhua Huang, and Jianyi Li. Do 3D Printing Models Improve Anatomical Teaching About Hepatic Segments to Medical Students? A Randomized Controlled Study. *World Journal of Surgery*, 40(8):1969–1976, August 2016.

[9] Leigh V. Evans, Kelly L. Dodge, Tanya D. Shah, Lewis J. Kaplan, Mark D. Siegel, Christopher L. Moore, Cara J. Hamann, Zhenqiu Lin, and Gail D'Onofrio. Simulation Training in Central Venous Catheter Insertion: Improved Performance in Clinical Practice:. *Academic Medicine*, 85(9):1462–1469, September 2010.

[10] Daniil I. Nikitichev, Anamaria Barburas, Kirstie McPherson, Jean-Martial Mari, Simeon J. West, and Adrien E. Desjardins. Construction of 3-Dimensional Printed Ultrasound Phantoms

With Wall-less Vessels. *Journal of Ultrasound in Medicine*, 35(6):1333–1339, 2016. _eprint: https://onlinelibrary.wiley.com/doi/pdf/10.7863/ultra.15.06012.

[11] Justin Ceh, Tom Youd, Zach Mastrovich, Cody Peterson, Sarah Khan, Todd A. Sasser, Ian M. Sander, Justin Doney, Clark Turner, and W. Matthew Leevy. Bismuth Infusion of ABS Enables Additive Manufacturing of Complex Radiological Phantoms and Shielding Equipment. *Sensors*, 17(3):459, March 2017. Number: 3 Publisher: Multidisciplinary Digital Publishing Institute.

[12] Frederick A. Zeiler, Bertram Unger, Andreas H. Kramer, Andrew W. Kirkpatrick, and Lawrence M. Gillman. A Unique Model for Ultrasound Assessment of Optic Nerve Sheath Diameter. *Canadian Journal of Neurological Sciences*, 40(2):225–229, March 2013. Publisher: Cambridge University Press.

[13] Benjamin W. Turney. A New Model with an Anatomically Accurate Human Renal Collecting System for Training in Fluoroscopy-Guided Percutaneous Nephrolithotomy Access. *Journal of Endourology*, 28(3):360–363, March 2014.

[14] D. Jarvis, P. D. Griffiths, and C. Majewski. Demonstration of Normal and Abnormal Fetal Brains Using 3D Printing from In Utero MR Imaging Data. *AJNR. American journal of neuroradiology*, 37(9):1757–1761, September 2016.

[15] Jason S. Naftulin, Eyal Y. Kimchi, and Sydney S. Cash. Streamlined, Inexpensive 3D Printing of the Brain and Skull. *PLOS ONE*, 10(8):e0136198, August 2015. Publisher: Public Library of Science.

[16] Ian M. Sander, Matthew T. McGoldrick, My N. Helms, Aislinn Betts, Anthony van Avermaete, Elizabeth Owers, Evan Doney, Taimi Liepert, Glen Niebur, Douglas Liepert, and W. Matthew Leevy. Three-dimensional printing of X-ray computed tomography datasets with multiple materials using open-source data processing. *Anatomical Sciences Education*, 10(4):383–391, 2017. _eprint: https://onlinelibrary.wiley.com/doi/pdf/10.1002/ase.1682.

[17] Thore M. Bücking, Emma R. Hill, James L. Robertson, Efthymios Maneas, Andrew A. Plumb, and Daniil I. Nikitichev. From medical imaging data to 3D printed anatomical models. *PLOS ONE*, 12(5):e0178540, May 2017.

[18] Holmes David R. and Reddy Vivek Y. Left Atrial Appendage and Closure. *Circulation: Cardiovascular Interventions*, 9(5):e002942, May 2016. Publisher: American Heart Association.

[19] Martin O. Culjat, David Goldenberg, Priyamvada Tewari, and Rahul S. Singh. A Review of Tissue Substitutes for Ultrasound Imaging. *Ultrasound in Medicine & Biology*, 36(6):861–873, June 2010.

[20] Jean-Rene Jacquet, Franck Levassort, Frederic Ossant, and Jean-Marc Gregoire. 3D printed phantom for high frequency ultrasound imaging. In *2015 IEEE International Ultrasonics Symposium (IUS)*, pages 1–4, Taipei, Taiwan, October 2015. IEEE.

[21] Marina Bakaric, Piero Miloro, Ashkan Javaherian, Ben T. Cox, Bradley E. Treeby, and Michael D. Brown. Measurement of the ultrasound attenuation and dispersion in 3D-printed photopolymer materials from 1 to 3.5 MHz. *The Journal of the Acoustical Society of America*, 150(4):2798–2805, October 2021.

[22] Anthony Saxton, Muhammad Ali Tariq, and Bruno Bordoni. Anatomy, Thorax, Cardiac Muscle. In *StatPearls*. StatPearls Publishing, Treasure Island (FL), 2023.

[23] Jerry L. Prince and Jonathan M. Links. *Medical imaging signals and systems*. Pearson, Boston, 2 edition, 2015.

[24] Thomas L. Szabo. *Diagnostic ultrasound imaging: inside out*. Academic Press series in biomedical engineering. Elsevier Academic Press, Amsterdam ; Boston, 2004. OCLC: ocm57744110.

[25] Haim Azhari. *Basics of Biomedical Ultrasound for Engineers: Azhari/Ultrasound*. John Wiley & Sons, Inc., Hoboken, NJ, USA, February 2010.

[26] Pierre C. Wong and Wanda C. Miller-Hance, editors. *Transesophageal Echocardiography for Congenital Heart Disease*. Springer London, London, 2014.

[27] Ronald H Silverman. Focused ultrasound in ophthalmology. *Clinical Ophthalmology*, 10:1865–1875, December 2016. Publisher: Dove Medical Press _eprint: https://www.tandfonline.com/doi/pdf/10.2147/OPTH.S99535.

[28] Olaf T. Von Ramm and Stephen W. Smith. Beam Steering with Linear Arrays. *IEEE Transactions on Biomedical Engineering*, BME-30(8):438–452, August 1983.

[29] Elizabeth Garber. The Beginnings of Piezoelectricity: A Study in Mundane Physics. *Annals of Science*, 67(2):261–265, April 2010. Publisher: Taylor & Francis _eprint: https://doi.org/10.1080/00033790802318292.

[30] Stephen Andrew Mosey. Resolution Enhancement of B-Mode Ultrasound Images.

[31] Introduction to Phased Array Ultrasonic Technology Applications, 2010.

[32] Rachael Nightingale. Linear array | Radiology Reference Article | Radiopaedia.org.

[33] Rachael Nightingale. Phased array | Radiology Reference Article | Radiopaedia.org.

[34] D. L. King. Real-time cross-sectional ultrasonic imaging of the heart using a linear array multi-element transducer. *Journal of clinical ultrasound: JCU*, 1(3):196–201, September 1973.

[35] Maurice Bellanger and John C. C. Nelson. *Digital Processing of Signals: Theory and Practice*. Wiley, April 2000.

[36] Yuh-Tay Sheen. On the study of applying Morlet wavelet to the Hilbert transform for the envelope detection of bearing vibrations. *Mechanical Systems and Signal Processing*, 23(5):1518–1527, July 2009.

[37] Lucas C. Wilcox, Georg Stadler, Carsten Burstedde, and Omar Ghattas. A high-order discontinuous Galerkin method for wave propagation through coupled elastic–acoustic media. *Journal of Computational Physics*, 229(24):9373–9396, December 2010.

[38] DAVIDM. Boore. Finite Difference Methods for Seismic Wave Propagation in Heterogeneous Materials. In BRUCE A. Bolt, editor, *Methods in Computational Physics: Advances in Research and Applications*, volume 11 of *Seismology: Surface Waves and Earth Oscillations*, pages 1–37. Elsevier, January 1972.

[39] Gordon D. Smith. *Numerical Solution of Partial Differential Equations: Finite Difference Methods*. Clarendon Press, 1985. Google-Books-ID: hDpvljaHOrMC.

[40] Alan Levander. Fourth-order finite-difference P-S. *Geophysics*, 53:1425–1436, November 1988.

[41] Peter Moczo, Jozef Kristek, Vaclav Vavrycuk, Ralph Archuleta, and L. Halada. 3D Heterogeneous Staggered-Grid Finite-Difference Modeling of Seismic Motion with Volume Harmonic and Arithmetic Averaging of Elastic Moduli and Densities. *Bulletin of the Seismological Society of America*, 92:3042–3066, December 2002.

[42] Heiner Igel, Peter Mora, and Bruno Riollet. Anisotropic wave propagation through finite-difference grids. *GEOPHYSICS*, 60(4):1203–1216, July 1995. Publisher: Society of Exploration Geophysicists.

[43] Ekkehart Tessmer. 3-D seismic modelling of general material anisotropy in the presence of the free surface by a Chebyshev spectral method. *Geophysical Journal International*, 121(2):557–575, May 1995.

[44] Martin Käser, Heiner Igel, Malcolm Sambridge, and Jean Braun. A comparative study of explicit differential operators on arbitrary grids. *Journal of Computational Acoustics*, 9:1111–1125, September 2001.

[45] R. M. Alford, K. R. Kelly, and D. M. Boore. ACCURACY OF FINITE-DIFFERENCE MODELING OF THE ACOUSTIC WAVE EQUATION. *GEOPHYSICS*, 39(6):834–842, December 1974.

[46] K. R. Kelly, R. W. Ward, Sven Treitel, and R. M. Alford. Synthetic seismograms: a finite -difference approach. *GEOPHYSICS*, 41(1):2–27, February 1976. Publisher: Society of Exploration Geophysicists.

[47] Raul Madariaga. Dynamics of an expanding circular fault. *Bulletin of the Seismological Society of America*, 66(3):639–666, June 1976.

[48] Jean Virieux. SH-wave propagation in heterogeneous media: Velocity-stress finite-difference method. *GEOPHYSICS*, 49(11):1933–1942, November 1984. Publisher: Society of Exploration Geophysicists.

[49] Jean Virieux. P-SV wave propagation in heterogeneous media: Velocity-stress finite-difference method. *GEOPHYSICS*, 51(4):889–901, April 1986. Publisher: Society of Exploration Geophysicists.

[50] Leandro Di Bartolo, Cleberson Dors, and W.J. Mansur. A new family of finite-difference schemes to solve the heterogeneous acoustic wave equation. *Geophysics*, 77:T187–T199, August 2012.

[51] Leandro Di Bartolo, Ana Vieira, Cleberson Dors, and W.J. Mansur. Memory optimized acoustic-elastic FD coupling for offshore seismic simulations. September 2015.

[52] Leandro Di Bartolo, Cleberson Dors, and W.J. Mansur. Theory of equivalent staggered-grid schemes: Application to rotated and standard grids in anisotropic media. *Geophysical Prospecting*, 63, February 2015.

[53] Leandro Di Bartolo, Rosário Romão Manhisse, and Cleberson Dors. Efficient acoustic-elastic FD coupling method for anisotropic media. *Journal of Applied Geophysics*, 174:103934, March 2020.

[54] Bruno Lombard and Joël Piraux. Numerical treatment of two-dimensional interfaces for acoustic and elastic waves. *Journal of Computational Physics*, 195(1):90–116, March 2004.

[55] Warwick D. Smith. The Application of Finite Element Analysis to Body Wave Propagation Problems. *Geophysical Journal International*, 42(2):747–768, August 1975.

[56] F. J. Serón, F. J. Sanz, M. Kindelán, and J. I. Badal. Finite-element method for elastic wave propagation. *Communications in Applied Numerical Methods*, 6(5):359–368, July 1990.

[57] Thomas J. R. Hughes. *The Finite Element Method: Linear Static and Dynamic Finite Element Analysis*. Courier Corporation, May 2012. Google-Books-ID: cHH2n_qBK0IC.

[58] Olgierd C. Zienkiewicz, Robert L. Taylor, and J. Z. Zhu. *The finite element method: its basis and fundamentals*. Elsevier, Amsterdam Heidelberg, 6. ed., reprint., transferred to digital print edition, 2010.

[59] David Gottlieb and Steven A. Orszag. *Numerical Analysis of Spectral Methods: Theory and Applications*. SIAM, January 1977. Google-Books-ID: 7afHrqGFjSoC.

[60] José Carcione. Priolo, E., Carcione, J. M., and Seriani, G., 1994, Numerical simulation of interface waves by high-order spectral modeling techniques, J. Acous. Soc. Am., 95, 681-693. January 1994.

[61] Dimitri Komatitsch and Jean-Pierre Vilotte. The Spectral Element method: an efficient tool to simulate the seismic response of 2D and 3D geological structures. *Bulletin of the Seismological Society of America*, 88:368–392, April 1998.

[62] Géza Seriani. 3-D large-scale wave propagation modeling by spectral element method on Cray T3E multiprocessor. *Computer Methods in Applied Mechanics and Engineering*, 164(1):235–247, October 1998.

[63] Emmanuel Chaljub and Bernard Valette. Spectral element modeling of three dimensional wave propagation in a self-gravitating Earth with an arbitrarily stratified outer core. *Geophysical Journal International*, 158(1):131–141, July 2004. arXiv: physics/0308102.

[64] Dimitri Komatitsch, Seiji Tsuboi, and Jeroen Tromp. The spectral-element method in seismology. In Alan Levander and Guust Nolet, editors, *Geophysical Monograph Series*, volume 157, pages 205–227. American Geophysical Union, Washington, D. C., 2005.

[65] Nicholas W. Taylor, Lawrence E. Kidder, and Saul A. Teukolsky. Spectral methods for the wave equation in second-order form. *Physical Review D*, 82(2):024037, July 2010. Publisher: American Physical Society.

[66] Dimitri Komatitsch, Christophe Barnes, and Jeroen Tromp. Wave propagation near a fluid-solid interface: A spectral-element approach. *GEOPHYSICS*, 65(2):623–631, March 2000.

[67] P. K. Banerjee, Prasanta Kumar Banerjee, and Roy Butterfield. *Boundary Element Methods in Engineering Science*. McGraw-Hill Book Company (UK), 1981. Google-Books-ID: FJBRAAAA-MAAJ.

[68] W.J. Mansur and C.A. Brebbia. Numerical implementation of the boundary element method for two dimensional transient scalar wave propagation problems. *Applied Mathematical Modelling*, 6(4):299–306, August 1982.

[69] Emmanuel Dormy and Albert Tarantola. Numerical simulation of elastic wave propagation using a finite volume method. *Journal of Geophysical Research*, 100:2123–2133, February 1995. ADS Bibcode: 1995JGR...100.2123D.

[70] Randall J. LeVeque. *Finite Volume Methods for Hyperbolic Problems*. Cambridge Texts in Applied Mathematics. Cambridge University Press, Cambridge, 2002.

[71] T. Schwartzkopff, C. D. Munz, and E. F. Toro. ADER: A High-Order Approach for Linear Hyperbolic Systems in 2D. *Journal of Scientific Computing*, 17(1):231–240, December 2002.

[72] M. Dumbser, T. Schwartzkopff, and C.-D. Munz. Arbitrary high order finite volume schemes for linear wave propagation. In Egon Krause, Yurii Shokin, Michael Resch, and Nina Shokina, editors, *Computational Science and High Performance Computing II*, Notes on Numerical Fluid Mechanics and Multidisciplinary Design, pages 129–144, Berlin, Heidelberg, 2006. Springer.

[73] Randall Wade Hoberecht. A Finite Volume Approach to Modeling.

[74] P. Voinovich, A. Merlen, E. Timofeev, and K. Takayama. A Godunov-type finite-volume scheme for unified solid-liquid elastodynamics on arbitrary two-dimensional grids. *Shock Waves*, 13(3):221–230, November 2003.

[75] Lonny L. Thompson and Peter M. Pinsky. A space-time finite element method for structural acoustics in infinite domains part 1: Formulation, stability and convergence. *Computer Methods in Applied Mechanics and Engineering*, 132(3):195–227, June 1996.

[76] Michael Dumbser. *Arbitrary High Order Schemes for the Solution of Hyperbolic Conservation Laws in Complex Domains*. Shaker Verlag GmbH, Germany, Aachen, 2005.

[77] Bernardo Cockburn, George E. Karniadakis, Chi-Wang Shu, M. Griebel, D. E. Keyes, R. M. Nieminen, D. Roose, and T. Schlick, editors. *Discontinuous Galerkin Methods: Theory, Computation and Applications*, volume 11 of *Lecture Notes in Computational Science and Engineering*. Springer Berlin Heidelberg, Berlin, Heidelberg, 2000.

[78] Martin Käser and Michael Dumbser. An arbitrary high-order discontinuous Galerkin method for elastic waves on unstructured meshes - I. The two-dimensional isotropic case with external source terms. *Geophysical Journal International*, 166(2):855–877, August 2006.

[79] Michael Dumbser and Martin Käser. An arbitrary high-order discontinuous Galerkin method for elastic waves on unstructured meshes - II. The three-dimensional isotropic case. *Geophysical Journal International*, 167(1):319–336, October 2006.

[80] Josep de la Puente, Martin Käser, Michael Dumbser, and Heiner Igel. An arbitrary high-order discontinuous Galerkin method for elastic waves on unstructured meshes - IV. Anisotropy. *Geophysical Journal International*, 169(3):1210–1228, June 2007.

[81] Bing Tie, Anne-Sophie Mouronval, V Nguyen, L. Series, and Deny Aubry. A unified variational framework for the space discontinuous Galerkin method for elastic wave propagation in anisotropic and piecewise homogeneous media. *Computer Methods in Applied Mechanics and Engineering*, 338:299–332, August 2018.

[82] Bing Tie and Anne-Sophie Mouronval. Systematic development of upwind numerical fluxes for the space discontinuous Galerkin method applied to elastic wave propagation in anisotropic and heterogeneous media with physical interfaces. *Computer Methods in Applied Mechanics and Engineering*, 372:113352, December 2020.

[83] Bernardo Cockburn, San-Yih Lin, and Chi-Wang Shu. TVB Runge-Kutta local projection discontinuous Galerkin finite element method for conservation laws III: One-dimensional systems. *Journal of Computational Physics*, 84(1):90–113, September 1989.

[84] Bernardo Cockburn and Chi-Wang Shu. The Runge-Kutta local projection -discontinuous-Galerkin finite element method for scalar conservation laws. *ESAIM: Mathematical Modelling and Numerical Analysis*, 25(3):337–361, 1991. Number: 3 Publisher: EDP Sciences.

[85] Bernardo Cockburn and Chi-Wang Shu. The Runge–Kutta Discontinuous Galerkin Method for Conservation Laws V: Multidimensional Systems. *Journal of Computational Physics*, 141(2):199–224, April 1998.

[86] Bernardo Cockburn, Suchung Hou, and Chi-Wang Shu. The Runge-Kutta Local Projection Discontinuous Galerkin Finite Element Method for Conservation Laws. IV: The Multidimensional Case. *Mathematics of Computation*, 54(190):545, April 1990.

[87] T. Warburton. A Low-Storage Curvilinear Discontinuous Galerkin Method for Wave Problems. *SIAM Journal on Scientific Computing*, 35(4):A1987–A2012, January 2013. Publisher: Society for Industrial and Applied Mathematics.

[88] Ruichao Ye, Maarten V. de Hoop, Christopher L. Petrovitch, Laura J. Pyrak-Nolte, and Lucas C. Wilcox. A discontinuous Galerkin method with a modified penalty flux for the propagation and scattering of acousto-elastic waves. *Geophysical Journal International*, 205(2):1267–1289, May 2016.

[89] Jesse Chan. Weight-adjusted discontinuous Galerkin methods: Matrix-valued weights and elastic wave propagation in heterogeneous media. *International Journal for Numerical Methods in Engineering*, 113(12):1779–1809, 2018. _eprint: https://onlinelibrary.wiley.com/doi/pdf/10.1002/nme.5720.

[90] Khemraj Shukla, Jesse Chan, Maarten V. de Hoop, and Priyank Jaiswal. A weight-adjusted discontinuous Galerkin method for the poroelastic wave equation: Penalty fluxes and micro-heterogeneities. *Journal of Computational Physics*, 403:109061, February 2020.

[91] Kaihang Guo, Sebastian Acosta, and Jesse Chan. A weight-adjusted discontinuous Galerkin method for wave propagation in coupled elastic-acoustic media. *Journal of Computational Physics*, 418:109632, October 2020.

[92] Paola F. Antonietti, Francesco Bonaldi, and Ilario Mazzieri. A high-order discontinuous Galerkin approach to the elasto-acoustic problem. *Computer Methods in Applied Mechanics and Engineering*, 358:112634, January 2020.

[93] P.F. Antonietti and I. Mazzieri. High-order Discontinuous Galerkin methods for the elastodynamics equation on polygonal and polyhedral meshes. *Computer Methods in Applied Mechanics and Engineering*, 342:414–437, December 2018.

[94] Qiwei Zhan, Qiang Ren, Mingwei Zhuang, Qingtao Sun, and Qing Huo Liu. An exact Riemann solver for wave propagation in arbitrary anisotropic elastic media with fluid coupling. *Computer Methods in Applied Mechanics and Engineering*, 329:24–39, February 2018.

[95] Qiwei Zhan, Mingwei Zhuang, Yiqian Mao, and Qing Huo Liu. Unified Riemann solution for multi-physics coupling: Anisotropic poroelastic/elastic/fluid interfaces. *Journal of Computational Physics*, 402:108961, February 2020.

[96] Thomas J. R. Hughes and Gregory M. Hulbert. Space-time finite element methods for elastodynamics: Formulations and error estimates. *Computer Methods in Applied Mechanics and Engineering*, 66(3):339–363, February 1988.

[97] X. D. Li and N. E. Wiberg. Implementation and adaptivity of a space-time finite element method for structural dynamics. *Computer Methods in Applied Mechanics and Engineering*, 156(1):211–229, April 1998.

[98] Bing Tie, Denis Aubry, and Arnaud Boullard. Adaptive computation for elastic wave propagation in plate/shell structures under moving loads. *Revue Européenne des Éléments Finis*, 12(6):717–736, January 2003.

[99] Bing Tie and Denis Aubry. Adaptive time discontinuous Galerkin method for numerical modelling of wave propagation in shell and 3D structures. *European Journal of Computational Mechanics*, pages 729–757, June 2006.

[100] B. Tie, D. Aubry, A.-S. Mouronval, D. Solas, J. Thébault, B.-Y. Tian, Jane W. Z. Lu, Andrew Y. T. Leung, Vai Pan Iu, and Kai Meng Mok. High Frequency Elastic Wave Propagation in Media with a Microstructure. pages 299–304, Hong Kong- Macau (China), 2010.

[101] Bing Tie, Denis Solas, Julien Thébault, Colette Rey, Thierry Baudin, and Anne-Sophie Mouronval. Modélisation numérique de la propagation des ultrasons dans des milieux polycristallins. In Société Française d'Acoustique SFA, editor, *10ème Congrès Français d'Acoustique*, pages –, Lyon, France, April 2010.

[102] Bing Tie. Remaillage adaptatif et contrôle d erreurs en quantité d intérêt pour la modélisation numérique de la propagation des ondes élastiques. In *10e colloque national en calcul des structures*, page Clé USB, Giens, France, May 2011.

[103] A. Grédé, B. Tie, and D. Aubry. Elastic wave propagation in hexagonal honeycomb sandwich panels: Physical understanding and numerical modeling. *Journal de Physique IV (Proceedings)*, 134:507–514, August 2006. Publisher: EDP Sciences.

[104] Bill Kapralos, Michael Jenkin, and Evangelos Milios. Sonel Mapping: A Probabilistic Acoustical Modeling Method. *Building Acoustics*, 15(4):289–313, December 2008.

[105] Ru-Shan Wu and Keiiti Aki. Introduction: Seismic wave scattering in three-dimensionally heterogeneous earth. *pure and applied geophysics*, 128(1):1–6, March 1988.

[106] Mi-Kyung Yoon. Seismische Abbilder heterogener Medien:.

[107] Claude Boutin. Rayleigh scattering of acoustic waves in rigid porous media. *The Journal of the Acoustical Society of America*, 122:1888–905, November 2007.

[108] Oleg Godin. Rayleigh scattering of a spherical sound wave. *The Journal of the Acoustical Society of America*, 133:709–20, February 2013.

[109] Guillaume Bal. Kinetics of scalar wave fields in random media.

[110] Donald O. Thompson and Dale E. Chimenti, editors. *Review of Progress in Quantitative Nondestructive Evaluation: Volume 3A*. Springer US, Boston, MA, 1984.

[111] Xue Bai. Modélisation par éléments finis de la propagation des ondes ultrasonores dans des matériaux polycristallins. page 140.

[112] Yih-Hsing Pao. Dynamical Stress Concentration in an Elastic Plate. *Journal of Applied Mechanics*, 29(2):299–305, June 1962.

[113] Robert P. Banaugh and Werner Goldsmith. Diffraction of Steady Elastic Waves by Surfaces of Arbitrary Shape. *Journal of Applied Mechanics*, 30(4):589–597, December 1963.

[114] C. C. Mow and Y. H. Pao. The Diffraction of Elastic Waves and Dynamic Stress Concentrations. Technical report, RAND Corporation, January 1971.

[115] H. L. Wong. Effect of surface topography on the diffraction of P, SV, and Rayleigh waves. *Bulletin of the Seismological Society of America*, 72(4):1167–1183, August 1982.

[116] Francisco J. Sánchez-Sesma, L. Eduardo Pérez-Rocha, and Sergio Chávez-Pérez. Diffraction of elastic waves by three-dimensional surface irregularities. Part II. *Bulletin of the Seismological Society of America*, 79(1):101–112, February 1989.

[117] J. S. Martin, G. D. Larson, and W. R. Scott, Jr. An investigation of surface-contacting sensors for the seismic detection of buried landmines. *The Journal of the Acoustical Society of America*, 120(5):2676–2685, November 2006.

[118] Steve S. T. Ho, Ilene J. Busch-Vishniac, and David T. Blackstock. Noise reduction by a barrier having a random edge profile. *The Journal of the Acoustical Society of America*, 101(5):2669–2676, May 1997.

[119] Eric Johnsen and Tim Colonius. Shock-induced collapse of a gas bubble in shockwave lithotripsy. *The Journal of the Acoustical Society of America*, 124(4):2011–2020, October 2008.

[120] J. E. Gubernatis, E. Domany, and J. A. Krumhansl. Formal aspects of the theory of the scattering of ultrasound by flaws in elastic materials. *Journal of Applied Physics*, 48(7):2804–2811, July 1977. Publisher: AIP Publishing.

[121] Fred E. Stanke and G. S. Kino. A unified theory for elastic wave propagation in polycrystalline materials. *The Journal of the Acoustical Society of America*, 75(3):665–681, March 1984.

[122] Sigrun Hirsekorn. The scattering of ultrasonic waves in polycrystalline materials with texture. *The Journal of the Acoustical Society of America*, 77(3):832–843, March 1985.

[123] R. L. Weaver. Diffusivity of ultrasound in polycrystals. *Journal of the Mechanics and Physics of Solids*, 38(1):55–86, January 1990.

[124] A. B. Bhatia. Scattering of High-Frequency Sound Waves in Polycrystalline Materials. *The Journal of the Acoustical Society of America*, 31(1):16–23, July 2005.

[125] Xue Bai. *Modélisation par éléments finis de la propagation des ondes ultrasonores dans des matériaux polycristallins*. phdthesis, Université Paris-Saclay, February 2017.

[126] X. Bai, B. Tie, J. H. Schmitt, and D. Aubry. Finite element modeling of grain size effects on the ultrasonic microstructural noise backscattering in polycrystalline materials. *Ultrasonics*, 87:182–202, July 2018.

[127] X. Bai, B. Tie, J. H. Schmitt, and D. Aubry. Comparison of ultrasonic attenuation within two- and three-dimensional polycrystalline media. *Ultrasonics*, 100:105980, January 2020.

[128] Adrien Renaud, Bing Tie, Anne-Sophie Mouronval, and Jean-Hubert Schmitt. Multi-parameter optimization of attenuation data for characterizing grain size distributions and application to bimodal microstructures. *Ultrasonics*, 115:106425, August 2021.

[129] J. R. Willis. Polarization approach to the scattering of elastic waves–I. Scattering by a single inclusion. *Journal of the Mechanics and Physics of Solids*, 28(5):287–305, December 1980.

[130] F.J. Sabina and J.R. Willis. A simple self-consistent analysis of wave propagation in particulate composites. *Wave Motion*, 10(2):127–142, April 1988.

[131] J. R. Willis. A polarization approach to the scattering of elastic waves–II. Multiple scattering from inclusions. *Journal of the Mechanics and Physics of Solids*, 28(5):307–327, December 1980.

[132] F Sabina, V. P. Smyshlyaev, and J. R. Willis. Self-consistent analysis of waves in a matrix-inclusion composite–I. Aligned spheroidal inclusions. *Journal of the Mechanics and Physics of Solids*, 41(10):1573–1588, October 1993.

[133] P.G.J. Bussink, P.L. Iske, J. Oortwijn, and G.L.M.M. Verbist. Self-consistent analysis of elastic wave propagation in two-dimensional matrix-inclusion composites. *Journal of the Mechanics and Physics of Solids*, 43(10):1673–1690, October 1995.

[134] V Smyshlyaev, J. R. Willis, and F. J. Sabina. Self-consistent analysis of waves in a matrix-inclusion composite–II. Randomly oriented spheroidal inclusions. *Journal of the Mechanics and Physics of Solids*, 41(10):1589–1598, October 1993.

[135] Jin-Yeon Kim. Models for wave propagation in two-dimensional random composites: A comparative study. *The Journal of the Acoustical Society of America*, 127(4):2201–2209, April 2010.

[136] P. C. Waterman and Rohn Truell. Multiple Scattering of Waves. *Journal of Mathematical Physics*, 2(4):512–537, July 1961. Publisher: American Institute of Physics.

[137] P. Lloyd and V. Berry M. Wave propagation through an assembly of spheres IV Relations between different multiple scattering theories. *Proc Phys Soc*, 91(3):678–688, 1967.

[138] S. K. Kanaun and V. M. Levin. Effective medium method in the problem of axial elastic shear wave propagation through fiber composites. *International Journal of Solids and Structures*, 40(18):4859–4878, September 2003.

[139] M. Kitahara, K. Nakagawa, and J. D. Achenbach. Boundary-integral equation method for elastodynamic scattering by a compact inhomogeneity. *Computational Mechanics*, 5(2-3):129–144, 1989.

[140] Yue-Sheng Wang and Duo Wang. Scattering of elastic waves by a rigid cylindrical inclusion partially debonded from its surrounding matrix—I. SH case. *International Journal of Solids and Structures*, 33(19):2789–2815, August 1996.

[141] Hirotaka Sato and Yasuhide Shindo. Influence of microstructure on scattering of plane elastic waves by a distribution of partially debonded elliptical inclusions. *Mechanics of Materials*, 34(7):401–409, July 2002.

[142] Zhongxian Liu, Fengjiao Wu, and Dong Wang. The multi-domain FMM-IBEM to model elastic wave scattering by three-dimensional inclusions in infinite domain. *Engineering Analysis with Boundary Elements*, 60:95–105, November 2015.

[143] Marijan Dravinski and Ramtin Sheikhhassani. Scattering of a plane harmonic SH wave by a rough multilayered inclusion of arbitrary shape. *Wave Motion*, 50(4):836–851, June 2013.

[144] Zhanli Liu, Jay Oswald, and Ted Belytschko. XFEM modeling of ultrasonic wave propagation in polymer matrix particulate/fibrous composites. *Wave Motion*, 50(3):389–401, April 2013.

[145] M. Kristekova, J. Kristek, P. Moczo, and S. M. Day. Misfit Criteria for Quantitative Comparison of Seismograms. *Bulletin of the Seismological Society of America*, 96(5):1836–1850, October 2006.

[146] Miriam Kristeková, Jozef Kristek, and Peter Moczo. Time-frequency misfit and goodness-of-fit criteria for quantitative comparison of time signals. *Geophysical Journal International*, 178(2):813–825, August 2009.

[147] Asim Biswas and Bing Cheng Si. Application of Continuous Wavelet Transform in Examining Soil Spatial Variation: A Review. *Mathematical Geosciences*, 43(3):379–396, April 2011.

[148] R. Hill. A self-consistent mechanics of composite materials. *Journal of the Mechanics and Physics of Solids*, 13(4):213–222, August 1965.

[149] B. Budiansky. On the elastic moduli of some heterogeneous materials. *Journal of the Mechanics and Physics of Solids*, 13(4):223–227, August 1965.

[150] Linda C. Sawyer, David T. Grubb, and Gregory F. Meyers. *Polymer Microscopy*. Springer, New York, NY, 2008.

[151] Simon C. W. Richardson, Kerri-Lee Wallom, Elaine L. Ferguson, Samuel P. E. Deacon, Matthew W. Davies, Alison J. Powell, Robert C. Piper, and Ruth Duncan. The use of fluorescence microscopy to define polymer localisation to the late endocytic compartments in cells that are targets for drug delivery. *Journal of Controlled Release*, 127(1):1–11, April 2008.

[152] Bartosz Gapinski, Piotr Janicki, Lidia Marciniak-Podsadna, and Michał Jakubowicz. Application of the Computed Tomography to Control Parts Made on Additive Manufacturing Process. *Procedia Engineering*, 149:105–121, January 2016.

[153] Angeles Castro-Sastre, Ana Isabel Fernández-Abia, Pablo Rodriguez-Gonzalez, Susana Martínez-Pellitero, and Joaquin Barreiro. Characterization of Materials Used in 3D-Printing Technology with Different Analysis Techniques. In Branko Katalinic, editor, *DAAAM Proceedings*, volume 1, pages 0947–0954. DAAAM International Vienna, 1 edition, 2018.

[154] Rachael M. Carew, Francesco Iacoviello, Carolyn Rando, Robert M. Moss, Robert Speller, James French, and Ruth M. Morgan. A multi-method assessment of 3D printed micromorphological osteological features. *International Journal of Legal Medicine*, 136(5):1391–1406, September 2022.

[155] Susan C Shelmerdine, Ian C Simcock, John Ciaran Hutchinson, Rosalind Aughwane, Andrew Melbourne, Daniil I Nikitichev, Ju-ling Ong, Alessandro Borghi, Garrard Cole, Emilia Kingham, Alistair D Calder, Claudio Capelli, Aadam Akhtar, Andrew C Cook, Silvia Schievano, Anna David, Sebastian Ourselin, Neil J Sebire, and Owen J Arthurs. 3D printing from microfocus computed tomography (micro-CT) in human specimens: education and future implications. *The British Journal of Radiology*, 91(1088):20180306, July 2018. Publisher: The British Institute of Radiology.

[156] Maria Vittoria Spampinato, Ahad Abid, and Maria Gisele Matheus. Current Radiographic Iodinated Contrast Agents. *Magnetic Resonance Imaging Clinics of North America*, 25(4):697–704, November 2017.